Elementary exciton mediated Raman scattering mechanisms in pristine and functionalized single walled carbon nanotubes

Dissertation

zur Erlangung des Grades eines Doktors der Naturwissenschaften am
Fachbereich Physik der Freien Universität Berlin

eingereicht von
Georgy Gordeev

Berlin, im März 2019

Erstgutachter:	Prof. Dr. Stephanie Reich
Zweitgutachter:	Prof. Dr. Ralph Krupke
Tag der Abgabe:	08.03.2019
Tag der Disputation:	11.04.2019

“All my life through, the new sights of Nature made me rejoice like a child”

Marie Curie

Abstract

In this work I study the fundamental scattering mechanisms mediated by the exciton (coupled electron and hole). The nanotube excitons have extremely high binding energies and unfold in states of different symmetries and center of mass momenta. Bright states couple directly to light and dark states, only when assisted by phonons. The exciton-induced light-matter coupling in carbon nanotubes is studied in this work. First, I demonstrate, how the phonon-mediated scattering pathways between the bright and dark states alter the resonance Raman profiles of the G mode at the second excitonic transition (E_{22}). These pathways induce a translation-like asymmetry in the Stokes and anti-Stokes profiles, where the incoming resonance dominates for the Stokes and outgoing resonance dominates for the anti-Stokes processes. Measured resonance profiles of the G mode were reproduced by fifth-order perturbation theory. The correlated analysis of the Raman profiles yield a chiral dependence of exciton-phonon matrix elements, reflecting coupling strength between them. The chiral dependence of the matrix elements agrees well with the values obtained by tight-binding calculations.

Exciton-photon coupling in carbon nanotubes increases by reducing the exciton transition number or transition energy. I verified this by comparing the resonance Raman profiles between the E_{11} and E_{22} transitions. The coupling between the bright and dark excitons and the phonons increases by three times inducing a 30 times increase in the Raman intensity at the E_{11} compared to the E_{22} transition. The exciton-photon coupling in carbon nanotubes is very strong and results in exciton-polariton formation. I propose a theory that incorporates polaritons into the description of the Raman process in nanotubes. The dispersion of the 2D mode excited via the bright E_{22} exciton was measured in five nanotube chiralities. The dispersion shows three distinct slopes determined by the spatial dispersion of the exciton polariton. The dark state provided by the first exciton is the dominant intermediate step in the Raman process of the 2D mode. The same dark state participates in the scattering, when the 2D mode is excited via the bright transition of the first exciton. This assignment is corroborated by comparing the dispersion of the 2D mode between the second and first transitions measured for three nanotube chiralities. I performed a simulation by fourth-order perturbation theory for the (6,5) 2D mode, with implemented exciton-polariton effects. The simulated resonance Raman profiles, as well as the 2D mode dispersion, agreed very well with the experimental data. The model presented here, succeeded for the first time to provide a coherent framework for the exciton-based Raman process in carbon nanotubes.

I modify the vibrational properties of the nanotubes by applying covalent functionalizations. Three approaches were probed: [2+1] cycloaddition, light activated reaction with diazonium bromide salt, and carboxylation. Cycloaddition changes the RBM, G, and 2D phonons in metallic nanotubes. The dominant mechanism for these effects is the electron-phonon interaction, where additional charge carriers are provided by the functional groups. The resonant analysis of the G mode yields stronger effects for nanotubes with smaller diameters. For the functionalization with DzBr we developed a new approach, where the vibrational properties are monitored in-situ during the functionalization. This enabled a precise control over the local reaction by laser power. The incident light shed onto the sample has two functions; it excites the Raman process and drives the local reaction. The lateral Raman mapping of the defect density over the functionalization yielded a Gaussian distribution of the defects, where a Gaussian beam profile was used for the activation. The chiral selectivity of the reaction was confirmed by the analysis of the bright exciton energies, obtained from resonance Raman profiles of the RBMs. The resonant nanotube chirality has the largest shift of the E_{22} transition energy due to the functionalization. The carboxylation induces strain and doping in the nanotube. The strain is identified by the shift of the optical transition energies in the nanotubes. Both strain and doping account for the strong modification of the G and 2D modes in metallic and semiconducting nanotubes.

1 | Introduction

Single walled carbon nanotubes (CNTs) are nanoscale tubular systems build out of a hexagonal carbon lattice. Since their discovery they have been a puzzling object of research due to their highly crystalline, symmetric, and one-dimensional structure [1,2]. A CNT is a unique object with a diameter in the nanometer range and length in the micrometer range bridging the molecular and solid state worlds [3]. Many applications of carbon nanotubes have been already realized including an excellent implementation in electrical circuits [4–6], mechanical resonators [7,8] actuators [9], and photonic devices [10]. In addition to its high potential in many different applications, the low dimensionality and high symmetry of the CNT yield a plethora of new physical phenomena [11–13]. One of the most remarkable properties of nanotubes is the presence of room temperature excitons (bound states of electrons and holes) [14]. The CNT excitons unfold in series of bright and dark states and have extremely large binding energies (up to 1 eV) [15,16]. These binding energies allow the excitonic effects to govern the optical properties at high temperatures [14], whereas the standard three dimensional semiconductors demonstrate such effects only at cryogenic temperatures [17].

Although the excitonic nature of optical transitions has been long since been proven [14], only a few experimental and theoretical works were focused on exciton specific interactions with light. The exciton induces an energy mismatch between the electrical and the optical bandgaps [18] and imposes optical selection rules [19]. Low dimensionally CNT excitons and phonons form coupled states modifying the absorbance, photoluminescence and photoconductivity responses of the nanotube [20–22]. Inelastic light scattering is also altered through the interaction with an exciton. This applies particularly to Raman scattering, comprising energy and momentum exchange between light and optical lattice vibrations.

Raman scattering is a perfect tool, designed by nature, to study exciton-photon and exciton-phonon interactions. The Raman cross section of nanotubes is remarkably high, e. g. allowing investigations of a single CNT. This occurs due to the strong exciton-phonon and exciton-photon coupling in nanotubes during the scattering process. Resonant Raman spectroscopy permits the analysis of scattering efficiency and phonon energies as function of excitation wavelength. This provides details about the excitonic states involved in the scattering, gives us insights into the intrinsic scattering mechanisms, and allows us to evaluate the coupling factors.

In Chapter 2, I focus on the structural and transition energy dependence of the exciton-phonon coupling. Nanotubes exist in a large variety of chiralities (rolling options of a graphene sheet). The chirality of the tube defines points on the graphene lattice, where the exciton forms and interacts with the lattice. By selecting a specific nanotube chirality one can “tune” the strength of the exciton-phonon interaction and increase or decrease the coupling between them. In order to understand that, I investigate the asymmetry of the G mode resonance Raman profiles, where the intensity of the phonon mode is plotted over the excitation energy, in Section 2.3. The asymmetry occurs due to the strong coupling between the exciton and phonon enabling higher order scattering pathways between the dark and bright excitonic states [23–25]. The scattering pathways compete with one another, creating a stronger or a weaker asymmetry in the Raman profile. However, many coupling factors (matrix elements) altering the Raman cross sections are unknown; the Stokes profile is insufficient to unambiguously define them. I will show how the combination of the Stokes

and anti-Stokes profiles yields matrix elements that are proportional to the coupling strength. Thus, the phonon coupling between the dark and bright excitons is compared in four different chiralities. The chiral dependence of exciton-phonon coupling is confirmed through the calculation by the tight binding method.

For a fixed nanotube chirality, different transitions can form an exciton (i.e. symmetric pairs of the valence and conduction bands) [26]. The change in transition number enables an additional degree of freedom on the model graphene lattice system. Similar to the change of chirality, it alters the exciton-phonon coupling [27]. The reduction of transition number positions the exciton-phonon interaction closer to the K point in the graphene lattice. I explore the changes in the exciton-phonon coupling by acquiring resonance Raman profiles of the Brillouin zone (BZ) centre phonon for the first and the second excitonic transitions of CNTs within the same chiralities in Section 2.4. By analysing the relative intensities and the asymmetries of the Raman profiles, the 3-4x stronger exciton-phonon coupling is obtained for the first excitonic transition compared to the second excitonic transition. The increase in coupling efficiency occurs between both dark- and bright-exciton phonons channels. In the beginning of Chapter 2, I introduce the basic concepts of CNT physics. I briefly describe structural, electronic and vibrational properties, as well as the structure of excitonic states and its coupling to the vibrational states. To understand the details of different Raman scattering mechanism, I also give a summary of the perturbation theory and its primary application for resonance Raman profiles.

The low-dimensional coupling between photon and exciton is another unique aspect of the Raman scattering process, which I explore in Chapter 3. It differs in many ways from coupling between electron and photon in conventional semiconductor crystals. The electron-photon interaction occurs in the whole BZ, with all electronic states participating simultaneously. Whereas inside an excitonic crystal the light propagates in the form of an exciton-polariton (EP), a quasiparticle formed by a single coupled pair of e-h states (exciton) and photon. The EP has energy equal to the energy of the incident photon, and has a left-right anisotropy, multiple branches, and can carry and share the momentum acquired from excitonic component. The momentum-energy exchange between the incident photon and the scattered phonon(-s), which depends on the excitation energy portrays the spatial dispersion of the EP.

The energy of the BZ centre phonons is fixed, which prevents the investigation of effects induced by photon-exciton coupling. Theses phonons have a flat dispersion relation and a relatively small range of resonant phonon wave vectors is involved in the scattering. The phonons away from the BZ centre allow a greater selection of strongly dispersive phonons. The double resonant Raman scattering mechanism in carbon materials offers two Raman modes D and 2D, allowing the study exciton-polariton mediated effects. The 2D mode is preferable, as it is formed by two K point phonons and stronger effects are expected (larger displacement of phonon frequency with excitation energy). The first phonon scatters the bright exciton into the dark state and the second scatters the dark exciton back into the bright state. I study two different scattering configurations for a number of nanotube chiralities.

- The bright exciton is excited at the second transition (E_{22}) and scattered by the K phonons into the dark exciton from the first excitonic transition (E_{11}).
- The bright exciton is excited in the first excitonic transition (E_{11}) and is scattered into the dark exciton from the same first transition (E_{11}).

The change of the 2D mode energy with respect to the excitation energy (2D mode dispersion) exhibits the behaviour determined by the exciton-polariton spatial dispersion (energy momentum dependence). The simulations in the framework of fourth-order perturbation theory have reproduced the 2D mode scattering efficiency and energy for both scattering configurations. In the beginning of the Chapter 3, I give an introduction for inelastic scattering selection rules by exciton-polariton and double resonant Raman scattering in carbon materials.

Finally, I explore the ways to modify the phonons in a fixed nanotube chirality and transition in Chapter 4. Compared to multi-dimensional solid-state systems both optical excitation and lattice vibrations can be easier amended in the CNT. The one-dimensional structure of the nanotube allows an easy access to its physical properties through the surface. Pursuing this goal, I apply different covalent approaches to functionalize the nanotube walls by molecules. On the other hand, the covalent methods are advantageous over non-covalent ones as they provide a highly stable molecule-tube hybrid. Further, the covalent bond perturbs the carbon network of the nanotube introducing strong changes in the lattice and altering electronic states. This allows functional moieties to tune the lattice vibrations. The capacities to change the phonons in the three different covalent approaches were tested; [2+1] cycloaddition, light activated diazonium salts functionalization, and carboxylation as discussed in Sections 4.2 - 4.4.

In Section 4.2 I explore the vibrational properties of the nanotubes after [2+1] cycloaddition. This type of covalent functionalization preserves the sp^2 hybridization of C-C bonds in the nanotube. The [2+1] cycloaddition efficiently changes energies of the metallic RBM, G, and 2D phonons. The frequency and lifetime of the phonon are tuned through electron-phonon coupling. The overlap of the molecular orbitals with electronic states of the nanotube induces a change in the Fermi level. The cycloaddition induced effects increase the nanotube diameter, as I demonstrate by resonant Raman scattering of the G mode. Unfortunately, this method is incapable of changing the semiconducting phonons, requiring a different covalent approach valid for semiconducting phonons.

The diazonium bromide reaction has been reported to successfully functionalize semiconducting nanotube species [28]. It provides a way of selectively functionalizing any semiconducting species by matching the energies of the activation light with the transition of this particular nanotube [29,30]. We developed a new approach, outlined in Section 4.3, where the vibrational properties of the nanotube are probed in situ during the functionalization. This allowed us to study the reaction kinetics, which enabled excellent control over the phonon energies and the reaction product. The D and G modes continuously upshift their frequencies in accordance with the number of attached molecules. Each functional molecule creates a defect by resetting the hybridization of carbon atoms, from sp^2 to sp^3. The concentration of defects progresses with the phonon density inducing a Gaussian distribution of defects under the laser spot, where a Gaussian beam profile was used to activate the reaction. The chiral selectivity of the reaction has been confirmed by the deviating shift on the exciton transition energies, where the transition energy of the nanotube resonant with activation light undergoes the largest shift. The transition energies are studied by resonant Raman spectroscopy of radial breathing modes.

The carboxylation is the last approach I probe in Subchapter 4.4. This approach is especially useful, as the –COOH functional group interacts both with metallic and semiconducting phonons. The width of the G mode phonon in metallic and semiconducting species increased due to a high concentration of defects (D/G intensity ratio > 0.6). The doping also alters the G phonon lifetimes,

although with the reversed effects for phonons in metallic and semiconducting nanotubes. The width of the G mode in semiconducting (metallic) nanotubes increases (decreases) with doping. Doping and strain both linearly contribute to the shift of Raman modes. The amount and type of the strain is deduced by the analysis of transition energies in semiconducting phonons. The expansive strain induces a downshift of the 2D mode, whereas the hole doping leads to an increase of the 2D mode. All approaches are evaluated by their capacity to change the frequencies and lifetimes of the phonons in metallic and semiconducting nanotubes. In the beginning of Chapter 4, I present the theoretical background for the electron-phonon coupling studied by correlated Raman measurement and electrochemical gating. I also give an overview over studies reporting the transition energies dependence of the tubes undergoing uniaxial strain and dielectric screening in order to understand the effects of functionalization.

Contents

Abstract ..... (i)
1 |**Introduction** 1
2 |Exciton-phonon coupling in CNTs 7
2.1 Theoretical background 7
2.1.1 Structural properties 7
2.1.2 Vibrational properties 9
2.1.3 Electronic properties 11
2.1.4 Excitonic properties 13
2.1.5 Coupled states of excitons and phonons 16
2.1.6 Microscopic theory of Raman scattering 17
2.1.7 Resonant Raman scattering in carbon nanotubes 21
2.1.8 Fifth-order perturbation theory 25
2.2 Experimental methods 29
2.2.1 Single chirality enrichment by gel permeation chromatography 29
2.2.2 Resonant Raman spectroscopy setup 30
2.2.3 Calibration of Raman spectra 33
2.3 Chirality dependence of exciton-phonon coupling 35
2.3.1 Introduction 35
2.3.2 Manifestation of the Boltzmann factor 36
2.3.3 Determination of the E22 transition energies by resonant Raman 37
2.3.4 Fifth-order perturbation theory for Stokes and anti-Stokes scattering 39
2.3.5 Anti-Stokes resonance Raman profiles 41
2.3.6 Theory of the exciton-phonon matrix element calculation 45
2.3.7 Summary 49
2.4 Transition dependence of Exciton-Phonon coupling 50
2.4.1 Introduction 50
2.4.2 Asymmetric resonance Raman profiles at the first excitonic transition 51
2.4.3 Transition number dependence of the exciton-phonon matrix element 53
2.4.4 Summary 56
3 |Exciton photon coupling in CNTs 57
3.1 Theoretical background 58
3.1.1 Exciton-polaritons in semiconducting crystals 58
3.1.2 Double resonant Raman scattering in carbon materials 61
3.1.3 Phonon dispersion in carbon nanotubes 63
3.2 Resonant Raman scattering by exciton-polaritons in CNT 64
3.2.1 Scattering mechanism between the exciton polariton (EP) and dark excitonic state 64
3.2.2 Resonant behavior of the 2D mode at the second excitonic transition 66
3.2.3 Scattering via bright E11 excitonic state 72
3.2.4 Simulation of the 2D mode in (6,5) nanotube 74
3.2.5 Conclusion 76
4 |Electron-phonon coupling in CNTs 77

4.1 Theoretical background ... 77
4.1.1 Doping induced effects in carbon nanotube ... 78
4.1.2 Strain and screening effects ... 80
4.2 **[2+1] Cycloaddition** ... 81
4.2.1 Optical and XPS characterization of functionalized ... 82
4.2.2 Electron-phonon coupling ... 83
4.3 **Diazonium salt functionalization** ... 114
4.3.1 In situ reaction tuning ... 90
4.3.2 Influence of the photon density ... 93
4.3.3 Chiral selectivity of the reaction ... 96
4.4 **Carboxylation, strain and doping disentanglement** ... 100
4.5.1 Structural effects in the nanotubes, evaluation of strain ... 101
4.5.2 Electron-phonon coupling in metallic COOH-nanotubes ... 103
4.5.3 Electron-phonon coupling in semiconducting COOH-nanotubes ... 104
4.5.4 Conclusion ... 105
4.5 Summary over studied functionalization methods ... 106
5 |Summary ... 107
Zusammenfassung ... 111
Appendix A: 2D mode calculation details ... 112
Appendix B: Functionalization routines and methods ... 113
List of publications ... 116
Acknowledgments ... 116
Bibliography ... 118
Selbstständigkeitserklärung ... 127

2 | Exciton-phonon coupling in CNTs

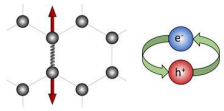

2.1 Theoretical background

2.1.1 Structural properties of CNTs

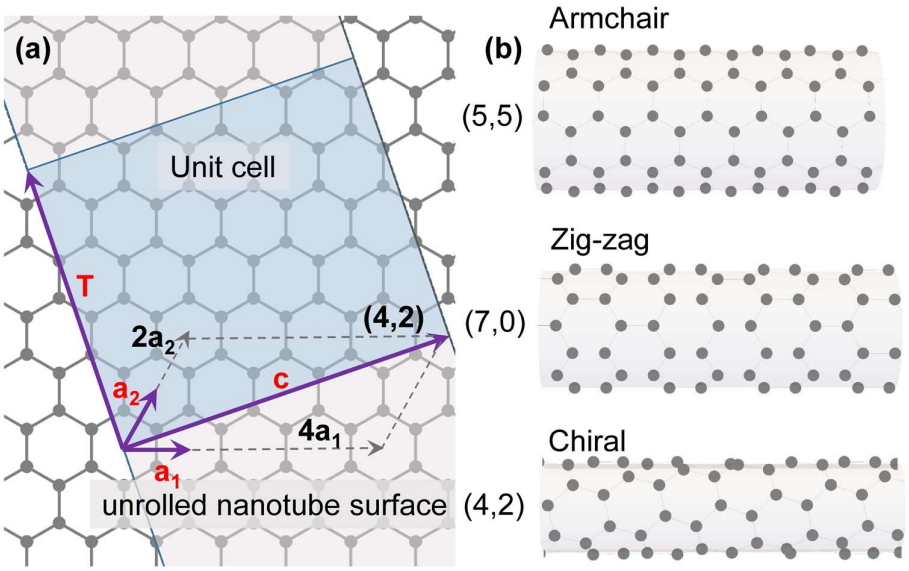

Figure 2.1 *Origins of different (n,m) chiralities in carbon nanotubes.* ***(a)*** *Representation of unrolled (4,2) carbon nanotube is illustrated on a graphene sheet. Chiral vector c is the vector sum of graphene unit vectors* $\boldsymbol{a_1}$ *and* $\boldsymbol{a_2}$*. Translational vector* $\boldsymbol{T}$ *is orthogonal to* $\boldsymbol{c}$ *and reflects the translational symmetry of the one dimensional nanotube system. The blue area marks the unit cell of (4,2) nanotubes.* ***(b)*** *Rolled nanotubes of different (5,5), (7,0), and (4,2) chiralities, representing three structural types of SWCNTs armchair, zigzag, and chiral, respectively.*

In this section, I summarize basic concepts related to the physical properties of carbon nanotubes serving as a background of this work [14-70]. The structure of a carbon nanotube can be reconstructed in real space from the 2D hexagonal lattice of graphene, see Figure 2.1. The graphene crystal basis consists of two lattice vectors $\boldsymbol{a_1}$ and $\boldsymbol{a_2}$, with $|\boldsymbol{a_1}| = |\boldsymbol{a_2}| = 2.461$ Å $= a_0$. The chiral vector equals

$$c = n\boldsymbol{a_1} + m\boldsymbol{a_2}, \tag{2.1}$$

where the chiral numbers n and m with $n > m$. Each pair of chiral indices (n, m) represents a unique nanotube species and stands for its chirality. I will show later that, one can derive structural and electronic properties from the chirality of the tube. The diameter of a carbon nanotube can be obtained from the length of the chiral vector

$$d = \frac{|c|}{\pi} = \frac{a_0\sqrt{n^2 + nm + m^2}}{\pi}. \tag{2.2}$$

The translation vector then takes the form of

$$\boldsymbol{T} = \frac{2m+n}{nR}\boldsymbol{a_1} - \frac{2n+m}{nR}\boldsymbol{a_2}, \tag{2.3}$$

with the length

$$|\boldsymbol{T}| = \frac{\sqrt{3n^2+nm+m^2}}{N_r R}a_0. \tag{2.4}$$

where $R = 3$ if $(n-m)$ is an integer and $R = 1$ otherwise. N_r is the greatest common divisor of n and m. The number of carbon atoms in the primitive cell of the nanotube is $2q$, with [31]

$$q = \frac{2(n^2+m^2+nm)}{N_r R}, \tag{2.5}$$

The chiral angle is then an angle between $\boldsymbol{a_2}$ and $\boldsymbol{c}$ with

$$\cos\theta = \frac{\boldsymbol{a_1 c}}{|\boldsymbol{a_1}||\boldsymbol{c}|} = \frac{n+m/2}{\sqrt{n^2+nm+m^2}}. \tag{2.6}$$

The θ in zigzag tubes with chiral indices of $(m=0)$ equals 0º, in armchair tubes $(n=m)$ θ equals 30º. In chiral tubes (n,m), with $n \neq m \neq 0$, the chiral angle can take values $0 < \theta < 30$ º.

To apply the concepts of solid-state physics the reciprocal lattice vectors need to be implemented, see Figure 2.2a and b. The lattice vectors of reciprocal space are obtained by the relation $a_i k_i = 2\pi\delta_{ij}$

$$\boldsymbol{k_1} = \left(\frac{1}{\sqrt{3}}, 1\right)\frac{2\pi}{a_0}, \qquad \boldsymbol{k_2} = \left(\frac{1}{\sqrt{3}}, -1\right)\frac{2\pi}{a_0}. \tag{2.7}$$

Unlike the Brillouin zone of graphene, where **k** values are not restricted, in carbon nanotubes periodic boundary condition along the circumference limits the possible values of **k**.

$$k_{\perp,l} = \frac{2\pi}{\lambda} = \frac{2\pi}{|c|} = \frac{2}{d}l, \tag{2.8}$$

with l taking integer values from $-\frac{q}{2}$+1,…0,1,…. $\frac{q}{2}$ and λ being the wavelength. The tube axis is considered continuous between $-\pi/|T|$ and $\pi/|T|$. The reciprocal lattice vectors, representing quantized waves are obtained for a (n,m) carbon nanotube by a similar relation as for graphene

$$\begin{aligned} \boldsymbol{k_\perp}\cdot\boldsymbol{c} &= 0, \quad \boldsymbol{k_\perp}\cdot\boldsymbol{T} = 2\pi \\ \boldsymbol{k_z}\cdot\boldsymbol{c} &= 0, \quad \boldsymbol{k_z}\cdot\boldsymbol{T} = 2\pi. \end{aligned} \tag{2.9}$$

The system above yields the following reciprocal lattice vectors of a nanotube [32]

$$\boldsymbol{k_\perp} = \frac{2n+m}{qgR}k_1 + \frac{2m+n}{qgR}k_2 \tag{2.10}$$

$$\boldsymbol{k_z} = \frac{m}{q}k_1 + \frac{mn}{q}k_2. \tag{2.11}$$

$\boldsymbol{k_z}$ is the vector along the tube axis and $\boldsymbol{k_\perp}$ the vector along the nanotube circumference, see Figure 2.2c. The system of allowed wave vectors $\boldsymbol{k_\perp}$ and $\boldsymbol{k_z}$ form parallel lines. These lines are often referred as cutting lines. The number of cutting lines N equals the number of hexagons in the primitive cell of the nanotube.

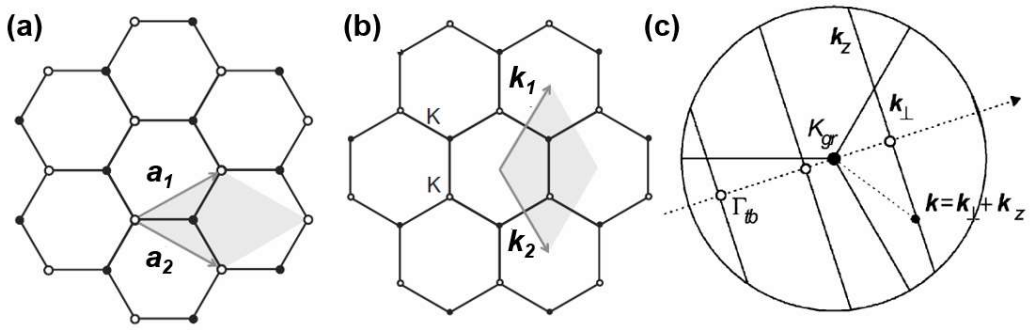

Figure 2.2 *The change of graphene lattice basis from real space (**a_1,a_2**) in **(a)** to reciprocal space (**k_1,k_2**) in **(b)** and **(c)** allowed momentum states in carbon nanotube (**k_z,$k_\perp$**), adapted from* 26*. The cutting lines in one graphene hexagon with allowed wave vectors of carbon nanotube, adapted from Ref.* [32].

$$N = 2 \cdot \frac{n^2 + nm + m^2}{NR}. \tag{2.12}$$

The cutting lines can be translated into the hexagonal unit cell of graphene. These lines "cut" electronic and vibrational states of graphene into the zones of allowed wave vectors [33]. The concept is called zone folding and provides a good first approximation for the properties of the nanotubes [1,34–37]. I will further discuss vibrational and electronic properties of the nanotube starting with the zone folding and then revising more sophisticated methods.

2.1.2 Vibrational properties

Vibrations in carbon nanotubes are divided into two categories. Low frequency vibrations 50-400 cm^{-1} and high frequency vibrations 1200-1600 cm^{-1}. The zone folding approach allows a qualitative determination of the high frequency vibrations also called the high-energy modes (HEM). These vibrational states in the nanotube originate from the sp^2 carbon-carbon bonds, which are even stronger than the sp^3 C=C bonds in diamond [32]. Due to the strong bond, the phonon can achieve high energies up to 0.2 eV [31]. I first consider the in plane vibration inside the graphene layer. The phonon dispersion of graphite in the $\Gamma MK\Gamma$ direction is shown in Figure 2.3 [1,32,38]. The cutting lines of the (4,4) nanotube along this direction are represented by the vertical dashed lines. These lines correspond to the points in the graphene BZ folded into the Γ point of the nanotube. Each line increases the number of Γ point vibrations of the nanotube. The lines are numbered by the eigenvalues μ, see Figure 2.3. The cutting lines can be understood in terms of periodic boundary conditions, where the wave traveling along the circumference of the nanotube must have the wavelength $\lambda_\mu = \frac{2\pi d}{\mu}$, where μ is an integer. In reciprocal space, the lines are positioned one by one with at distance $\frac{2\pi}{\lambda_\mu}$. The distance between the lines is defined by the diameter of the nanotube.

The first line in Figure 2.3, with μ = 0 induces a non-degenerate Raman active A_{1g} symmetry phonon with eigenvectors along the nanotube circumference. The phonons, originating from the cutting lines with μ = 1,2 are doubly degenerate and induce Raman active vibrations $E_{\mu g}$. Depending on the nanotube structural type zigzag, armchair, or chiral the direction of eigenvectors of these phonons can change from purely circumferential to axial and mixed. The same lines induce

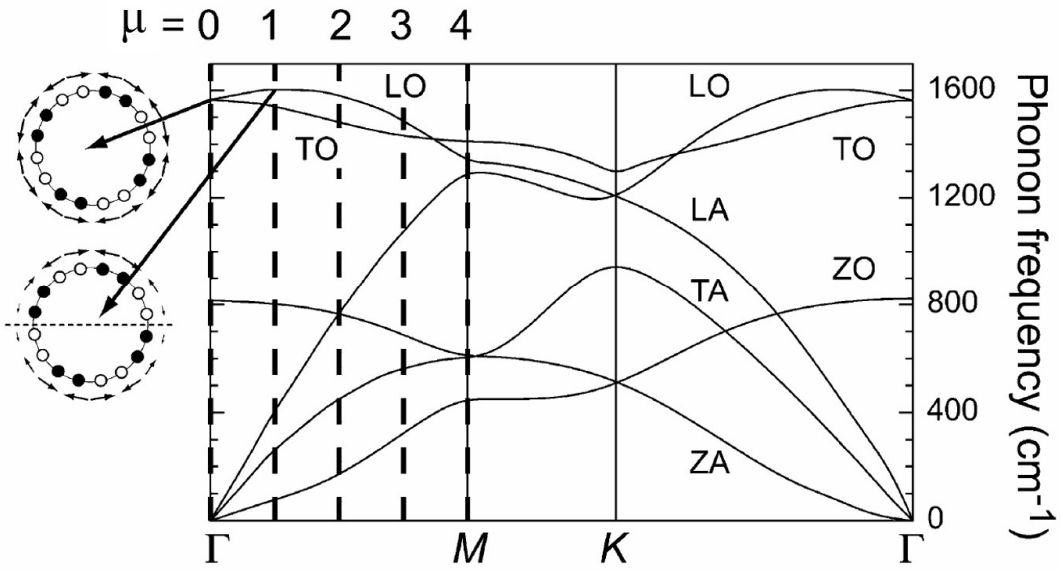

Figure 2.3 *The phonon dispersion of graphite in the ΓMKΓ direction. Vertical dashed lines represent the cutting lines, satisfying traveling wave condition along the circumference of the (4,4) nanotube. For these lined the* $\boldsymbol{k_z}$ *=0, therefore they belong to the Γ point. The number of the Γ point vibrations increases with number of cutting lines.* μ *labels the eigenvalues and is related to the z component of the angular momentum of the mode. Left panel shows the eigenvectors for Raman active* $\boldsymbol{A_{1g}}$ *(top) and infra-red active* $\boldsymbol{E_{1u}}$ *(bottom) phonons, adapted from Refs.* [1,32,38].

the infrared active $E_{\mu u}$ vibrations. The eigenvectors of the E_{1u} vibration in (4,4) nanotube are shown in Figure 2.3. The following cutting lines further induce E symmetry vibrations that are not Raman active. The full symmetries of the phonons along with directions of their eigenvector can be found in the literature [1].

The zone folding method ignores the curvature of the nanotube and produces a not entirely accurate result. This especially applies for nanotubes with small diameters, where the curvature is the strongest. The low frequency vibrations are also not accounted for. The alternative approach is based on the force constant model, where the carbon lattice is modelled by the harmonic potential interactions. Different number of neighbours from one to four may be included in the calculation [31,39]. This approach accounts for the change of the phonon energies of the nanotube with changing diameter and can reproduce low-frequency ring modes of the nanotube [39].

Particularly useful for the spectroscopic identification of carbon nanotubes is the radial breathing mode (RBM). This mode has a dominant radial component of phonon eigenvectors and vanishing axial component. The frequency ω_{RBM} of RBM depends on the diameter d of the tube [40]

$$\omega_{RBM} = \frac{215(nm * cm^{-1})}{d(nm)} + 18(cm^{-1}). \qquad (2.13)$$

The expression above applies to the nanotubes suspended in aqueous solution with an SDS surfactant. The unperturbed frequency of the RBM is determined by the chiral indices of the tube; however it can vary depending on the environment. A more general dependence on the diameter and the dielectric environment has been reported in Ref. [41]

$$\omega_{RBM} = \frac{227(nm * cm^{-1})}{d(nm)} \sqrt{1 + C_e(nm^{-2})d^2}, \tag{2.14}$$

where the parameter C_e accounts for the environmental effects. For suspended nanotubes in vacuum $C_e = 0$ and for the alcohol-assisted sample $C_e = 0.057$ nm^{-2}. The shift of the RBM can be used to distinguish between water filled and unfilled CNTs, $C_e = 0.073$ and 0.053 nm^{-2}, respectively [42].

2.1.3 Electronic properties

The allowed wave vectors from Eq. (2.10) and (2.11) can be used to derive the band structure of the carbon nanotube from the band structure of graphene [33,43,44]. The zone folding approach can be applied to deduce the electronic states of CNTs as was shown earlier for the vibrational states. It is based on restricting electronic states of graphene to the allowed wave vectors of the nanotube. In the frequency range of optical excitations, one can restrict this procedure to the π orbitals, which are closest to the Fermi level. The band structure of graphene can be calculated using the tight binding approach [45]:

$$E^{\pm}(\boldsymbol{k}) = \frac{\epsilon_{2p} \pm \gamma_0\sqrt{f_{12}(k_1, k_2)}}{1 \pm s_0\sqrt{f_{12}(k_1, k_2)}}, \tag{2.15}$$

where k_1 and k_2 are the components of the wave vector $\boldsymbol{k}$. s_0, γ_0, and ϵ_{2p} are empirical parameters. f_{12} is a trigonometric function reaching zero at the K point of the BZ. Figure 2.4a shows the one dimensional band structure of graphene along the MΓKM direction and Figure 2.4b displays the

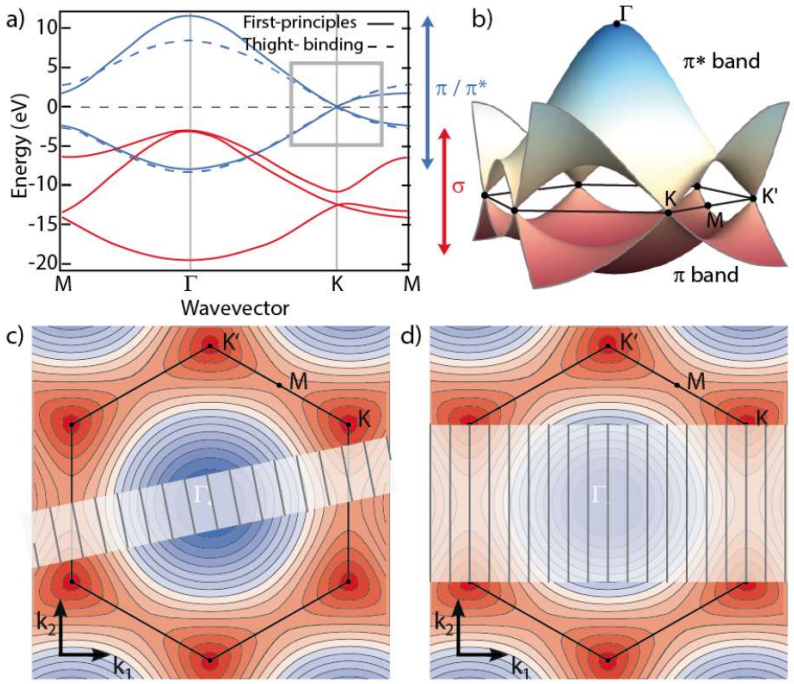

Figure 2.4 *Zone folding of graphene.* ***(a)*** *The band structure of graphene depicted in Brillouin Zone in MΓKM direction. Red lines represent* ***σ*** *orbitals and blue* ***π*** *orbitals.* ***(b)*** *Same as (a) but depicted in two dimensions, the Dirac cones are present in two unequal K and K' points.* ***(c)*** *Cutting lines in a semiconducting (8,4) nanotube. The cutting lines do not cross K points and* ***(d)*** *the cutting lines in a metallic (7,7) nanotube with cutting lines crossing the K point and defining a metallic electronic type of this tube, adapted from Ref.* [46].

same band structure in two dimensions [46]. The cutting lines for one chiral (8,4) and one armchair (7,7) tube are shown in Figure 2.4 c and d. In the (8,4) nanotube, no cutting line crosses the K or K', therefore no crossing of valence and conduction bands is found in the band structure of this tube. This assigns the (8,4) tube to a semiconducting electronic type. In the (7,7) nanotube, shown in Figure 2.4d, the lowest cutting line crosses the K point in graphene. At this point in the CNT band structure the valence and conduction bands touch, same as in graphene. This induces a metallic behaviour of (7,7) nanotube. The concept of zone folding easily predicts the electronic type of a nanotube based on its chiral indices (n, m).

If one of the cutting lines crosses the K point of graphene this chirality is metallic. This occurs if the condition $mod3(n-m) = 0$ is satisfied. The band structure of a metallic (10,10) tube is shown in Figure 2.5. When considering the nanotube curvature, only armchair nanotubes are purely metallic, whereas all other chiralities have tiny band gaps on the order of 10 meV [47–49]. If $mod3(n-m) \neq 0$ the tube is semiconducting, with a band gap that scales approximately with the inverse nanotube diameter [43]. The semiconducting tubes are divided into two groups where the cutting line, closest the K or K' point induces a large or a small bandgap. These groups are marked SI and SII and have $mod3(n-m) = 1$ and 2 respectively, labelled in blue and red colours in Figure 2.6, respectively. The band structure of semiconducting nanotubes is similar to the metallic ones, shown in Figure 2.5, except that the bands do not cross at the zero energy point. The valence and conduction bands created by a single cutting line have the band edges at the same wave vector $\boldsymbol{k}$, creating a direct band gap.

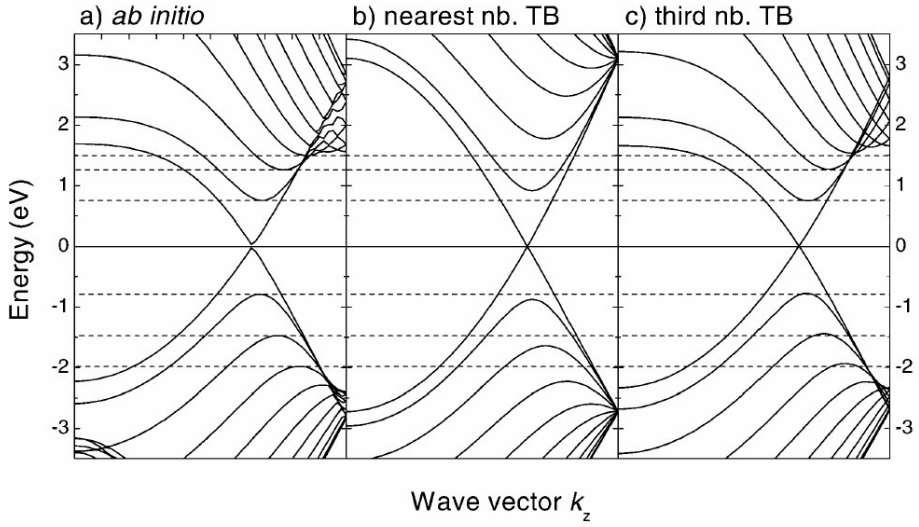

Figure 2.5 *Band structure of a metallic (10,10) armchair nanotube. Energy bands cross at the K point and each next pair of bands* $\boldsymbol{k}_\perp$ *forms a direct bandgap of greater energy.* ***(a)*** *ab initio calculation* ***(b)*** *nearest neighbour and* ***(c)*** *third nearest neighbour, adapted from Ref.* [32].

Within a single $mod3(n-m)$ type metallic and semiconducting nanotubes are classified by laola families. All nanotube chiralities belong to one single laola family if they have same $2n+m$ number. This number is laola family index and is useful for the identification and comparison between properties in the different nanotube chiralities. Figure 2.6 provides a schematic view onto the nanotubes, in the same diameter range as the CNTs studied in this work. Vertical lines indicate three different laola families, belonging to the SI semiconducting (in blue), SII semiconducting (in green), and M metallic types (in red).

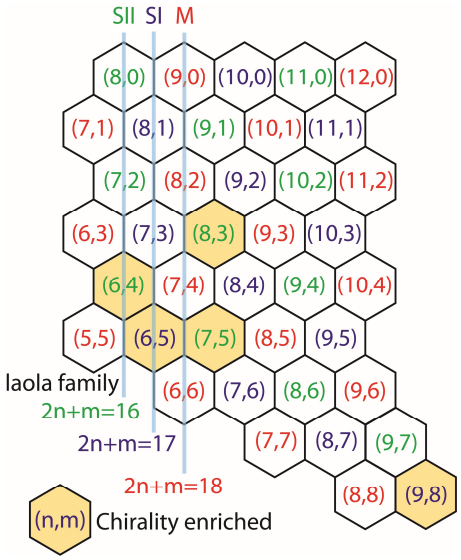

Figure 2.6 *Nanotube chiralities plotted on a graphene model sheet. 2n+m laola families are marked by the vertical lines. Mod3(n-m)=1,2, and 0 types are labelled by the blue (SI), green (SII), and red (M) colours, respectively. Yellow hexagons mark the chirality enriched samples investigated in Chapters 2 and 3.*

The optical transitions of metallic and a semiconducting tubes are labelled as M_{ij} and E_{ij}, respectively. The *ij* carry the numbers of valence *i* and conduction bands *j*. Optical transitions occur between the bands with the same quantum numbers, allowed for light polarized along the nanotube axis implying *i* = *j*. Optical transitions are numbered from one with the lowest energy to the ones with higher energy. The coupled electrons and holes rule the optical properties in nanotubes, where the one-dimensional structure of the nanotube enables strong interactions between them.

2.1.4 Excitonic properties

Strong coupling between electrons and holes in a semiconducting crystal forms a bound state called an exciton. The mathematical description of the exciton is similar to the hydrogen atom with an additional centre of mass momentum $\boldsymbol{K} = \boldsymbol{k_e} - \boldsymbol{k_h}$ [17], where $\boldsymbol{k_e}$ is the electron and $\boldsymbol{k_h}$ the hole momentum. In a three-dimensional crystal the binding energy E_b of the exciton is given by

$$E_b = \frac{m^*}{2\varepsilon_{cr}^2} Ry. \tag{2.16}$$

The binding energy is smaller than $1Ry = 13.6$ eV (ionization energy of hydrogen). The reason for that is the small effective mass of the exciton ($m^* \approx 0.02m_e$) and a high dielectric screening with $\varepsilon_{cr}^2 \approx 4$ in semiconducting materials. With these values one obtains binding energies on the order of a few meV. Indeed for three-dimensional crystals like GaAs and InSe binding energies are in the

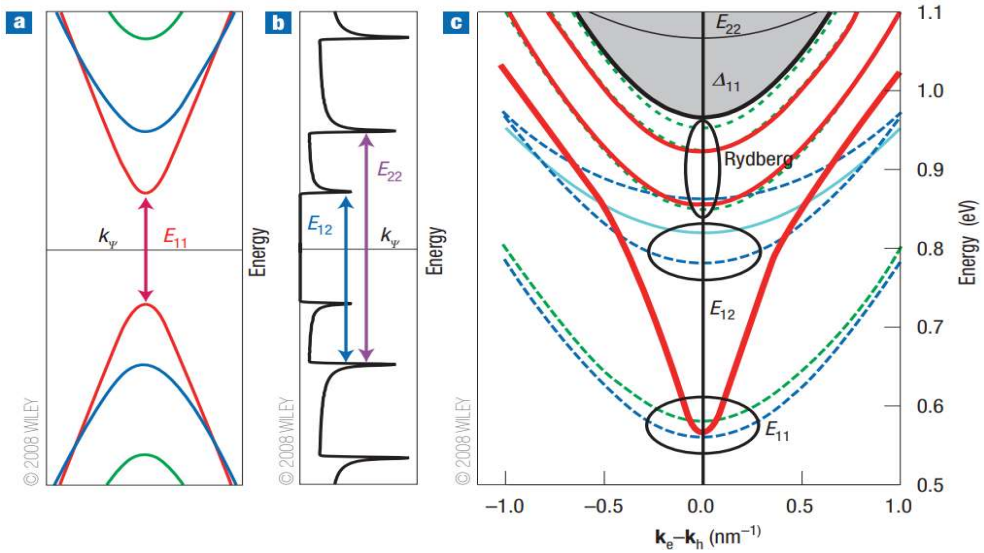

Figure 2.7 *Evolution from single particle transitions to excitonic states in (19,0) nanotube. From the single particle picture to excitonic states in (19,0) nanotube.* ***(a)*** *Valence (bottom) and conduction (top) bands. Different colours indicate different* $\boldsymbol{k}_\perp$ *perpendicular to the CNT axis, (red)* $\boldsymbol{k}_\perp = \pm\boldsymbol{k}_{\perp min}$*, (blue)* $\boldsymbol{k}_\perp = \pm\boldsymbol{2k}_{\perp min}$*, and (green)* $\boldsymbol{k}_\perp = \pm\boldsymbol{3k}_{\perp min}$*.* $\boldsymbol{k}_\psi = \boldsymbol{k}_z$*, see Eq.* (2.10) *and* (2.11)*.* ***(b)*** *The single particle density of states.* ***(c)*** *The dispersion of the lowest energy excitons of the same (19,0) nanotube embedded in medium with* $\boldsymbol{\varepsilon_{cr}^2 = 4}$*. Green dashed lines represent dark states with finite momentum (*$\boldsymbol{k}_\perp = \pm\boldsymbol{2k}_{\perp min}$*). Navy dashed lines represent a dipole forbidden dark excitonic state (*$\boldsymbol{k}_\perp = \boldsymbol{0}$*). Red and blue solid lines indicate allowed transitions of light parallel to the CNT axis and perpendicular to the CNT axis, respectively. Black ellipses indicate, where the latter excitons cross* $\boldsymbol{K_z = 0}$*. Both of these states form a Rydberg series. The grey area indicates the electron hole continuum of the first excitonic state, with lower energy the next allowed transition parallel to the nanotube axis* E_{22}*, adapted from Ref.* [16].

order of 15-30 meV [17]. Due to these small binding energies excitonic effects are observed only at low temperatures, where $k_b T \lesssim E_b$. The exciton dispersion obtained for parabolic valence and conduction bands is [17]:

$$E_n(\boldsymbol{K}) = E_g + \frac{\hbar \boldsymbol{K}^2}{2m^*} - \frac{E_b}{n^2}. \tag{2.17}$$

The excitonic Rydberg-like series has a number of excitonic states quantified by a quantum number n saturating at the electron-hole continuum. There are, however, a number of differences between the three-dimensional excitons and ones dwelling in carbon nanotubes. For instance due to the high binding energy the first n = 1 state has the highest oscillation strength. The reduction of crystal dimensions from 3d to 2d simplifies the interactions between charged particles and leads to an increase in binding energy by a factor of four [50]. The 2d model is most appropriate for carbon nanotubes, as excitons have a degree of freedom along the circumference of the tube. On top of that, the screening is less efficient, inducing $E_b^{2D} = 4E_b^{3D}(\varepsilon_{cr}^2, 1) \approx 300$ meV [32]. Calculations that are more sophisticated yield even higher values up to 1 eV [20,51,52]. This value is much higher than the thermal energy at room temperature $k_b T_{300K} = 25$ meV.

The strong binding energy enables excitonic effects to dominate optical transitions in nanotubes even at ambient temperatures. The weak dielectric screening and one-dimensional confinement induce a manifold of interactions between electronic states. As a result, a complex set

of multiple excitonic states of different symmetries and energies is present in carbon nanotubes. To illustrate this, I use the (19,0) nanotube as an example [15,16]. Figure 2.7a and b shows electronic bands and their density of states for the (19,0) carbon nanotube. Different colours indicate the variation in $\boldsymbol{k}_\perp$. The red line corresponds to the first band-to-band transition parallel to the nanotube axis E_{11}. The blue arrow indicates the excitonic transition with the lowest possible energy perpendicular to the nanotube axis E_{12}. The lowest set of excitonic states for the (19,0) nanotube is shown in Figure 2.7c. The transitions polarized parallel to the nanotube axis originate from coupled electrons and holes (excitons) of the same $\boldsymbol{k}_\perp$. The state with the lowest energy is E_{11}, see Figure 2.7a.

The dispersion of the bright exciton with its Rydberg series is represented by red solid lines. This state is dipole allowed and for $\boldsymbol{K} = 0$ directly interacts with light. States that cannot directly interact with the light are called dark states. One set of such states is dipole forbidden (navy dashed lines) and the other set of states is momentum forbidden (green dashed lines). The grey area above the Rydberg series is the exciton continuum Δ_{11}, where excitations are possible by uncorrelated electron-hole pairs. The second possible transition along the nanotube axis is E_{22} (solid black line) and lies inside the E_{11} e-h continuum. The excitation of carriers with light polarized perpendicular to the nanotube axis occurs through the interaction of electronic states of different $\boldsymbol{k}_\perp$**.** The lowest exciton resulting from such an interaction is E_{12}; it is shown by the blue solid lines in Figure 2.7b. Although these excitations are dipole allowed, their oscillator strength is very small due to the orientation perpendicular to the tube dipole.

Despite the large number of excitonic states, the interaction with light is mainly realized by the lowest energy, dipole and momentum allowed E_{ii} ($n = 0$ in Eq. (2.17)) excitons [11]. These excitons are often referred to as optical transitions, numbered by i. For instance, the first and second optical transitions of the CNT have E_{11} and E_{22} transition energies. The excitonic character of the optical transitions in carbon nanotubes were experimentally confirmed in a series of experiments [14,53]. E_{11} excitons of different symmetries were excited by one and two photon absorption. The

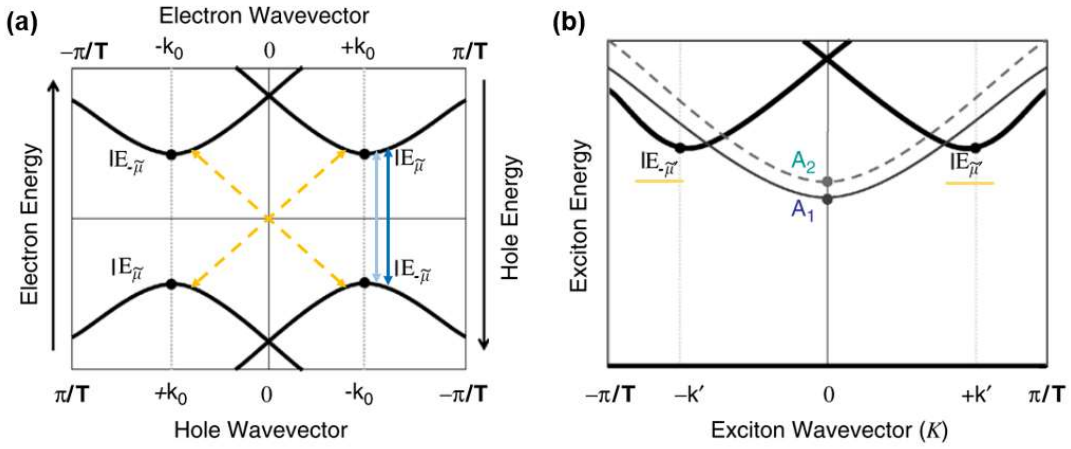

Figure 2.8 *Exciton formation in chiral single walled carbon nanotubes* ***(a)*** *Schematic structure of the electronic states in the chiral (n,m) nanotube. Valence and conduction bands have singularities at the K points of the BZ (*$\pm\boldsymbol{k_0}$*).* μ is the eigenvalue of *the corresponding electronic (hole)* state. ***(b)*** *Bright and symmetry forbidden excitonic states in the middle of the nanotube BZ and momentum forbidden excitonic states and the K points (*$\pm\boldsymbol{k'}$*). Dipole allowed (forbidden) states are labelled by full (dashed) lines, adapted from Ref.* **[**26**].**

energies of the states differed as expected for excitonic transition [48]. By comparing the excitation energies, binding energies up to 400 meV were obtained [14,53].

The structure of excitonic states can be different depending on the structural type of the nanotube. I focus on the chiral nanotubes, as they are particularly interesting for this study. I use (6,5), (6,4), (8,3), (9,8), and (7,5) nanotubes, as they can be enriched with outstanding chiral purity [54–56]. The symmetry of the excitonic states in chiral nanotubes is reported by Barros et. al [26]. The states $n \neq 0$ of the Rydberg series can be neglected due to their low oscillator strength. The relevant states are depicted in Figure 2.8b. Two states of A_1 and A_2 symmetries at the zero exciton momentum are the product of a direct interaction between the valence and conduction bands at the same electron momentum. These bands located at $\pm k_0$ are depicted in Figure 2.8a, with corresponding interaction marked by the blue and navy arrows.

The momentum forbidden dark states are located at the ±k' exciton momentum, see Figure 2.8b. Electronic states inducing this interaction are labelled by the yellow arrows in Figure 2.8a. The momentum forbidden dark excitonic states are a product of the interaction between electronic states of different momentum. The electronic state at $+k_0$ and the hole state at $-k_0$ (electron-hole momentum) form a dark exciton at +k' (exciton momentum). The symmetries of the dark excitonic states with finite momentum is E with an index owned by corresponding electronic bands. In carbon nanotubes the A_1 state interacts with photons and the dark E states interact with light by forming a hybrid with the phonon of the opposite momentum. I further revise spectroscopic investigations of the dark exciton-phonon coupled states and principals of their indirect interaction with light.

2.1.5 Coupled states of excitons and phonons

The momentum forbidden excitonic states indirectly modify light-nanotube interactions. The finite momentum needs to be compensated to push the dark exciton into the middle of the BZ. This role is taken by the K point phonons. While the momentum is compensated, the energy of the dark exciton increases or decreases by the phonon energy and the K point ($\hbar\omega_K$ = 0.16 eV). Figure

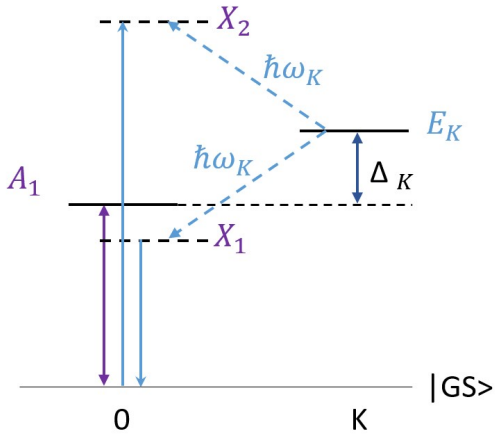

Figure 2.9 *Energy-momentum diagram for the pure and phonon coupled excitonic states. The bright A_2 exciton is located at zero momentum and the dark E exciton, at the K point of the BZ. When coupling to a phonon vibration of the opposite momentum, the energy of the E state decreases (increases) by the phonon energy. The phonon energy at the K point is 0.16 eV. The momentum of the coupled state is zero, enabling its interaction with light. Due to the highest energy the X_2 state is activated in the excitation channel, whereas in emission channel the X_1 state is at play. Δ_K represents the energetic difference between E_K and A_2.*

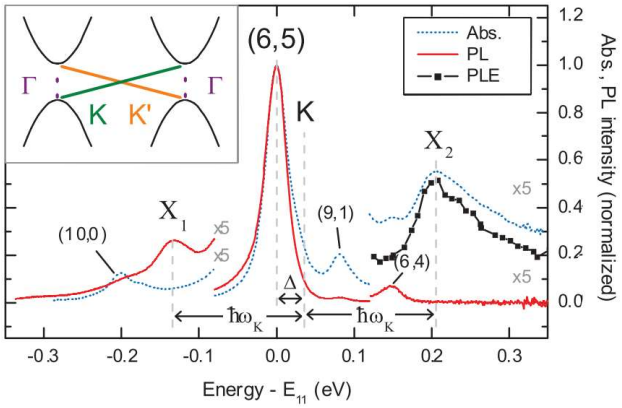

Figure 2.10 *Exciton-phonon sidebands in (6,5) CNT emission and absorbance. The red (blue) line shows the PL (absorbance) profiles. The dotted black line shows the PL emission profile. The* X_2 *and* X_1 *are phonon sidebands at* $\boldsymbol{E_K + \hbar\omega_K}$ *and* $\boldsymbol{E_K - \hbar\omega_K}$ *respectively, where* $\boldsymbol{\hbar\omega_K}$ *is the energy of the K phonon. The letter K marks the energy of the dark (6,5) exciton* $\boldsymbol{E_K}$ *and (n,m) indicate peaks corresponding to the bright excitonic transitions of different chiralities* [21]*. The inset shows possible interactions between valence and conduction bands, like in Figure 2.8a* [21].

2.9 shows the energy momentum diagram for the exciton-phonon coupling. The X_2 state with the highest energy absorbs the incident light, whereas X_1 state with the lowest energy and emits the light absorbed via A_2. The bright A_2 state works in both absorbance and emission directions. The energy of the dark K exciton is higher than the A_2 exciton with difference Δ_K between them.

Phonon assisted light interactions of the (6,5) nanotube with light are shown in Figure 2.10 [21]. The central line corresponds to the absorbance/emission of the A_2 exciton of the E_{11} excitonic transition. In the absorbance and photoluminescence-excitation, the phonon assisted absorption occurs at the X_2 energy ($E_K+\hbar\omega_K$). In the emission line the phonon-induced state X_2 emits light at an energy of ($E_K-\hbar\omega_K$). The energy levels are in line with the scheme shown in Figure 2.9**.**

Knowing the K phonon energy $\boldsymbol{\hbar\omega_K}$=0.16 eV the energy of dark exciton can be obtained from photoluminescence-excitation spectroscopy for a number of nanotube chiralities [57]. The energies of the splitting between the bright and dark states show a chirality and type (SI, SII) dependent behavior. The coupled states of excitons and phonons are also reported in the photocurrent response of a nanotube [22]. The presence of the exciton-phonon coupled features in the spectroscopy of the nanotubes indicates an immediate influence of the dark excitonic states. Raman scattering is naturally the most appropriate tool to study the exciton-phonon coupling, as the Raman process directly involves the exciton-phonon interactions. I will further outline how the photon-exciton and exciton-phonon interactions are included into the Raman process within the framework of perturbation theory.

2.1.6 Microscopic theory of Raman scattering

Raman scattering [58] is typically applied to study the phonon energies of the material and its crystalline structure. When monochromatic light is shone on a material the dominant light component is absorbed and the less dominant component is scattered. Light can be scattered elastically or ineastically with the scattered photon energy deviating from the incident one. The energy lost or obtained within this interaction is due to quantized lattice vibration. The vibrations of the crystalline solid are quantized in form of the phonons [17]. Analyzing the spectrum of the

scattered light, the energies of phonons (vibrations) are obtained. Two general types of Raman scattering occur. The first type is when the phonon is created in the material is Stokes scattering with the scattered photon at a lower energy compared to the incident light. The other type is anti-Stokes scattering where the phonon (already present in the medium) is destroyed in the material. The photon scattered in such process has higher energy compared to the incident light. The intensity of the anti-Stokes scattering is proportional to the phonon population. The population of the phonons is determined by the temperature, which induces the lattice vibrations.

While conventional Raman spectroscopy identifies phonon energies and populations, resonant Raman spectroscopy is sensitive to the electronic transitions. Within the Raman process the photon does not directly excite the phonon, but couples to the electron or exciton first depending on the optical properties of the material. For example when the excitation energy approaches the band gap of a semiconductor the intensity of Raman scattering increases. The electronic state or excitons and different aspects of electron (exciton)-phonon coupling can be studied by analyzing the dependence of Raman intensity on excitation energy. For instance the energy of the band gap and coherent lifetimes of the electron (exciton) can be directly obtained.

To implement the effect of a real or intermediate state on Raman intensity, the microscopic theory of Raman scattering needs to be reviewed. The Raman scattering process in a semiconductor involves three different systems; photons (ω_i and ω_s), electrons and phonons. In the initial state $|i\rangle$ in the whole system there are $\mathrm{N}(\omega_i)$ photons and $\mathrm{N}(\omega_s)$ (number photons with frequency ω_x). $\mathrm{N_q}$ is the initial number of phonons in the system, regulated by the Boltzmann factor. $\mathrm{N_q}$ is non-zero at temperatures above 0 K. Electrons in the initial state are not excited, i.e. all valence bands are occupied and conduction bands are empty. In the final state $|f\rangle$ the number of incident photons decreases and the number of scattered photons increases $\mathrm{N}(\omega_i) - 1$ and $\mathrm{N}(\omega_i) + 1$, respectively. The number of phonons also increases $\mathrm{N_q} + 1$. The electrons in the final state remain unperturbed,

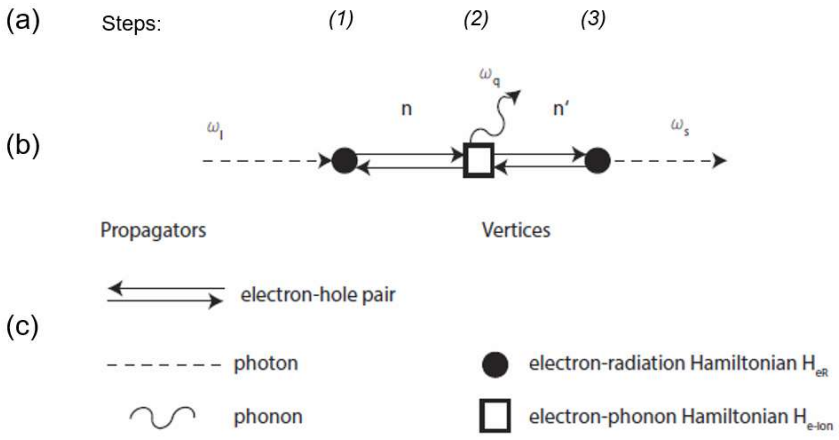

Figure 2.11 *An example of the standard Feynman diagram for Stokes scattering.* ***(a)*** *Steps involved in the scattering process.* ***(b)*** *Feynman diagram for three steps Raman process, where electron-hole pair is scattered by the phonons* $\boldsymbol{\omega_q}$. $\boldsymbol{\omega_i}$ *and* $\boldsymbol{\omega_s}$ *stand for the incident and scattered photons. Vertices represent interactions between different particles, round filled vertices represent an interactions between photons and electrons (holes) and quadrate represents an interaction between the phonon and electron. n and n' stand for electron-hole pair or exciton.* ***(c)*** *Different types of propagators and vertices used for construction of the diagram, adapted from Ref.* [59].

returning to their ground state during the scattering process. Electron-hole pairs or excitons mediate the light-vibrational coupling.

One phonon Raman scattering occurs in three steps, see Figure 2.11a.

Step *(1)*. The incident photon excites an electron-hole pair or exciton from the ground state into an intermediate state $|a\rangle$. This interaction is realized via the electron-radiation Hamiltonian $\mathcal{H}_{eR}$.

Step *(2)*. The excited electron-hole pair is scattered into a different state by emitting a phonon via the electron-phonon interaction Hamiltonian $\mathcal{H}_{e-ion}$. This intermediate state is denoted by $|b\rangle$.

Step *(3)*. The electron-hole pair recombines from $|b\rangle$ by irradiating the photon of frequency ω_s again via $\mathcal{H}_{eR}$.

The electrons directly participate in phonon scattering processes although they remain unchanged after this singular process. It means, when excited via electrons, the energy and momentum is exchanged between the phonons and the photons before and after the process. The visible light has almost no momentum and therefore can only interact with phonons of zero momentum. This can be realized by the one zone centre phonon or two arbitrary phonons with the same momentum magnitude and opposite sign.

The system of rules presented above provides a fundament for calculating probabilities of Raman scattering. Typically, when the interactions are weak, one can use third-order perturbation theory to mathematically describe all interactions occurring during the scattering process. The perturbation theory can be visually represented in the form of Feynman diagrams. Feynman diagrams are particularly useful when more sophisticated scattering pathways are involved. I give a short introduction of Feynman diagrams here following the three step exemplary process of one-phonon Raman scattering [17,59]. Following rules need to be followed, when drawing the diagram:

- Lines or **propagators** represent different types of excitation. Excitation may be photons, phonons, electron-hole pairs and more. The propagator can be labelled by the property of the excitation it represents (name, wave vector, frequency, polarization), see Figure 2.11c.
- The intersection of the propagators indicates their interaction and is depicted by vertices. The form of the **vertex** can vary, depending on the type of propagators intersecting on the vertex, see Figure 2.11c.
- Within an interaction (vertex) a particle can be created or annihilated. The type of interaction can be distinguished by the direction of the arrow. The arrow pointing towards (away) indicates a created (annihilated) particle.
- Unless specified differently, the order of the interaction is processed from the left to the right of the diagram.
- After one scattering pathway is represented by the diagram, other possible pathways can be derived by changing the order of vertexes.

An example of Feynman diagram constructed following the steps *(1)* to *(3)* of the Raman process and applying the rules above is shown in Figure 2.11b. I will further translate the diagram into an expression for scattering probabilities using perturbation theory as an example [60]. The first vertex is translated is form of

$$\sum_n \frac{\langle n|\mathcal{H}_{eR}(\omega_i)|i\rangle}{[\hbar\omega_i - (E_n - E_i)]} \tag{2.18}$$

the scattering probability. In this terms $|i\rangle$ and $|n\rangle$ are the initial and intermediate electronic states with energy E_i and E_n. The sign before $\hbar\omega_i$ indicates if the particle is absorbed (+ sign) or emitted (-sign). The summation is performed over all possible intermediate states $|n\rangle$. By adding the second vertex one obtains:

$$\sum_{n,n'} \frac{\langle n'|\mathcal{H}_{e-ion}(\omega_0)|n\rangle\langle n|\mathcal{H}_{eR}(\omega_i)|i\rangle}{[\hbar\omega_i - \hbar\omega_0 - (E_{n'} - E_n)][\hbar\omega_i - (E_n - E_i)]} \tag{2.19}$$

The sign of $\hbar\omega_0$ is negative because the phonon was created (Stokes scattering). The sum is extended over the second intermediate electronic state $|n'\rangle$. The electron-phonon Hamiltonian $\mathcal{H}_{e-io}$ responsible for the latter interaction appears in the nominator. If the Feynman diagram consists of more vertices, they will be added to the Eq. (2.19) one by one, except the last. In Figure 2.11b, the third vertex is the last one, which takes a different form. This form represents overall energy conservation condition:

$$\begin{aligned}\delta\big[\hbar\omega_i - (E_n - E_i) - \hbar\omega_0 - (E_{n'} - E_n) - \hbar\omega_s - \big(E_f - E_n\big)\big] = \\ = \delta\big[\hbar\omega_i - \hbar\omega_0 - \hbar\omega_s - \big(E_i - E_f\big)\big].\end{aligned} \tag{2.20}$$

If the initial and final states of electronic states are the same $E_i = E_f$, it simplifies to:

$$= \delta[\hbar\omega_i - \hbar\omega_0 - \hbar\omega_s]. \tag{2.21}$$

In order to include all three contributions (one for each vertex) we need to combine Eq. (2.21) and (2.19). The Golden Rule gives overall formula for scattering probability $P_{ph}(\hbar\omega_s)$:

$$\begin{aligned}P_{ph}(\hbar\omega_s) = \frac{2\pi}{\hbar}\sum_{n,n'}\left|\frac{\langle s|\mathcal{H}_{eR}(\omega_s)|n'\rangle\langle n'|\mathcal{H}_{e-ion}(\omega_0)|n\rangle\langle n|\mathcal{H}_{eR}(\omega_i)|i\rangle}{[\hbar\omega_i - \hbar\omega_0 - (E_{n'} - E_n)][\hbar\omega_i - (E_n - E_i)]}\right|^1 \delta[\hbar\omega_i \\ - \hbar\omega_0 - \hbar\omega_s].\end{aligned} \tag{2.22}$$

The nominator is completed by the scattered photon-exciton interaction like in the previous steps. The Raman efficiency can be directly obtained by squaring the probability:

$$\begin{aligned}R_{ph}^{(I)}(\hbar\omega_s) = \frac{2\pi}{\hbar}\sum_{n,n'}\left|\frac{\langle s|\mathcal{H}_{eR}(\omega_s)|n'\rangle\langle n'|\mathcal{H}_{e-ion}(\omega_0)|n\rangle\langle n|\mathcal{H}_{eR}(\omega_i)|i\rangle}{[\hbar\omega_i - \hbar\omega_0 - (E_{n'} - E_n)][\hbar\omega_i - (E_n - E_i)]}\right|^2 \delta[\hbar\omega_i \\ - \hbar\omega_0 - \hbar\omega_s].\end{aligned} \tag{2.23}$$

The process depicted in Figure 2.11 is not the only one possible. Following the Feynman diagram construction rules, all other processes can be deduced by changing the order of the scattering events. This results in six different diagrams instead of one [17]. Here, I pick another process (II) as an example. In this process, the order of the second and the third scattering events is reversed. First the photon $\hbar\omega_s$ is scattered and then the phonon $\hbar\omega_0$. Scattering order results in a different form for Raman intensity of the second process, compared to the first process, see Eq. (2.23). The individual efficiency of the second process follows:

$$\begin{aligned}R_{ph}^{(II)}(\hbar\omega_s) = \frac{2\pi}{\hbar}\sum_{n,n'}\left|\frac{\langle n'|\mathcal{H}_{e-ion}(\omega_0)|n\rangle\langle s|\mathcal{H}_{eR}(\omega_s)|n'\rangle\langle n|\mathcal{H}_{eR}(\omega_i)|i\rangle}{[\hbar\omega_i - \hbar\omega_s - (E_{n'} - E_i)][\hbar\omega_i - (E_n - E_i)]}\right|^2 \delta[\hbar\omega_i \\ - \hbar\omega_0 - \hbar\omega_s].\end{aligned} \tag{2.24}$$

In the entire Raman cross section both process *(I)* and *(II)* need to be accounted for. This is realized by the summation of the real and imaginary parts before they are squared:

$$R_{ph}^{(I)}(\hbar\omega_s) + R_{ph}^{(II)}(\hbar\omega_s) = \frac{2\pi}{\hbar}\sum_{n,n'}\left|\frac{\langle i|\mathcal{H}_{eR}(\omega_0)|n\rangle\langle n|\mathcal{H}_{e-io}\ |n'\rangle\langle n|\mathcal{H}_{eR}(\omega_i)|i\rangle}{[\hbar\omega_i - \hbar\omega_0 - (E_{n'} - E_n)][\hbar\omega_i - (E_n - E_i)]} + \frac{\langle n'|\mathcal{H}_{e-ion}(\omega_0)|n\rangle\langle s|\mathcal{H}_{eR}(\omega_s)|n'\rangle\langle n|\mathcal{H}_{eR}(\omega_i)|i\rangle}{[\hbar\omega_i - \hbar\omega_s - (E_{n'} - E_i)][\hbar\omega_i - (E_n - E_i)]}\right|^2 \delta[\hbar\omega_i - \hbar\omega_0 - \hbar\omega_s]. \quad (2.25)$$

Such summation enable an interference between the *(I)* and *(II)* processes. The possibility to interfere reflects a quantum principal of processes indistinguishability, where the processes cannot be separated from one another and can occur at the same time. If more than two quantum channels are involved, they are all summed up together in the same way. However, depending on the specific type of the process the quantum channels may or may not be allowed to interfere [17]. For the third-order perturbation theory (first-order Raman process) in a semiconductor the sum of all six diagrams can be used to calculate the scattering efficiency. Using typical values for semiconductors in the extended version of Eq. (2.22) a Raman efficiency of 10^{-6}-10^{-7} [sterad cm]$^{-1}$ can be estimated [60].

2.1.7 Resonant Raman scattering in carbon nanotubes

Knowing the fundamental process of first-order Raman scattering (third-order perturbation theory) I will demonstrate its advantages and limits by application on different one-phonon modes in the single walled nanotubes. A Raman spectrum of carbon nanotubes is shown in Figure 2.12. The modes attributed to a single phonon are the low-frequency radial breathing modes (RBMs) and the high frequency D and G modes [32,61]. The D mode originates from the scattering of a defect and the phonon is not described by the third-order scattering process, but the fourth-order process instead [62]. I will introduce this mode later in the subsequent Chapter 3, along with the 2D mode which is a two phonon process. The RBM is excessively studied by resonant Raman spectroscopy, where this mode was studied at multiple excitation energies. The frequency of this mode depends

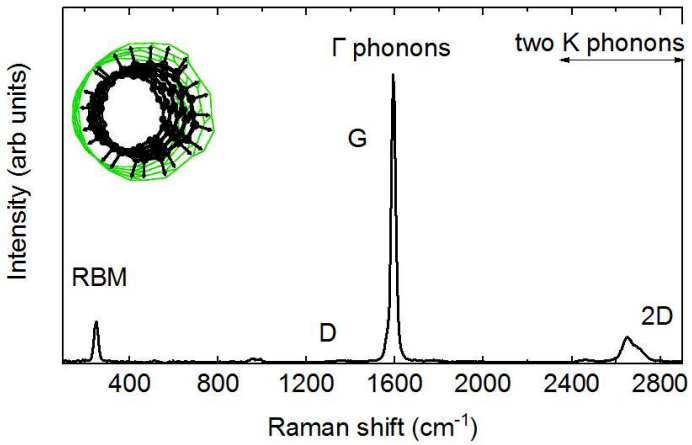

Figure 2.12 *Raman spectrum of a semiconducting carbon nanotube. The RBM of carbon nanotube is visualized to a breathing like motion of carbon atoms with a sketch indicating the eigenvectors. The G mode is due to the phonon from the middle of the BZ; D and 2D phonons are due to the phonons close to the K point of the BZ.*

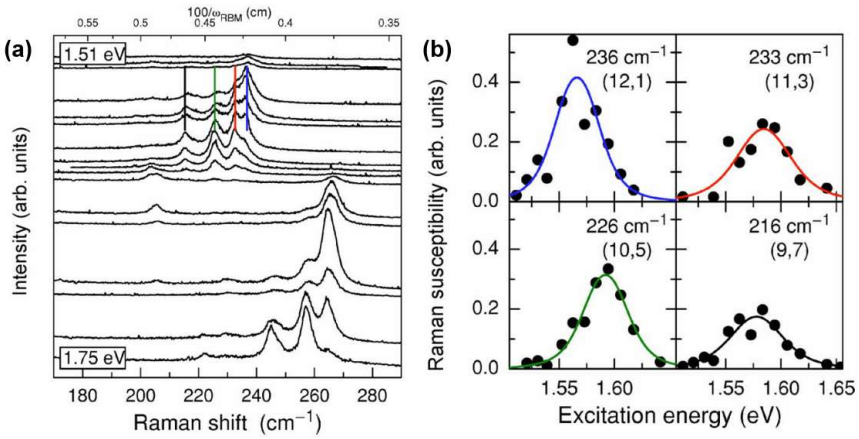

Figure 2.13 *Resonant Raman spectroscopy of the RBM mode in carbon nanotubes.* ***(a)*** *Radial breathing modes, measured for a number of excitation energies from 1.51 eV (top) to1.75 eV (bottom).* ***(b)*** *Intensity (integrated peak area) of the RBMs marked by the lines of the same colour in (a). Filled symbols are experimental data and lines are fits by Eq. (2.27). The mode frequencies and chiral indices and are shown in the top right corner of the sub window, adapted from Ref.* [12].

on the inversed diameter by Eq. (2.13) and (2.14). This mode is widely used to assign the chiral indices of the nanotube via Raman spectroscopy. The dependence of the RBM intensity on laser excitation energy E_L is due to the third-order perturbation theory [63,64]:

$$I_{RBM} \sim \left| \frac{M_{ex-photon}^2 M_{ph-RB}}{\left(E_L - E_B - \hbar\omega_{RBM} - i\frac{\Gamma}{2}\right)\left(E_L - E_B - i\frac{\Gamma}{2}\right)} \right|^2, \tag{2.26}$$

where $M_{ex-photon}$ and M_{ph-RB} are the exciton-photon and exciton-phonon matrix elements that are typically combined in a single matrix element M_c . E_B is the energy of the bright excitonic state and Γ is the broadening factor due to the finite lifetime of the exciton. The Feynman diagram for this process follows one to one Figure 2.11b, with the RBM phonon created in the process. Eq. (2.26) is sometimes used in an alternative form [40,65]:

$$I_{RBM} \sim \left| \frac{M_{c1}}{E_L - E_B - i\frac{\Gamma}{2}} - \frac{M_{c2}}{E_L - E_B - \hbar\omega_{RBM} - i\frac{\Gamma}{2}} \right|^2. \tag{2.27}$$

This form originates from molecular like transitions in the nanotube. Under the Condon approximation [66], where $M_{c1} = M_{c2}$ Eq. (2.26) and (2.27) differ by $\hbar\omega_{RBM}$ and are equally applicable for radial breathing modes in carbon nanotubes. The first term in Eq. (2.27) is responsible for the incoming Raman resonance occurring at the transition energy (E_B), whereas the second term is responsible for outgoing resonance occurring at the transition energy and phonon energy sum ($E_B + E_{ph}$). Same principal applies to the components of the denominator in Eq. (2.26).

Figure 2.13a shows Raman spectra in the RBM region, recorded with different excitation energies from 1.5 to 1.75 eV [12]. Each peak on the Raman spectra corresponds to a particular chirality *(n,m)* present in the sample. The frequency of the chirality is fixed by Eq. (2.13) and does not change with excitation energy. The intensity of the RBM increases when laser energy approaches the

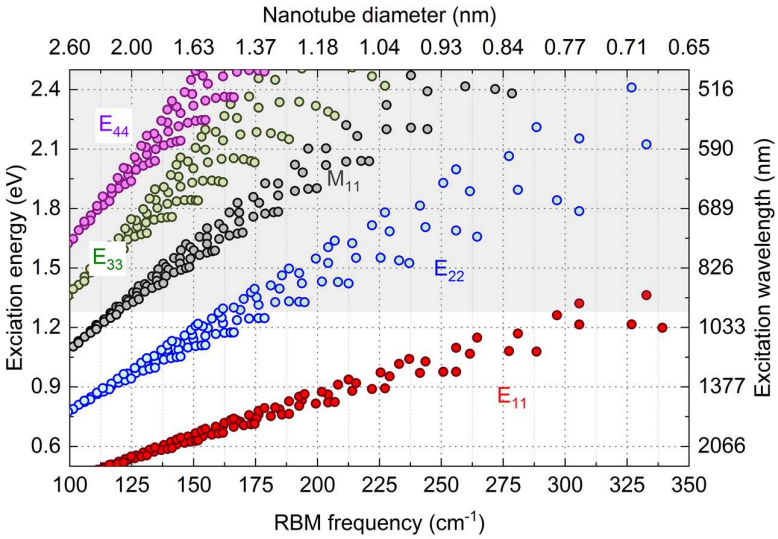

Figure 2.14 *Kataura plot of carbon nanotubes. The energy of the excitonic transition is plotted as a function of RBM frequency of a nanotube (diameter). For semiconducting nanotubes the first transition occurs at the lowest energy* E_{11} *in the near infrared, then comes the second* E_{22} *transition (in visible range for small diameter nanotubes). Between the second and third semiconducting transition, the first metallic transition of metallic tubes occurs. For this plot the transition energies are calculated following Ref.* [68] *and RBM frequencies by Eq. (2.2). The gray area indicated the available excitation range of our (experimental) setup, described Sec. 2.2.2.*

energy of the bright excitonic transition, whereas at the energies far from bright transition this RBM is not excited at all. The range of excitation energies where the particular phonon mode is observed is referred to as "excitation window". The excitation window is defined by the phonon energy and excitonic lifetime. In order to establish the energy of the bright transition and excitonic lifetime the third-order perturbation theory needs to be applied.

Four different modes are selected for demonstration. The vertical blue, green, red, and black lines mark these modes in Figure 2.13a. Figure 2.13b depicts resonance Raman profiles of these modes. In such type of representation the investigated intensity of the Raman mode is plotted as a function of excitation energy. The dots represent experimental values and full lines represent the fits by Eq. (2.27). The maximum of Raman intensity occurs between at E_B and $E_B + \hbar\omega_{RBM}$. This form of Raman profile is due to an overlapping of the incoming resonance at E_B with the outgoing resonance at $E_B + \hbar\omega_{RBM}$. The resonances are not resolved due to Γ being greater then $\hbar\omega_{RBM}$. The fitting of the resonance profile yields a bright excitation transition energy for each *(n,m)* present in the sample.

The paires of RBM and transition energy form a two-dimensional pattern. To represent nanotube optical properties in such form was first proposed by Kataura et al. [67]. In this plot, the x axis corresponds to the frequency of the RBM or its diameter, and the y axis corresponds to the excitonic transition energy. Both of these parameters are accesible by resonant Raman spectroscopy. An example of the Kataura plot is shown in in Figure 2.14. The transition energies of the nanotubes are calculated using the empirical formulas from Ref. [68]. The semiconducting E_{11} transition (red dots) occurs at the lowest energy, after that comes semiconducting the E_{22} transition (blue dots). Then first excitonic transition in metallic nanotubes occurs (black dots). Due to the RBMs observed in relatively short excitation windows of 100 -150 meV the Kataura plot

allows a simple identification of nanotube chiralities. This is realized by comparison of RBM frequency and transition energy defined by the laser excitation. As I explained in Sec. 2.1.4 the optical transition energy E_{ii} equals the energy of bright i-th excitonic state. It does not coincide with the energy of the electronic band gap, but instead they are related by [16]:

$$E_B = E_{ii} = E_g + E_{ee} - E_{eh}, \tag{2.28}$$

E_g is the single particle band gap, E_{ee} and E_{eh} are the energies implied by the electron-electron and electron-hole interactions. $E_g + E_{ee}$ is typically referred as nanotube band gap.

The high-frequency G band is due to longitudinal (LO) and transverse (TO) phonons from the graphene like Γ point in the nanotube BZ, see Figure 2.3. The frequency of the G band weakly depends on CNT diameter and the signals of different species cannot be distinguished from each other in a sample containing multiple chiralities. Recent developments provide single chirality samples allowing the investigation of the resonant behaviour of the G band [54,56].

A peculiar behavior for the dependence of the LO phonon intensity on excitation energy (resonance Raman profile) has been reported [69]. Figure 2.15 shows resonance profiles for a (10,2) chirality enriched sample. As expected, two resonances occur in the resonance profiles the incoming at E_{ii} and the outgoing at $E_{ii} + E_{ph}$. The heights of the resonances deviate from each other, with the incoming resonance dominating. Such asymmetric form of the profiles was unexpected and cannot be reproduced by simple models. The third-order perturbation theory produces resonances of the same height in the single particle and in the excitonic pictures [1,32].

However, as Figure 2.15 clearly shows, the experimentally obtained resonances have different intensities. The origins of asymmetries in excitation resonances of carbon nanotube have been a subject of extensive investigation [23,24,69,70]. One report attributes the asymmetry to the displacement of nuclear coordinates. This approach is based on molecular-like 0d excitations, where the excited and ground electronic states have a displacement in nuclear coordinates [71]. Depending on the vibrational symmetry and difference in nuclear coordinates between excited and ground electronic states, different asymmetries in resonance profiles can be obtained. However, nanotubes are solid-state systems and an approach based on the nanotube structure as one-dimensional crystal is required.

The second theory accounting for intrinsic nanotube properties is based on the third order perturbation theory and electronic excitation [70]. To reproduce the asymmetry of resonance Raman profile the interference between all electronic bands of a nanotube is considered. With implemented non-constant dependence of electron-phonon matrix elements in the BZ the asymmetry resonance profile can be reproduced. Despite reproduced asymmetries, this model ignores the established excitonic nature of optical transitions of nanotubes. The interaction of incident photon with an exciton occurs at a single point, defined by the exciton dispersion, the integration of electronic states over the whole BZ contradicts a physical background.

Finally, the most appropriate theory is based on the one-dimensional excitonic nature of optical transition in nanotubes. It fully accounts for the complex structure of excitonic states and implements the phonon mediated coupling between the dark and bright excitonic states. This theory is beyond third-order perturbation theory and is expressed by fifth-order perturbation theory instead [17].

2.1.8 Fifth-order perturbation theory

Here I will introduce the concepts of coupling between bright and dark excitonic states and show how it can account for the asymmetry of the resonance Raman profiles in carbon nanotubes [23]. The influence of the dark excitonic state on the higher-order scattering process needs to be considered [20–22,57]. A possible sequence of scattering events involving the scattering to a dark state is depicted in Figure 2.16. Higher-order processes can be dismissed when exciton-phonon coupling is weak, which is not valid for carbon nanotubes. In CNTs such processes enable phonon assisted coupling between excitonic states of different energy and momentum. The most prominent excitonic states are; the bright state at the Γ point, and the dark state at the K point. These states are

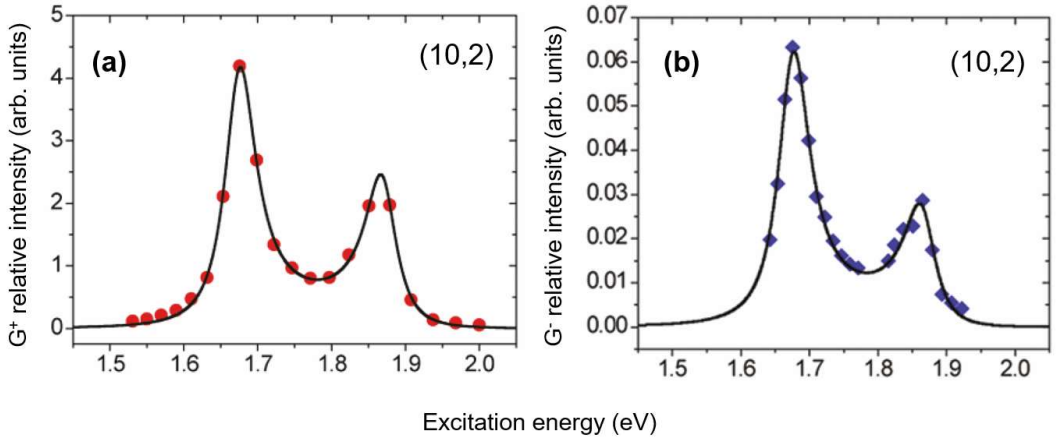

Figure 2.15 *Asymmetry in the G mode Stokes resonance profiles in (10,2) nanotube.* ***(a)*** *Intensity of the G^+ component and* ***(b)*** *G- component plotted over excitation energy. G^+ (G^-) corresponds to the longitudinal phonon (transverse) phonon. The symbols represent experimental points and the lines are the fits based on molecular like theory accounting for non-Condon effects, adapted from Ref.* [69].

well observed in the absorption spectra of metallic and semiconducting nanotubes, see Figure 2.17b and Figure 2.10.

The fourth-order process can only contribute to inelastic scattering or scattering of multiple phonon modes and is inapplicable to the one-phonon Raman scattering [23]. The coupling between the bright and dark states induces the firth-order process. The fourth-order process becomes relevant in Rayleigh scattering or two phonon modes, such as 2D mode [62]. In the simplified model reported for armchair nanotubes, a large number of phonon branches in a nanotube is reduced to only two phonons. The Γ point LO phonon with an energy $\hbar\omega_G$=0.197 eV and K point TO phonon with an energy $\hbar\omega_K$=0.163 eV. The manifold of excitonic states is reduced to one bright (*BΓS*) and one dark (*DKS*) singlet state at the Γ and K points respectively. The G phonon couples only to a dark state, where the K phonon can exchange between two excitonic states due to its finite momentum. The exciton phonon interaction Hamiltonian is then:

$$H_{XP} = M_G^{XP}\left[F_{B\Gamma S}^{\dagger}F_{B\Gamma S} + F_{DKS}^{\dagger}F_{DKS}\right]\left(b_G + b_G^{\dagger}\right) + M_K^{XP}\left[F_{B\Gamma S}^{\dagger}F_{DKS} + F_{DKS}^{\dagger}F_{B\Gamma S}\right]\left(b_K + b_K^{\dagger}\right), \tag{2.29}$$

and exciton-photon interaction is given by:

$$H_{XL} = \sum_{\omega} M_G^{XP}\left(F_{B\Gamma S}^{\dagger} + F_{B\Gamma S}\right)\left(a_{\omega} + a_{\omega}^{\dagger}\right). \tag{2.30}$$

$F_j(F_j^{\dagger})$ corresponds to the creation (annihilation) of an excitonic state in Eq. (2.29) and (2.30), j= *BΓS, DKS*. $b_K^{\dagger}$ *(*b_{ph}*)* is responsible for the creation (annihilation)of K or G phonons and $a_{\omega}^{\dagger}$ (a_{ω}) is the photon operator, again describing its creation (annihilation). Following the rules of transforming Feynman diagrams into the perturbation theory equation from the previous section, the Raman scattering probability $I_{Raman} \propto |W_G|^2$ is obtained [23], where

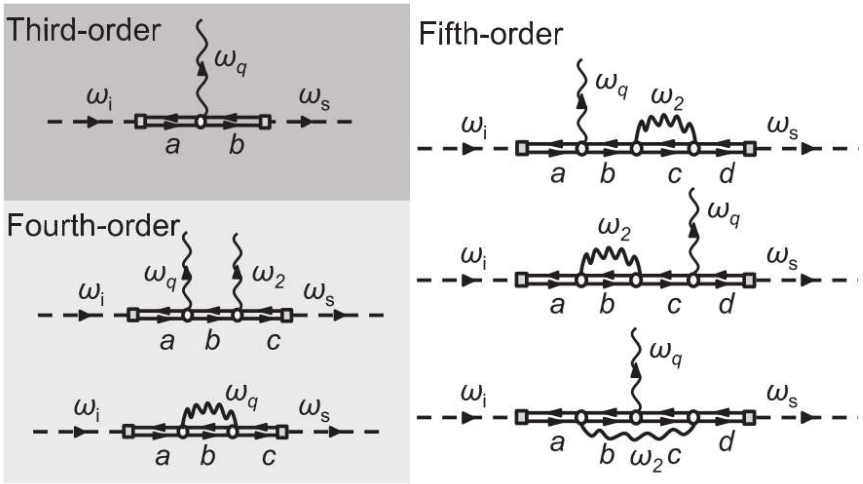

Figure 2.16 *Feynman diagrams corresponding to Raman processes of different orders. Third-order (top left) process where one phonon is involved, Fourth-order (bottom left), where two phonons are scattered. Possible fifth-order Raman scattering processes (Right panel).* $\boldsymbol{\omega_i}$ *and* $\boldsymbol{\omega_s}$ *represent incident and scattered photons,* $\boldsymbol{\omega_q}$ *is the G phonon and* $\boldsymbol{\omega_2}$ *can be the K phonon if corresponding excitonic state is dark and G if this state is bright.* ***a****,* ***b****,* ***c****, and* ***d*** *are different states of exciton, adapted from Ref.* [23].

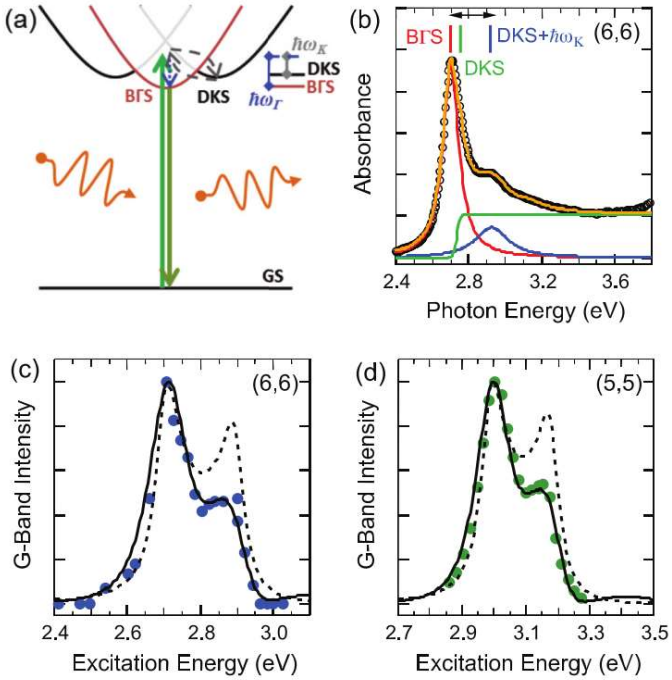

Figure 2.17 *Fifth-order Stokes scattering process with phonon assisted interaction between the dark and bright excitonic states.* ***(a)*** *Scheme of the scattering, where the bright (red) excitonic state is first excited by the incident photon, then it is scattered by the K phonon towards the dark (black) and back. Afterwards the G phonon is emitted and the exciton recombines by irradiating a photon of smaller energy.* ***(b)*** *Absorbance of the (6,6) nanotube where the dominant red peak is due to the bright exciton and blue peak due to the combination of dark exciton and K phonon.* ***(c)***, ***(d)*** *Resonance Raman profiles of (8,8) and (7,7) nanotube, dots are the experimental data points and solid lines are calculations by Eq.* (2.31)*, dashed lines are the calculations by the third-order model* [70]*, adapted from Ref.* [23].

$$W_G(E_L) = \frac{|M_{B\Gamma S}^{XL}|^2 M_G^{XP}}{(E_{B\Gamma S}+\hbar\omega_G-E_L)(E_{B\Gamma S}-E_L)}\left[1+\frac{|M_G^{XP}|^2}{(E_{B\Gamma S}+2\hbar\omega_G-E_L)(E_{B\Gamma S}+\hbar\omega_G-E_L)}+\right.$$
$$\frac{|M_G^{XP}|^2}{(E_{B\Gamma S}-E_L)(E_{B\Gamma S}+\hbar\omega_G-E_L)}+\frac{|M_K^{XP}|^2}{(E_{DKS}+\hbar\omega_G+\hbar\omega_K-E_L)(E_{B\Gamma S}+\hbar\omega_G-E_L)}+ \qquad (2.31)$$
$$\left.\frac{|M_K^{XP}|^2}{(E_{DKS}+\hbar\omega_G+\hbar\omega_K-E_L)(E_{DKS}+\hbar\omega_K-E_L)}+\frac{|M_K^{XP}|^2}{(E_{B\Gamma S}-E_L)(E_{DKS}+\hbar\omega_K-E_L)}\right].$$

The first term in square brackets corresponds to the third-order scattering. The following two terms are describing the fifth-order process between bright-bright states, depicted in Figure 2.16 with the G phonon as ω_2. First and second diagrams are degenerate; therefore, only two terms are inherited by Eq. (2.31). The three last terms represents the bright-dark scattering pathways, again depicted in Figure 2.16 with the K phonon as ω_2. Bright and dark excitons have real and imaginary components such as $E_{B\Gamma S} = E_{ii} + iy_\Gamma/2$ and $E_{DKS} = E_K + iy_K/2$. y represents the broadening of the corresponding excitonic state due to its finite lifetime.

In order to illustrate the fifth-order Raman process, one of the scattering pathways is shown in Figure 2.17a. This is the second pathway depicted in form of Feynman diagram in Figure 2.16. In this pathway, the following order of the scattering events occurs; the bright exciton (*BΓS*) is first

excited by the incident photon, then the K phonon scatters the exciton into the dark (*DKS*) state and back, and finally the bright exciton emits the photon of smaller energy. Figure 2.17 b shows absorbance spectra of (6,6) nanotube, where the strongest peak is due to the bright exciton (red). The smaller peak at higher energy (blue) is due to the coupled K phonon and exciton. A vertical green (red) line marks the energy of the dark (bright) excitonic state.

Figure 2.17b and Figure 2.17d compare experimentally obtained profiles of (6,6) and (5,5) tubes and calculated by Eq. (2.31). The asymmetry of the profiles with dominant incoming resonance is reproduced by the calculation. However, the ratio between the resonances is not reproduced. The discrepancy can arise due to low binding energies of excitons in metallic nanotubes. In semiconducting nanotubes the excitonic properties are more pronounced, which I will verify in the following chapters.

2.2 Experimental methods

2.2.1 Single chirality enrichment by gel permeation chromatography

The study of the fundamental properties of carbon nanotubes requires a single chirality, otherwise only a mixed response of all nanotubes present in the sample can be studied. As I have demonstrated in the previous sections, each nanotube chirality has a specific structure and optical properties. The optimization of the growth conditions can lower the distribution of diameters, but still a large number of chiralities are present in the samples [72]. The best-known strategy to obtain a monochiral (one chirality) sample is the post growth processing of the nanotubes. This approach can yield multiple (n,m) chiralities and extremely high purity (up to 95%) [54]. I shortly revise the steps involved in the samples preparation. The separation used to prepare my samples is performed in the gel permeation chromatography column. The interactions between the gel and surfactant are tuned by the pH during the elution.

The first important steps in acquiring a monochiral sample is isolation of nanotubes from each other. After growth in large quantities the nanotubes form bundles, where Van der Waals forces induce the aggregation of nanotubes. The treatment of nanotubes is required including sonication and ultracentrifugation. The sonication is performed with a mixture of nanotubes and surfactant, here SDS. This yields a micelle with nanotube in the middle and an outside layer of oriented surfactant with hydrophilic tail stabilizing nanotube in aqueous solution and hydrophobic tail attaching to the tube surface. The micelle structure is shown in Figure 2.18a.

The SDS layer on one hand provides structure dependent interactions with the tube, where the amount of surfactant depends on the tube diameter and coupling strength vary with the chirality of the tube. On the other hand, the Sephacryl gel in the column interacts with hydrophilic head of the surfactant. Optimization of the elution conditions, such as SDS concentration, pH gradient, and elution time, yield samples enriched by different species. Figure 2.18b shows the elution profile of

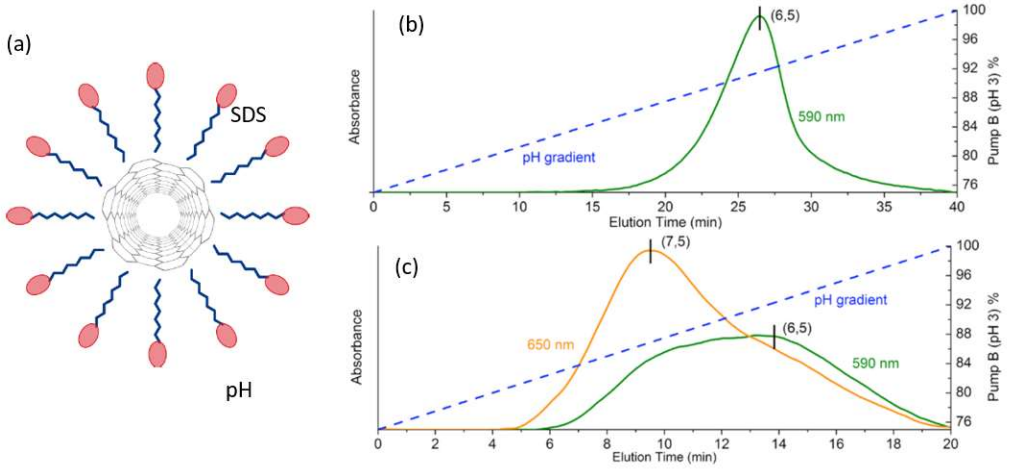

Figure 2.18 *Single chirality enrichment by pH gradient.* ***(a)*** *Micelle formed with the nanotube in the core and surfactant layer outside stabilizing the micelle in solution. Absorbance through the* E_{22} *transition of carbon nanotube as function of elution time and pH gradient,* ***(b)*** *for (6,5) nanotube in green with 1.6% SDS concentration and* ***(c)*** *for (7,5) and (6,5) nanotubes in yellow color with 1.4% SDS concentration, adapted from Ref.* [54].

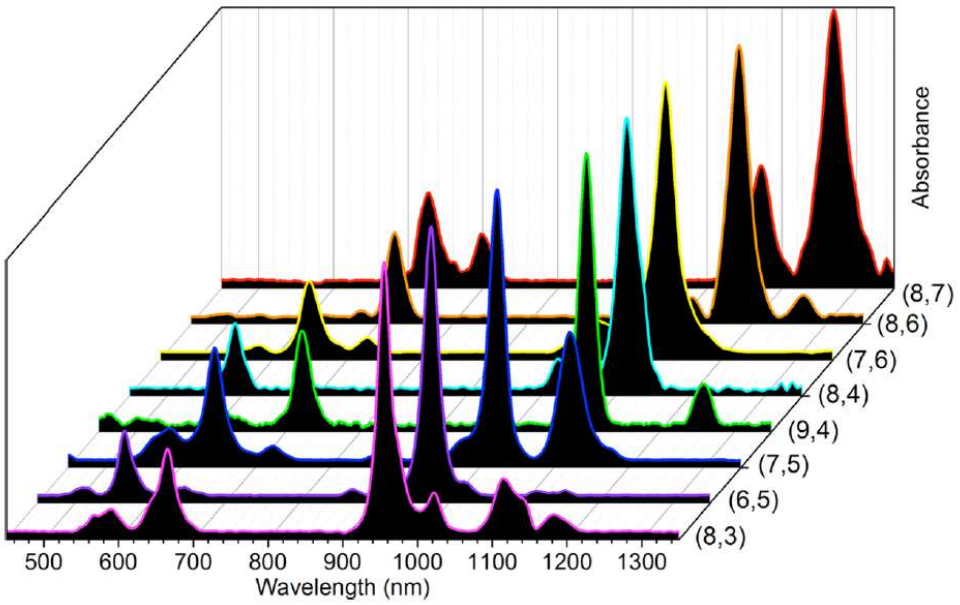

Figure 2.19 *Absorbance of different fractions of nanotubes enriched in the gel permeation column. Absorbance of different fractions of nanotubes enriched in the gel permeation column. The pH gradient, SDS concentration and elution time are optimized to obtain the best purity, adapted from Ref* [54].

(6,5) nanotube with 1.6% SDS. The intensity of (6,5) nanotube absorbance peak is probed under the variation of conditions. Figure 2.18c shows the same profile for (7,5) and (6,5) nanotubes with 1.4% SDS. Optimization of the parameters yields a dispersion of desired species with a high purity. A full absorbance spectrum over second and first transition allows the determination of the chiral purity of the sample. The absorbance of different fractions is shown in Figure 2.19. In the low wavelength range (500-800nm) semiconducting nanotubes absorb light via the second transition (E_{22}), in the high wavelength range (900-1400 nm) nanotubes absorb light via the first transition (E_{11}), see Figure 2.14. The quality of the samples is represented in percentage obtained by comparing the spectral weight corresponding to the targeted chirality and undesired chiralities.

2.2.2 Resonant Raman spectroscopy setup

After the samples of sufficient purity are produced, advanced optical characterization is performed. In this thesis, the exciton-phonon and exciton-photon coupling in nanotubes is accessed via multi-wavelength Raman scattering. Raman scattered light has a low scattering efficiency and typically is six orders of magnitude less intense than the Rayleigh light. I first show the setup for the measurement and then give guidelines and details of the intensity and Raman shift calibration. The setup consists of three different set pieces. First, the light is produced by a tunable laser systems, then focused on the sample, and finally the inelastic scattered light is analysed with the spectrometer and recorded with a detector.

The set-up for resonant Raman spectroscopy is shown in Figure 2.20. For resonant excitation multiple excitation sources need to be used. Three different laser sources are used, covering visible and infra-red spectral ranges, see options Ia-c in Figure 2.20. “Coherent Innova 70C” is an ion laser with a mixture of Argon and Krypton as active medium. This laser emits photons of energies corresponding to the atomic transition of corresponding gas atoms, providing

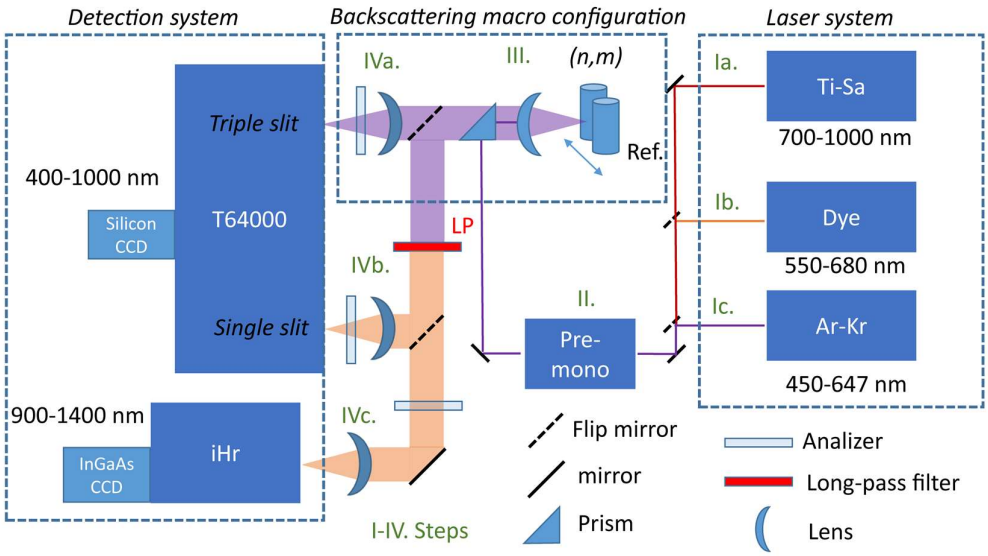

Figure 2.20 *Setup for resonant Raman spectroscopy. One of the lasers produces the light of desired wavelength in the system, steps Ia-c. Premono cleans the laser line from the spectral noises, with ~1nm precision, step II. The spectral noises arise from PL in dye and Ti-Sa lasers and plasma emission in Ar-Kr laser. The beam path is split by the prism in step III, where 80% of the incident light is reflected towards the sample bench and 80% of the scattered light is transmitted into the detection path. IVa. Double detection path and IVb. single detection path of the T64000 Horiba spectrometer equipped with a silicon CCD. IVc path is designed for the detection of infrared scattered light via iHR Horiba spectrometer equipped with an InGaAs array.*

discrete excitations from 450 to 648 nm. For tunable excitation in the visible range a "Radiant Dye" laser was used. The lasing principle is based on harvesting light of the narrow spectral line from the dye fluorescence. A number of different dyes was used; Rhodamin 110 (545-580 nm), R6G (560-615 nm), and DCM (525-680 nm). The dye is dissolved in a solution of high viscosity to form a stable free space stream in the laser cavity. Ethylene Glycol (EG) is used to dissolve R6G and Rhodamin 110, whereas for DCM a mixture 4:1 of Ethylene Glycol and BzOH is used due to insolubility of DCM in pure EG. The dye laser was pumped with a frequency doubled Nd:YAG (neodymium-doped yttrium aluminum garnet) 532 nm (2.3 eV) "Sprout G -18 W" pump laser. Same Nd:YAG laser is used to pump a "Coherent MBR-100" laser with the Titanium-Sapphire crystal as active medium. This laser emits photons in the infrared wavelength range (700-1000nm).

The laser light of desired frequency is then transmitted through a pre-monochromator to clean the laser line from spectral noises, see step II in Figure 2.20. Every laser in the system has noises corresponding to its lasing principal. After that, the light enters a macroscopic (macro-) Raman scattering setup. The light is further split by the prism, placed in between of the spectrometer slit and bench with the samples. The prism reflects most of the light (>80 %) towards the samples. The light is then focused by a lens with high aperture (N.A. = 0.8). The backscattering configuration implies, that the same lens is used to collect the light reflected and scattered from the sample. A small fraction of the backscattered light is lost through the reflection by the prism. The prism area is much smaller the diameter of the scattered beam.

In configuration IVa, the Raman light is filtered by a double monochromator and intermediate slit. The scattering angle of the grating and the slit width can be adjusted to any laser

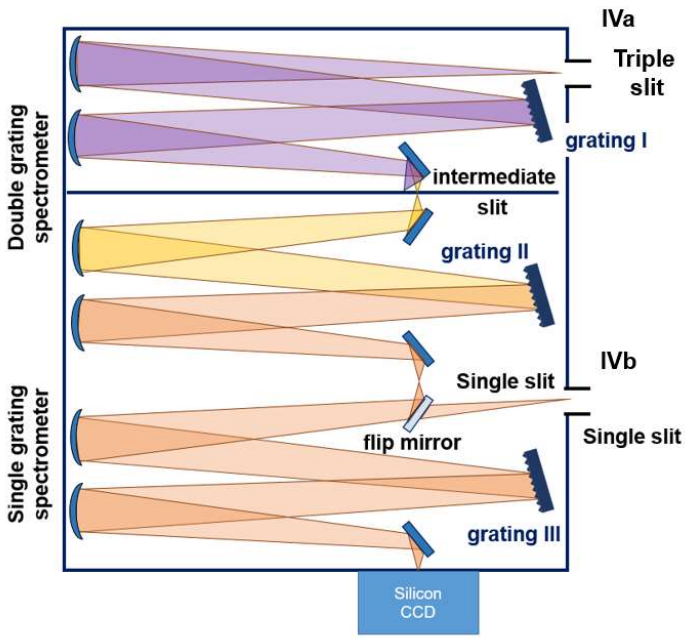

Figure 2.21 *Scheme of the T64000 spectrometer. In* IVa *configuration the Rayleigh and Raman light enter through the double slit (top), the intermediate slit selects the spectral width of the transmitted light. All three grating are engaged in this configuration. In* IVb *configuration already filtered light enters the single slit (bottom) and one grating III is engaged in the detection process.*

frequency and phonon mode. The sensitivity of this detection pathway is the lowest and is ruled by the scattering efficiency of double monochromator gratings, see Figure 2.21. The low energy vibrations, such as RBMs, are typically analysed in IVa configuration. For phonon modes of high energy, such as the G and 2D modes, the configurations IV b and c are used. In these configurations a long-pass (LP) filter is required to block the Rayleigh light (low-pass for anti-Stokes scattering). The LP filter is adjusted to laser wavelength and phonon mode. In order to specify the scattering polarization in which the Raman intensity is calibrated and account for different vibrational symmetries of nanotube mode and reference, an analyzer is put each beam path. The scattered light is focused on the slit of the spectrometer.

Depending on the frequency of the scattered light different types of spectrometers are used to disperse and detect scattered photons. For the scattered light below 1000 nm the Horiba T64000 spectrometer is used, equipped with 600 and 900 grooves per mm gratings and silicon CCD. For the scattered light of wavelength above 1000 nm the iHR320 Horiba spectrometer equipped with 150 grooves per mm grating. Figure 2.21 shows the scheme for light propagation inside the spectrometer. In triple grating detection configuration three grating I-III are engaged. The Rayleigh light is blocked with the intermediate slit, where the spatial positions of Raman and Rayleigh light are different due to the grating I. In the single grating detection configuration only one grating III is involved. The pale blue mirror is flipped and light coupling through the single slit is dispersed by the spectrometer. The scheme of the iHR320 Horiba spectrometer is similar to the single grating spectrometer part of T64000, as it also contains only one grating.

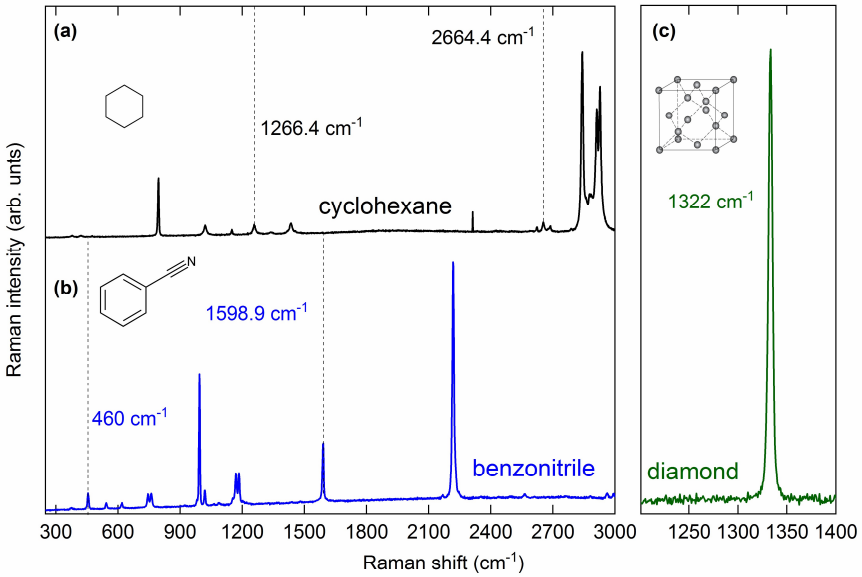

Figure 2.22 *Raman spectra of reference materials, used for Raman calibration.* ***(a)*** *Cyclohexane, best suited for the calibration of the RBM, G, D, and 2D modes in carbon nanotubes,* ***(b)*** *benzonitrile, which is used to calibrate the intensity of the G mode and* ***(c)*** *diamond with sp^3 hybridized carbon lattice in the same range as the D mode.*

2.2.3 Calibration of Raman spectra

In order to obtain correct values for intensity and positions of Raman modes, the latter needs to be calibrated. The calibration of the Raman shift is rather trivial and can be performed by a neon lamp or another Raman reference. Whereas the calibration of Raman intensity is more sophisticated. The optical elements inside the spectrometer have wavelength dependent transmission and reflection curves. Especially sensitive to different wavelengths are the gratings and the detector shown in Figure 2.21. The calibration of the Raman intensity is required to account for different wavelength selectivity of the set-up. By applying the calibration Raman profiles can be obtained. The incident and scattered photons in resonant Raman scattering are always at different spectral positions and a correct and reliable calibration of Raman intensity and Raman shift remains a challenging task. Different calibration strategies are known. One of the most common ones is the pre-calibration of the spectrometer. Raman spectra of a reference material with known Raman cross section are acquired and the material of interest is calibrated on this curve. The wavelength of the scattered photon should cover the region, where the resonance profiles will be measured. Diamond is a well-known material, with no optical resonances in visible and near infrared range for the first-order scattered phonons [73]. The scattering intensity is therefore constant. The typical Raman spectrum of diamond in the first order scattering region is shown in Figure 2.22c. The energy of the Γ point phonon is E_{ph}=0.164 eV (1322 cm^{-1}). Raman spectra of diamond are measured with laser excitations from 488 to 940 nm in IVa configuration depicted in Figure 2.21a. The integrated Raman intensity of diamond is plotted in Figure 2.23a. The different sensitivity for parallel and perpendicular polarizations is due to the scattering anisotropy of the diffraction gratings. The points represent experimental values and lines are fits by simple functions. These functions can be used to calibrate the intensity of any material of interest. The intensity of the Raman mode should be corrected by the sensitivity of the spectrometer at the frequency of the scattered photon (E_L-E_{ph} for

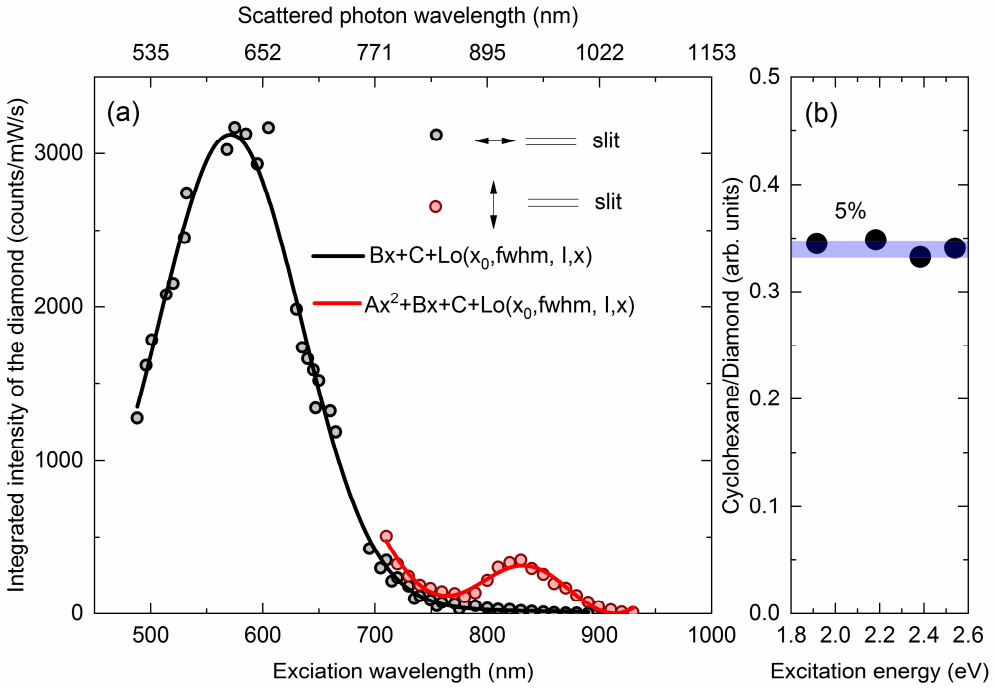

Figure 2.23 *Calibration of Raman profile.* ***(a)*** *Pre-calibration of the Horiba T64000 spectrometer sensitivity, in* IVa *configuration with 900 grooves/mm grating. Measured intensity of the first-order Raman mode in diamond at different scattered polarizations and same laser intensities. The black (red) point represent experimentally obtained data in polarization parallel (perpendicular) to the triple slit. The lines of corresponding colors represent fits by simple functions. The fitting parameters are listed in Table 2.1.* Lo() *stands for Lorentzian function.* ***(b)*** *Raman intensity of the cyclohexane 1266.4 cm^{-1} vibration, calibrated on diamond.*

Stokes scattering), top axis in Figure 2.23. Despite this method being easy to perform, it implies the same experimental conditions for the whole resonance Raman profile with no possible chance to improve the system alignment. The intensity of the laser always needs to be measured or kept constant.

A different calibration procedure accounting for different laser intensities and differences in alignment, is achieved by acquiring reference spectrum for each measurement set (laser energy and intensity, gratings positions, and alignment). It also allows for instant switching between detecting pathways in Figure 2.20. A reference material in liquid form is optimal for such a calibration, as it can be put it in the same scattering geometry as the suspended nanotubes.

In my experiments, I use two different types of liquid molecules, benzonitrile and cyclohexane. These molecules have vibrational energies similar to dominant modes in nanotubes (D, G, and 2D modes). The closer the spectral position of the reference and investigated samples are, the more accurate is the calibration. Typical Raman spectra of the molecules are shown in Figure 2.22a and Figure 2.22b. Both molecules have their electronic resonances in the deep UV [74,75], therefore the Raman cross section is flat in the visible and IR excitation ranges [73]. Still, this behavior is verified in the high-energy visible excitation range. Figure 2.23b shows the intensity of cyclohexane calibrated on diamond in the range from 1.9 to 2.5 eV. The resulting Raman cross section is flat, indicating suitability of these materials for calibration purposes. In addition, no

enhancement is also observed in the high-energy part of the spectrum, close to resonances of the molecules.

Table 2.1 *Fitting parameters for Raman intensity calibration in the T64000 spectrometer, see equations in Figure 2.23*

polarization	A (nm^{-2})	B (nm^{-1})	C	I	fwhm (nm)	x_0 (nm)
parallel		-0.1	121	3072	149	571
perpendicular	0.06	40122	-97	879	121	835

2.3 Chirality dependence of exciton-phonon coupling [1]

2.3.1 Introduction

Resonant Raman scattering of the high-energy modes reported an atypical asymmetric dependence of Raman cross section on excitation energy. The asymmetry was found to depend on nanotube chirality [23,69,70]. The suggested mechanism to account for varying cross-sections of the incoming and the outgoing Raman resonance involves competing scattering channels between bright and dark excitonic states. All previous experiments analyzed the Stokes scattering [23,69,70]. The anti-Stokes scattering mechanism has same additional scattering channels, only the primary phonon is absorbed instead of being emitted. Resonance profiles of anti-Stokes scattering will verify the proposed scattering pathways and deliver additional information about the photon-exciton and exciton-phonon coupling in nanotubes. Depending on the anti-Stokes Raman cross section, exciton resonances may potentially be exploited for phenomena like vibrational cooling [76–78] and generating correlated Raman photons [79,80].

Anti-Stokes spectra of the high energy modes were previously reported at mixed chiralities concentrated powder, high temperatures or plasmon enhanced Raman scattering [81–83]. Despite the interest in anti-Stokes Raman scattering of the high-energy modes in nanotubes no systematic studies of their resonance profiles have been reported. This is due to the low intensity of the anti-Stokes process, which is proportional to the occupancy of the phonon branch. At room temperatures, the high-energy G modes of nanotubes are three orders of magnitude less intense in anti-Stokes than in Stokes scattering preventing measurements on individual nanotubes. Samples with nanotubes suspended in solution contain many different chiralities with overlapping resonances. The mixed response prohibits a detailed analysis of the resonance profiles as a function of chirality.

I report the anti-Stokes resonant behavior in the Raman profiles of chirality sorted single-walled carbon nanotubes. Further, bulk samples containing nanotubes of four chiralities (8,3), (6,5), (7,5) and (6,4) suspended in water are investigated. In all the chiralities I observe an asymmetry between incoming and outgoing resonances of the anti-Stokes signal of the high-energy LO mode. The Stokes (blue) and anti-Stokes (red) resonance profiles are excellently described by a Raman scattering process involving interferences with dark excitonic states. We calculate the ratio of the Stokes and anti-Stokes intensity depending on the energy difference between the bright exciton and

[1] The contents of this Section are published in "Gordeev, G et. al. *Phys. Rev. B* **96,** 245415 (2017)". The coauthors agree on using the data in this work.

the laser energy. The exciton-phonon matrix elements of different chiralities extracted from the experimental data qualitatively follows the behavior predicted by tight-binding calculations.

2.3.2 Manifestation of the Boltzmann factor

To extract the resonance behavior of Stokes and anti-Stokes scattering in nanotubes the impact of different phonon populations needs to be accounted. I calibrate the scattering efficiency on reference material with close vibrational energy at the same temperature. The Stokes/ anti-Stokes difference is determined by the Boltzmann factor. The Stokes process creates phonons, whereas the anti-Stokes process annihilated phonons (already present in material) and depends on the phonon population. The equilibrium phonon population is

$$N_0 = \left[e^{\frac{\hbar\omega_G}{KT}} - 1\right]^{-1}, \tag{2.32}$$

where KT is the thermal energy and $\hbar\omega_G$ is the phonon energy. The ratio between the Stokes and anti-Stokes populations is then expressed as

$$\frac{N_{Stokes}}{N_{anti-Stokes}} = \frac{N_0}{N_0 + 1} = e^{\frac{\hbar\omega_G}{KT}}. \tag{2.33}$$

The general dependence of the Raman scattering cross section on the scattered photon frequency is $I \sim \omega^3$. The ratio between the Stokes and anti-Stokes with this included than follows:

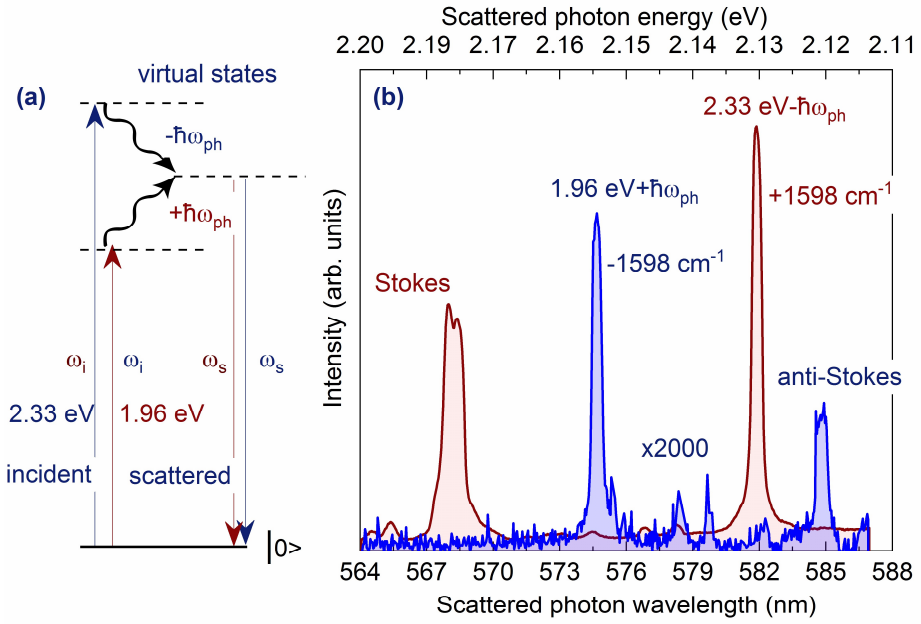

Figure 2.24 *Stokes (blue) and anti-Stokes (red) scattering in benzonitrile.* ***(a)*** *The energy diagram of the Stokes and anti-stokes scattering. The vertical arrows represent incident* ($\boldsymbol{\omega_i}$) *and scattered* ($\boldsymbol{\omega_s}$) *photons and wave arrows phonons* ($\boldsymbol{\hbar\omega_{ph}}$). *The Stokes (anti-Stokes) phonon is destroyed (created) and reduces (increases) the scattered photon energy.* ***(b)*** *Raman spectra of benzonitrile ±1598 cm^{-1} vibration acquired with the same laser power. Spectra of anti-Stokes (blue) and Stokes (red) are excited with 2.33 eV and 1.96 eV excitations, respectively. The excitation wavelengths are selected for the spectral positions of the scattered photons to be as close as possible.*

$$\frac{I_{Stokes}}{I_{anti-Stokes}} = \frac{\omega_S^3 \sigma(\omega_L, \omega_S)}{\omega_{aS}^3 \sigma(\omega_L, \omega_{aS})} e^{\frac{\hbar\omega_G}{KT}}, \quad (2.34)$$

where $\sigma(\omega_L, \omega_S)$ and $\sigma(\omega_L, \omega_{aS})$ are the geometrical cross sections for the Stokes and anti-Stokes respectively. ω_S and ω_{aS} are the frequencies of the scattered photons. In our scattering geometry $\sigma(\omega_L, \omega_{aS}) = \sigma(\omega_L, \omega_S)$.

To compare the Boltzmann factor we adjust the laser energies to match the energies of the Stokes and anti-Stokes scattered photons $\omega_S = \omega_{aS}$. The scheme for the scattering is shown in Figure 2.24a. The laser for the Stokes (anti-Stokes) is 2.33 eV (1.96 eV), with difference of $2\hbar\omega_{ph}$. Figure 2.24b shows Raman spectra excited by different laser energies for Stokes (red) and anti-Stokes (blue). The positions of the scattered photons for both scattering types are very close and laser powers are the same. The intensities of the Stokes and anti-Stokes in this configuration are insensitive to ω^3 and spectrometer sensitivities. The ratio between blue (Stokes) and red (anti-Stokes) peaks yields 2578, which is in good agreement with the calculation $e^{\frac{\hbar\omega_{Benz}}{KT_{room}}} = 2517$. I further will use the Stokes and anti-Stokes phonon modes for calibrating of the corresponding scattering types in nanotube phonons.

2.3.3 Determination of the E_{22} transition energies by resonant Raman scattering

Before measuring the resonance effects of the G phonons I characterize my chirality sorted samples. An essential parameter for our analysis is the purity of the chirality-sorted samples and the exact energetic position of the exciton transitions. We determined the energy of the bright exciton for each nanotube chirality by resonant Raman spectroscopy of the RBMs. Figure 2.25 shows examples of RBMs for four different nanotube chiralities excited at the energies close to their E_{22} transition. Figure 2.25a shows an example of the Stokes (red) and anti-Stokes (blue) scattering components of the (7,5) RBM at $\omega_{RBM} = \pm 284$ cm^{-1}. The appearance of a single RBM

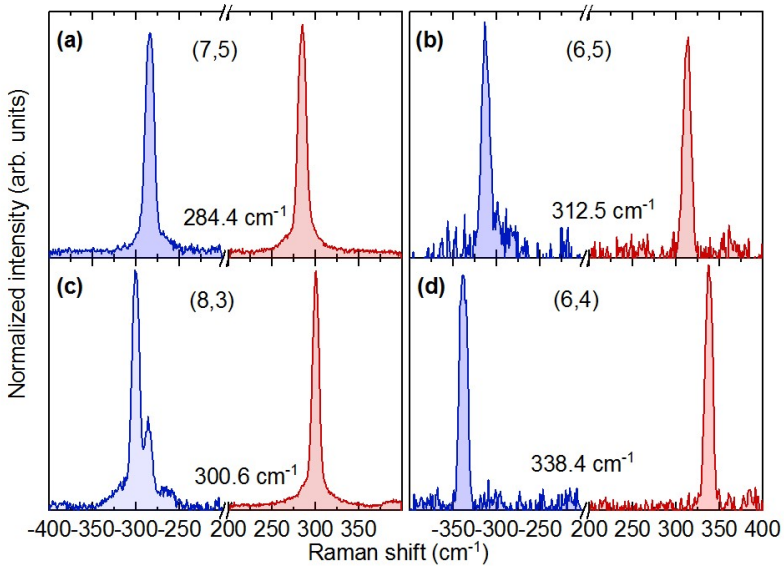

Figure 2.25 *Radial breathing modes of the (7,5), (6,5), (8,3), and (6,4) enriched samples. Stokes components in red and anti-Stokes components in blue. Each nanotube is excited at its E_{22} transition. The RBM frequency of the tube is determined by its chirality.*

peak verifies a successful single chirality enrichment of the sample. The only sample containing a faint contamination is the (8,3) nanotube, containing a fraction of (7,5) chiralities, see Figure 2.25c.

The RBM resonance profile exhibits a symmetric shape [84], due to the identical intensity of the incoming and outgoing resonance [85] (Figure 2.26b). The phonon energy is small, compared to the width of the resonance profile, therefore incoming and outgoing resonances are not resolved. The maxima of the scattering efficiency are between the two resonances because of the overlap of both. The exciton energy is obtained by fitting the scattering intensity Eq. (2.27), respecting phonon emission and phonon absorption in Stokes and anti-Stokes scattering:

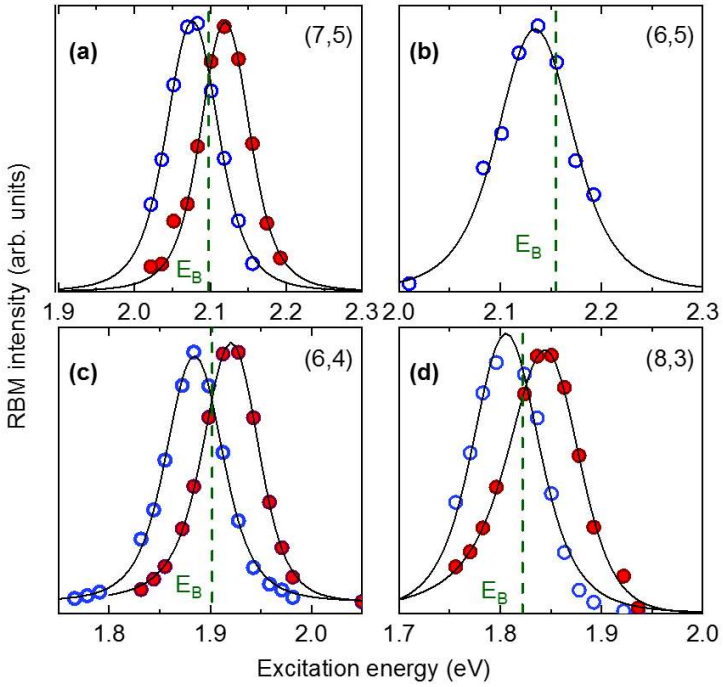

Figure 2.26 *Stokes (filled red symbols) and anti-Stokes (blue open symbols) RBM Raman intensity plotted over the excitation energy for a different nanotube chiralities. Solid lines are fits by Eq. (2.35). The energy of the bright exciton is marked by the vertical dashed line and is determined by the fitting, see Table 2.2.*

$$I_{RBM} \sim \left| \frac{M_1}{E_L - E_B - i\frac{\Gamma}{2}} - \frac{M_2}{E_L - E_B \pm \hbar\omega_{ph} - i\frac{\Gamma}{2}} \right|^2, \tag{2.35}$$

where E_L is the laser energy, E_B is the energy of the second exciton transition (bright exciton), $\hbar\omega_{ph}$ is the phonon energy, and Γ represents the finite lifetime broadening. The first term in Eq. (2.35) is responsible for the incoming resonance, the second term for the outgoing resonance. To fit a symmetric cross section we use a combined matrix element with $M_1 = M_2$. Separate fits of the Stokes and anti-Stokes resonance profiles yielded identical energy and lifetime broadening of the bright exciton, see Table 2.2.

The transition energies (E_B) are comparable with previous studies, but are shifted by up to 45 meV to smaller energies [40,84], see Table 2.2. There are possibly two contributing mechanisms, bundling of the tubes and water molecules encapsulation. Encapsulation of water molecules induces

Table 2.2. *Fitting parameters of the RBM resonance profiles by Eq. (2.35)*

(n,m)	2n+m	Scattering type	$\Gamma/2$ (meV)	E_B (eV)	E_B (eV) Ref. [40]
(6,5)	17	anti-Stokes	60	2.155	2.18
(7,5)	19	Stokes	41	1.902	1.92
		anti-Stokes	42	1.902	
(8,3)	19	Stokes	59	1.822	1.86
		anti-Stokes	52	1.824	
(6,4)	16	Stokes	47	2.098	2.11
		anti-Stokes	52	2.097	

a red shift of our enrichment method towards empty or filled nanotubes shift of the transition energies ∼15 meV [86]. The selectivity is possible, but has not been studied yet. Bundling does not affect the frequency of the RBM [87], but water encapsulation is accompanied by a frequency upshift [42,86]. The difference between our measured RBM frequencies and previously reported values corroborates the water encapsulation mechanism as the dominant effect [40,84] (Table 2.2). The remaining shift is due to the formation of small nanotube bundles. The (8,3) sample was most strongly affected with a bundling-induced shift of ∼25 meV.

2.3.4 Fifth-order perturbation theory for Stokes and anti-Stokes scattering

In Subsection 2.1.8 I discussed in detail the fifth-order perturbation theory. Here, I will show how to apply it to the anti-Stokes scattering. Figure 2.27a illustrates the scattering pathways corresponding to one of the possible Stokes (B) and anti-Stokes scattering processes (B'). In the Stokes process (B), the incident photon excites the bright exciton from the ground state (*a*). The exciton is scattered to the dark state by creating the K phonon (*b*). Then backscattering occurs, where the system gets to the same excited state of bright exciton by reabsorbing the K phonon (*c*). After that, the G phonon is created (*d*) and the bright exciton relaxes by emitting the photon of smaller energy.

The scattering via a dark exciton applies equally to Stokes and anti-Stokes processes; the K point phonon is first created and then annihilated (Figure 2.27a). The probability of the inverse process of the interaction with the dark exciton is strongly reduced by the Boltzmann factor. In the anti-Stokes B' process, the time order is reversed compared to process B. The excited bright exciton absorbs a G phonon, increasing its energy (*a*, *b*) followed the emission (*c*) and the reabsorption of the K phonon takes place (*d*). Finally, the bright exciton relaxes by emitting a photon of higher energy.

The Feynman diagrams summarizing all contribution to the fifth-order process are depicted in Figure 2.27b. The left panel shows the Stokes processes. The difference between the Stokes processes A-C arises from the multiple possible scattering sequences, where the scattering and backscattering (interference) between the excitonic states takes place at various steps of the third order Raman process. The ω_2 phonon participating in the interference are ω_K and ω_G when scattered between bright-dark and bright-bright states, respectively. The right panel of Figure 2.27b shows possible fifth-order anti-Stokes processes. For each A – C Stokes process there is a time reversed A' – C' anti-Stokes process with an inverted direction of the G phonon arrow**.** On vertexes, where in the Stokes process the G phonon is created in the anti-Stokes process phonon annihilation occurs.

The combination of the third- and fifth-order processes results in Raman cross-sections $|W_G|^2$ as a function of the laser energy reads [23]

$$W_{G\pm}(E_L) = \frac{|M_{B\Gamma S}^{XL}|^2 M_G^{XP}}{(E_{B\Gamma S}\pm\hbar\omega_G - E_L)(E_{B\Gamma S} - E_L)}\left[1 + \frac{|M_G^{XP}|^2}{(E_{B\Gamma S}+\hbar\omega_G\pm\hbar\omega_G - E_L)(E_{B\Gamma S}+\hbar\omega_G - E_L)} + \right.$$
$$\frac{|M_G^{XP}|^2}{(E_{B\Gamma S} - E_L)(E_{B\Gamma S}\pm\hbar\omega_G - E_L)} + \frac{|M_K^{XP}|^2}{(E_{DKS}\pm\hbar\omega_G+\hbar\omega_K - E_L)(E_{B\Gamma S}\pm\hbar\omega_G - E_L)} +$$
$$\left.\frac{|M_K^{XP}|^2}{(E_{DKS}\pm\hbar\omega_G+\hbar\omega_K - E_L)(E_{DKS}+\hbar\omega_K - E_L)} + \frac{|M_K^{XP}|^2}{(E_{B\Gamma S} - E_L)(E_{DKS}+\hbar\omega_K - E_L)}\right]. \quad (2.36)$$

M^{XL} is the exciton-photon and M^{XP} the exciton-phonon matrix element. The energy of the bright exciton is expressed as $E_{B\Gamma S} = E_B + i\Gamma_B/2$ and the energy of the dark exciton as $E_{DKS} = E_D + i\Gamma_D/2$. Γ_B (Γ_D) is the damping parameter associated with the lifetime of the bright (dark) exciton. $\hbar\omega_G$ is the phonon energy of the G mode observed in experiment. $\hbar\omega_K$ represents the phonon

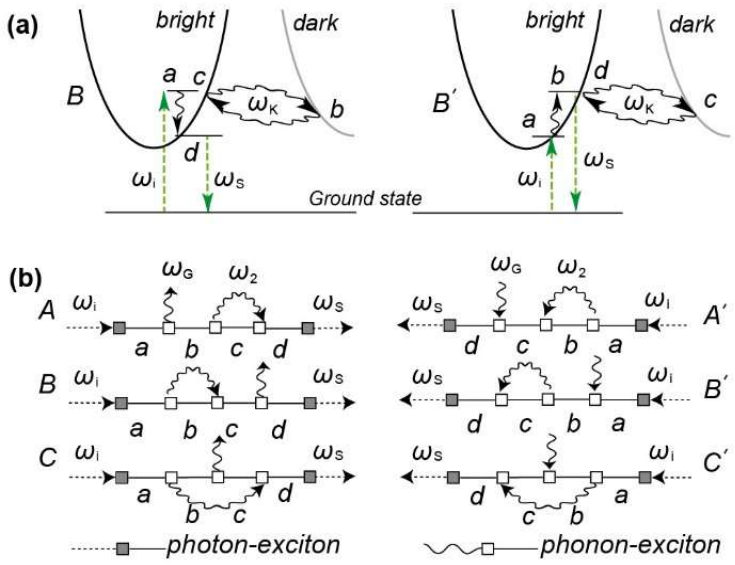

Figure 2.27 *Fifth-order Raman process.* ***(a)*** *scheme of the scattering, corresponding to the Stokes B (left panel) and time reversed anti-Stokes B' (right panel) processes.* ***(b)*** *Feymann diagrams (A-C) of the fifth-order contributions for Stokes and (A'-C') of the time reversed processes for anti-Stokes Raman scattering.*

energy involved in the coupling to the dark exciton. The positive sign of the phonon energy $\hbar\omega_G$ in Eq. (2.36) corresponds to the Stokes process, the negative sign to the anti-Stokes process. The first term in Eq. (2.36) describes the third-order process, the second and third fifth-order describe bright-bright process, and three last terms are due to the fifth-order bright-dark process.

2.3.5 Anti-Stokes resonance Raman profiles

Figure 2.28a shows the Stokes and anti-Stokes Raman spectra of the G mode of an (8,3) nanotube, normalized as described in the experimental section (Sec. 2.2.3). The energy range covers the resonance window of the second exciton transition at E_{22} =1.83 eV. The strongest peak at ±1584 cm^{-1} corresponds to the longitudinal optical phonon (LO). The maxima in the scattering efficiency occur at excitation energies that match the incoming and outgoing resonances for this phonon mode, see Figure 2.28b. The incoming resonance coincides with the energy of excitonic transition, while the outgoing resonances are shifted to higher (Stokes) and lower (anti-Stokes) excitation energies. The incoming Stokes resonance is higher in intensity than the outgoing Stokes resonance. This agrees with the asymmetric shapes of the Stokes cross-section previously reported in semiconducting and metallic nanotubes [23,69,70].

The anti-Stokes resonance profile also shows a strong asymmetry between incoming and outgoing resonance, see Figure 2.28. Remarkably, the asymmetry between the resonances is inverted compared to Stokes scattering. The incoming resonance in the anti-Stokes profile is weaker than the outgoing resonance, as seen in the plot of the Raman cross-section versus laser energy in

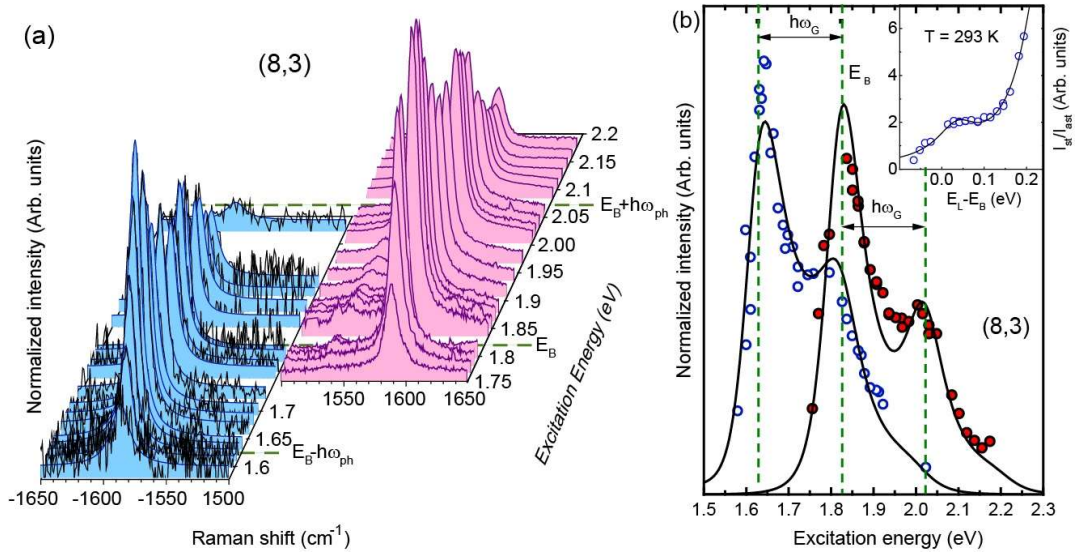

Figure 2.28 *G mode Stokes and anti-Stokes Raman spectra of (8,3) nanotubes.* ***(a)*** *Normalized Raman spectra covering the incoming and outgoing resonances. The anti-Stokes spectra include fits with a Lorentzian for clarity.* ***(b)*** *Excitation energy dependence of the LO phonon for Stokes (filled circles) and anti-Stokes (open circles) resonance scattering. The full lines are fits by Eq. (2.36). The dashed vertical lines represent the calculated positions on the incoming resonance at E_B and outgoing resonances at $E_B \pm \hbar\omega_G$. The open dots in the inset are the Stokes/anti-Stokes ratio plotted versus energy difference between the laser and the bright exciton $(E_L - E_B)$. The line is a fit by Eq.* (2.37) *standing for the resonant correction factor.*

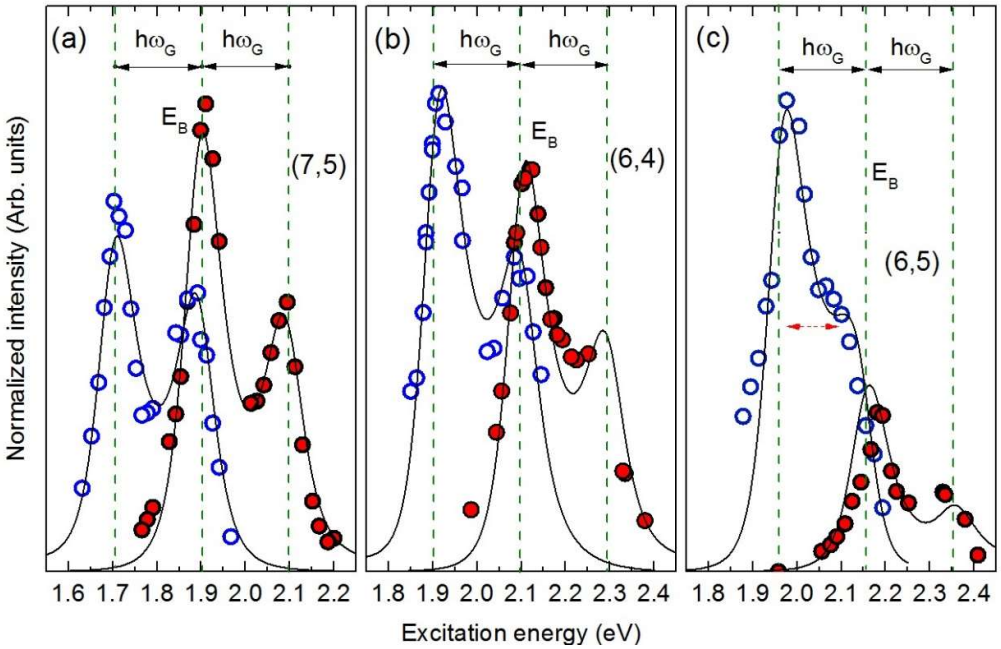

Figure 2.29 *The LO phonon Stokes (filled circles) and Anti-Stokes (open circels) calibrated resonance Raman profiles of the single chirality (6,5), (7,5) and (6,4) samples. The vertical dashed lines correspond to the positions of the incoming and outgoing resonances obtained from the RBM analysis of E_{22} and measured phonon frequencies. The data is fitted by Eq. (2.36).*

Figure 2.28b. Figure 2.29 shows the measured Raman cross section of three additional chiralities (6,5), (7,5) and (6,4). The (8,3), (7,5) and (6,5) Stokes Raman profiles resemble the previously reported data[69], while the (6,4) Stokes profile is presented for the first time. The intensity ratios between incoming and outgoing resonances vary for the chiralities but overall the behavior is similar to the (8,3) tube in Figure 2.28a. The reversed ratio in the intensity maxima of the Stokes and anti-Stokes is understood by considering time reversal symmetry. When inverting the time order we turn A, B and C processes into the A', B' and C' processes (Figure 2.27). Considering $I_S(\omega_i, \omega_S) = I_{AS}(\omega_S, \omega_i)$ the equivalence between outgoing Stokes and incoming anti-Stokes becomes apparent. At frequencies corresponding to such resonances, the interference between the scattering channels in Eq. (2.36) is destructive and leads to a quenching of the Raman intensity.

The presence of multiple excitonic states and several scattering pathways in the Raman process shifts the positions of the intensity maxima away from incoming and outgoing resonances at E_B and $E_B \pm E_{ph}$ expected in two-level systems. The strength of the shift depends on the energetic separation of the excitons and the electron-phonon matrix elements. This shift is strongest in the (6,5) tube, where the intensity maxima of the anti-Stokes resonance profile are separated by only 130 meV compared to 196 meV phonon energy, as marked by horizontal dashed arrow on in Figure 2.29c. Similar behavior was reported for armchair nanotubes [23].

Stokes and anti-Stokes intensities are crucial when evaluating the effective phonon temperature in carbon nanotubes by Raman scattering. The anti-Stokes/Stokes ratios are no longer exclusively dependent on the temperature and so resonance effects have to be considered (Figure 2.28b). We suggest simplified empirical correction factors, which depend on the energy of the bright exciton and the laser energies $\Delta = (E_L - E_B)$:

$$\frac{I_{Stokes}}{I_{anti-Stokes}}(T,\Delta) = e^{\frac{\hbar\omega_G}{KT}} \cdot \frac{|W_{G+}(E_L)|}{|W_{G-}(E_L)|} \approx e^{\frac{\hbar\omega_G}{KT}} \cdot \left[\frac{C_1 y}{y+(\Delta-\Delta_1)^2} + \frac{C_2 y}{y+(\Delta-\Delta_2)^2}\right], \quad (2.37)$$

where Δ_1 and Δ_2 correspond to the effective positions of the Stokes and anti-Stokes resonances. $2\sqrt{y}$ is the width of the combined profiles and C_1, C_2 are constants reflecting the varying intensity of the Raman resonances, see Table 2.3. As shown in the inset of Figure 2.28 the experimental results are reproduced by Eq. (2.37) in the regions where both signals are well detectable. It should be mentioned that the additional correction on ω^3 and spectrometer sensitivity should be applied depending if the Raman intensity is calibrated on a non-Raman reference, see Eq. (2.34).

Table 2.3 *Constants for Stokes/anti-Stokes intensity ratios, Eq. (2.37)*

(n,m)	y (meV)	C_1	C_2	Δ_1 (meV)	Δ_2 (meV)
(6,5)	1.22	1.69	3.64	45	180
(7,5)	2.03	1.57	13.6	31	187
(8,3)	3.6	1.33	10.09	35	248
(6,4)	3.1	1	4.6	28	170

I now analyze the Stokes and anti-Stokes resonance profiles in the framework of third – and fifth-order perturbation theory, Eq. (2.36). We fit the Stokes and anti-Stokes resonance profiles imposing identical exciton-phonon and exciton-photon matrix elements for both profiles for a single chirality. The energies of the bright excitons were taken from the RBMs measurements. For the energy splitting between dark and bright excitons the values of the first excitonic transition E_{11} were used, reported for all chiralities except the (6,4) nanotube [57]. For which we use an average value of the other tubes. The fitting parameters for all nanotubes are summarized in Table 2.4. For the three SII tubes (7,5), (8,3), (6,4) [(n – m) mod3 = 2] I obtain excellent fits of the Stokes and anti-Stokes resonance profiles, see Figure 2.29 and Figure 2.28a. For the (6,5) chirality the fitted Stokes resonance profile lies at lower energies compared with the experimental data, Figure 2.29c.

The exciton- phonon matrix element of the bright state is plotted in Figure 2.30a as a function of chiral angle. The matrix element of (7,5) is significantly smaller than in (8,3) (6,4) and (6,5). In the 2m+n=19 family, the dramatic decrease of M_G^{XP} is corroborated by the tight binding calculation, performed according to Refs. [27,88,89] to verify this behavior. The calculated matrix element decreases from (8,3) tube to (7,5) tube by a factor of 24, in good agreement with the 30 times drop obtained experimentally. The M_K^{XP} dependence on the chiral angle is shown in Figure

Table 2.4 *Stokes (S) and anti-Stokes (a-S) fitting parameters of the LO (G^+) Raman cross-sections with Eq. (2.36)*

(n,m)	Scattering type	E_B (eV)	E_D (eV)	$M_{B\Gamma S}^{XL}$ (meV)	M_G^{XP} (meV)	M_K^{XP} (meV)	$\Gamma_B/_2$ (meV)	$\Gamma_D/_2$ (meV)
(6,5)	S	2.155	2.184	83	195	140	75	72
	a-S	2.155	2.184	83	195	140	75	72
(7,5)	S	1.902	1.938	764	7	130	73	37
	a-S	1.902	1.938	764	7	130	73	37
(8,3)	S	1.822	1.855	115	154	152	84	52
	a-S	1.824	1.857	115	154	152	84	41
(6,4)	S	2.098	2.131	71	152	321	90	229
	a-S	2.097	2.131	71	152	321	74	1400

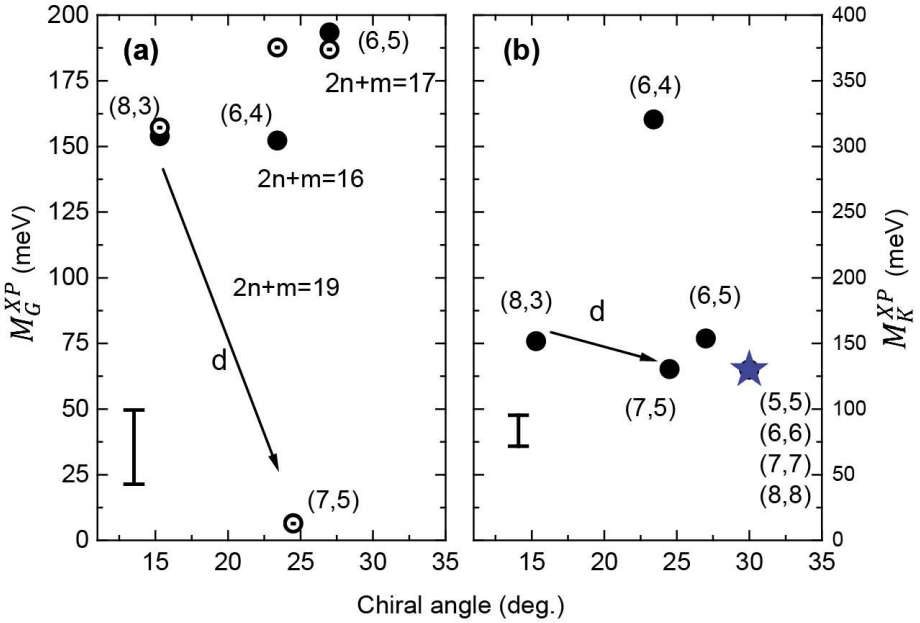

Figure 2.30 *Fitting parameters of the Stokes and anti-Stokes profiles versus chiral angle.* ***(a)*** *bright exciton-phonon matrix element* $\boldsymbol{M_G^{XP}}$ *obtained from the experiment (filled dots) and calculated (open circles)* [27,88,89]. ***(b)*** *Dark exciton-phonon matrix element* $\boldsymbol{M_K^{XP}}$ *as function of chiral angle. Arrows indicate the direction along which d is increasing in single 2n+m nanotube family. Dark exciton-phonon matrix element* $\boldsymbol{M_K^{XP}}$*, filled circles our data, stars data for armchair nanotubes* [23]*. Vertical error bars show the averaged standard error.*

2.30b. We observe the same trend as M_G^{XP} in SII type tubes, where the matrix element decreases with the chiral angle. The matrix elements of achiral tubes in our experiment is close to the values reported for armchair (5,5), (6,6), (7,7) and (8,8) tubes [23].

The scattering between bright and dark excitons can also be realized by impurities. Defects can provide momentum to reinforce the interaction pathways and thus alter the asymmetry of the resonance Raman profile of nanotubes. The effect is similar to the double resonant Raman processes involved in the defect induced mode (D) formation [62]. Our experiments and past studies were performed on material with excellent crystal quality and low defects concentration. It is of future interest to perform similar experiments for more defective tubes to further advance our understanding of Raman scattering in nanotubes and, particularly, interactions between dark and bright excitons.

The strong outgoing anti-Stokes Raman resonances of carbon nanotubes point towards the possibility of engineering the population of selected phonon branches controlled by light. A population increase may be achieved at laser energies matching the outgoing Stokes resonance. Remarkably, for nanotubes a reduction of a phonon population may occur under certain condition (phonon cooling). It requires the efficiency of the anti-Stokes process to overtake the efficiency of the Stokes process. We observed comparable intensities of the Stokes and anti-Stokes process at the energy matching the outgoing anti-Stokes resonance for (6,5) tube after normalization. G phonon cooling may occur in carbon nanotubes at room temperatures [78].

2.3.6 Theory of the exciton-phonon matrix element calculation

In the previous subchapter, I demonstrated how the remarkably high exciton-phonon coupling in nanotubes can be tuned by the selection of the chirality. In order to extrapolate this result for a desired coupling factor, I further demonstrate how the tight binding method can calculate the exciton-phonon matrix elements [2]. The calculated values for the matrix element for four particular chiralities are shown in Figure 2.30a. The calculation below is specified for the A_1 exciton LO phonon interaction at the second excitonic transition, reflecting M_G^{XP}. However it can be generalized for any exciton/transition and phonon type. To investigate the exciton-phonon coupling, the exciton-phonon Hamiltonian is decomposed into the electron- and hole-phonon interactions. The electron-phonon interactions are due to the deformation potential of the π orbitals formulated by density functional theory (DFT) and simplified by the local density approximation. The interaction of the exciton and phonon is then calculated for the graphene lattice. After that, the matrix elements can be selected for a particular chirality and excitonic transition by knowing the point in cutting line forming the exciton.

First the excitonic eigenfunction $\Psi_{\boldsymbol{q}}^{n}(\boldsymbol{r})$ must be defined. This function corresponds to an exciton with momentum $\boldsymbol{q}$ and energy $\Omega_{\boldsymbol{q}}^{n}$. This expression for the wave function follows [88]:

$$\Psi_{\boldsymbol{q}}^{n}(\boldsymbol{r}) = \sum_{k} Z_q^n(k)\psi_{k+q}^{c}(r)\psi_k^{\vartheta *}(\boldsymbol{r}), \tag{2.38}$$

where $Z_q^n(k)$ is the amplitude, reflecting the probability to find an electron-hole pair with an electron in state ψ_{k+q}^{c} and a hole in state $\psi_k^{\vartheta *}(r)$. I will use further use index b both for all electronic states. For the electron $b = c$ (conduction band) and hole $b = \vartheta$ (valence band). Within the tight-binding approach the electron eigenfunction can be written as [90]:

$$\begin{cases} \psi_k^b(\boldsymbol{r}) = \sum_{s,o} C_{so}^b(\boldsymbol{k})\Phi_{so}(\boldsymbol{k},\boldsymbol{r}) \\ \Phi_{so}(\boldsymbol{k},\boldsymbol{r}) = \dfrac{1}{\sqrt{N_u}}\sum_{u=1}^{N_u} e^{ik\cdot\boldsymbol{R}_{us}}\phi_0(\boldsymbol{r}-\boldsymbol{R}_{us}) \end{cases}, \tag{2.39}$$

with $C_{so}^b(\boldsymbol{k})$ are so-called Bloch amplitudes and $\Phi_{so}(\boldsymbol{k},\boldsymbol{r})$ normalized Bloch sums; ϕ_0 and $\boldsymbol{R}_{us}$ are atomic orbitals and atomic positions, N_u is the total number of units cells in the system. The unit cell index u and sublattice index s indicate the position of each atom. The index o labels the orbital of the atom and b is the energy band index.

The Hamiltonian representing the exciton-phonon interaction is [88,91]

$$\mathcal{H}_{EP} = \sum_{\boldsymbol{kqv}} \left[M_{\boldsymbol{kc},\boldsymbol{qv}}^{EP} c_{(\boldsymbol{k}+\boldsymbol{q})c}^{\dagger} c_{\boldsymbol{kc}} - M_{\boldsymbol{k}\vartheta,\boldsymbol{qv}}^{EP} c_{(\boldsymbol{k}+\boldsymbol{q})\vartheta}^{\dagger} c_{\boldsymbol{k}\vartheta}\right]\left(b_{\boldsymbol{qv}} + b_{-\boldsymbol{qv}}^{\dagger}\right), \tag{2.40}$$

[2] Theory for exciton-phonon matrix element calculation was developed by Bruno M. G Vieira

where $M^{EP}_{\boldsymbol{kc,qv}}$ is the electron-phonon matrix element for an electron in the initial state given by k and b and a phonon of mode v and momentum $\boldsymbol{q}$. $c^{\dagger}_{\boldsymbol{kb}}(c_{\boldsymbol{kb}})$ is the creation (annihilation) operator for an electron $b = c$ and hole $b = \vartheta$ in a state given by $\boldsymbol{q}$. $b^{\dagger}_{\boldsymbol{qv}}(b_{\boldsymbol{qv}})$ is the creation (annihilation) operator for a phonon given by $\boldsymbol{q}$ and v.

Using the latter expression for the Hamiltonian and exciton eigenfunction, we write the exciton-phonon matrix element in terms of electron-phonon interaction (matrix-elements):

$$M^{XP}_{n_i,n_f,v}(\boldsymbol{q}_i,\boldsymbol{q}_f) = \left\langle \Psi^{n_f}_{\boldsymbol{q}_f} \middle| \mathcal{H}_{EP} \middle| \Psi^{n_i}_{\boldsymbol{q}_i} \right\rangle = \sum_{k} \left[M^{EP}_{n_i,\pm\boldsymbol{q}v} Z^{nf}_{\boldsymbol{k}\pm\boldsymbol{q},\boldsymbol{k}-\boldsymbol{q}_i} Z^{n_i}_{\boldsymbol{k},\boldsymbol{k}-\boldsymbol{q}_i} - M^{EP}_{\boldsymbol{k}v,\pm qv} Z^{nf}_{\boldsymbol{k}+\boldsymbol{q}_f,k} Z^{n_i}_{\boldsymbol{k}+\boldsymbol{q}_f,\boldsymbol{k}\pm\boldsymbol{q}} \right], \tag{2.41}$$

Where the $\boldsymbol{q} = \pm(\boldsymbol{q}_i - \boldsymbol{q}_f)$ expression arises from the momentum conservation. The ± signs stand for the phonon emission and absorption i.e. Stokes and anti-Stokes scattering. The electron-phonon matrix element $M^{EP}_{\boldsymbol{kb},\boldsymbol{qv}}$ are calculated as follows [27] :

$$M^{EP}_{\boldsymbol{kb},\boldsymbol{qv}} \equiv M^{v}_{\boldsymbol{bk}\to b\boldsymbol{k}'} = -\sqrt{\frac{\overline{n_v}(\boldsymbol{q})}{N_u}}\, g^{v}_{\boldsymbol{bk}\to b\boldsymbol{k}'}, \tag{2.42}$$

With $\boldsymbol{k}' = \boldsymbol{k} + \boldsymbol{q}$, and $\overline{n_v}(\boldsymbol{q})$ is a temperature dependent factor accounting for the phonon occupation number and distinguishes between the Stokes and anti-Stokes scattering.

The matrix element $g^{v}_{\boldsymbol{bk}\to b\boldsymbol{k}'}$ is

$$g^{v}_{\boldsymbol{bk}\to b\boldsymbol{k}'} = -\sqrt{\frac{h}{m_C \omega_v(\boldsymbol{q})}}\, D^{v}_{\boldsymbol{bk}\to b\boldsymbol{k}'}. \tag{2.43}$$

Considering only the π orbitals and implementing Eq. (2.39) the $D^{v}_{\boldsymbol{bk}\to b\boldsymbol{k}'}$ can be expressed as:

$$\begin{aligned} D^{v}_{\boldsymbol{bk}\to b\boldsymbol{k}'} = {} & \sum_{s'} C^{b^*}_{s}(\boldsymbol{k}') C^{b}_{s'}(\boldsymbol{k}) \sum_{us} e^{-i\boldsymbol{q}\cdot\boldsymbol{R}_{0s'}} e^{v}_{q}(\boldsymbol{R}_{us}) \cdot \lambda_{\pi\pi}(\boldsymbol{R}_{us} - \boldsymbol{R}_{0s'}) \\ & + \sum_{ss'} C^{b^*}_{s'}(\boldsymbol{k}') C^{b}_{s}(\boldsymbol{k}) \sum_{u} e^{-ik\cdot(\boldsymbol{R}_{us}-\boldsymbol{R}_{0s'})}\, e^{-i\boldsymbol{q}\cdot\boldsymbol{R}_{0s'}} \left[e^{v}_{q}(\boldsymbol{R}_{0s'}) \right. \\ & \left. - e^{v}_{q}(\boldsymbol{R}_{us}) \right] \cdot a_{\pi\pi}(\boldsymbol{R}_{us} - \boldsymbol{R}_{0s'}) \ , \end{aligned} \tag{2.44}$$

In which the condition $C^{b}_{s}(\boldsymbol{k}) \equiv C^{b}_{s\pi}(\boldsymbol{k})$. $e^{v}_{\boldsymbol{q}}(\boldsymbol{R}_{us}) = e^{-i\boldsymbol{q}\cdot\boldsymbol{R}_{us}} e^{v}_{\boldsymbol{q},s}$ is fulfilled for all elements, where $e^{v}_{\boldsymbol{q},s}$ stands for the phonon normal mode displacement. $a_{\pi\pi}(\boldsymbol{R})$ and $\lambda_{\pi\pi}(\boldsymbol{R})$ are the deformation potential vectors for the π band. Using DFT local density approximation (LDA) we can determine the deformation potential [92]. Considering the potentials are negligible for the $R > R_1$, with R_1 being the distance between the nearest neighbors.

$$a_{\pi\pi}(\boldsymbol{R}_{us}-\boldsymbol{R}_{0s\prime})=\begin{cases}a\widehat{\boldsymbol{R}}_{1j}^{(s\prime)},\text{for }|\boldsymbol{R}_{us}-\boldsymbol{R}_{0s\prime}|<R_1\\0,\text{otherwise}\end{cases},$$
$$\lambda_{\pi\pi}(\boldsymbol{R}_{us}-\boldsymbol{R}_{0s\prime})=\begin{cases}\lambda\widehat{\boldsymbol{R}}_{1j}^{(s\prime)},\text{for }|\boldsymbol{R}_{us}-\boldsymbol{R}_{0s\prime}|<R_1\\0,\text{otherwise}\end{cases} \tag{2.45}$$

In which $a\equiv a_1=a(R_1)=a(a_{cc})$ and $\widehat{\boldsymbol{R}}_{1j}^{(s\prime)}$ Is the unit vector of the j-th neighbor of atom *0s*. Now we turn to the analysis of the particular case of the Γ point phonons with $q=0$ and $(k=k')$. Considering the symmetry of the deformation potential $\sum_{j=0}^{3}\widehat{\boldsymbol{R}}_{1j}^{(s\prime)}=0$ Eq. (2.44) with inserted Eq. (2.45) can be simplified to:

$$D^{v}_{b\boldsymbol{k}\to b\boldsymbol{k}'}=\sum_{s\prime}C^{b^*}_{s\prime}(\boldsymbol{k}')C^{b}_{-s\prime}(\boldsymbol{k})\sum_{j=1}^{3}e^{i\boldsymbol{k}\cdot\widehat{\boldsymbol{R}}_{1j}^{(s\prime)}}\,a\widehat{\boldsymbol{R}}_{1j}^{(s\prime)}\left[e^{v}_{0,s\prime}-e^{v}_{0,-s\prime}\right]. \tag{2.46}$$

The sublattices are reindexed $s'=A$ and $-s'=B$ and

$$D^{v}_{b\boldsymbol{k}\to b\boldsymbol{k}'}=d^{(a)}_{bv}(AB)+d^{(a)}_{bv}(BA),where$$

$$\begin{aligned}d^{(a)}_{bv}(AB)&=C^{b^*}_{A}(\boldsymbol{k}')C^{b}_{B}(\boldsymbol{k})\sum_{j=1}^{3}e^{i\boldsymbol{k}\cdot\widehat{\boldsymbol{R}}_{1j}^{(A)}}\,a\widehat{\boldsymbol{R}}_{1j}^{(A)}\left[e^{v}_{0,A}-e^{v}_{0,B}\right]\\&=aC^{b^*}_{A}(\boldsymbol{k}')C^{b}_{B}(\boldsymbol{k})\sum_{j=1}^{3}e^{i\boldsymbol{k}\cdot\widehat{\boldsymbol{R}}_{1j}^{(A)}}\,T^{(AB)}_{vj}\end{aligned} \tag{2.47}$$

$T^{(AB)}_{vj}$ is the new function implemented in order to simplify mathematical expression. Noticing that $d^{(a)}_{bv}(AB)=d^{(a)}_{bv}(BA)^*$ we can now calculate

$$D^{v}_{b\boldsymbol{k}\to b\boldsymbol{k}'}=2Re\left[d^{(a)}_{bv}(AB)\right] \tag{2.48}$$

By using the simple tight binding method $C^{\pm^*}_{A}(\boldsymbol{k})C^{\pm}_{B}(\boldsymbol{k})=\pm C^{\pm}_{B}(\boldsymbol{k})^2$ we can further simplify $d^{(a)}_{bv}(AB)$, we denoted here $b=+\,(b=-)$ corresponding to the valence (conduction) band. This results in the final expression

$$\begin{aligned}D^{v}_{(\pm)\boldsymbol{k}\to(\pm)\boldsymbol{k}'}&=\pm 2aC^{\pm}_{B}(\boldsymbol{k})^2\sum_{j=1}^{3}e^{i\boldsymbol{k}\cdot\widehat{\boldsymbol{R}}_{1j}^{(A)}}\,T^{(AB)}_{vj}=\pm 2a\sum_{j=1}^{3}e^{i\boldsymbol{k}\cdot\widehat{\boldsymbol{R}}_{1j}^{(A)}}\,C^{\pm}_{B}(\boldsymbol{k})^2\,T^{(AB)}_{vj}\\&=\pm 2a\sum_{j=1}^{3}Re\left[F^{\pm}_{j}(\boldsymbol{k})\right]T^{(AB)}_{vj}\,.\end{aligned} \tag{2.49}$$

$F^{\pm}_{j}(\boldsymbol{k})$ can be found by substituting the simple tight-binding expression [90] for $C^{\pm}_{B}(\boldsymbol{k})$. Now we can define the A_1 exciton-Γ point phonon matrix element in the form of

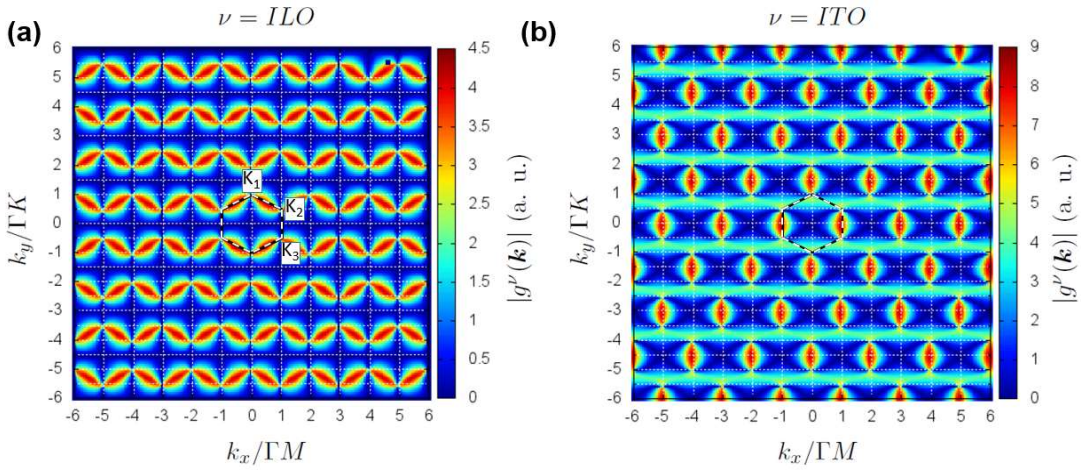

Figure 2.31 *Matrix element* $\boldsymbol{M_G^{XP}} \sim |\boldsymbol{g^{\nu}(k)}|$ *plotted over the graphene lattice for* ***(a)*** *LO and* ***(b)*** *TO phonon modes.* $\boldsymbol{k_x}$ *is normalized by the distance between the Γ and M points while* $\boldsymbol{k_y}$ *in normalized by the distance between the Γ and K points. The hexagon in the middle indicates the Brillouin zone of graphene.*

$$g^{\nu}(k) = D^{\nu}_{(-)\boldsymbol{k}\to(-)k} - D^{\nu}_{(+)\boldsymbol{k}\to(+)k}. \tag{2.50}$$

This form allows us to study how the exciton-phonon matrix element varies over the graphene lattice. Finally, the phonon eigenvectors need to be defined. For the LO phonon we select

$$\begin{aligned} e^{\nu}_{0,A} - e^{\nu}_{0,B} &\propto \hat{y} \\ T^{AB}_{vi} &= (T, 0, -T). \end{aligned} \tag{2.51}$$

And for the TO phonon

$$\begin{aligned} e^{\nu}_{0,A} - e^{\nu}_{0,B} &\propto \hat{x} \\ T^{AB}_{vi} &= (T, -2T, -T). \end{aligned} \tag{2.52}$$

The value of $g^{\nu}(\boldsymbol{k})$ is proportional to the exciton-phonon matrix element. $|g^{\nu}(k)|$ is plotted in reciprocal space as a function of $\boldsymbol{k} = (k_x, k_y)$ in Figure 2.31. The exciton-phonon coupling varies from zero to its maximum inside a single unit cell of graphene, shown by the dashed hexagon in the middle of Figure 2.31a and b. The distribution of the exciton-phonon matrix elements differs between LO and TO phonons. This occurs due to the different directions of eigenvectors, defined by Eq. (2.51) and (2.52). The degeneracy of the K points in graphene gets lifted in carbon nanotubes. The maxima of the exciton-LO phonon matrix elements occur on the line between the K_1 and K_2, see Figure 2.31a. The maxima of the exciton-TO phonon matrix element occurs on the line between K_2 and K_3, see Figure 2.31b.

For further analysis, an approach similar to the zone folding can be applied [33] to the matrix elements of graphene. The cutting line responsible for the excitonic transition of interest will preselect allowed exciton-phonon matrix element. This line in the graphene lattice defines the

strength of the exciton-phonon interaction. The matrix element is extracted from Figure 2.31 by applying the coordinates from Eq. (2.10) for a defined nanotube chirality and transition. When moving from the second to the first transition the cutting line moves closer to the K point. The closer the transition lies to the K point the higher exciton-phonon matrix element gets. In the next Chapter, I will verify this behavior.

2.3.7 Summary

The anti-Stokes cross-section of the high-energy LO modes was measured in carbon nanotubes. The excitonic nature of the optical transitions alters the Stokes and anti-Stokes Raman scattering cross-section. It results in strong incoming Stokes and outgoing anti-Stokes resonances, as we observed in four different semiconducting nanotube species (8,3), (7,5), (6,4) and (6,5). The resonant factors, including the asymmetry of the resonant Raman profiles, for a future evaluation of Stokes/anti-Stokes ratio are developed. The resonance profiles are well explained by a quantum interference of third- and fifth-order scattering processes. By a simultaneous fitting of the Stokes and anti-Stokes cross sections, we obtained exciton-phonon matrix elements for various carbon nanotubes in agreement with the tight binding model.

2.4 Transition dependence of Exciton-Phonon coupling [3]

2.4.1 Introduction

In the previous Chapter, I focused on the asymmetry of the LO phonon resonance profile at the second excitonic transition (E_{22}) of semiconducting nanotubes [24,69]. However, the second excitonic state is located inside the uncorrelated electron hole (e-h) continuum of the first excitonic transition, which can contribute to the scattering efficiency. Such interactions were reported for three-dimensional (3d) crystals with excitonic properties [93]. The lowest energy excitonic transition (E_{11}) provides the cleanest excitonic level where the interference with uncorrelated e-h pairs (higher excitonic states) is impossible due to the large binding energy of the excitonic state [53,94]. The resonant Raman study of the first transition is essential to clarify the origin of the asymmetry.

The comparison between the asymmetry in Stokes resonance Raman profiles between the E_{22} and the E_{11} transitions will clarify two main controversies found in the literature surrounding this subject. First, to understand if the absence of the asymmetry reported for the E_{33} transition is related to the high transition number, or the large diameter of the investigated nanotube [95]. Second, the validity of the alternative theory attributing the asymmetry to the displacement of the nuclear coordinate can be tested based on its predictions for the transition number dependence [69].

Complementary to the asymmetry effect in resonance Raman profiles, the width and absolute scattering efficiency are induced by the coherent excitonic lifetime and exciton-phonon coupling strength respectively. The resonant Raman study of radial breathing modes (RBMs) at the first and second excitonic transitions reported strong enhancement of the Raman intensity up to $3 \cdot 10^2$ times accompanied by the reduced width of the resonant Raman profile of the E_{11} transitions compared to E_{22} transition [96]. The potential enhancement of the G mode intensity at first transition will be of interest for possible biomedical applications. The higher intensity simplifies the detection process and the first transition of small diameter tubes covers the transparency region of tissue [97]. In this wavelength range (700 - 1350 nm), the localization and vibrational properties of CNTs, serving as markers or transporters [98,99], can be probed without disturbing or damaging the living cells.

Despite the fundamental interest in Raman scattering of semiconducting CNTs at E_{11} little experimental work has been published, reporting only the RBMs intensities [65,96]. In contrast to the RBM, the frequency of the G band depends weakly on nanotube chirality. The G mode of different species cannot be separated in samples containing tubes of different chirality. The techniques providing samples of high chiral purity were only recently developed [55]. Moreover, recovering E_{22} and E_{11} G mode resonances profiles from one nanotube chirality requires a very broad excitation source and multiple detection instruments.

[3] The contents of this Section are published in "Gordeev, G et al. *Phys. Rev. B* **96,** 245415 (2017)". The coauthors agree on using the data in this work.

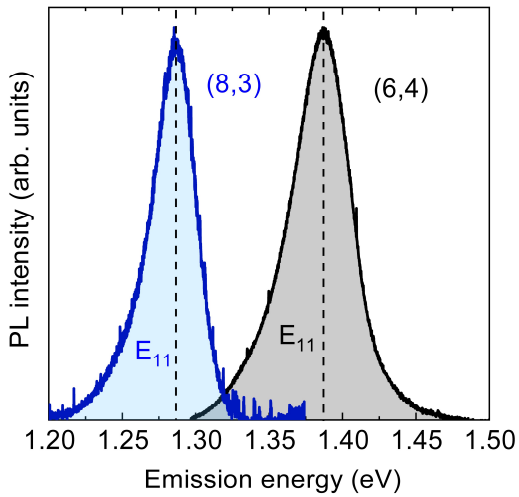

Figure 2.32 *The E_{11} photoluminescence of the (8,3) and (6,4) samples excited at 1.96 and 2.11 eV respectively.*

Here, I report a complete study of the high-energy modes at the E_{11} transition by applying resonant Raman scattering. I investigated the transition dependence of resonant Raman profiles. All chiralities demonstrated a narrower width of the Raman profiles compared to second transition and showed a dominant incoming resonance. The degree of asymmetry varied between profiles at first and second transitions. A fifth-order perturbation theory model involving the scattering to dark excitonic states describes the Raman profiles well. We observed an increase of the LO Raman intensity with a maximum factor of 30. The increase of the intensity and the change in asymmetry we attribute to the strengthening of the dark and bright exciton-phonon interactions at the first excitonic state.

2.4.2 Asymmetric resonance Raman profiles at the first excitonic transition

For the modelling of the Raman resonance profiles the position of the bright exciton needs to be established. The E_{11} photoluminescence (PL) peak was recorded for each chirality in the above-described set up and calibrated with a neon spectrum. The tubes are excited at E_{22}. Figure 2.32 shows the PL spectra of (6,4), and (8,3) tubes. The maximum of the PL corresponds to the energy of the allowed bright excitonic transition E_B^{11}. By fitting the PL profiles, the E_B^{11} is determined and listed in Table 2.5. The measured transition energies are in a good agreement with previously reported values [65,100]. I use the energy difference between bright and dark excitonic states reported in experimental photoluminescence-excitation studies[57] to determine the energy of the dark excitonic states at E_D^{11}.

Table 2.5 *Nanotube chirality and ν=|n-m|mod3 type, nanotube diameter d, chiral angle θ and resonant energies of bright (E_{11}^B) and dark excitons (E_{11}^D) established from PL and Ref.* [57]

(n,m)	ν index	d (Å)	θ (deg)	E_B^{11}, (eV)	E_D^{11}, (eV)
(6,4)	-1	6.83	23.4	1.39	1.424
(8,3)	-1	7.72	15.3	1.29	1.323

Before discussing the resonant effects, we outline the differences in the G mode structure between second and first transitions. Figure 2.33 shows a normalized Raman spectrum of the G mode excited at the first (bottom spectra) and second (top spectra) excitonic transitions for two different nanotube chiralities (6,4), and (8,3). The component (G^+) at ~1589 cm^{-1} is the longitudinal optical vibration (LO), the weak component (G^-) at 1521 cm^{-1} in (6,4) and 1540 cm^{-1} (8,3) is the transverse vibration (TO). The corresponding frequencies and LO/TO intensity ratios match

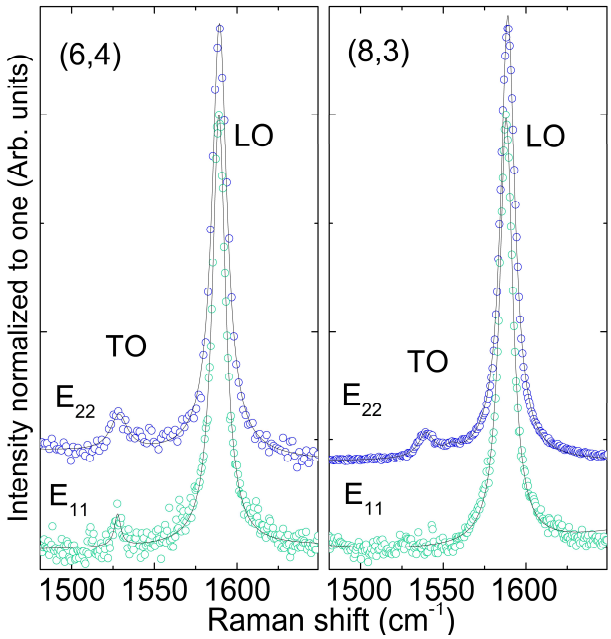

Figure 2.33 *The G modes of (6,4) and (8,3) SWCNTs at first (bottom spectra) and second excitonic transition (top spectra). TO and LO indicate the transverse and longitudinal phonons, respectively. Solid lines represent fits with Lorentzian line shapes.*

reported theoretical and experimental values for the second excitonic transition quite well [88,101,102]. The I_{TO}/I_{LO} are listed in Table 2.6.

Table 2.6 *Chirality (n,m) and transition E_{ii} dependent intensity ratios between TO and LO phonons, full width at half maxima (FWHM) of the TO and LO phonons*

(n,m) E_{ii}	$\frac{I_{TO}}{I_{LO}}$	LO FWHM, cm^{-1}	TO FWHM, cm^{-1}
(6,4) E_{22}	0.06	11	8
(6,4) E_{11}	0.03	10	4
(8,3) E_{22}	0.06	10	11
(8,3) E_{11}	0	10	

At E_{11} we observe different I_{TO}/I_{LO} ratios compared to E_{22}, such that the ratio decreases in the (6,4) and (8,3) nanotubes [ν=-1 type]. The TO intensity of the (8,3) is even below the instrumental noise level. An increase of the I_{TO}/I_{LO} with chiral angle at the first excitonic transition is similar to the trend I reported for the E_{22} transition in Chapter 2 [88,101].

To gain further insight into the Raman scattering mechanisms, we investigate the intensity dependence of the LO mode on excitation energy. For each nanotube, we evaluated the intensity of the Raman mode as a function of excitation wavelengths. We compare the resonance Raman profiles at the first E_{11} and second E_{22} excitonic transitions in Figure 2.34a-b. The filled symbols represent modes intensity excited via E_{11} and the open symbols via the E_{22}, reported in Chapter 2. The Raman profile comprises two resonances incoming at E_{ii}^{B} and outgoing at $E_{ii}^{B} + \hbar\omega_{LO}$ (marked by the dashed lines), where E_{ii}^{B} and $\hbar\omega_{LO}$ are the energy of the bright exciton and phonon, respectively. Both incoming and outgoing resonances have narrower line shapes at the E_{11} than at the E_{22} transition.

The different intensities at the incoming and outgoing resonances (asymmetry) observed at the E_{22} resonances distinguishes nanotubes from most other crystalline materials [17]. The asymmetry is also observed in resonance with the E_{11} transition, again with dominating incoming resonance. The degree of asymmetry varies with transition number and chirality. We observe the resonance Raman profile of the (6,4) species to be more symmetric at E_{11} than at E_{22} (Figure 2.34 a and b), whereas the (8,3) profile becomes more asymmetric at E_{11} compared to E_{22} (Figure 2.34b).

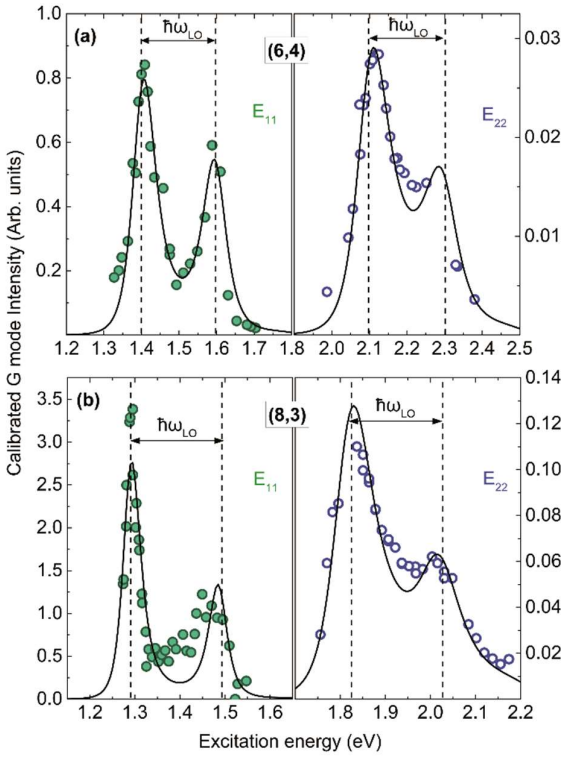

Figure 2.34 *Resonance Raman profiles of the LO (G^+) mode of* ***(a)*** *(6,4), and* ***(b)*** *(8,3) nanotubes.. The filled (open) symbols indicate the intensity of the G mode excited in first (second) excitonic transition. E_{22} data from Chapter 2. The calibration of Raman intensity is described in the experimental section. The solid lines represent theoretical resonant Raman profiles by Eq.* (2.53).

The absolute intensity of the LO mode at E_{11} is up to 30 times higher at the incoming resonance varying with tube chirality, see Table 2.7. To understand the shape of the resonance Raman profiles and the changes in scattering efficiencies between different exciton transitions, I analyze the experimental results in the framework of fifth-order Raman scattering including phonon interactions between bright and dark excitonic states mediated by phonons [23]. This model excellently reproduced Stokes and anti-Stokes Raman profiles of semiconducting nanotubes at E_{22} and Stokes resonance profiles as well as in metallic nanotubes at the E_{11} transition [23,24].

2.4.3 Transition number dependence of the exciton-phonon matrix element

The difference between fifth-order scattering process for first and second excitonic transition can be seen in Figure 2.35a. The order of scattering events is the same for the transitions, discussed in Subsection 2.1.8. The excitonic states participating in scattering are however different. The first (second) bright exciton is scattered to the first (second) dark excitonic state. The second excitonic state has larger energy, therefore the interference with e-h continuum of the first state is

possible, see Figure 2.3. Different coupling factors for each *ii* transition alter Raman cross section resulting in Eq. (2.31) taking form of

$$W_G(E_L) = \frac{\left|\left(M_{B\Gamma S}^{XL}\right)_{ii}\right|^2 \left(M_G^{XP}\right)_{ii}}{\left(E_{B\Gamma S}^{ii}+\hbar\omega_G-E_L\right)\left(E_{B\Gamma S}-E_L\right)}\left[1+\frac{\left(\left|M_G^{XP}\right|\right)_{ii}^{\ 2}}{\left(E_{B\Gamma S}^{ii}+2\hbar\omega_G-E_L\right)\left(E_{B\Gamma S}^{ii}+\hbar\omega_G-E_L\right)}+\right.$$
$$\frac{\left|\left(M_G^{XP}\right)_{ii}\right|^2}{\left(E_{B\Gamma S}^{ii}-E_L\right)\left(E_{B\Gamma S}+\hbar\omega_G-E_L\right)}+\frac{\left|\left(M_K^{XP}\right)_{ii}\right|^2}{\left(E_{B\Gamma S}^{ii}+\hbar\omega_G+\hbar\omega_K-E_L\right)\left(E_{B\Gamma S}^{ii}+\hbar\omega_G-E_L\right)}+$$
$$\left.\frac{\left|\left(M_K^{XP}\right)_{ii}\right|^2}{\left(E_{DKS}^{ii}+\hbar\omega_G+\hbar\omega_K-E_L\right)\left(E_{DKS}^{ii}+\hbar\omega_K-E_L\right)}+\frac{\left|\left(M_K^{XP}\right)_{ii}\right|^2}{\left(E_{B\Gamma S}^{ii}-E_L\right)\left(E_{DKS}^{ii}+\hbar\omega_K-E_L\right)}\right]. \quad (2.53)$$

The energies of the bright and dark excitons from Table 2.5 were used for the fitting of the experimental data by using the matrix elements and exciton damping energies as free parameters. The resonance Raman profiles (depicted by solid lines in Figure 2.34 a and b) are in good agreement with the experimental data (symbols). The relative coupling strength between bright and dark excitons is defined by the ratio of the exciton phonon matrix elements $\frac{M_K^{XP}}{M_G^{XP}}_{ii}$. With damping parameter Γ_B it determines the asymmetry of Raman profile; the values are given in Table 2.7. In (6,4) nanotube the ratio does not significantly change. The increase of symmetry at the E_{11} transition is due to the reduction of the excitonic lifetime. In (8,3) nanotube, Γ_B follows the same trend as in

Table 2.7 *Intensity ratio of the LO phonon between E_{11} and E_{22} transitions. The ratios between dark exciton-phonon and bright exciton-phonon matrix elements for the first and second excitonic transitions[24], damping parameters for the bright and dark excitons and bright exciton-photon/ bright exciton-phonon matrix elements obtained by fitting the experimental profiles in Figure 2.34 by Eq. (2.53) for E_{11} and extracted from Chapter 2 for E_{22}*

(n,m)	$\frac{I_{11}}{I_{22}}$	$\frac{M_K^{XP}}{M_G^{XP}}_{11}$	$\frac{M_K^{XP}}{M_G^{XP}}_{22}$	$\left(\Gamma_B/2\right)_{11}$, (meV)	$\left(\Gamma_B/2\right)_{22}$, (meV)	$M_{B\Gamma S}^{XL}{}_{11}$, (meV)	$M_G^{XP}{}_{11}$, (meV)	$\left(\Gamma_D/2\right)_{11}$, (meV)
(6,4)	23	1.8	2.1	54	90	56	715	680
(8,3)	15	3	1	35	84	13	700	3244

(6,4) nanotube, but $\frac{M_K^{XP}}{M_G^{XP}}_{11}$ exceeds $\frac{M_K^{XP}}{M_G^{XP}}_{22}$ by a factor of three, causing a higher asymmetry of the (8,3) E_{11} resonance profile, see Figure 2.34.

The relative ratio between the bright exciton-phonon and the dark exciton-phonon matrix elements affects the asymmetry of resonance Raman profile, whereas the change of the bright

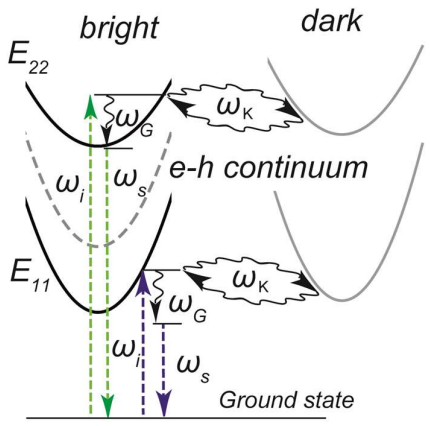

Figure 2.35 *Scattering pathways from the first and second excitons. The scheme demonstrates one of possible scattering pathways, the bright (dark) E_{11} and E_{22} states are located at the Γ (K) point of Brillouin Zone. The Feynman diagrams of all the pathways can be found in Figure 2.16b.*

exciton matrix element M_G^{XP} enhances or decreases the absolute Raman intensity. This effect is directly observed in Figure 2.33b, where the TO/LO intensity ratio dramatically decreases in (8,3) nanotubes at the E_{11} transition indicating a decrease of M_{TO}^{XP}/M_{LO}^{XP} at E_{11} compared to the E_{22} transition.

The quantitative behavior of M_{LO}^{XP} can be extracted from the measured profiles at the E_{11} and E_{22} transition due to the uniform intensity calibration. M_{LO}^{XP} increases approximately by a factor of four from the second to the first transitions, inducing a mean increase in Raman intensity by 30 at E_{11}, see Figure 2.34. This estimate is based on the exciton-photon matrix element $M_{B\Gamma S}^{XL}$ tight binding calculations [88]. When moving from the first to the second transition it increases by 15% [88].

The resonance Raman profile at the E_{11} transition is narrower in frequency compared to the E_{22} transition. The change of the width in the resonant Raman profiles widths is related to the variation of the damping parameters (Γ_B), in Eq. (2.53). The damping parameters at the E_{22} transition are up to factor of two stronger than at E_{11}, see Table 2.7. The damping parameter is inversely proportional to the exciton lifetime $\Gamma_B \sim \frac{1}{\tau}$. The second exciton lies at a higher energy and has a higher number of radiative and non-radiative relaxation pathways compared to the lowest E_{11} excitonic state [103]. This explains the smaller exciton lifetime and broader Raman profile at E_{22} compared to the E_{11} transition.

The resonant Raman profiles exhibit asymmetry and are excellently fitted by fifth-order perturbation theory. This indicates that the scattering at both transitions (E_{11} and E_{22}) is ruled by the same phonon mediated interactions with dark states. The interference of the second transitions with uncorrelated e-h pairs is negligible, possibly due to the low oscillator strength of such uncoupled pairs. Now I can discuss the symmetric resonance Raman profile [95]. The lack of asymmetry is not likely a cause of the high transition number. This would contradict the facts that we did not observe any qualitative differences in the profiles by varying the transition. Rather this effect is related to

the big diameter of the investigated species. The diameter dependence of the $\frac{M_K^{XP}}{M_G^{XP}}_{ii}$ may be a key factor here.

The alternative theory explaining the asymmetry of resonance Raman profiles is based on the molecular system, where the atom displacement along the phonon oscillation direction induces non Condon effects.[69] This model fits well with the Stokes resonance profiles at second excitonic transition. It predicts an increase (decrease) of non-Condon parameter C moving from the second to the first transition in SI (SII) type nanotubes. The non-Condon parameter is proportional to the asymmetry.[69] However, we observe the varying trends in our experiment, where asymmetry decreases in one SI (6,4) nanotube and increases in the other SI (8,3) nanotube at the E_{22} transition, compared to the E_{11} transition.

2.4.4 Summary

In conclusion, I studied the resonance Raman profiles in several nanotubes when exciting the G mode in resonance with the E_{11} transition. The resonant profiles of the LO phonon are similar to E_{22} I reported earlier in Chapter 2. I observe asymmetric profiles with unequal incoming and outgoing resonances, where the incoming resonance dominates. I found the asymmetry of Raman profile to depend on the nanotubes chirality and transition number. The (6,4) profile is more symmetric and the (8,3) is more asymmetric at the E_{11} transition compared to the E_{22} transition. I attribute the asymmetry to the fifth-order scattering process and find excellent agreement between the experimental data and fit of the E_{11} and E_{22} Raman profiles. The change of the asymmetry is due to a competing increase of the bright and dark exciton-phonon coupling elements. Overall, the Raman scattering at the E_{11} transition is, by a factor of 30, more intense than for the E_{22} transition. The superior Raman intensity makes the excitation region of the first transition even more attractive for probing CNTs by means of Raman scattering in all application requiring strong Raman signals. I observe narrower resonance Raman profiles at first excitonic transition attributed to the long lifetime of the lowest-energy exciton.

3 | Exciton photon coupling in CNTs

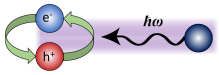

In this chapter, I explore low dimensional effects induced by strong coupling between nanotube excitons and photons. First, I outline the specification of the double resonant Raman scattering process (DRRS). The DRRS is a unique process observed in carbon-based systems[62,104]. In graphite and graphene, the Raman modes related to the DRRS process linearly shift with the excitation energy[105]. In this process, the phonon scatters between resonant states in the K valleys. Electronic bands tuned by Fermi velocities near the Dirac points provide these resonant states [2]. In carbon nanotubes, the one dimensional confinement of electronic bands yields a number of excitonic states of different symmetries and center of mass momenta. The zone center states can interact with light depending on their symmetry, whereas excitonic states with finite center of mass momenta do not directly interact with light. The phonon mediated interactions between bright and dark excitonic states alter the optical response of nanotubes, particularly the Raman profiles of one-phonon G band at first and second transitions I reported in Chapter 2 [24,106].

A few experimental studies reporting DRRS modes resonant behavior at the second transition contradict each other, where one study reports a dispersive D mode [107], the other a constant 2D mode for a defined nanotube chirality [108]. Both results were interpreted within a single particle model. The presence of multiple chiralities in the sample by the 2D analysis, the incomplete excitation range in the D mode analysis, impeded the capturing of the exciton-induced behavior.

The double phonon 2D mode in carbon nanotubes is commonly attributed to the DRRS, however the mechanism of its formation and resonant behavior remained unclear. Sophisticated theoretical attempts to deduce the excitation energy dependence of the D mode were conducted without implementation of the excitonic effects, yielding a graphene like linear dispersion in metallic tubes and a dispersion with one turning point in chiral semiconducting species [107,109]. We propose an excitonic-based theoretical model including specific exciton-phonon coupling effects and a dark excitonic state supported by experimental evidence. The dark state is not directly accessible by light due to the high center of mass momentum. It gets activated when the momentum is compensated by the phonon momentum.

In the following Chapter, I aim to demonstrate the excitonic nature of double resonant Raman scattering in carbon nanotubes. First, a brief overview for the exciton-photon coupling and exciton-polariton (EP) formation [110] in carbon nanotubes is given along with its expected relation to the resonant behavior of the 2D mode. Next, we experimentally determine the excitation energy dependence of the 2D band position and intensity, excited via second excitonic transitions (E_{22}) in five nanotube chiralities. Excitation energy tunes the initial position where the exciton polariton is excited, thereby determining energies of the resonant phonons contributing to the Raman peak. Three dispersion regions observed in all nanotube chiralities are due to the varying spatial dispersions of the EP above and below its bottleneck, where the photon and exciton dispersions merge close to the transition energy. The comparison between the 2D dispersion at the first and second transitions allowed me to unambiguously identify the excitonic states, participating in the scattering. The analysis of the 2D mode intensity provides additional information about the scattering channels at a given excitation energy. The resonant Raman profiles have weaker incoming than outgoing resonances at second transition due to a larger number of resonant states above the transition. The incoming resonance at first transition is absent, again due to the nature of

the dark excitonic state provided by the lowest excitonic transition. The fourth order perturbation theory, implementing the effects of the EP and dark states, reproduced the dispersion and resonant Raman profiles of the 2D mode at both transitions, in excellent agreement with experimental findings.

3.1 Theoretical background

3.1.1 Exciton-polaritons in semiconducting crystals

Here I review the basics of the exciton-polariton. In an excitonic crystal, excitons can couple to photons in a peculiar way [111]. The simple superposition of exciton and photon does not account for the interaction of excitonic crystals with light. Figure 3.1 shows the dispersion of uncoupled excitons and photons by dashed lines. The spatial dispersion of photons is linear $\omega = ck$, whereas the dispersion of exciton is parabolic, see Eq. (2.17). The dispersion of an exciton-polariton is shown in solid lines in Figure 3.1. Two types of EP branches are formed. Exciton-like (II) and photon-like (I) branches following exciton and photon dispersion at energies higher than ω_L, respectively. At energies below ω_L, only the exciton like branch can be excited. In such a coupling regime, the light propagates within the crystal only in the form of the exciton-polaritons. When the photon enters the crystal in this model it transforms into the polariton running in the left direction. It propagates further until the other edge of the crystal is reached, then the polariton transforms into the photon. The transformation occurs without energy lost. The energy only can be changed during an inelastic scattering process. Inelastic scattering occurs during the interactions with lattice vibration. In such a model, the exciton does not interact with the photon, as we discussed in the previous section, but the polariton does.

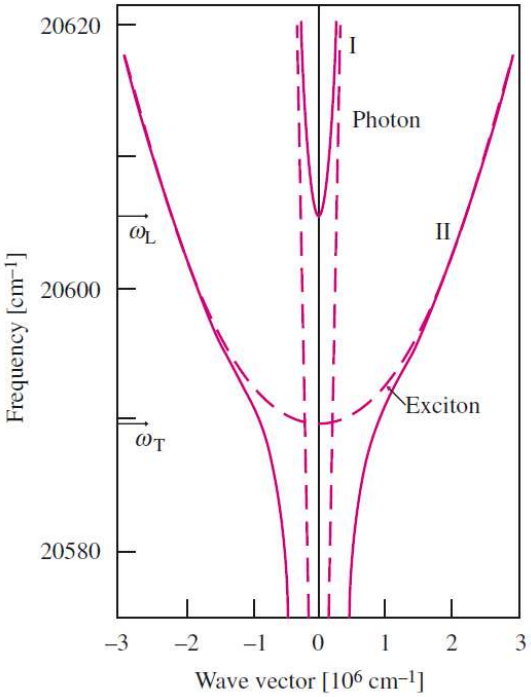

Figure 3.1 *Exciton-polariton (EP) spatial dispersion. "Bare" exciton and photon dispersions are shown in dashed lines. Solid curves are the branches of an exciton-polariton, where "*I*" labels the photon-like branch and "*II*" labels the exciton-like branches.* ω_T *and* ω_L *define longitudinal and transverse frequencies of EP, adapted from Refs.* [17, 111].

To account for extended interactions of excitons and photons, first the exciton-polariton dispersion must be deduced. I use a well-known dispersion of a coupled photon with phonon. This quasi particle is called phonon-polariton. The polariton dispersion corresponding to a coupling with a dispersionless energy state $\hbar\omega_e$ (e.g. phonon) is well-known an can be expressed as [112]

$$\frac{\varepsilon}{\varepsilon_0} = \frac{c^2k^2}{4\pi\varepsilon_0\varepsilon_\infty\omega^2} = 1 + \frac{\omega_L^2 - \omega^2}{\omega_e^2 - \omega^2 - i\omega\Gamma}, \tag{3.1}$$

where k, ω, and Γ are momentum, frequency, and broadening of the polariton, respectively. ε_0 is the dielectric constant of the medium. ω_L is the transverse polariton frequency or uncoupled phonon frequency and ω_L is the longitudinal polariton frequency, which is defined at $\omega(0)$, with Γ = 0. The level $\hbar\omega_e$ gets dispersive when the photon couples to the exciton. The exciton dispersion is defined by Eq. (2.17):

$$\hbar\omega_e = \hbar\omega_T + \varphi k + \frac{\hbar k^2}{2M}. \tag{3.2}$$

$\hbar\omega_T$ is the transverse exciton energy. The linear term φ is negligibly small in most semiconductors including semiconducting nanotubes [20,111]. Only the first exciton from the Rydberg series is considered here. M is the effective mass of the exciton. By substituting Eq. (3.2) in Eq. (3.1) I find [112]

$$\frac{\varepsilon(\omega,k)}{\varepsilon_0} = \frac{c^2k^2}{4\pi\varepsilon_0\varepsilon_\infty\omega^2} \cong 1 + \frac{\omega_L^2 - \omega^2}{\omega_T^2 + \frac{\hbar k^2}{2M} - \omega^2 - i\omega\Gamma}. \tag{3.3}$$

The polariton of the above equation is an actual propagating polariton if the real component of *k* is larger than the imaginary component of *k*. Thus damping of the polariton can be easily evaluated by comparing these components [113]. The imaginary component can be dismissed for evaluation of resonant phonon wave vectors (Γ = 0).

I further discuss possible polariton lattice interactions. The best studied ones, are the interactions of polaritons with acoustic phonons. Due to their high dispersion in the middle of BZ the polariton dispersion can be obtained. In three-dimensional excitonic crystals the polariton is typically scattered within one excitonic valley. I demonstrate the scattering laws mediated by the EP first on Brillouin scattering [111]. It gives a good example, as it incorporates both phonon dispersion and scattering efficiencies of polaritons.

The backscattering process occurs, when the polariton changes its propagation direction (from left to the right or from right to the left). Figure 3.2a shows the scheme for the scattering. Depending on the energy range, different pathways are possible. At high excitation energies four pathways are possible. When the excitation energy is decreased only two ($2 \rightarrow 2'$) and ($1 \rightarrow 2'$) and finally only one process is possible below ω_L ($2 \rightarrow 2'$). The energies of the corresponding scattered phonons can be easily calculated using these dispersion relations. The latter are plotted in Figure 3.2b in solid lines. It fits well with the experimental points. It should be noted, that the parameters in Eq. (2.17) are adjusted for the best fit [17]. The corresponding scattering efficiencies are shown in Figure 3.2c. The fundamental properties of the GaAs exciton-polariton were obtained by the fitting. The experimental efficiencies are shown in Figure 3.2a. While the calculation of phonon energies is straight-forward, the calculation of the scattering efficiencies is performed in two steps.

- Calculation of the transformation of coefficients at the edge of the crystal.
- Calculation of the scattering probabilities by phonons inside the crystal.

In the first step, additional boundary conditions (ABC) between the crystal-vacuum interface have to be applied. Two different polaritonic waves of the same energy can propagate inside the crystal, whereas only one type of wave (photon) outside of it. The electro-magnetic fields are equalized by

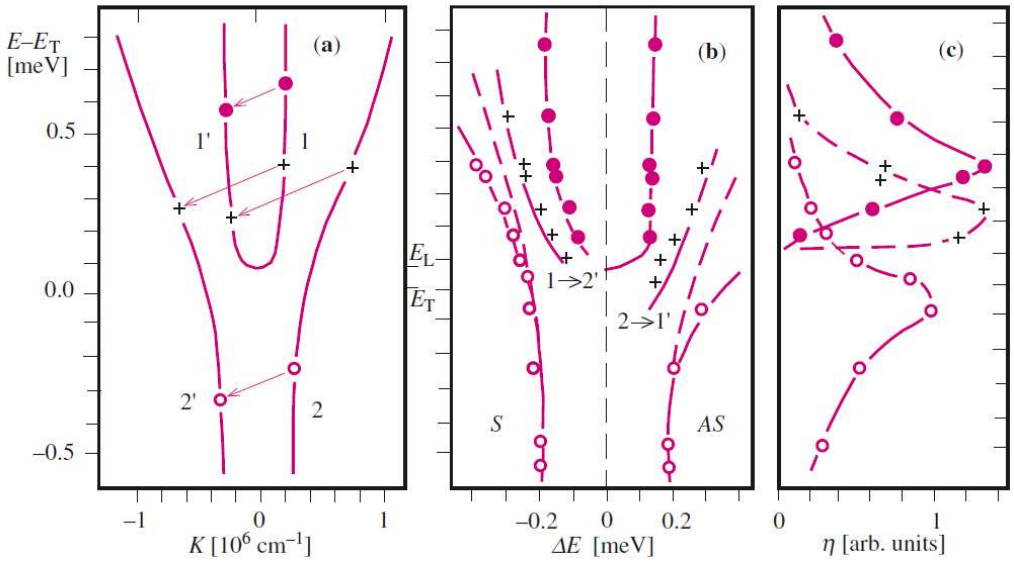

Figure 3.2 *Brillouin scattering in GaAs by polaritons.* ***(a)*** *Dispersion curve of the polariton calculated with corresponding parameters. The arrows indicate the four possible Stokes scattering channels. Each channel is responsible for a Brillouin peak.* ***(b)*** *Energies of the scattered phonons by tuning the excitation energy, the curves are calculated by Eq.* (2.17). ***(c)*** *Scattering efficiencies for corresponding phonons, adapted from Refs.* [17,111]**.**

implementing additional coefficients for the amplitudes of the polaritonic waves by considering the ABC.

Similar rules apply to resonant Raman scattering by an exciton-polariton. The four branch model, including polariton transformation coefficients and ABC has been developed by Birman et. al.[114] . Even without explicit polariton-phonon interactions, this model well reproduced scattering efficiencies of longitudinal phonons. In a case, when only one excitonic state is involved the phonon close to the BZ zone centre participate in the scattering. However, in order for the dispersion of the exciton-polariton to influence the Raman mode energy it requires at least one strongly dispersive phonon. The optical phonons have a flat dispersion around the Γ, whereas acoustic phonons provide linear dispersion, see Figure 3.2. Carbon materials have a unique double resonant Raman scattering mechanism allowing phonon scattering between electronic states of different K points in graphite and between dark and bright states in nanotubes. The K point longitudinal phonons in carbon materials have a strong dispersion due to the Kohn anomaly [115]. In order to understand how such scattering works in carbon nanotubes, I first revise double resonance Raman scattering in other carbon materials.

3.1.2 Double resonant Raman scattering in carbon materials

The variation of the D band frequency in graphite with laser excitation energy was a long standing problem until the mechanism of DRRS was proposed by C. Thomsen and S Reich [62]. In this process, the phonons are scattered between two resonant states instead of one. The linear band structure in graphite allows such scattering processes to occur at a large variety of excitation energies. The scheme for DRRS is shown in Figure 3.3. Two linear band, with different Fermi velocities cross at a single point. The energy of the incident photon E_L defines the k vector, where

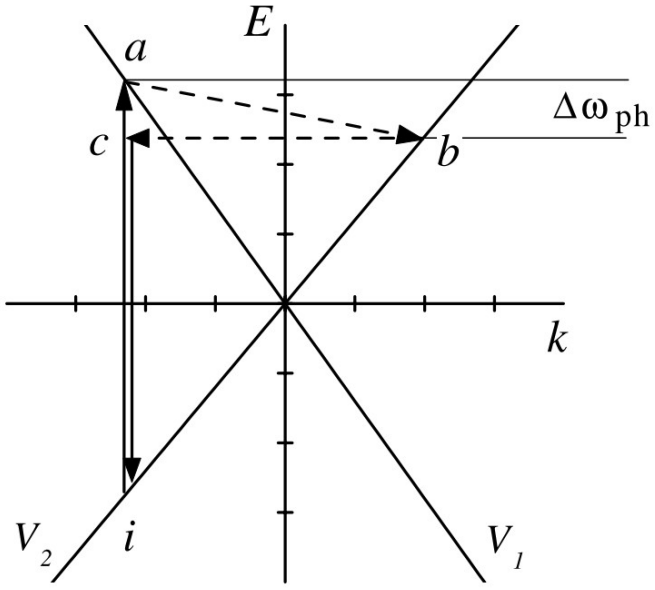

Figure 3.3 *Scheme of double resonance Raman scattering in graphite, shown in one dimension for the D mode. The electronic dispersion bands are linear with the Fermi velocities V_1 and V_2. Electronic bands tune the energy and the momentum of the resonant phonon. For a given excitation energy only one resonant phonon is allowed. In this process an impurity scatters the electron back to band 1, adapter from Ref.* [62].

the electron on band 2 is scattered into band 1. The step can be followed in Figure 3.3 ($i \to a$). In the following step ($a \to b$), the phonon scatters the electron from band 1 to band 2. For a monotonic phonon dispersion, there is only one phonon with suitable energy and momentum. This phonon gives maximum contribution to the D mode. The lattice defect scatters the electron back to band 1. The defects have large momenta and negligible energy. a and c have similar momentum and can differ only by the momentum of light.

The efficiency of this process can be evaluated by perturbation theory. Fourth-order perturbation theory can be used due to the four steps involved in the process [116].

$$K_{2f,10} = \sum_{a,b,c} \frac{M_f M_{ba} M_{cb} M_o}{(E_L - E_{ai}^e - i\hbar\gamma)(E_L - \hbar\omega_{ph} - E_{ai}^e - i\hbar\gamma)(E_L - \hbar\omega_{ph} - E_{ai}^e - i\hbar\gamma)}. \quad (3.4)$$

Here $M_{o,f}$ are matrix elements for the incoming and outgoing photons (not dependent on E_L). M_{ba} (M_{cb}) represent the electron-phonon (electron-defect) matrix element, scattering the electron from a to b (b to c). Considering a linear band structure, Eq. (3.4) turns into a one level integral over k, where k is a point in the Brillion zone. Even with the linear bands approximation the displacement of the D band with laser energy was reproduced. Away from the K point the bands become rather parabolic, see Eq. (2.15). After the electronic states have been implemented in Eq. (3.4) the D mode can be calculated for different excitation energies. Figure 3.4a shows such modes for E_L =2,3, and 4 eV. The mode shifts to higher energies when excitation energy increases in agreement with experiments. To provide a quantitative comparison between the theory and experiment, the calculated position for a number of excitation energies is plotted in Figure 3.4b. The experimentally obtained values [117–119] are in very good agreement with the theory of DRRS validating the proposed scattering mechanism.

A single layer of graphite (graphene) possesses the honeycomb structure with the corresponding Dirac cones at the K points of the lattice. The same double resonant Raman scattering process is present in graphene [105]. In carbon nanotubes, the nature of the optical excitations changes from electronic band-to-band transitions into excitonic. When the CNT excitations are (over)simplified by the band-to-band transitions framework, the double resonant Raman process

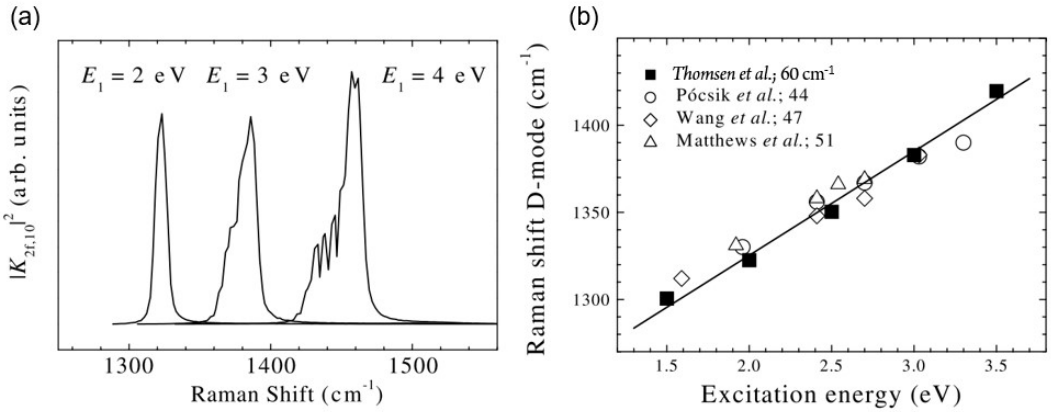

Figure 3.4 *Calculation of the D mode in graphite by Eq. (3.4).* ***(a)*** *The profile of the D mode for a number of excitation energies and* ***(b)*** *the peak position plotted versus excitation energy (filled squares). The line is a linear fit to calculated values. Open symbols represent experimental values [117–119] reported by different authors given with cm^{-1} per eV shift of the D mode, adapted from Ref.* [62].

yields a linear dispersion of the D band in metallic nanotubes and a dispersion with one turning point for chiral semiconducting tubes [107,109].

3.1.3 Phonon dispersion in carbon nanotubes

To understand the origin of the 2D mode, the phonon dispersion in the entire BZ needs to be studied. To obtain phonon dispersion of nanotubes two main approaches are applied; zone folding and force constants calculation [31,120]. The zone folding approach is similar to the one applied for the electronic band structure in Section 2.1.3. It is again based on restricting the 2d phonon dispersion of graphene[104] by the allowed wave vectors $\boldsymbol{k}_{\perp}$ and $\boldsymbol{k}_{\boldsymbol{z}}$. Despite the zone folding approximation beeing more visual, the force constant approach accounts for curvature effects on the π bonds and yields more precise dispersion relations. Both approaches lead to similar phonon dispersion bands with slightly deviating phonon frequencies.

Figure 3.5 shows the phonon dispersion bands in a (14,5) nanotube calculated by the force constant approach. The phonon dispersion relation can be obained in two types of coordinate systems; linear and helical shown in Figure 3.5. In the helical coordinates, the helical vector does not follow the circumference of the tube, but rotates a few times around it following the tube symmetry. In such a construction, the BZ is larger, which keeps the number of phonon branches low. The helical quantum numbers $\tilde{m}$ of phonon bands span from $-\frac{N}{2}+1$ to $\frac{N}{2}$, where N is the greatest common divisor of (n, m). In linear construction, the number of bands increases to $\frac{q}{N}$, where q is the number carbon atoms in the BZ, see Eq. (2.5) [31].

The phonons from the Γ point of the BZ comprise following symmetries A_{1g}, E_{1g} and E_{2g}. In the remaining space of the Brillion zone the phonon branches of $E_{m,g}$ symmetries can be found, where m is the linear quantum number of the phonon band [31]. The phonons from the Γ (K) points contribute to the G (D and 2D) modes in Figure 2.14. The K like point is marked by the vertical dashed line in Figure 3.5.

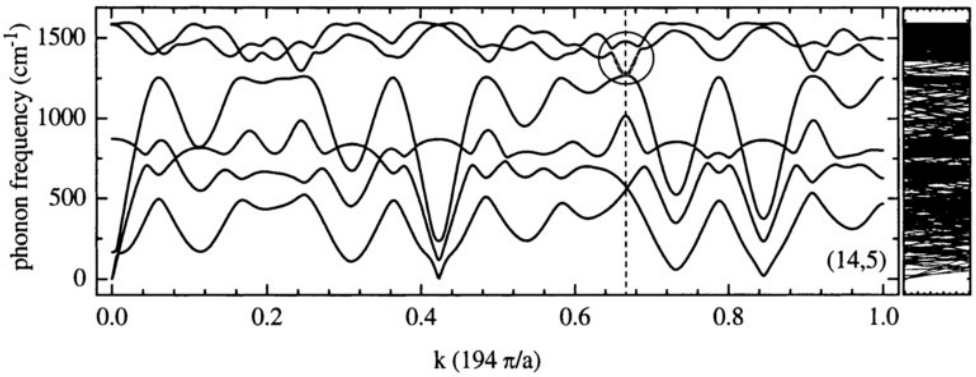

Figure 3.5 *Phonon dispersion in a (14,5) nanotube calculated by the force constant approach. On the left side, the dispersion is plotted in helical units, where the unit cell is larger in real space and number of phonon branches is reduced. On the right side, the phonon dispersion is depicted in linear units. Here the size of a unit cell is smaller, but the number of phonon branches scales with the number of carbon atoms in CNT unit cell. The phonon branches in linear units have a linear quantum number - m, which accounts for the rotational crystal momentum. For this nanotube m varies from -97 to 97 and the absolute number of the bands is 1164, adapted from Ref.* [31].

3.2 Resonant Raman scattering by exciton-polaritons in CNTs

3.2.1 Scattering mechanism between the exciton polariton (EP) and dark excitonic state

To understand the 2D mode resonant behavior I clarify how the energy momentum exchange inside the polariton depends on the excitation energy. The interaction between exctions and photons occurs at the crossing point of their dispersions [1]. When the photon interacts with the excitonic crystal, the exciton-photon coupling generates an exciton-polariton [17,110]. As long as the light is propagating inside the medium, excitons and photons are indistinguishable. The EP was previously reported to be inelastically scattered by phonons and defects within a branch [114]. In nanotubes, the EP is instead scattered to the dark state and back, forming the 2D mode [26,88].

The photon energy after escaping the medium matches the energy of the EP inside the medium. The dispersion of the EP branches $f_i(\kappa)$ is deduced by solving the expression [17]:

$$\frac{c^2k^2}{4\pi\varepsilon_0\varepsilon_\infty f(k)^2} = 1 + \frac{\omega_L^2 - \omega_T(0)^2}{\omega_T(0)^2 + \omega_T(0)\left(\frac{\hbar k^2}{M_{ii}}\right) - f(k)^2}. \qquad (3.5)$$

M_{ii} is the effective mass of the corresponding bright exciton, and $\omega_T(0)$ and (ω_L) are the energies of the EP branch and uncoupled exciton in the middle of the Brillouin zone, respectively. The solutions of this equation are shown in Figure 3.6a, with two types of EP branches. The I is the photon-like branch converging with the photon dispersion in the region above the ω_T. The II is the exciton-like branch coinciding with the exciton dispersion above the ω_T and photon dispersion below the ω_L. The II branch forms a bottleneck between ω_T and ω_L, see Figure 3.6a.

The scheme of the scattering is displayed in Figure 3.6a. The EP formed by the bright A_1 exciton and incident photon runs though the material. Depending on the incident laser energy either one or two EP branches can propagate simultaneously. When the E_L is smaller (larger) than ω_T

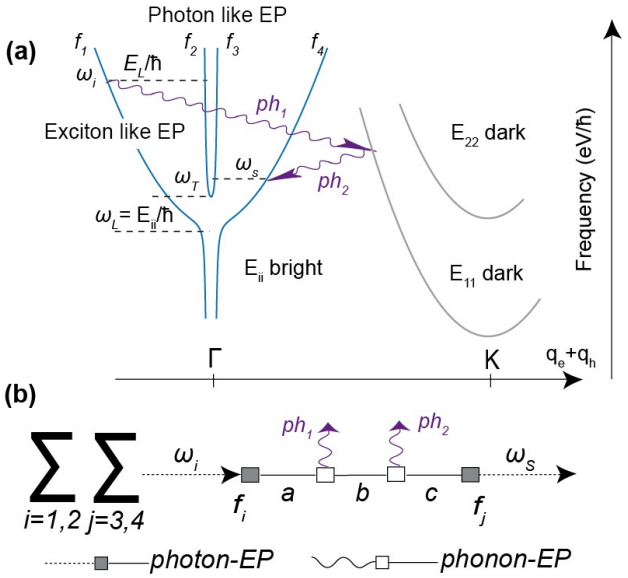

Figure 3.6 *Raman processes incorporated in the formation of the 2D mode in carbon nanotubes.* ***(a)*** *a scheme of the scattering, where the left hand branches of the EP formed by the bright exciton serve as initial states and the right hand branches as final states of Raman process. The intermediate state is the dark exciton at the K point.* ***(b)*** *Feynman diagram summing up possible scattering pathways with the i left hand (initial) and j right hand (final) branches of the EP.*

one (two) polaritonic branches are activated. In the polariton medium, right or left hand branches of the EP define the direction of polariton propagation. In the Raman process, the EP can only be backscattered into the opposite side, indicating a change in its propagation direction, as depicted in Figure 3.6a. In 2D mode scattering process, the first phonon scatters the EP to the dark state at K while the second phonon scatters the dark exciton to the opposite side of the EP. After the EP escapes the CNT, it is transformed into a photon with energy matching the EP.

The corresponding Feynman diagram, a pictorial demonstration of the scattering pathways, is shown in Figure 3.6b. The first and last vertex vary between scattering pathways. At the second and third steps of the Raman process, two phonons ph_1 and ph_2 are emitted by scattering to the dark state of E_{11} and back. The two phonon Raman processes are described by fourth-order perturbation theory. The contributions of all scattering channels (mediated by all EP branches) needs to be included in the Raman cross section. The overall Raman cross section yields

$$K_{2D} = \sum_{\hbar\omega_+} \left| \sum_{f_i} \sum_{f_j} \sum_{\hbar\omega_-} \frac{|M_{EP}(E_L)|^2 \left|M_{exiton-phonon}\right|^2}{D_1^{2D} D_2^{2D} D_3^{2D}} \right|^2 , \tag{3.6}$$

where D_i^{2d} are the following functions of $E_L, \hbar\omega_+, \hbar\omega_-$.

$$\begin{gathered} D_1^{2D} = E_L - f_i(k_i) - i\ {}^{\Gamma}/_{2}, \\ D_2^{2D} = E_L - \frac{1}{2}(\hbar\omega_+ + \hbar\omega_-) - E_{11}\left(k_i + \frac{1}{2}\big(q(\hbar\omega_+) + q(\hbar\omega_-)\big)\right) - i\,{}^{\Gamma}/_{2}, and \\ D_3^{2D} = E_L - \hbar\omega_+ - f_j\big(k_i + q(\hbar\omega_-)\big) - i\,{}^{\Gamma}/_{2}. \end{gathered} \tag{3.7}$$

$f_i(q)$, $f_j(q)$ are the branches of EP determined by the Eq. (3.5), serving as initial and final states correspondingly. $\hbar\omega_{\pm} = \hbar\omega_1 \pm \hbar\omega_2$ variables are implemented to distinguish between the phonon pairs having the same and different energy sum. $E_{11}(q) = E_{11}(\Gamma K) + \frac{\hbar(q-\Gamma K)^2}{M_1}$ is the spatial dispersion of the lowest dark exciton at the K point and q($\hbar\omega$) represents the dependence of the phonon wave vector on its energy, determined by the phonon dispersion. ${}^{\Gamma}/_{2}$ is the exciton damping parameter responsible for the width of the resonant Raman profile.

For a given laser energy E_L, the Raman spectrum of the 2D is calculated based on Eq. (3.6) as

$$2D(\hbar\omega_+) = \left| \sum_{f_i} \sum_{f_j} \sum_{\hbar\omega_-} M\left(\frac{|M_{EP}(E_L)|^2 \left|M_{exiton-phonon}\right|^2}{D_1^{2D} D_2^{2D} D_3^{2D}} \right) \right|^2 , \tag{3.8}$$

where $\hbar\omega_+$ represent the phonon energy (Raman shift) and $2D(\hbar\omega_+)$ is the intensity at this phonon energy. Thus, the integration area below this curve reproduces the 2D mode intensity for a given E_L. The extremum in Eq. (3.8) is reached when all three terms simultaneously approach their minimum. The energy sum of the corresponding pair of phonons yields the 2D position observed in the experiment. I provide a simulated example by Eq. (3.6) of the (6,5) 2D mode in the section 3.2.4, where the position dependence on the excitation energy and resonance Raman profiles are discussed.

3.2.2 Resonant behavior of the 2D mode at the second excitonic transition

The 2D mode of the (7,5) and (6,5) nanotube are presented in Figure 3.7. The excitation energy is 0.2-0.3 eV above the transition energy, with the strongest 2D signal (asymmetry in the 2D mode resonance profile I focus on later). A number of differences is observed in the spectra. First, the 2D mode belonging to the (7,5) nanotube is asymmetric, whereas the 2D mode of the (6,5) nanotubes is symmetric. I attribute this asymmetry to multiple peaks (two) comprising the (7,5) 2D mode. One peak is found to be broad, with fwhm = 42 cm^{-1} (blue) and the other narrow, with fwhm = 17 cm^{-1} (gray). The width of the symmetric peak of the (6,5) 2D mode (fwhm = 37 cm^{-1}) is comparable with the broad component of the (7,5) 2D mode. I attribute the components to the longitudinal LO (blue) and transverse TO (gray) phonons at the K point of the BZ. The ratios between the LO and TO modes depend on the chirality of the nanotube at the Γ point of BZ and possibly at the K point, where the (6,5) TO mode may have a faint intensity. The resonant analysis will verify this assumption. Second, the position of (7,5) 2D mode is red-shifted compared to the (6,5) 2D mode. The difference between the LO and TO modes of (7,5) nanotube is 13 cm^{-1}. The

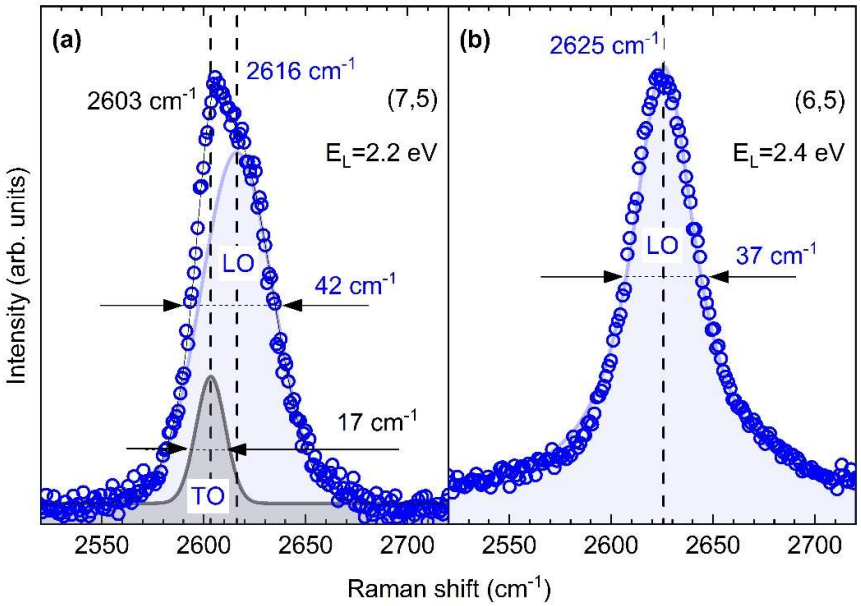

Figure 3.7 *Spectral structure of the 2D mode, open circles represent the experimental data and lines the fits.* ***(a)*** *Raman spectrum of the (7,5) 2D mode excited at 2.2 eV, comprising two peaks with the low energy component at 2603 cm^{-1} (grey) and the high energy component at 2616 cm^{-1} (blue). (b) Raman spectrum of the (6,5) 2D mode excited at 2.4 eV. The FWHMs for each peak are given at each peak, the maxima of the components are marked by the vertical dashed lines.*

difference between LO mode of (6,5) and (7,5) is 9 cm^{-1}, both acquired at the outgoing resonance.

I start the resonant analysis of the 2D mode at the E_{22} exciton-polariton with its energy lying in the visible wavelength range. Figure 3.8a shows the normalized 2D mode of the (7,5) nanotubes excited with varying excitation energies spanning the second excitonic transition. The energy of the exciting laser increases from the bottom to the top. The displacement of Raman peak with the excitation energy is directly observed. The 2D mode position changes from

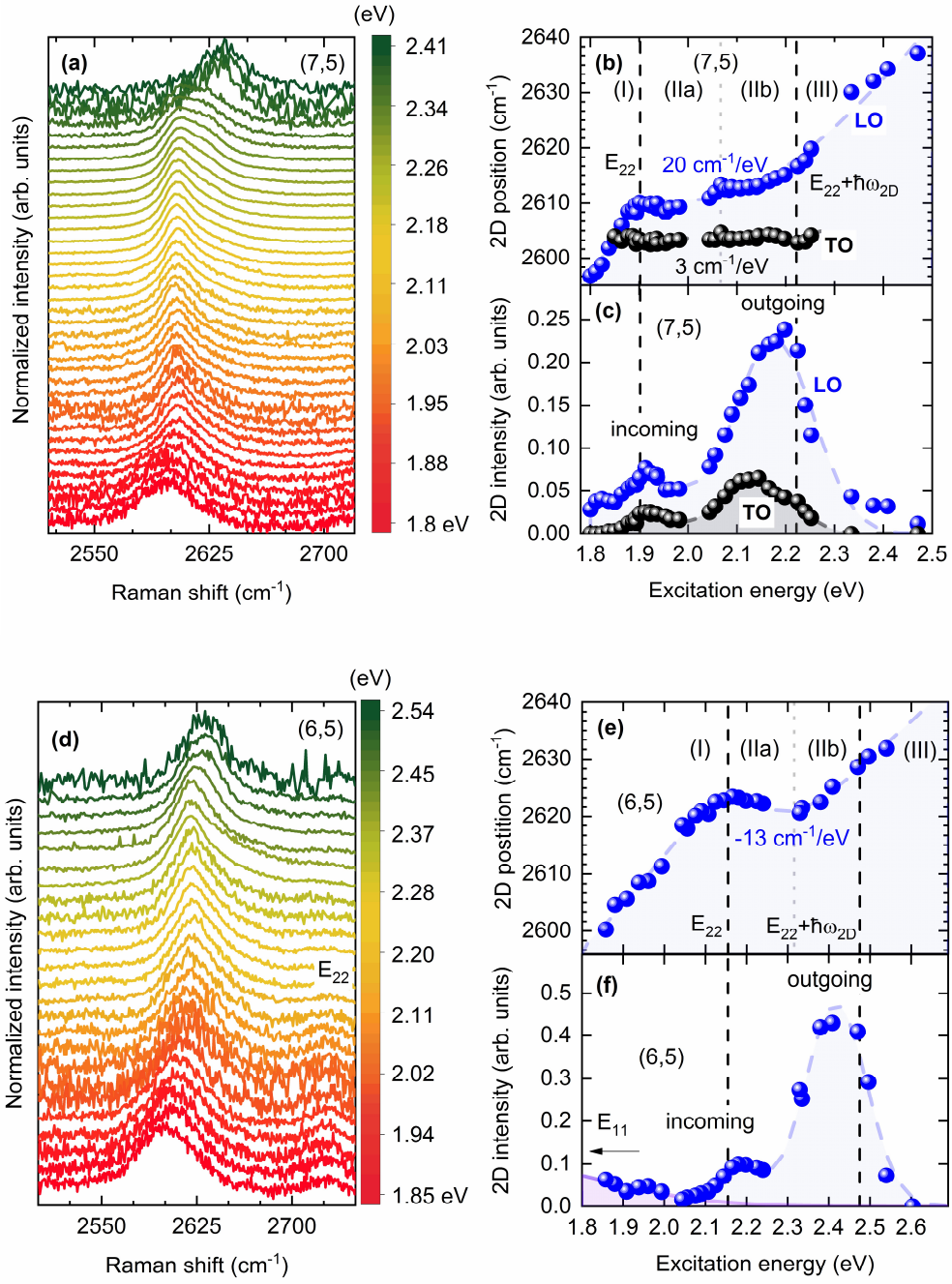

Figure 3.8 *The resonant behaviour of the position and the intensity of the 2D mode in carbon nanotubes.* ***(a)*** *Waterfall plot of the normalized to one 2D mode of the (7,5) nanotube recorded at different excitation energies, excitation energy increases from bottom to the top. The position* ***(b)*** *and the intensity* ***(c)*** *of the 2D mode components as function of intensity. The components comprising the 2D mode are shown in Figure 3.7. The vertical dashed lines correspond to the expected positions of the incoming and outgoing Raman resonances of the second transition at E_{22} and $E_{22}+E_{2D}$ energies.* ***(d)*** *Waterfall plot of the 2D mode of the (6,5) nanotube. The symmetric 2D mode is fitted with a single peak.* ***(e)*** *The 2D mode displacement with laser energy and* ***(f)*** *corresponding resonant Raman profile.*

2997 to 2639 cm^{-1}. The 2D Raman mode of (7,5) tubes exhibits an asymmetric line shape consisting of two symmetric contributions. They are labeled with grey and blue peaks in Figure 3.7a. All 2D mode peaks are fitted in the same manner and the maxima positions are plotted as a function of excitation energy in Figure 3.8b, following the same color scheme.

Three different regions in the 2D mode dispersion can be distinguished in Figure 3.8b. Below the transition energy of the bright exciton (marked as left vertical dashed line), the LO frequency continuously increases with the laser energy and TO is very weak (I). Between E_{22} and $E_{22}+E_{2D}$ a plateau region is observed, with the dispersion slope turning horizontal for both peaks with no substantial shift of the 2D energy (II). In the top region ($E_L > 2.25$), above the outgoing Raman resonance $E_{22}+ E_{2D}$, the frequency continues to increase (III). Two turning points of the 2D mode dispersion form a plateau between incoming and outgoing resonances. The three regions in the dispersion are determined by the exciton-polariton bottleneck. In the upper region ($E_L > 2.25$ eV) both resonant phonons are tuned by the EP dispersion above the EP bottleneck. The plateau region in the middle (1.92 eV > E_L > 2.25 eV) region occurs when the first and second phonons scatter EP below and above the bottleneck. The behavior exhibited in the lower region ($E_L < 1.92$ eV) is due to both phonons scattering EP below its bottleneck. The turning points dividing these regions are roughly separated by the energy of two resonant phonons (E_{2D}). Both symmetric contributions TO and LO show a similar resonant behavior between the incoming and outgoing Raman resonances, the narrower (TO) peak has a smaller intensity and is difficult to trace far from the resonant conditions, see Figure 3.8b and c. The slope in the plateau region of the green peak is flatter. In order to investigate the origins of the multiple peak structure, we analyze and compare the resonant Raman profiles of both peaks comprising the 2D mode.

The integrated intensities of the 2D mode components are plotted over excitation energy in Figure 3.8c (resonance Raman profiles). The vertical lines correspond to the positions of the incoming and outgoing Raman resonances. The position of the incoming resonance coincide with the energy of the corresponding bright exciton, and is determined by the analysis of radial breathing modes in Chapter 2. The outgoing resonance in the Stokes scattering is at ~0.32 eV above the incoming resonance. While the incoming resonance matches the expected position, the outgoing resonances of both 2D components deviate from the expected position (marked by the vertical dashed lines). Moreover, the distance between incoming and outgoing resonance is smaller for the gray peak. The outgoing resonance is more efficient and exceeds the incoming by 4x and 2.5x in the broad (blue) and narrow (gray) components respectively. The dominance of the outgoing resonance is due to a larger number of resonant states favoring these conditions.

The two symmetric components comprising the 2D mode are attributed to the longitudinal (LO) and transverse (TO) zone edge phonons participating in the formation of the 2D mode. Such assignment is in line with experimentally observed dispersions of the 2D components. The energy and momentum provided by the EP is the same for both components but the phonon dispersion of the LO-derived and TO-derived modes have a small opposite tilt [107]. Selection rules derived from group theory allow scattering of both phonon modes. The optically active bright exciton of A_2 symmetry and can be scattered to the dark singlet states, exhibiting $E_{2\mu}(2k)$ symmetry by a phonon with $E_{2\mu}(2k)$ symmetry i.e. linear momentum $2k$ and angular momentum 2μ [26]. However, in chiral semiconducting tubes, both G^+ (LO) and G^- (TO) vibrations combine the A + E symmetries as reported for the center of Brillouin zone (BZ) [121]. The conservation of angular momentum is achieved by selecting the corresponding phonon branch indexed m = 2μ [31]. The conservation of

linear momentum is considered in Eq. (3.6). As a result, both of phonon branches contribute to the 2D mode. The TO branch has a smaller energy (2603 cm^{-1} at E_{22}), as the LO branch has a higher energy (2610 cm^{-1} at E_{22}). Analogously to the G mode, the TO vibration is less intense than the LO vibration. Alternatively, the additional peak can be attributed to a different scattering pathway. However, I found that such a process yields a deviation from the experimentally observed dispersion. The dispersion of the alternative process is much steeper between incoming and outgoing Raman resonances. The alternative scattering process is not observed experimentally due to its low scattering efficiency strongly reduced by interference effects. In order to gain further insights into the mechanisms of the 2D mode formation we investigate the resonance effects in the (6,5) nanotube.

Figure 3.8d shows a waterfall plot of the normalized 2D modes of (6,5) nanotubes recorded at various excitation energies. In contrast to the (7,5) tube, the peak shape of the (6,5) 2D mode is symmetric and is fitted by a single peak. The excitation energy increases from bottom to the top. Qualitatively the 2D mode of the (6,5) nanotubes follows the same resonant behavior, as for the (7,5) tube with three dispersion regions. The 2D mode energy first increases with laser energy, then reaches a plateau of the constant frequency at the incoming resonance. Near the outgoing resonance its behavior changes again and its energy continues to increase with the laser energy. The position and intensity of the single symmetric 2D peak can be traced in Figure 3.8e and f. The outgoing Raman resonance is more intense than the incoming by a factor of four. The experimentally observed maximum of the scattering intensity does not precisely match the expected positions marked by the vertical lines. The incoming resonance is shifted to higher energies and the outgoing resonance to lower energy. The absence of the TO component may be due to its low intensity compared to the LO component. Indeed when the latter phonons are scattered in the zone center, strong variation between LO and TO modes (G^+ and G^-) intensities are reported [25]. The intensity ratios vary strongly between SI tubes as the (6,5) and SII tubes as the (7,5). To confirm a type dependent 2D mode asymmetry, we perform the analysis for three other different nanotubes, two of the SII type, (8,3) and (6,4) and one of the SI type (9,8).

Figure 3.9a and b shows the 2D mode for the (9,8) and (8,3) chiralities. The line shape of the 2D mode in the (9,8) chirality (SI type) is symmetric, while in the (8,3) (SII type) it is asymmetric, thereby confirming type dependent asymmetry. The phonon energy difference between LO and TO components of 9 cm^{-1} is the largest for (8,3) tube. This corroborates the assumption that the presence of additional TO peak is due to the intrinsic nanotube effects, i.e. low exciton-TO phonon matrix element in SI tubes near the K point. The 2D Raman signal provided by the (6,4) (SII type) is quite low compared to the other species, see Figure 3.9c. However, the asymmetric line shape of the 2D mode of the (6,4) can be identified. Despite the asymmetry, the mode was fitted with one single peak for the resonant Raman analysis due to its low intensity.

The dispersions of the 2D mode for (9,8), (8,3), and (6,4) are shown in Figure 3.9d-f. Three regions of the 2D mode dispersion are observed in each case, similarly to (7,5) and (6,5) nanotubes. This indicates a uniform resonant behavior of all nanotube chiralities studied in this work. The slope of the 2D mode varies for each nanotube, and is tuned by the spatial dispersion of the bright and dark excitonic states. The latter is defined by the binding energy of the corresponding exciton. In the region between incoming and outgoing resonances, the energy of the first (second) resonant

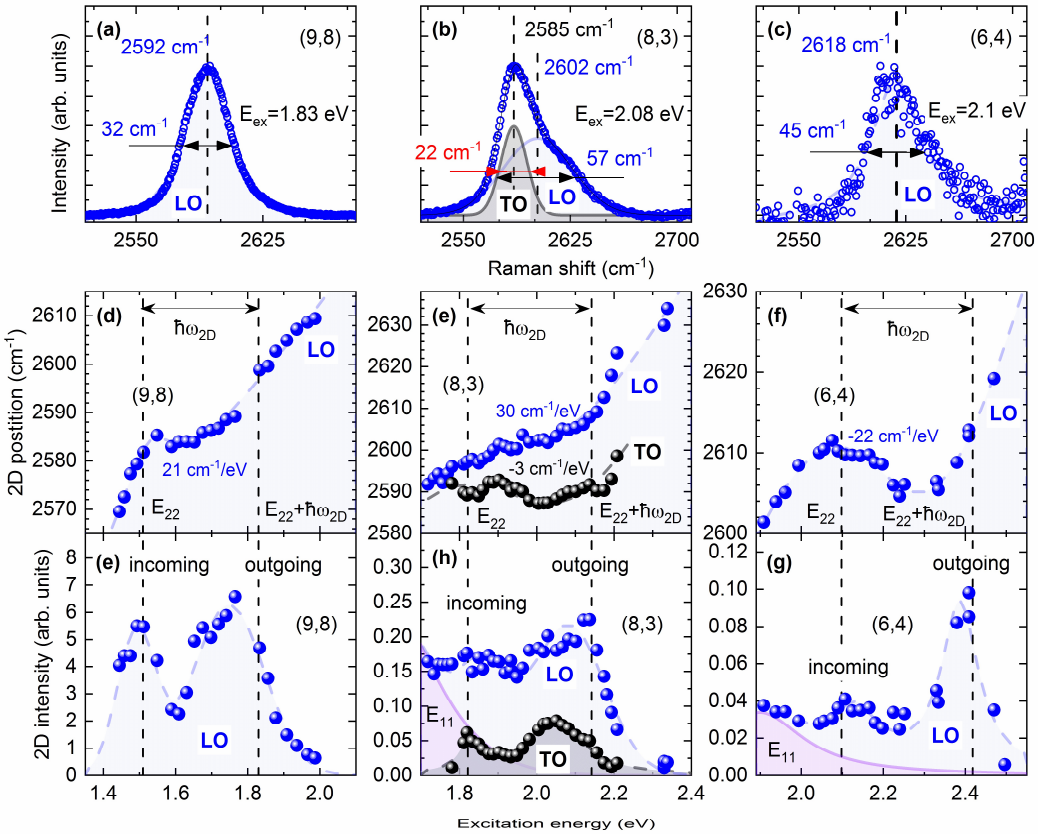

Figure 3.9 *2D mode in (9,8) (8,3) and (6,4) nanotubes excited at the E_{22} transition.* ***(a-c)*** *Examples of the 2D modes, accompanied by the fits. The blue peaks indicate LO components and the grey peaks TO components with their positions (vertical dashed lines) and FWHMs (horizontal double arrows).* ***(d-f)*** *The position of the 2D mode component plotted over the excitation energy. The vertical dashed lines correspond to the expected positions of the incoming and outgoing Raman resonances at E_{22} and $E_{22}+E_{ph}$ respectively. The numbers indicate the dispersion of the 2D mode (component) between incoming and outgoing resonances in cm^{-1} per eV.* ***(e-g)*** *The resonant Raman profiles where the calibrated 2D mode intensity is plotted versus the excitation energy.*

phonon increases (decreases) with excitation energy. This region is therefore very sensitive towards relative binding energies of bright and dark states. The dispersion slope (cm^{-1} per eV) of the LO in the middle region component varies from negative values, in (6,5) and (6,4), and to zero in (9,8), and positive values in (7,5) and (8,3), all listed in Table 3.1. This value reflects the ratio between bright and dark exciton effective masses.

Figure 3.10a shows the intensity of the 2D mode normalized on the G mode, both acquired at E_{22}. The matrix elements for the G mode vary only by 15 % between different charialities, as reported by tight binding calculation [88]. Therefore, the ratio between the 2D and G modes measured at the incoming resonance accurately reflects relative intensity of the 2D mode. The (6,5) and (9,8)

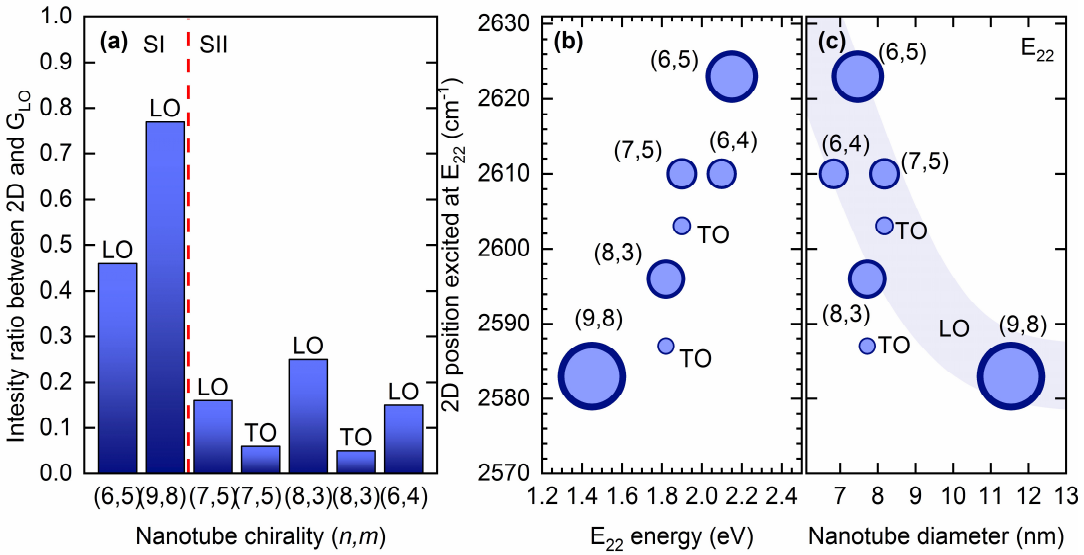

Figure 3.10 *Chiral dependence of the 2D mode in carbon nanotubes.* ***(a)*** *The bar height reflects the intensity of the 2D mode normalized on the G_{LO} mode measured at the incoming resonance. On top of the bar the LO or TO type of the 2D component is given. The vertical dashed line divides SI and SII type nanotubes. The position of the 2D mode excited at the E_{22} energy* ***(c)*** *plotted over E_{22} and* ***(c)*** *plotted over nanotube diameter. The size of the symbol reflects the intensity of the 2D mode. The number for this plot are given in Table 3.1.*

nanotubes of the SI type have a larger 2D/G intensity ratio compared to the nanotubes of the SII type. In combination with the chirality depending ratios reported for G/RBM [101], these ratios can be used to assign the 2D modes in the samples containing mixed chiralities. Further, I plot the energy of the 2D mode for different chiralities over the energy of the second optical band gap and nanotube diameter in Figure 3.10b and c, respectively. The size of the symbol reflects the intensity of the 2D mode. The position of the 2D mode increases with E_{22} and decreases with the diameter. The Kataura like dependence of the 2D mode is due to 2D frequency depending on the relative energies of the first and second band gaps, as well as exciton effective masses. These parameters scale with the nanotube diameter and nanotube type. The positions of the 2D modes at the incoming resonance are listed in Table 3.1. In combination with the chirality depent ratios reported for G/RBM [101], these ratios can be used to assign the 2D modes in the samples containing mixed chiralities.

The resonance Raman profiles of the 2D mode are shown in Figure 3.9e-g. The incoming and outgoing resonances are present in all nanotubes. The ratio between the outgoing and incoming Raman resonances varies from one to four. For the case of the (6,4) and (8,3) tubes, the incident resonance is not as pronounced due to interferences with the tail of the outgoing E_{11} resonance, marked in violet in Figure 3.9h-g. The energy difference between E_{11} and E_{22} energies is the smallest for these nanotube species. The intensity ratios for all five studied chiralities, between incoming and outgoing resonances, are listed in Table 3.1.

Table 3.1 *Characteristics of the 2D mode in (6,5), (7,5),(9,8),(8,3) and (6,4) nanotubes excited via second excitonic transition. Nanotube type, energy of the bright exciton, 2D mode position excited at the incoming resonance, the calibrated ratio between 2D and G modes, the slope of the region between incoming and outgoing resonances, Intensity ratio between the incoming and outgoing resonances and full width at half maxima (FWHM) of the 2D mode (component)*

(n,m)	Nanotube type	E_{22}, eV	2D position at E_{22}, cm^{-1}	2D/G	Plateau slope, cm^{-1}/eV	I_{out}/I_{in}	FWHM, cm^{-1}
(6,5)	SI	2.15	2623	0.46	-13	4.3	38
(7,5) LO	SII	1.90	2610	0.16	20	3.4	42
(7,5) TO	SII	1.90	2603	0.06	3	2.6	17
(9,8)	SI	1.45	2583	0.77	21	1.2	32
(8,3) LO	SII	1.82	2596	0.25	30	1.4	42
(8,3) TO	SII	1.82	2587	0.05	-3	1.3	19
(6,4)	SII	2.10	2610	0.15	-22	2.6	35

When the EP is mediated by the second excitonic state, there are two possible scattering pathways from the Γ to the K point. The EP can be scattered to the dark exciton of the first or the second transition. However when the exciton is scattered from the EP mediated by the first excitonic state, there is only the dark excitonic state able to participate in DRRS. In the next section, we analyze the scattering via E_{11} bright state and compare it with the scattering via E_{22} bright state.

3.2.3 Scattering via bright E_{11} excitonic state

Figure 3.11a shows the 2D mode position of the (6,5) nanotubes excited via the first excitonic transition. The line shape of the 2D mode is symmetric, see Figure 3.11a. By decreasing the excitation energy the position of the 2D mode shifts to smaller energies. The first turning point in the dispersion occurs at the position of the outgoing resonance. At lower energies, the 2D mode position approaches its minimum at 2567 cm^{-1}. Notably, a very large difference of 50 cm^{-1} between the 2D mode position excited at the incoming resonance position of the first and second excitons is observed, a similar trend I reported in Chapter 2 for the G mode. The increase of Raman intensity occurs through increase in exciton-phonon coupling at the first transition compared to the second transition.

Table 3.2 *Characteristics of the 2D mode excited at the first excitonic transition*

(n,m)	(E_{11}) eV	2D(E_{11}) cm^{-1}	Iout11/ Iout22	2D slope cm^{-1}/eV	FWHM cm^{-1}
(6,5)	1.26	2568	50	43	29
(8,3)	1.29	2563	40	82	34
(6,4) LO	1.4	2576	15	85	40
(6,4) TO	1.4	2555	-	215	24

The (6,5) nanotube is the perfect candidate to establish the origin of the dark state as it provides resonances with the largest energy separation between E_{11} and E_{22}. The difference of the 2D modes dispersion at the first and second excitonic transitions is shown in Figure 3.12a. The energy of the 2D mode excited via E_{11} is lower and the behavior in the transition region between outgoing E_{11} and incoming E_{22} resonances is quasi continuous. These two factors clearly point towards the common dark excitonic state, provided by the lowest exciton (E_{11}). The strong enhancement of exciton–phonon matrix elements at the lowest excitonic transition, observed for the high-energy Raman modes, in carbon nanotubes can be a key factor for establishing this scattering channel.

The resonant Raman profile of the (6,5) nanotube at the first transition is shown in Figure 3.11d. The outgoing resonance occurs near the expected position. At the incoming resonance, no enhancement of the Raman intensity is observed. The incoming resonance vanishes due to absence of the dark state for the corresponding excitation energy $E_L - E_{11}^{dark} < \hbar\omega_{ph}$. As a result, the second term in the denominator of Eq. (3.6) does not reach its minimum. The intensity of the 2D mode at E_{11} is 50x stronger than the resonance with the E_{22} transition. The exciton-phonon matrix elements tend to increase when the transition number is decreased.

The 2D mode of the (8,3) nanotube follows exactly the same resonant behavior as the (6,5), see Figure 3.11. The incoming resonance is not present and the position of the symmetric 2D mode at the incoming E_{11} resonance is 40 cm^{-1} below the same resonance position at E_{22}. The maxima of

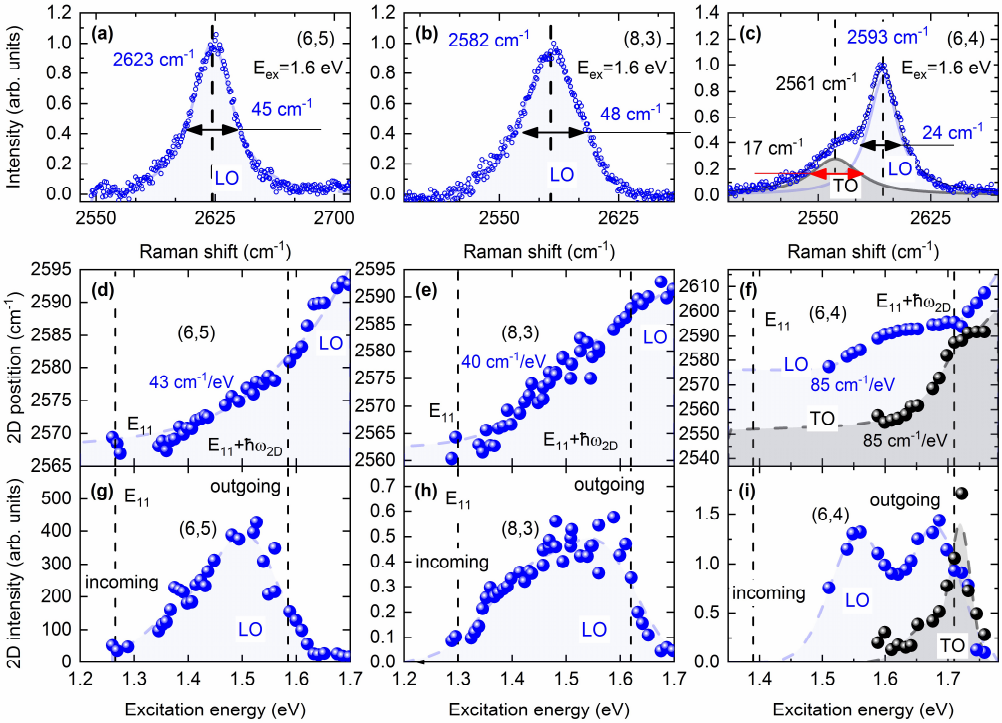

Figure 3.11 *Excitation energy dependence of the 2D mode in (6,5),(8,3) and (6,4) carbon nanotubes excited at first excitonic transition. Vertical dashed lines mark the positions of the incoming and outgoing Raman resonances at E_{11} and $E_{11}+E_{2D}$ energies respectively.* ***(a)***, ***(b)***, *and* ***(c)*** *examples of the 2D Raman modes.* ***(d)***, ***(e)***, *and* ***(f)*** *the position of the 2D mode as a function of excitation energy. The numbers indicate the dispersion of the 2D mode (component) between incoming and outgoing resonances in cm^{-1} per eV.* ***(g)***, ***(h)***, *and* ***(i)*** *show the resonant Raman profiles. See Table 3.2 for 2D mode details.*

the 2D mode of the E_{11} resonance Raman profile is 40 times larger than the maximum intensity of the E_{22} resonance Raman profile. Both maxima are observed at the outgoing resonance positions of the corresponding profiles. The higher intensity of the 2D resonance of the lower transition number can interfere with the 2D mode at higher transition and should be taken into account i.e. when E_{22}- E_{11}- E_{2D} is comparable with the width of the 2D mode resonance profile (0.5-1 eV).

The only nanotube showing an asymmetric line shape in the 2D mode at the first excitonic transition is the (6,4) nanotube, see Figure 3.11c. Figure 3.11f shows the dispersion of the LO (blue) and TO (gray) 2D components. In the same fashion as for the second transition, the 2D mode of the LO (TO) component exhibits a higher (lower) energy. Their positions anti-cross at a single point at 1.73 eV excitation close to the outgoing resonance. This experimental result accords excellently with the calculated TO-derived and LO-derived phonon dispersions, having a single touching point near the K point and then their energies go apart until they reach the K point [107]. The approximated difference between LO and TO approaches ~20 cm^{-1} at their minima. The splitting between TO and LO is observed in (6,4) possibly due to the very low diameter of this species. The energy difference between LO and TO were reported to decrease with the nanotube diameter [102,122].

The EP mediated by the bright state of the first and second states only differ by the bottleneck energy, and exciton-like branch dispersion tuned by the effective mass. A large energy separation of up to 50 cm^{-1} between the 2D modes excited at the E_{11} and E_{22} transitions as well as differences in the resonant Raman profiles are due to the different dispersion regions of the dark excitonic state. In order to prove my interpretation, I simulate the excitation energy dependence of the 2D Raman mode of the (6,5) tube and compare them with the experimental data.

3.2.4 Simulation of the 2D mode in (6,5) nanotube

Figure 3.12a and b show the positions of the 2D mode obtained from the experiment and simulations plotted over excitation energy. The points show the maxima of the experimentally obtained and simulated 2D mode. The vertical lines show the positions of the incoming and outgoing resonances of the two transitions. The simulated Raman spectra perfectly capture the dispersion behavior of the 2D mode at the second transition with the plateau region between incoming and outgoing resonances. Above the outgoing and below the incoming E_{22} resonances, the 2D mode energy increases with laser energy. The positions of the calculated 2D mode converge in the region between two excitonic transitions in line with the 2D mode dispersion observed in the experiment. For the E_{11} case, the simulated 2D mode position excited at the first transition also reproduces the experimental behavior. However, the experimentally observed dispersion of the 2D mode is not as flat as the simulated one in the region between the incoming and outgoing resonances. Below the E_{11} transition energy there no dispersion is expected, however could not be experimentally resolved.

The intensity of the experimental and simulated 2D mode are compared in Figure 3.12c and d. The increase of intensity is observed in the calculated profile at the incoming and outgoing resonances of the E_{22} transition. The outgoing/incoming resonances ratio, 1 to 4, is well reproduced in the calculated resonance Raman profiles, providing 1 to 3 ratio. The simulated resonant Raman profile of the 2D mode at E_{11} is also in good agreement with experiment. At the first transition, only the outgoing resonance is present both in the simulated and experimental resonance Raman profiles. Note the similar maximal intensity of the simulated 2D intensity at first and second transitions. This corroborates our initial assumption that the enhanced Raman intensity at E_{11} is due to the increase of matrix elements taken to be equal for first and second transition simulations, and not due to the resonance effect (change of the denominator in Eq. (3.6)).

All five investigated nanotube chiralities provide a similar resonant behavior with a number of differences between SI and the SII types. I will review and discuss these differences. When excited at the second transition, the 2D mode dispersion exhibits three regions. Below the incoming and above the outgoing resonance, the 2D mode frequency increases with laser energy. Between the incoming and outgoing resonances, the plateau region is observed, with no or very small change of the 2D frequency with laser energy. In SII type nanotubes, the second turning point in the 2D dispersion occurs exactly at the position of the outgoing resonance. In SI type, the flat dispersion region ends before reaching the outgoing resonance. Such behavior can be explained by the non-parabolic bright exciton dispersion with energy varying as $q^2 \ln|q|$ near its band edge, rather than

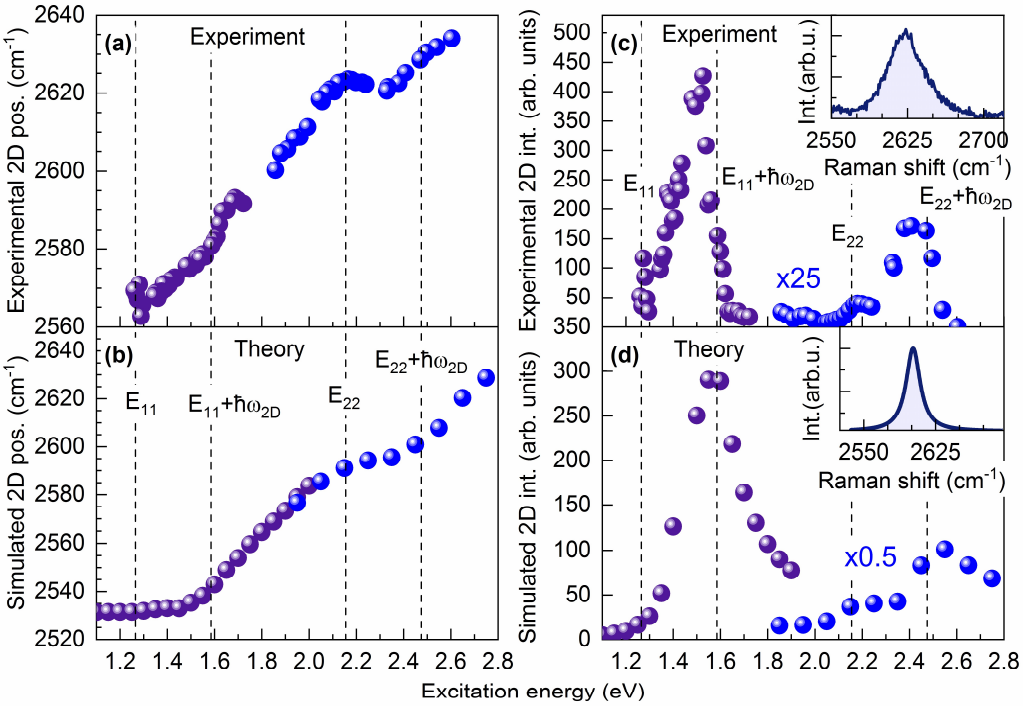

Figure 3.12 *Comparison between the calculated by Eq. (1) and (2) and the experimentally obtained 2D mode in the (6,5) nanotube. Vertical dashed lines mark expected positions of the incoming and outgoing resonances at first and second excitonic transition. The simulation details are described in the methods section. The position of* ***(a)*** *the experimentally obtained and* ***(b)*** *simulated 2D mode.* ***(c)*** *Experimental intensity of the 2D mode. In the E_{22} region (right side) is multiplied by a factor of 25.* ***(d)*** *The intensity (area below the peak) of the simulated Raman mode calculated separately for the first and second transitions. The details of the calculation can be found in Appendix A.*

q^2 as I used in parabolic approximation [15,89]. However, the reason for this effect, for it to be nanotube chirality specific, needs a deeper theoretical investigation.

The SI type nanotubes have a symmetric line shape and the SII type nanotubes an asymmetric one comprising of two symmetric components, attributed to the LO and TO vibration. For both components, the outgoing resonance has a lower energy than predicted in the simulations. It is observed in asymmetrically structured 2D modes in (7,5) and (8,3) tubes excited via the second excitonic transition (Figure 3.8c and Figure 3.9e) and in (6,4) nanotube excited via first transition (Figure 3.11f). In our simulations, the position of the outgoing resonance coincides with the expected position at $E_{11} + E_{2D}$ for the first transition and is even at higher energy for the second excitonic transition, see Figure 3.12d. When the constant matrix element approximation is lifted, and a linear dependence of matrix elements is introduced, the simulated positions of the outgoing resonances will provide a better match to the experimental data. By comparing the positions of outgoing resonances, we conclude the stronger dependence for the $M_{exciton-TO}$ than for $M_{exiton-LO}$ in Eq. (3.6) at the second excitonic transition, and vise versa for the first excitonic transition.

The displacement of the 2D mode in carbon nanotubes captures the information of large variety of phonons near the K point. It enables the exploration of physical effects in the extended BZ region. For example, in doped nanotubes the phonon and exciton renormalization can be monitored [123]. Moreover, the analysis of the 2D mode can be used to decompose electronic and excitonic contributions to the optical bandgap. The position of the first turning point at the incoming resonance reflects the energy of bright exciton due to the electronic band gap, and the exciton binding energy tunes the slope of various dispersion regions due to the change of exciton effective mass related to the binding energy.

3.2.5 Conclusion

In conclusion, we experimentally established the excitation energy dependence of the position and intensity of the 2D mode in carbon nanotubes. The five chiralities investigated at second excitonic transition demonstrated a uniform behavior with three dispersion regions. The resonant Raman profiles exhibit incoming and outgoing Raman resonances, near E_{22} and $E_{22}+E_{2D}$ respectively. The outgoing resonance is always dominating and provides up to 4x times higher intensity. The position of the 2D mode shifts with the excitation energy and its dispersion is divided into three regions. Below the incoming and above the outgoing resonance, the 2D mode energy increases with excitation energy. Between the resonances, a plateau region is observed. The slope of the plateau varies between chiralities from negative to positive values. The turning points originate from the resonant phonons sliding into the bottleneck of the exciton-polariton dispersion. The resonant behavior of the 2D mode in (6,5),(8,3), and (6,4) was complemented for the first transition. The comparison of the 2D mode dispersion between the transitions allowed us to identify the dark state of E_{11} as the channel used for the second step of Raman process. The intensity of the 2D mode is up to 50x higher when excited at the first transition compared to the second one. The displacement of the 2D mode with excitation energy as well as the resonant Raman profile of the (6,5) nanotube were excellently reproduced by fourth-order perturbation theory with implemented elements of the exciton-polariton effects.

4 | Electron-phonon coupling in CNTs

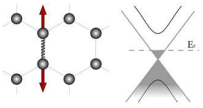

In this Chapter, I probe the pathways to control and tailor the phonons and excitons in a fixed *(n,m)* chirality. The ability to modify the electronic and vibrational properties is reliant on the surface accessibility of the nanotube due to its one-dimensional structure. The most elaborated ways to tune the phonons in the nanotube is the application of strain and injection of charge carriers. The charge carriers can be introduced into the nanotube system in different ways. The most common one is electrical back-gating [4], where a bias difference between the nanotube and a dielectric layer (mostly SiO_2) injects additional charges into the nanotube. A similar working principal has the electrochemical gating, where the ionic liquid shares its charges with the nanotube [123–125]. These two approaches require a direct contact between the nanotube and the gate. The tubes doped in such a way have altered phonon modes [123].

However, they cannot be further treated or used in the electrical and optical circuits. Intercalation can be another efficient way to dope solid-state systems [126]; unfortunately, single walled nanotubes do not provide intralayer spaces for the intercalant, therefore no stable material can be produced by these methods. Efficient intercalation is only possible when the number of nanotube walls is greater than one realized in few- and multi-walled nanotubes [127].

The only remaining way to tailor the CNT phonons is the functionalization. Chemical functionalization is regularly applied to improve and tailor properties of the nanotube, such as solubility [128–130] and luminescence quantum yield [131–134]. Additionally, absorption and emission bands [135] and the thermal conductivity can be tailored by adding functional moieties [136]. The functionalization methods are divided into covalent and non-covalent approaches [137]. The non-covalent approaches rely on the weak bonding between the nanotube and the functional group. This type of bond is easily reversed by changing the ambient conditions of the hybrid system. The covalent approach creates the most stable compounds. The covalent bond is strong enough to survive the standard physical-chemical treatment of the nanotube. Functionalization can yield charge injection from the molecule onto the nanotubes. The covalent bond can also result in a distortion of the lattice inducing strain. Both these physical effects alter the phonon frequencies and lifetimes. The modified phonons in functionalized nanotubes will permanently “freeze” in such condition. In this Chapter, I test three different covalent approaches; (i) [2+1] cycloaddition with triazines, (ii) photo activated diazonium salt functionalization, and (iii) standard acid treatment. The detailed description of each reaction is given in the beginning of the corresponding subchapter. Depending on the electronic type of the nanotube, the phonons behave differently under lattice perturbations and doping. Therefore, the reaction effects are studied separately for metallic and semiconducting nanotubes. Functionalization routines and experimental methods are summarized in *Appendix B*. Each approach is evaluated by its ability to change the frequency and lifetime of the phonons. First, I provide a theoretical background of doping and strain induced effects occurring in the nanotubes due to the functionalization.

4.1. Theoretical background

Chemical functionalization can induce different physical effects on carbon nanotubes. The proximity of a molecular shell to the CNT changes its transition energies by screening the exciton wave function, when a sufficient amount of molecules are attached to the nanotube surface. If these

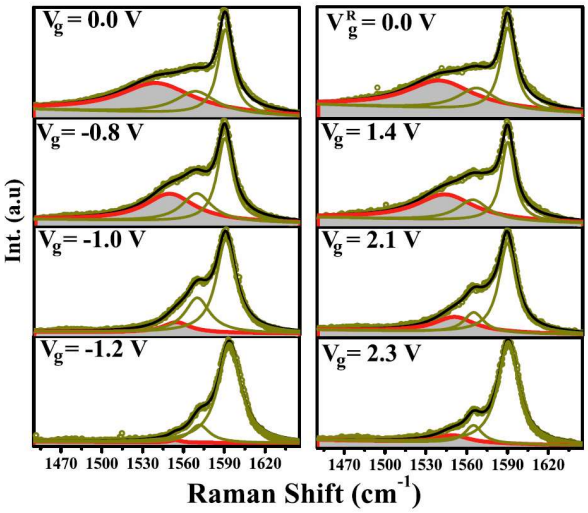

Figure 4.1 *Electrolyte gating in metallic nanotubes of 1.4-1.6 nm diameters excited with a 1.96 eV laser. At zero gate voltage the width of the metallic LO phonon is at maximum and decreases by the injection of charge carriers. The change direction is uniform for positive and negative charge carriers, adapted from Ref.* [139].

molecules are covalently attached to the nanotubes carbon network, they moreover induce a lattice strain. The strain alters both the phonon and exciton energies. Finally, the electrons of the functional groups overlap with the electronic states of the nanotube, withdrawing or sharing charge carriers depending on the electronic potential. Thus, the doping is introduced into the system. I shortly outline below how all these effects alter the vibrational and optical properties of the CNT.

4.1.1. Doping induced effects in carbon nanotube

Effects on phonons in metallic CNTs. The metallic LO phonon has a broad Fano line shape due to the coupling to the electron continuum [138]. The intrinsic width of the phonon varies from 150 to 50 cm^{-1} as function of nanotube diameter [122]. Metallic nanotubes have electronic bands close to the neutral Fermi level. The change of the Fermi level (doping) modifies the scattering mechanisms of the phonon and leads to a change of its lifetime. The phonon lifetime is proportional to the width of the corresponding Raman mode. Even the finest shifts of the Fermi level can be traced reliably by analyzing the phonon width [139].

Figure 4.1 shows the evolution of Raman spectrum by the injection of charge carriers via electrochemical gating. The metallic LO phonon is marked by the red line. In neutral doping position the width is at its maximum is 40 cm^{-1}. After injection of positive or negative charges into the nanotube by controlling the voltage between the nanotube and the gate, the LO width reduces together up to 10 cm^{-1} and the LO frequency upshifts to higher energy.

The changes in the linewidth of the phonon can be directly translated into the doping level. Figure 4.2 shows an experiment, where electrolyte gating is performed on metallic nanotubes of smaller diameter, compared to one displayed in Figure 4.1. The FWHM is at maximum (70 cm^{-1}) at zero gate voltage and then decreases to the minimum levels (12 cm^{-1}) with the gate voltage, see Figure 4.2a. The energy difference between the LO phonon width is reduced by half from its maximum values corresponding to the phonon energy (~ 0.19 eV), see blue line in Figure 4.2a. The

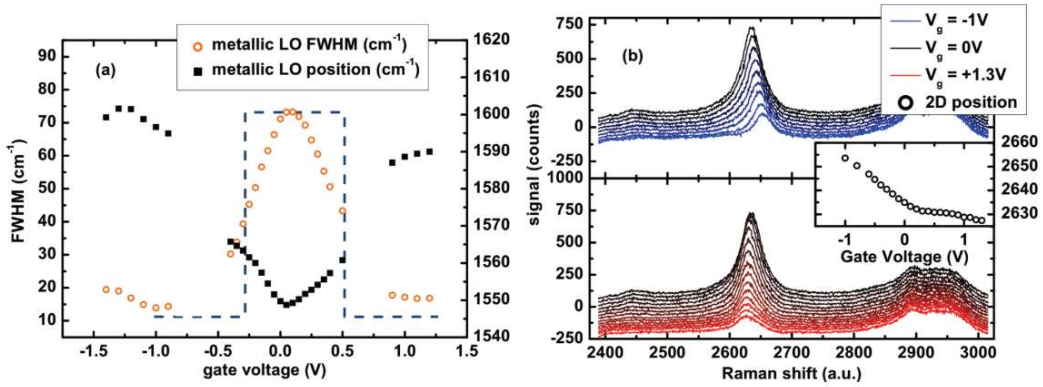

Figure 4.2 *Doping induced changes of the metallic nanotube phonons.* ***(a)*** *LO phonon FWHM (left axis) and position (right axis) as function of gate voltage. The spectrum can be recalibrated in eV considering the distance between mean values is one phonon energy (blue dashed line).* ***(b)*** *2D mode as function of positive (red) and negative (blue) gate voltages. The middle panel shows the position of the 2D as function of gate voltage, adapted from Ref.* [164].

lifetime of the phonon is expected to change by half of its maximum value by the Fermi energy shift of the half phonon energy. The blue dashed line marks the points where half of the maximum value is reached. The position of the LO phonon undergoes a mirror like behavior, where it is at its minimum (1550 cm^{-1}) at zero gate voltage and increases to 1590-1600 cm^{-1} by applying the gate voltages. The changes in the LO modes serve as highly sensitive sensors of the Fermi level displacement.

Figure 4.2b shows the evolution of the 2D mode under doping. The doping induces the shifts of the 2D mode energy, with the positive-negative anisotropy. The 2D mode shifts to higher (lower) energy by negative (positive) gate voltages, making the shift of the 2D mode in metallic nanotubes a good metric for monitoring higher energy Fermi level shift with ($\Delta E_F > E_{LO}$). At such doping levels no further doping induced changes occur in the LO phonon.

Effects on phonons in semiconducting CNTs. In semiconducting nanotubes detectable changes in the G mode occur only after the Fermi energy reaches the first conductive band and charge carriers bridge the band gap [125]. When the concentration of charge carriers fills the band gap, the transport behavior of a semiconducting CNT transistor changes from isolating to conductive. This is observed in Figure 4.3c and d for (10,5) and mixed chirality CNTs, respectively. The G band frequency and linewidth changes from the pristine position, as shown in Figure 4.3a and b as function of gate voltage. The LO phonon starts to shift rapidly after the singularity is bridged. The linewidth of the semiconducting LO phonon increases with doping unlike the linewidth of metallic LO phonon, decreasing with doping from pristine condition.

The doping in semiconducting nanotubes at low charge carrier concentration can be monitored by an analysis of the D and 2D modes. The changes in the position and linewidth of these phonons occur at doping levels below ±0.2 eV [140,141]. It should also be noted, that the pure doping does not significantly affect the energies of excitons in semiconducting CNTs. This has been reported in electrolyte gating experiments, where even at extremely high doping levels the excitonic energy corresponding to the bright exciton remained unperturbed [142].

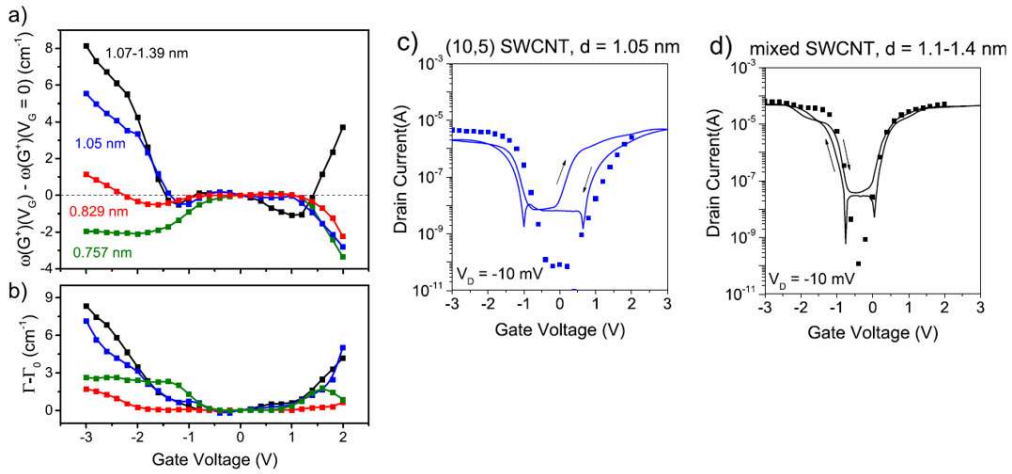

Figure 4.3 *Doping induced changes in the LO mode of the chirality enriched semiconducting nanotubes. Blue (10,5), green (6,5), red (7,5), and black mixed CNTs* ***(a)*** *LO phonon position and* ***(b)*** *FWHM as function of gate voltage.* ***(c)*** *and* ***(d)*** *transport characteristics of the fractions as function of gate voltage, adapted from Ref.* [125].

4.1.2. Strain and screening effects

Deformations due to the covalent attachment of molecules induce strain in the nanotube carbon lattice and screening effects in the nanotube excitons. Both strain and screening induce changes in the transition energies in carbon nanotubes. However, these effects can be clearly distinguished from each other by analyzing the transition energies of different nanotubes. Screening changes the dielectric environment of the exciton due an the alteration of the electron-hole interactions. The binding energy of the exciton increases, changing the optical transition energy. The transition energies in all CNTs uniformly red-shift with dielectric constant of the environment [143,144].

Such kind of screening induced changes in transition energies are visualized in the pseudo PLE map shown in Figure 4.4a. The y axis on this map represents the E_{22} transition energies (excitation) and x-axis represents the E_{11} transition energies (emission). Each set of points stands for a given *(n,m)* chirality, embedded in different dielectric environments.

The strain induced by the molecules is mainly uniaxial, due to the high aspect ratio of the nanotube. It is experimentally difficult to attach multiple groups along a circumference of the tube; even if theoretically possible. Such radial strain would induce strong changes in the nanotube Radial breathing mode frequencies, similar to the effects occurring in nanotubes under the hydrostatic pressure [145]. The uniaxial strain modifies the carbon lattice and changes the electronic band gaps in the CNT [146]. By applying strain, the transition energies of different types (SI and SII) shift in opposite directions. Figure 4.4b shows the shifts in transition energies of different chiralities loaded by being strained by the same magnitude inside of a polymer matrix. Filled symbols represent the shifts of the E_{11} transition energies and open symbols the shifts of the E_{22} transition energies. The amount of change in the electronic band gap depends on the orientation of the carbon lattice along the nanotube axis (i.e. chiral angle on the nanotube). The spectral shift of the E_{22} occurs in the tubes with larger chiral angle, by the same amount of applied strain, see Figure 4.4b. Analyzing the slope of the linear fitting lines for a number of CNT chiralities one can obtain the amount of uniaxial strain and its direction.

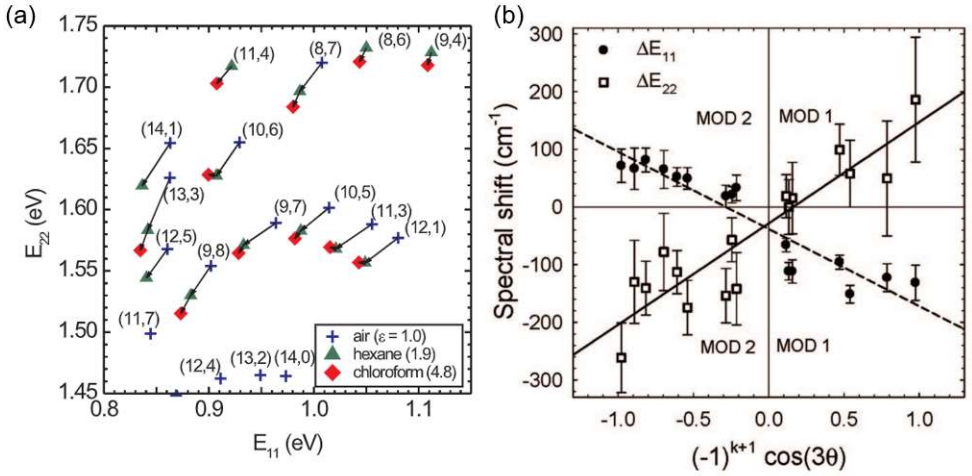

Figure 4.4 *Changes in transition energies in carbon nanotube.* ***(a)*** *PLE map of suspended nanotubes with E_{22} plotted versus E_{11} in various environments with dielectric constants ε =1,1.9,and 4.8, adapted from Ref.* [143]**.** ***(b)*** *Strain induced shifts in carbon nanotube, with transition energies of different CNT types shifting in the opposite direction, adapted from Ref.* [146].

The strain modifies the carbon-carbon vibrational interaction as well, leading to changes in phonon frequencies. The strain induces linear shifts of the Raman bands, proportional to the strain. Such behavior is reported by Cronin et al. [147], where an individual nanotube was strained by an AFM tip. The G (2D) mode shifts by 14 cm^{-1} (23 cm^{-1}) per 1 % strain. The shift is negative for extensive strain and positive for compressive uniaxial strain [148]. Those are the macroscopically induced effects of doping and strain, now let's see how these effects manifest in our functionalized CNTs.

4.2. [2+1] Cycloaddition [4]

The cycloaddition reaction has the potential to overcome the main drawback of covalent functionalization techniques, where the sp^2 network of the CNTs is disturbed. The distortion of the network leads to a disturbance of the mechanical and optoelectrical properties [157] and can even cause the breakdown of the nanotube [158]. The [2+1] cycloaddition reaction creates defect-free covalent bonds [159]. Two different types of bonds can be formed between the triazine and the CNT's sp^2 network. It can either stabilize in the closed or in the open ring configuration, shown in Figure 4.5a and b, respectively. The closed ring configuration changes the sp^3 hybridization of the carbon atoms and induces a defective state, whereas the open ring configuration retains sp^2 hybridization of carbon introducing only a weak perturbation of the carbon lattice. Quantum chemical calculations show that the open ring configuration is the stable one [149].

[4] The contents of this Section are published in "Setaro, A et al. *Nat. Commun.* **8,** 14281 (2017)". The coauthors agree on using the data in this work.

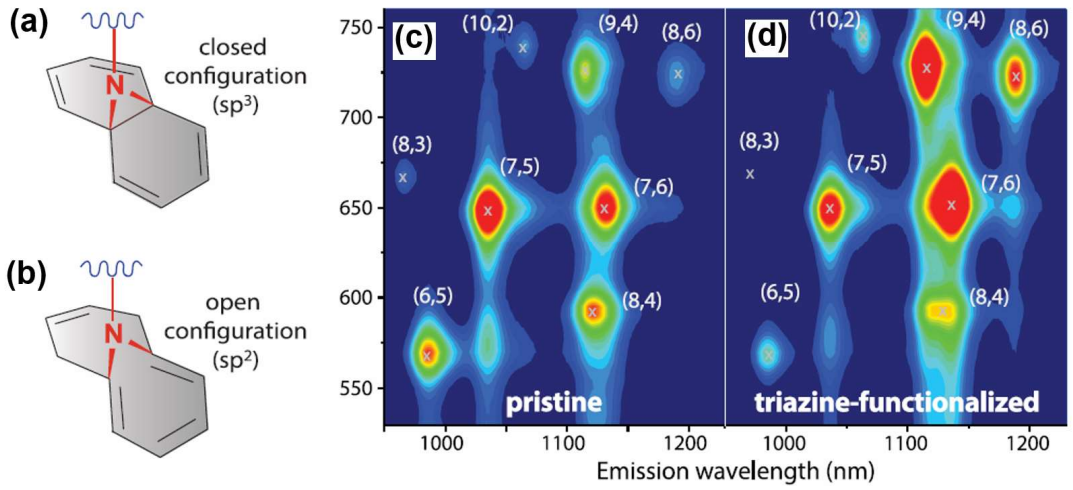

Figure 4.5 *Possible products of [2+1] cycloaddition reaction.* ***(a)*** *Closed configuration and* ***(b)*** *open configuration of the nitrogen-carbon bond, including two sp^3 and sp^2 hybridized carbon atoms. Photoluminescence-excitation maps of the* ***(c)*** *pristine and* ***(d)*** *functionalized CNTs.*

4.2.1. Optical and XPS characterization of functionalized CNTs

The low distortion of the CNT's initial hybridization preserves optical properties of the nanotube material. Figure 4.5c compares the PLE maps of the pristine and functionalized samples. The luminescence in some CNT chiralities, such as (7,6), (9,4), and (8,6) substantially increases (de-bleaches). This effect occurs due to charge transfer effects and suggests that the pristine nanotubes are initially in the doped state. The positions of the intensity maxima correspond to the transition energies ([5]). The peak positions do not change between the functionalized and pristine samples. This indicates that nether strain, nor dielectric screening occur by the functionalization of nanotubes. The size of the molecule is too small to screen the exciton and cover density is not sufficient to induce the strain.

X-ray photoelectron spectroscopy (XPS) is a useful technique to characterize the functionalized material. It is sensitive to the chemical composition and types of the chemical bonds in the sample ([6]). The covalent functionalization induces covalent bonds between the CNT and functional moiety. These bonds can be sensed by XPS and serve as a solid evidence of successful functionalization along with presence of non-carbon chemical elements. Figure 4.6a compares XPS spectra of the functionalized and pristine material in the region of carbon bond binding energy. Red filled peaks highlight the new bonds arising through the functionalization. The functionalized nanotubes are present in two different configurations, low and high functionalized, see the inset in Figure 4.6a. The comparison between nitrogen and carbon peaks allows calculation of covering density of CNT by triazine. The covering ranges for the samples are one molecule per 104 (24) carbon atoms in the high- (low-) functionalized samples. The ratio between the peaks corresponding

[5] PLE measurements were carried out by Mareen Glaeske.
[6] XPS characterization of the sample was performed by Daniel Przyrembel, the full XPS survey can be found in "Setaro, A et al. *Nat. Commun.* **8,** 14281 (2017)".

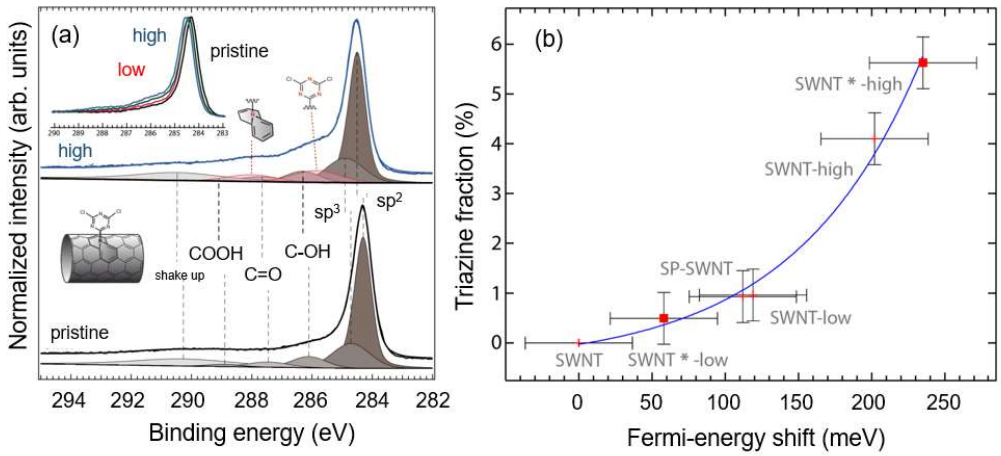

Figure 4.6 *XPS characterization of the functionalized samples.* ***(a)*** *C1s XPS spectra of SWCNTs* ***(bottom)*** *and functionalized samples* ***(top)****, given along with spectral fits for each chemical component present in the samples. The maxima of the fit correspond to the energies of the bonds, marked by vertical dashed lines. The components are normalized on the height of* sp^2 *component. The red peaks correspond to the new bond with the nitrogen atoms.* ***(b)*** *Fraction of triazine molecules plotted over Fermi-energy shift. The samples with * and without * represent different preparation batches.*

for sp^2 and sp^3 hybridized carbon remains constant in the functionalized material. The XPS confirms the open configuration of the triazine ring, see Figure 4.6a,b.

As illustrated in Figure 4.6 the shift of the C1s XP level to higher binding energy directly reflects an upward shift of the Fermi level towards the SWNT conduction-band. Interestingly, a deposition of triazine on graphene without a chemical interaction results in the opposite behavior (lower C 1s binding energy and a decrease in Fermi energy) [160]. The ratio between carbon and nitrogen peaks is plotted versus the Fermi level shift from the displacement of the binding energy. The Fermi level increases with the content of nitrogen atoms in the samples. The analysis of the Fermi level yields 60-120 meV in low-functionalized samples and 210-240 meV in the high-functionalized samples. After confirming a charge transfer from the triazine onto the nanotubes, I turn to the investigation of the coupling between the phonon and electron.

4.2.2. Electron-phonon coupling in CNTs functionalized by triazine molecules

The moderate Fermi energy shifts estimated from XPS analysis (59-250 meV) suggest, that the coupling between metallic phonons and electrons can be potentially observed. The Fermi level shift is however not high enough to interact with the semiconducting phonons. In order to confirm that, I compare the RBM phonons in the metallic and semiconducting tubes. Two different excitation regions are used to excite mostly metallic CNTs at 2.33 eV and mostly semiconducting nanotubes at 1.9 eV. Figure 4.7a and b compare the RBM spectra excited at 1.9 eV of the pristine and high-functionalized samples, respectively. Using a Kataura plot in Figure 2.14 four semiconducting species (10,3), (11,2), (7,5), and (9,1) are identified [40]. Vertical dashed lines show the positions of the RBMs. The RBMs shift by maximally 0.5 cm^{-1} near the accuracy of the measurement. The magnitudes of the shifts are shown in form of column bars in Figure 4.7e for each identified species. Higher concentration of charge carriers is required for coupling with phonons of semiconducting nanotubes.

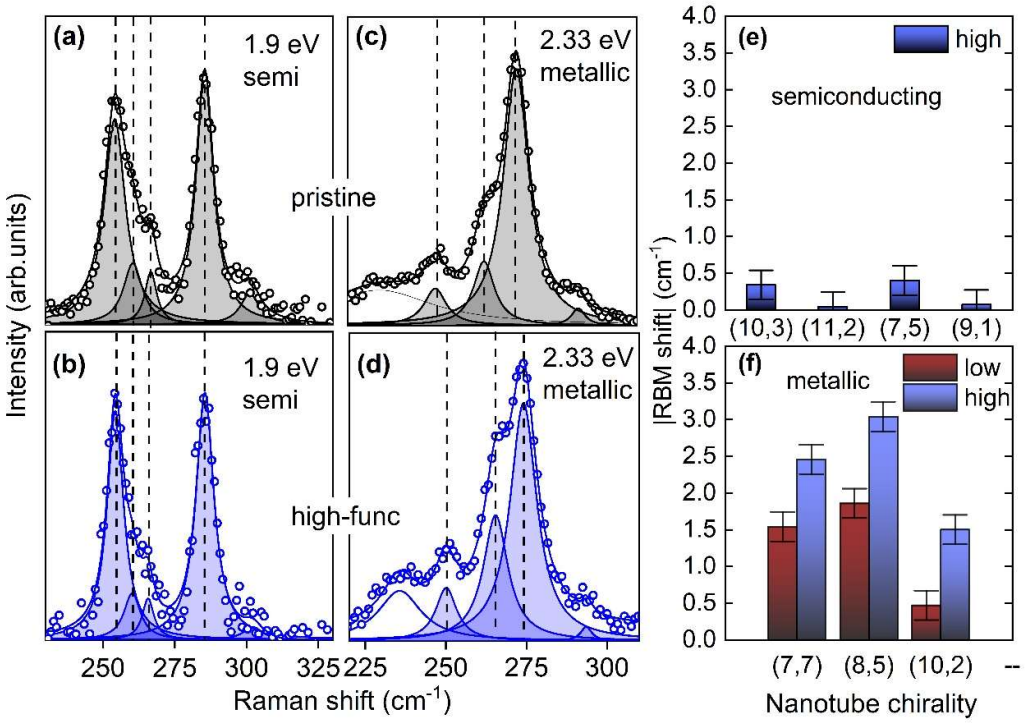

Figure 4.7 *Functionalization induced effects on the Raman spectrum in metallic and semiconducting carbon nanotubes. Raman spectra excited at 1.9 eV in RBM region showing the modes of different semiconducting species in* ***(a)*** *pristine* ***(b)*** *high-functionalized samples. RBMs excited at 2.33 eV in* ***(c)*** *pristine and* ***(d)*** *high-functionalized samples. Dots represent experimental data and lines are fits, where a filled Lorentzian line shapes represent each RBM. Vertical dashed lines mark the identified RBM positions. Absolute RBM shifts extracted from the fit for* ***(e)*** *semiconducting and* ***(f)*** *metallic nanotubes.*

The situation is quite different for metallic nanotubes. The RBMs excited at 2.33 eV are shown in Figure 4.7c and d for pristine and high-functionalized samples, respectively. In a similar manner as earlier for semiconducting species, the RBMs are identified. Three metallic species (7,7), (8,5), and (9,3) are index assigned [40]. The positions of RBMs significantly change after functionalization. The RBM shift up to 3 cm^{-1} in (8,5) nanotubes to higher energy. The magnitude of the shift is shown in form of a column bar in Figure 4.7f. The shifts are progressive with stronger functionalization. The higher the density of the functional moiety, the greater is the shift of the RBM. This is nicely observe by comparing the RBMs in low-functionalized sample to the high-functionalized sample. This fact allows me to conclude that a strong coupling occurs between the electron and the RBM phonon in metallic nanotubes due to the functionalization.

The difference in electron-phonon coupling between metallic and semiconducting nanotubes is due to the deviating structure of the electronic states. In semiconducting nanotubes with d~1nm the first state of electronic states is around 0.5 eV above and below the zero level [84]. Low doping levels do not significantly perturb the electronic structure of a semiconducting nanotube and the phonon frequency remains constant. In metallic nanotubes the lowest energy electronic states are very close to the zero energy level. The bands cross at zero in armchair nanotubes and in other metallic species, there are small band gaps 20-40 meV [47–49] , as discussed in Section 2.1.3. Due to these electronic states, even the low doping levels induce a significant

Table 4.1 *Parameters of the metallic LO phonon in pristine, low-, and high-functionalized samples excited 2.33 eV*

sample	LO asymmetry	LO FWHM (cm^{-1})	LO posittion (cm^{-1})	Fermi level ±10 (meV)
pristine	-0.09	67.4	1535.8	-85
low-func.	-0.10	84.9	1528.0	-34
high-func.	-0.14	93.6	1527.7	25

difference in the RBM phonon frequencies [161]. In addition to the doping induced effects, the frequency of metallic RBMs is very sensitive towards small perturbations of any kind in the electronic structure. Changes in the electronic structure in metallic nanotubes can be caused by lattice perturbations such as strain or mirror symmetry breaking [162,163]. These effects can occur due to the functionalization, providing an additional pathway to control the RBM phonon frequency. I further investigate the coupling between the high-energy metallic phonons and electrons.

The longitudinal phonon (LO) in metallic nanotubes has a Fano lineshape due to the intrinsic interaction between phonon and electron [122]. As described in the theoretical section 4.1.1, the displacement of the Fermi level influences its position and linewidth. The G band of the pristine,

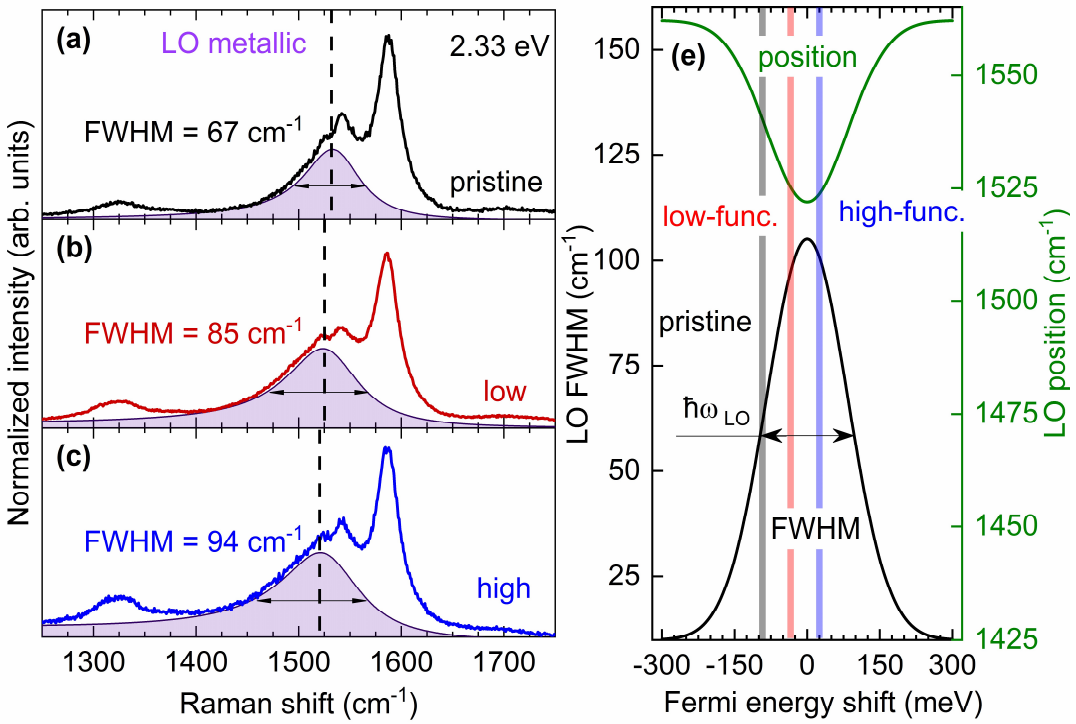

Figure 4.8 (a)-(c) *Evolution of the metallic G mode with functionalization (excited at 2.33 eV). Filled peak represents the longitudinal phonon, with its position (FWHM) marked by the vertical dashed (horizontal full) line.* ***(e)*** *Changes of the LO position (green) and LO FWHM (black) as function of the Fermi energy shift. Horizontal arrow indicates the energy of the LO phonon. Vertical lines correspond to the pristine, low-functionalized, and high-functionalized samples marked by the black, red, and blue colors. Parameters of the LO phonons and corresponding Fermi level shifts are listed in Table 4.1.*

low-, and high-functionalized samples is shown in Figure 4.8a-c. With functionalization the LO phonon broadens and shifts to smaller energies, see Table 4.1. This is a clear evidence of the phonon-electron interaction at each functionalization step. These changes indicate, that the pristine material was initially p-doped and the charges from the molecules move the Fermi level closer to the charge neutrality point. The Fermi level quantifies the number of injected charges. The changes in the phonon position (black) and width (green) as a function of Fermi energy shift can be traced in Figure 4.8e. The vertical lines correspond to the different states of functionalization. The width of the line corresponds to the measurement precision. The position and the FWHM of the G mode undergo similar changes when the nanotube is doped. They form a peak with the width of the phonon energy $\hbar\omega_{LO}$ and with the minimum (maximum) at the charge neutrality point for the FWHM (position). The doping values are smaller than the ones reported by XPS analysis. The discrepancy is related to a different selection of materials investigated by these techniques. Raman analysis at a fixed excitation energy reflects a Fermi level for metallic nanotubes of narrow diameter distribution (here 8-9 nm), while the XPS shows an averaged Fermi level over all nanotube chiralities (metallic and semiconducting).

An important part of the doping induced LO phonon broadening analysis is the setting of the maximum FWHM (amplitude) in Figure 4.8e. However, the theoretical values for a certain diameter of metallic tubes can be used here as an estimation [122]. The FWHM maximum decreases with the diameter of the nanotube. The resonant at 2.33 eV nanotubes have a mean diameter of 0.85 nm, their RBM and G modes are shown in Figure 2.14c,d and Figure 4.8a-c, respectively. For such species the FWHM is set to 110 cm^{-1}, see Figure 4.8e. The same principal applies to the maximum and minimum position of the LO phonon. The displacement of the phonon is smaller than the change of phonon FWHM almost by half. Both LO FWHM and position can be used to estimate

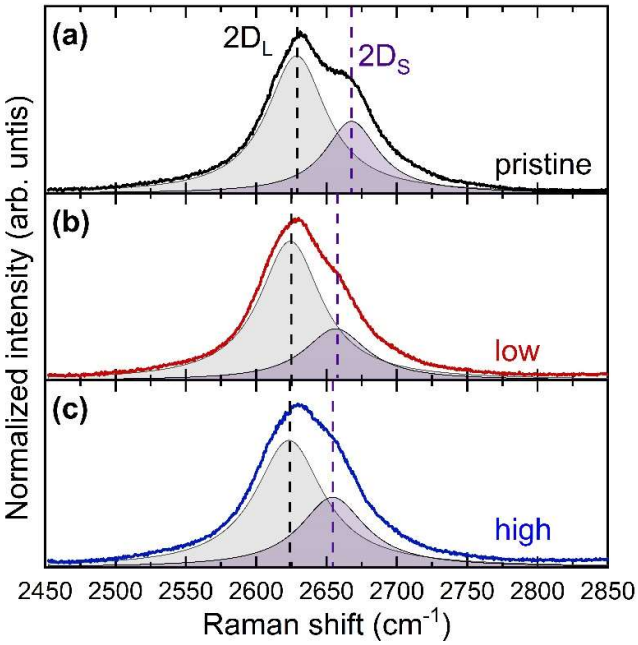

Figure 4.9 (a)-(c) *Evolution of the metallic 2D mode excited at 2.33 eV with functionalization. $2D_L$ (gray) and $2D_S$ (violet) stand for different components of the 2D mode. Vertical dashed lines of respective color indicate the positions of the sub peaks.*

the Fermi level, however for a quantitative analysis the FWHM is better. The changes of the LO phonon are symmetric towards negative and positive charges, which means the Fermi position of the pristine sample can be equally attributed to the p- or n-doping. By analysing only the G mode it is impossible to rule out either possibility. The coupling between the 2D mode and the electron is asymmetric towards the sign of the injected charge. The analysis of the 2D mode allows a correct set of the doping lines in Figure 4.8e [164].

The 2D mode comprises of two peaks $2D_L$ and $2D_S$, see Figure 4.9. $2D_L$ peak corresponds to nanotubes of greater diameter than 0.85 nm and $2D_S$ peak corresponds to the nanotubes resonant with the laser. This assignment is based on the diameter dependence of the 2D mode reported in previous chapter, see Figure 3.10. The 2D mode of smaller diameter nanotubes ($2D_S$) is at the outgoing resonance, whereas the 2D mode of larger nanotubes ($2D_L$) is at the incoming resonance. The resonances of the 2D mode can be found in Chapter 3. Both 2D components shift to smaller energies with functionalization. The $2D_L$ mode shift by 5 cm^{-1} and $2D_S$ mode by 14 cm^{-1}. The shift to smaller energies indicates a positive sign of the Fermi energy shift in Figure 4.8e. The larger shift of the 2D mode of CNTs indicates that cycloaddition functionalization has diameter selective effects.

The deviating shifts of the 2D mode components can be attributed either to the diameter dependent 2D mode-electron coupling or to the faint reactivity of large diameter tubes. In order to confirm the diameter dependence of functionalization effects, I study the metallic G modes of two different diameters. The nanotubes studied earlier have the average diameter of 0.85 nm and were excited with a 2.33 eV laser. In order to study larger nanotubes, lower excitation energies should be picked. The G mode excited at 2.2 eV is shown in Figure 4.10 a,b with G modes for pristine and functionalized samples. These spectra correspond to nanotubes of 1 nm average diameter. The G mode has a clear metallic character with a broad Fano component (filled peak) corresponding to the metallic LO phonon. During the functionalization the width of this peak increases from 35 cm^{-1} to 54 cm^{-1}. The position of the LO phonon red shifts. This indicates that the Fermi level position is below the charge neutrality point in pristine nanotubes and shifts to a higher energy assisted by the functionalization. Same behavior of the Fermi level was observed for 0.85 nm dimeter nanotubes, see Figure 4.8.

The smaller tubes with 0.75 nm are excited with higher excitation energy of 2.6 eV. The G mode of pristine and functionalized samples is shown in Figure 4.10c and d, respectively. The metallic LO phonon undergoes similar changes as for larger tubes. The mode broadens and position red shifts during the functionalization. The FWHM increases from 48 cm^{-1} to 86 cm^{-1}. Assuming the functionalized tubes are close to the zero Fermi level, I can compare the doping efficiency for nanotubes of different diameters. The full set of fitting parameters of the metallic LO phonon for each diameter can be found in Table 4.3. The relative FWHM changes can be used as a scale for

Table 4.2 *Parameters of the metallic $2D_i$ mode in pristine, low-, and high-functionalized samples. i = L and S for nanotubes of larger and smaller diameters, respectively*

sample	$2D_L$ FWHM (cm^{-1})	$2D_L$ position (cm^{-1})	$2D_S$ FWHM (cm^{-1})	$2D_S$ position (cm^{-1})
pristine	51.6	2628.6	46.1	2667.8
low-func.	53.5	2624.2	53.7	2656.5
high-func.	58.5	2623.3	56.2	2654.3

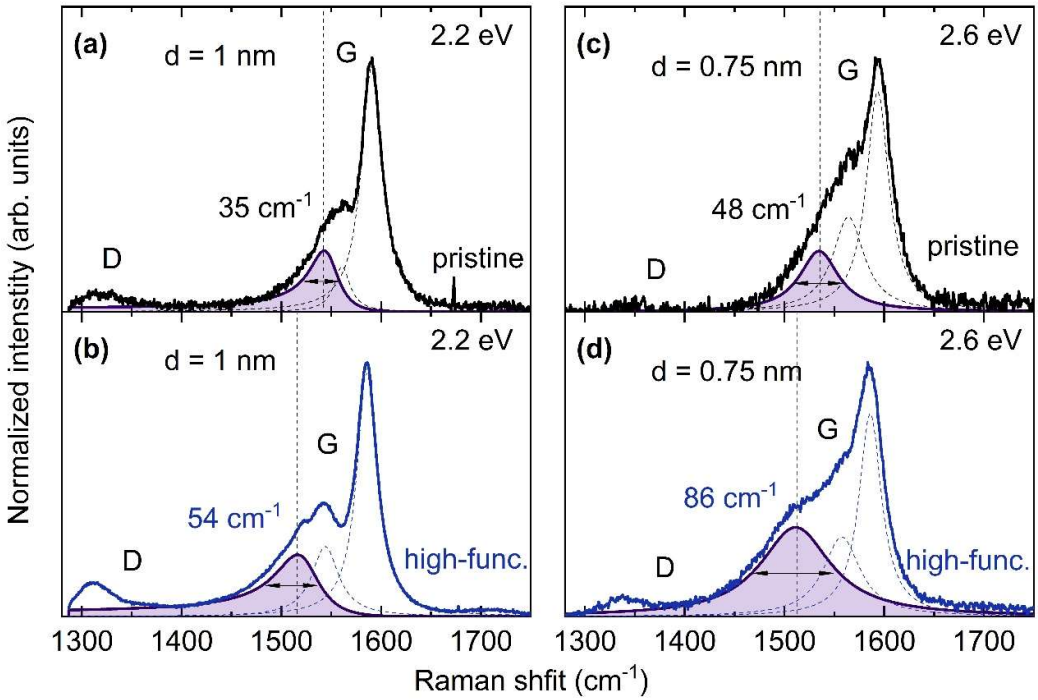

Figure 4.10 *Functionalization induced changes in the G mode of metallic nanotubes of different diameters. Filled peak indicates metallic LO phonon, with its FWHM given in the number above and its position marked by the vertical dashed line.* ***(a)***, ***(b)*** *Pristine and high-functionalized large diameter nanotubes (d = 1nm) excited at 2.2 eV.* ***(c)***, ***(d)*** *Pristine and high-functionalized small diameter nanotubes (d = 0.75 nm) excited at 2.6 eV.*

Table 4.3 *Phonon modes for nanotubes of different diameters. E_L is the excitation energy, d average nanotube diameter, the parameters of the longitudinal phonon (LO) fitted by a Fano line shape; LO FWHM, LO position and asymmetry (LO a-s). D_{pos} is the position of the D mode*

sample	E_L (eV)	d (nm)	LO FWHM (cm^{-1})	LO pos. (cm^{-1})	LO a-s	D pos. (cm^{-1})
pristine	2.2	1	19.9	1546.4	-0.2	1320.1
high-func.	2.2	1	32.8	1522.3	-0.2	1312.3
pristine	2.6	0.75	17.4	1534.7	0	1347.9
high-func.	2.6	0.75	46.0	1511.2	0	1334.6

the comparison between Fermi energy shifts in nanotubes of different diameters. In small metallic tubes the FWHM changes by 55%, versus 66 % in large metallic tubes. The smaller this number is, the stronger electron-phonon coupling is induced. Therefore, I conclude that phonons in smaller tubes are indeed tuned more efficiently by the cycloaddition reaction, as follows from the analysis of the 2D mode. One option is the peculiar reaction specifications, which allow more functional groups per carbon in the nanotubes of smaller diameters. It is generally accepted that high curvature reduces the reaction potential and favors small nanotubes for the functionalization [165]. The second option is the uniform for all diameters cover density and the same doping, but higher 2D mode shifts for smaller diameter nanotubes. A metrology experminat containing diameter dependent electrocemical gating study of LO phonon width is required here. Such studies are not yet reported in the literature.

The cycloaddition cannot efficiently couple to the semiconducting phonons. In contrast to the metallic RBMs, the RBMs of the semiconducting nanotubes remain unchanged, as observed in Figure 4.7. However, the Fermi-level is still different between functionalized and pristine samples, which is reflected in the bleaching of the photoluminescence in Figure 4.5d. The position of the G mode also remains unchanged [149]. The change in the Fermi energy is just not sufficient to provide the differences in the frequencies of the semiconducting phonons. A different type of functionalization is required to enable the coupling between the semiconducting phonons and the electrons.

4.3. Diazonium salt functionalization 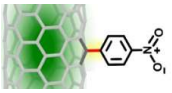

4.3.1. In situ reaction tuning

The reaction between the nanotube and diazonium salt provides a different type of bond between the nanotube and functional group, when compared to cycloaddition investigated earlier. Due to the functionalization, the hybridization changes from sp^2 to sp^3 in the pristine and functionalized states respectively[166]. The defect induced in the crystalline structure of the nanotube creates a bond excitonic state. This state lies below the lowest bright excitonic level (E_{11}). The energy of the bound exciton strongly depends on the type of the radical in the functionality. The energy can be tuned by up to 1.5 eV by simply selecting a type of diazonium salt for the nanotube decoration. Due to the spatial confinement the bound state can emit single photons [10]. Compared to other single photon emitters, functioning at cryogenic temperatures, nanotubes keep their photonic properties at ambient conditions. The ability to serve as a single photon emitter and energy tunability makes diazonium functionalized nanotubes a perfect material for quantum computing in the telecom wavelength range.

A different facet of diazonium reaction is its photosensitivity [29]. When the reaction is carried out in dark conditions, it takes long time scales to succeed (weeks). Whereas under light illumination this time can be reduced to several hours. A further increase of reaction rate can be achieved by choosing a resonant light for the activation. The resonant light is defined by the energies of the bright excitonic states in the nanotube (E_{11}, E_{22}, etc) [28,29]. The difference in reaction yield between resonant and non resonant activation varies by one order of magnitude.

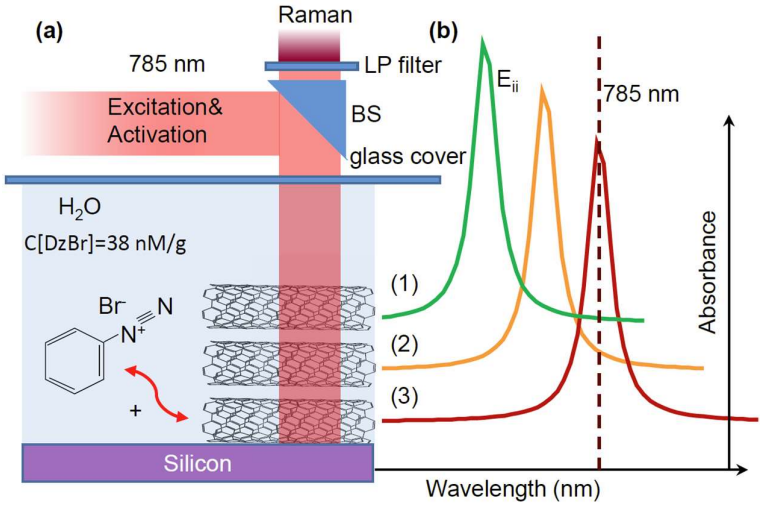

Figure 4.11 *Laser assisted functionalization of drop casted CNTs on a silicon substrate.* ***(a)*** *The infra-red light (785 nm) focused on the nanotubes drives the reaction and scatters Raman active phonons. The concentration of DzBr under the glass cover is 38nM/g. BS-beam splitter, LP-long pass filter.* ***(b)*** *Schematic absorbance of three different nanotubes, with the third one (3) resonant with the laser. The diazonium salt will bind selectively with this nanotube. E_{ii} – the transition energy of the ii transition.*

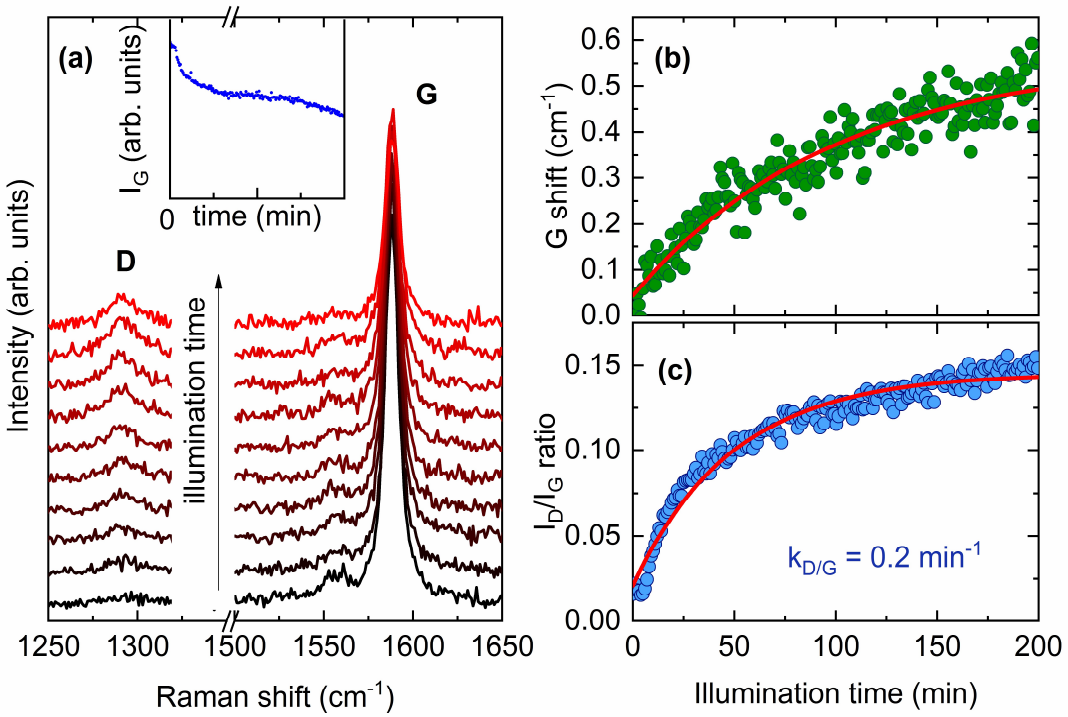

Figure 4.12 *In situ monitoring of light activated nanotube functionalization by diazonium salt during 200 min. illumination with 20 mW laser power, 38 nM/g diazonium salt concentration.* ***(a)*** *Raman spectra in the region of the D and G modes excited at 785 nm, illumination time increases from the bottom (black) to the top (red). The inset indicated the intensity (integrated area) on the G band as function of time.* ***(b)*** *The doping induced shift on the G mode [$G_{prist.}$-$G_{func.}$] and* ***(c)*** *intensity ratio between D and G modes plotted over illumination time. I_D/I_G reflects the defect concentration.*

All previously reported approaches of diazonium salt functionalization were based on the bulk functionalization of the previously chirality enriched materials [166–168]. Here the functionalization degree is controlled by adjusting the concentrations of nanotubes and molecules in numerous batches. It doesn't provide a precise control over the reaction kinetics and the vibrational and photonic properties are investigated in a post treatment analysis. As long as I am interested in controlling the electron-phonon coupling, a new approach is required. I pursue in-situ approach, where vibrational properties are monitored during the reaction process [7]. Several problems arise in setting up such an experiment; (i) the confinement of resonant light and capturing of the scattering light, as well as (ii) the nanotube localization under the illumination spot and (iii) in what degree unresonant nanotubes are affected by the functionalization. The most intuitive solution is placing the nanotube on a substrate, covering it with a solution filled with functional molecules and illuminating the tubes in a Raman setup, see Figure 4.11 The incident light will both drive a functionalization and the inelastic scattered fraction of it will be spectroscopically analyzed

[7] Functionalization with DzBr was performed together with Thomas Rosenkranz

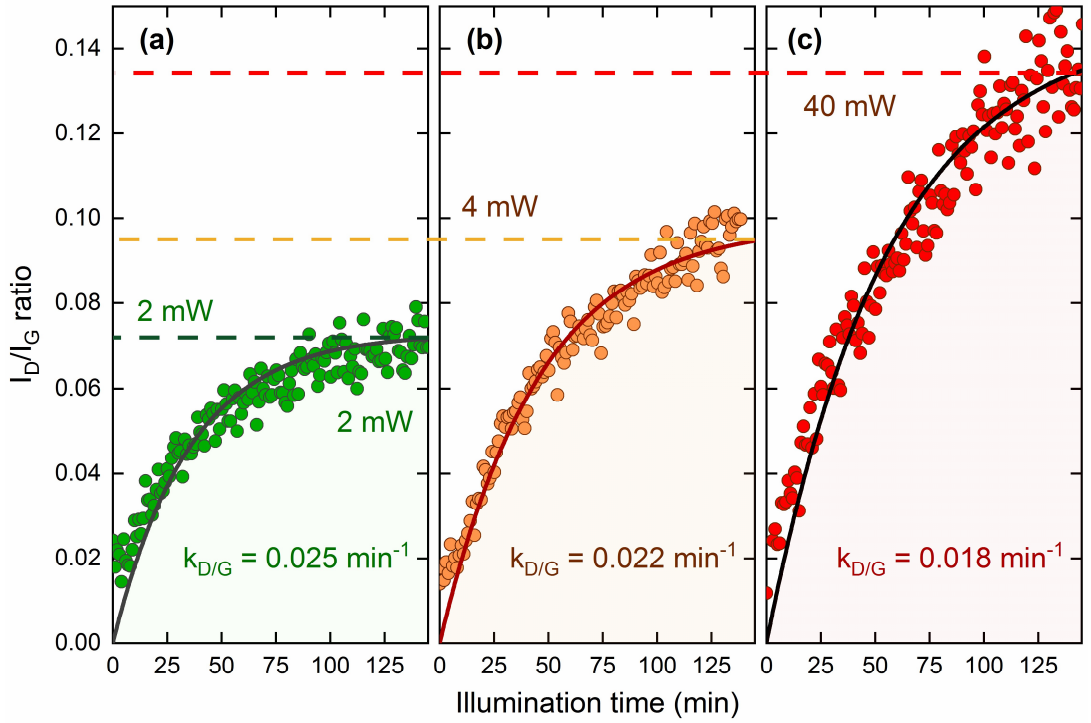

Figure 4.13 *Intensity ratio between D and G modes as function of reaction time for three different laser powers 2 mW, 4 mW, and 40 mW in* ***(a)-(c)*** *respectively (785 nm excitation). Vertical dashed lines correspond to an averaged maximum of the D/G intensity ratios after 130 min. Symbols are experimental data, and solid lines are fits by Eq. (4.1). The fit parameters are listed in Table 4.4. Diazonium concentration is 38 nM/g.*

to monitor the effects on the phonon of interest. An additional problem occurs here as the number of reactive centers reduces in the nanotubes attached to the substrate. As I will later show this does not prevent the functionalization to proceed.

In order to control the electron-phonon coupling induced by the functionalization, the following experiment is realized. A solution of HiPCO nanotubes with diameters 0.8 – 1.2 nm is drop casted on a silicon substrate. I select (9,8) nanotube species as a functionalization target. It is important to notice, that it can be any arbitrary *(n,m)* species. The E_{22} energy lies at 1.7 eV, therefore, the 785nm (1.72 eV) excitation is used. Figure 4.12a shows Raman spectra of the D and G modes acquired in-situ during the functionalization. The D mode intensity reflects the number of carbon-carbon bonds changing their hybridization due to the attachment of the diazonium salt. The intensity of the D mode increases during the functionalization. The intensity ratio between the D and G modes directly reflects the concentration of defects. Figure 4.12c shows this ratio plotted over the reaction time. The reaction kinetics follows standard differential law, with defect concentration $\sim \frac{I_D}{I_G}(t)$ depending on time t as:

$$\frac{I_D}{I_G}(t) = \frac{I_D}{I_{G\,\infty}}\left(1 - e^{-k_D t}\right), \tag{4.1}$$

where $\frac{I_D}{I_{G\infty}}$ reflects the defects density at infinite reaction time. The experimental data are fitted by Eq. (4.1) and the fit is shown in Figure 4.12c by the solid line. The reaction rate is k = 0.02 min^{-1} and the maximum reachable ratio between D and G mode $\frac{I_D}{I_{G\infty}} = 0.12$ for the 20 mW laser power are extracted from the fit.

Along with the increase of the D mode, the G mode intensity decreases. This can be seen in the inset of Figure 4.12a and is attributed to the doping. The doping of the nanotube is confirmed by the changes in the G mode; an upshift of the position, an increase of the width, and a decrease of its intensity. Such alterations in the Raman spectrum are typical for doping in semiconducting nanotubes [125]. The FWHM of the G mode increases from 8.9 to 9.6 cm^{-1}. The G mode intensity is shown in Figure 4.12b as a function of reaction time, it decreases almost by 50 % in 200 min. The displacement of the G mode directly indicates that the desired effect of electron-phonon coupling is achieved. The kinetics of the G mode shift can be described by a similar equation as Eq. (4.1):

$$\Delta_G(t) = \Delta_{G\infty}\left(1 - e^{-k_G t}\right), \tag{4.2}$$

The fit through the experimental points by Eq. (4.2) is shown by the solid line in Figure 4.12c. The trends between the G shift and the D/G intensity ratios are slightly different due to the non-linear G mode shift with doping. The D/G ratio however is directly proportional to the concentration of defects. Each induced defect corresponds to a bond formation between the molecule and the nanotube. Therefore, the rate of defects formation in Figure 4.12c corresponds to a reaction rate. The phonon can be tuned through electron-phonon coupling by controlling the reaction time, see Figure 4.12c. Next, I explore the influence of the photon density on the reaction to enable an additional control pathway over electron phonon coupling through laser power.

4.3.2. Influence of the photon density

The defect induction kinetics are investigated for three additional laser powers; 2 mW, 4 mW, 40 mW, shown in Figure 4.13a-c. The defect concentration achieved during 130 min illumination increases with laser power, see horizontal dashed lines. Interestingly, not only the maximum changes but the reaction rate. While by 2 mW laser power the curve already saturates in 130 min, by 40 mW laser power further increase is expected. This effect is expressed quantitatively in different reaction rates, evaluated by fitting the experimental data by Eq. (4.1). The corresponding fits are plotted in Figure 4.13 by the solid lines. The reaction rates drop with laser power from 0.025 min^{-1} to 0.018 min^{-1}, with 2 mW and 40 mW laser power respectively. The complete list of reaction rates can be found in Table 4.4. The laser densities are given along with power densities aimed at researchers repeating this experiment in different conditions. This demonstrates nicely, that not only the final product is optically controlled, but also the kinetics.

Table 4.4 *Power dependence of the reaction kinetics between the diazonium salt and the nanotube*

Laser power (mW)	Power density (W/mm^{-2})	k_D (min^{-1})	$\frac{I_D}{I_{G\infty}}$	D position (cm^{-1})	G FWHM (cm^{-1})
2	8	0.025	0.07	1288.8	8.6
4.	16	0.022	0.10	1289.5	8.7
20	79	0.020	0.12	1291.5	9.3
40.	158	0.018	0.15	1291.7	9.4

The increase of defect density with laser power after 130 min illumination is observed in Figure 4.13. However, by further illumination higher densities can be achieved. In Eq. (4.1) the highest reachable density corresponds to the $\frac{I_D}{I_{G\infty}}$ parameter. These parameters are listed in Table 4.4 for four investigated laser powers. In order to correlate the changes in the defect concentration along with the reaction rate, they are plotted over the laser power in Figure 4.14b and c. A logarithmic scale is used for the laser power. The D/G ratio increases with laser power, whereas the reaction rate decreases. When a rapid functionalization is desired, the highest available laser power can be used, but the reaction should be stopped after the required amount of defect is produced. In a different case, where an accurate amount of defects is needed, a moderate laser power (adjusted

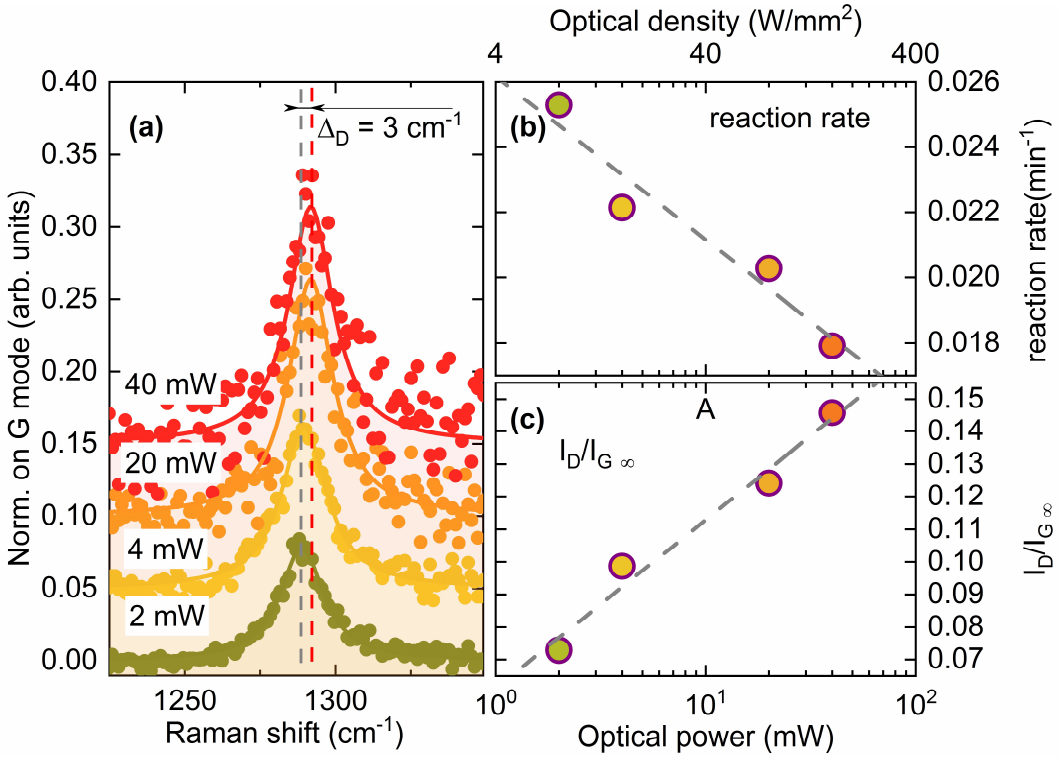

Figure 4.14 *Reaction tuning via photon density.* ***(a)*** *D mode after 130 min illumination normalized on the intensity of the G mode. With such normalization the intensity of the D mode reflects the defect density (excited at 785nm, C_{Dz}=38 nM/g). The vertical dashed lines mark the positions of the mode, with highest and lowest excitation power.* ***(b)*** *The reaction rate* $\boldsymbol{k_D}$ *and* ***(c)*** $\frac{I_D}{I_{G\infty}}$ *plotted over logarithmically scaled laser power. The parameters are listed in Table 4.4.*

to the defect concentration) should be used with an illumination time more than three hours. The appropriate photon densities can be extrapolated or interpolated from Figure 4.14c. The linear fit of the logarithmic plot in Figure 4.14b and c indicates a saturation-like behavior of the reaction rate and the defect density, where further increase of the laser power yields minor effects.

Further, I investigate in detail the phonons-electron interactions. The D mode, normalized on the amplitude of the G mode is shown in Figure 4.14a. The higher the power density, the larger the upshift of the D mode. Between 2 mW and 40 mW laser powers difference of 3 cm^{-1} is observed, see Figure 4.14a. This behavior reflects the electron-D mode coupling. The charge carriers are induced into the nanotube through the DzBr salt. The positions of the D mode for each laser power

are summarized in Table 4.4. In similar fashion the G mode is tuned by the laser power via the coupling between the electron and the phonon. A larger shift is observed for higher laser powers, see Table 4.4. A positive direction of the shift unambiguously identifies a hole doping of the nanotube [141]. It should be noted that hole doping enables more efficient electron-D phonon coupling compared to the doping with electrons.

This type of functionalization is supposed to occur much faster when assisted by resonant light [28]. The reported result cannot be simply extrapolated to our case as their experiment was performed on individual nanotubes, whereas we have substrate supported CNT bundles. In order to study the chiral selectivity, I induce a stronger functionalization. The LAF is repeated with doubled concentration of diazonium salt (70 nM/g), see details in *Appendix B*. The higher concentration is used to achieve a higher defect density. After the reaction (~2 hours illumination time) the D/G ratio is mapped across the illumination area, see Figure 4.15a. The resolution of the mapping is higher than the spot size used to drive the functionalization, 1 µm compared to 2 µm respectively. The defect density is the highest in the functionalization center and decreases away from it towards

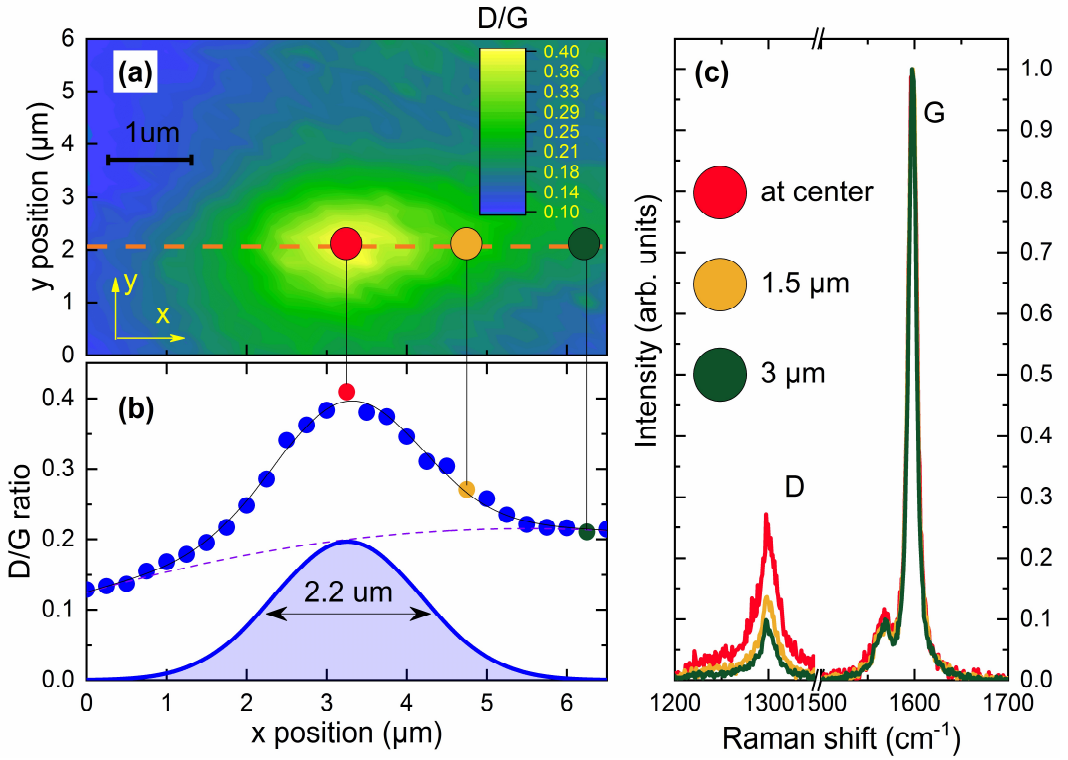

Figure 4.15 *Functionalization control with the laser beam profile (E_f, = E_L = 1.58 eV).* ***(a)*** *The ratio between the D and G modes mapped over lateral x and y positions across the spot, where the functionalization was performed. The D/G intensity ratio increases from blue (low) to yellow (high). The horizontal dashed line indicates, where* ***(b)*** *D/G ratio is plotted over x position. The symbols represent experimental data and the line represents a fit with a Gaussian profile (filled peak) and cubic background (dashed line). The background reflects functionalization anisotropy in dark areas, whereas the Gaussian form is due to the Gaussian beam profile. The width of the profile converges with the width of the focused laser beam (~2 µm).* ***(c)*** *Raman spectra including the D and G modes at different distance from the functionalization center, from the middle (red) to side (green). The distance between the center and the spot is given in the Figure, also see positions with the same colors in* ***(a)*** *and* ***(b)****. Laser power during the mapping is 200µW, and acquisition time is 10s.*

not illuminated areas. The center is defined by the position, where the light was focused. In the center the D/G intensity ratio is at 0.4 and three μm away from the center varies between 0.1-0.14. Individual Raman spectra corresponding to different distances from the center are shown in Figure 4.15c. The colors correspond to the dots, where these spectra were acquired in Figure 4.15a and b. A small increase of the D/G ratio in the non illuminated areas (from 0.05 to 0.1) is due to the white light illuminating the sample during the positioning of the activation beam. Some leftovers may not entirely rinsed and remain in the areas not illuminated during the LAF.

To activate the reaction a Gaussian laser beam profile was used. The photon density is expected to vary within the illumination spot. In order to investigate the influence of photon density gradient, a single line in x direction from the two-dimensional defect map is plotted in Figure 4.15b. Symbols represent experimental data points and the line represents a fit with Gaussian function. The background below the Gaussian peak corresponds to the defect in the dark areas. The fit excellently reproduces the experimental data. The FWHM of the fitted peak converges with the FWHM of the illumination beam, 2.2 μm compared to 2 μm. This demonstrates quite well how the functionalization degree is controlled in μm scale by the beam profile. The lateral resolution can be further increased and pushed in the nm scale by using resonant light with higher energy. For this, the photon frequency should be adjusted to higher optical transitions of the nanotube (E_{33}, E_{44}, etc.). The diffraction limit at these transitions t of light is noticeably larger (e.g. 150 nm for 4 eV).

As I have successfully demonstrated, that the cover density is patterned by the beam profile. The same pattern should have the CNT phonons, tuned through the interaction with the DzBr molecular orbitals. The positions of the G and D modes vary by 0.5 and 1.5 cm^{-1} between the dark and bright areas respectively. The dopant influences not only the phonon energy, but also its lifetime. This is best observed in the FWHM of the D mode, increasing from 14 cm^{-1} in the dark area to 21 cm^{-1} in the functionalization center. This indicates the ability to engineer light controlled junctions with patterned Fermi-levels, phonons, and PL profiles in individual tubes and films. An additional PL peak corresponding to sp^3 hybridized carbon occurs at a certain defect density. Sophisticated patterns and arbitrary textures can be achieved by applying non-Gaussian beam intensity profiles [169].

4.3.3. Chiral selectivity of the reaction

All the above Raman investigations were conducted at the same laser frequency, as used for the activation of the reaction. I further investigate the degree in which other non-resonant nanotubes are affected during the functionalization. First, I compare the defect density between the nanotubes of different diameters. The reaction was activated 1.7 eV energy (*Ef*), therefore stronger effects are expected for the nanotubes resonant with this energy. The larger is the detuning between the activation energy and the nanotube transition energy (E_{ii} - E_f), the less efficient nanotubes are

Table 4.5 *The properties of the RBM phonons before and after the DzBr functionalization*

(n,m)	position pristine (cm^{-1}).	position func. (cm^{-1}).	FWHM prist. (cm^{-1}).	FWHM func. (cm^{-1}).
(8,6)	247.6	247.3	6.8	5.4
(8,7)	232.5	232.7	6.2	4.8
(9,7)	219.5	220.0	7.1	5.0

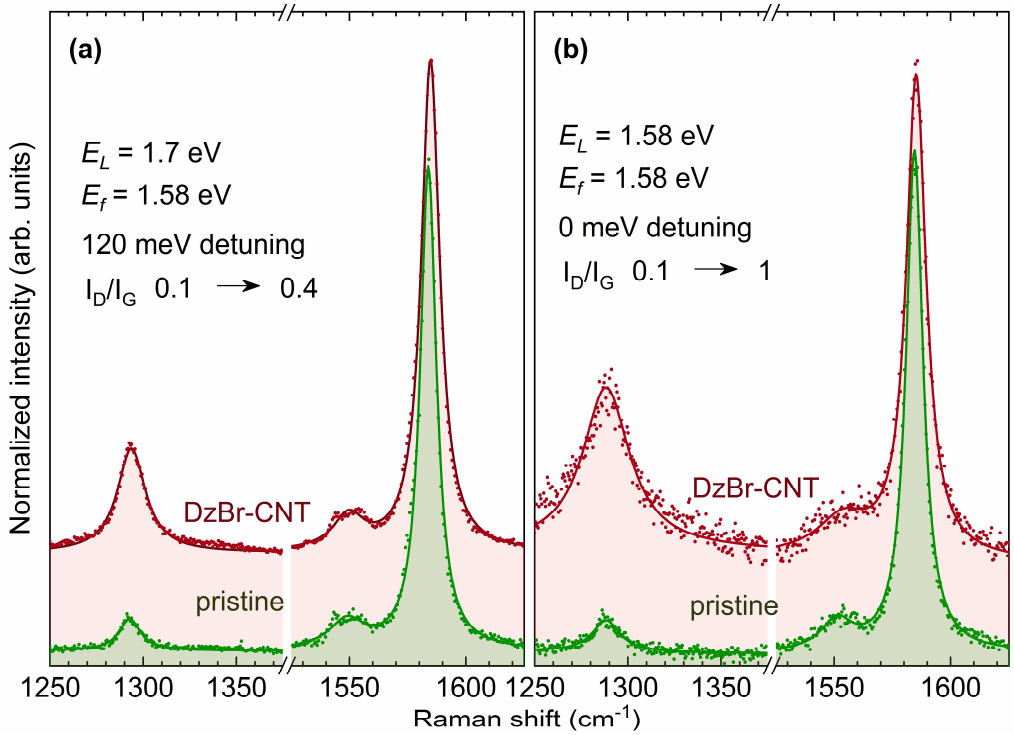

Figure 4.16 *Evolution of the D and G mode due to the functionalization for different detuning energies, difference between the activation energy and nanotube transition energy (here laser energy) (E_{ii}-E_f). Green color stands for pristine material and red for functionalized material in the functionalization center.* ***(a)*** *Raman spectra excited at 1.7 eV (120 meV detuning). In the functionalization center (green) and before the functionalization (blue).* ***(b)*** *same as* ***(a)*** *for 785 nm excitation (0 meV detuning).*

functionalized. Figure 4.16 compares the D and G modes excited at E_{ii} =1.7 and 1.58 eV. In the pristine material I_D/I_G is 0.1, in the nanotubes with 0 meV detuning it increases to 1, whereas in the nanotubes detuned by 120 meV the ratio increases only up to 0.4. Such behavior confirms the reaction selectivity toward the resonant species. However the analysis of the D and G phonon modes does not allow investigation of functinalization effects down to a single chirality level. The resonant windows are 0.16 and 0.2 eV for D and G and contain the accumulated signals from all the chiralities with transition energies in this range. To obtain a quantitave measure of the functionalization degree in each nanotube chirality I turn to the analysis of the RBMs.

The D and G modes comprise the signals from several nanotubes in resonance with the laser. To investigate the chiral selectivity of the reaction in detail, I study the RBMs. Figure 4.17 compares the normalized Raman spectra in the RBM region before and after the functionalization for three different wavelengths. Three nanotube species (9,7), (8,7), and (8,6) are identified. In these nanotubes the functionalization causes a slight shift of the RBM to lower frequencies. This effect can be due to the defects distorting the nanotube lattice. As shown in Figure 4.16, the concentration of defects increases for all chiralities. Interestingly the relative ratio between (8,7) and (8,6) RBMs

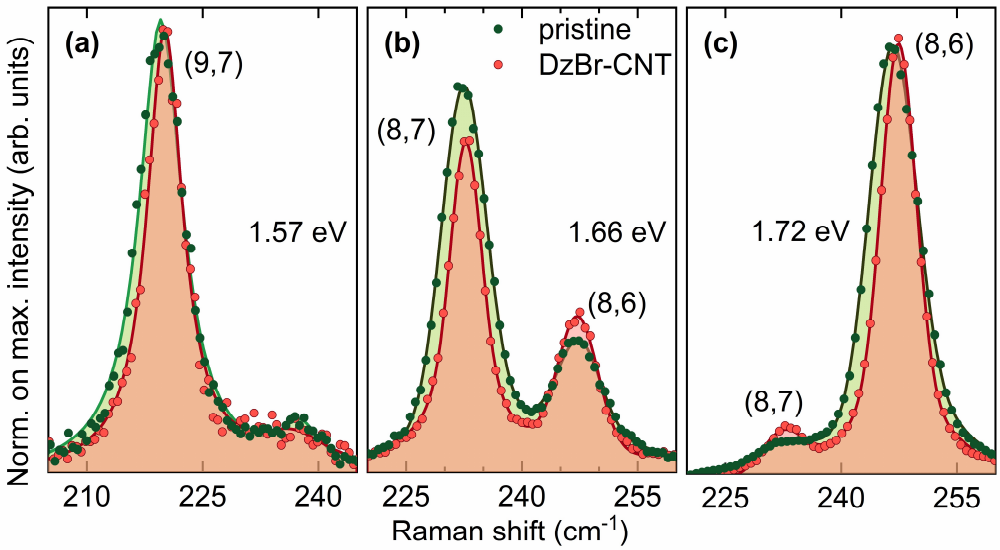

Figure 4.17 *Radial breathing modes before (green) and after (red) functionalization excited at three different wavelengths* ***(a)*** *1.57 eV,* ***(b)*** *1.66 eV, and* ***(c)*** *1.72 eV. Symbols represent experimental points and lines the fits with Lorentzian profiles.*

changes in Figure 4.17b. This can be attributed to the nanotube transition energies changing at different degrees. I further apply resonant Raman spectroscopy to analyze the transition energies of individual nanotube chiralities. Figure 4.18a-c shows Raman profiles before and after the functionalization. The (9,7) has the lowest detuning and (8,6) has the highest detuning from activation light energy. Experimental data are fitted by Eq.(2.26), see full lines in Figure 4.18. The

Table 4.6 *Bright exciton parameters at second excitonic transition for pristine (prist.) and functionalized (func.) nanotubes acquired by fitting resonance Raman profiles in Figure 4.18a-c, detuning is* E_{22}-E_f *and* E_{22} *shift* = $E_{22}^{func.} - E_{22}^{prist.}$

(n,m)	Family type	detuning (meV)	$E_{22}^{prit.}$ (eV)	$E_{22}^{func.}$ (eV)	E_{22} shift (meV)	$\Gamma/2^{prist.}$ (meV)	$\Gamma/2^{func.}$ (meV)
(8,6)	SII	84	1.65	1.66	4.48	17	37
(8,7)	SI	-22	1.55	1.54	-10.49	32	28
(9,7)	SII	136	1.71	1.70	-1.12	31	39

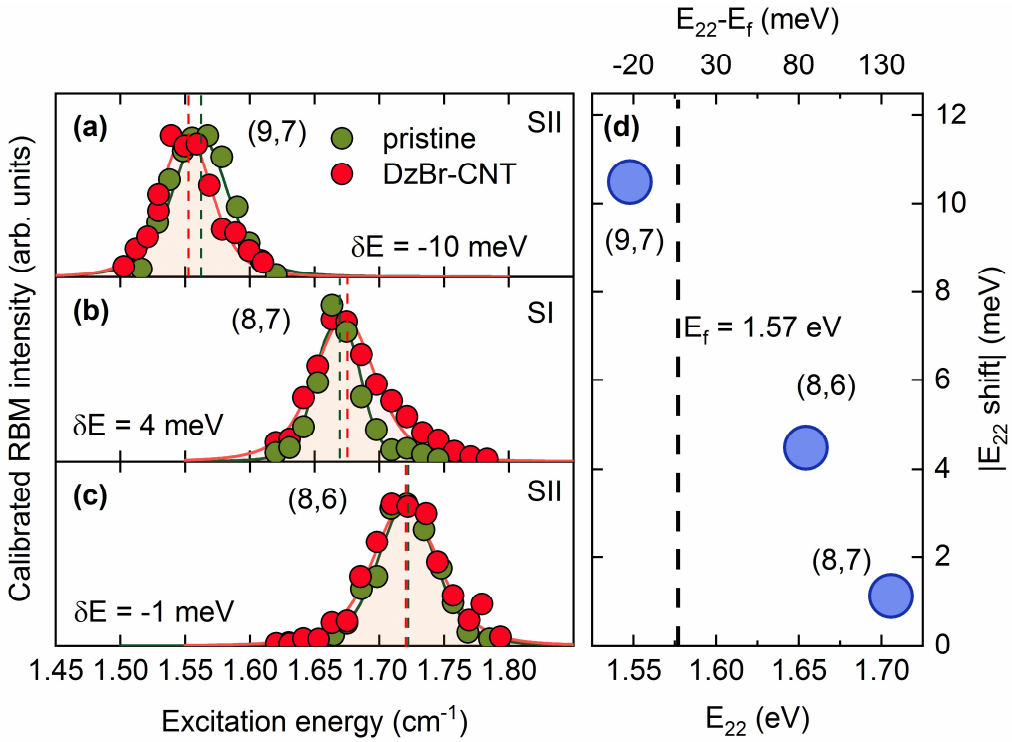

Figure 4.18 *Radial breathing mode intensities as function of excitation energy* ***(a), (b), (c)*** *for (9,7), (8,7), and (8,6) nanotubes, respectively. The symbols represent the experimental data before (green) and after (red) functionalization. Symbols represent experimental data and lines are the fits with Eq.(2.26). Vertical dashed lines mark the intensity maxima of the RBM at* $E_{22}+E_{RBM}/2$. ***(d)*** *Absolute shift of the transition energy due to the functionalization plotted over* E_{22} ***(bottom)*** *and detuning* $[E_{22}-E_f]$ ***(top)***. *The vertical dashed line indicates the laser energy* (E_f) *used to drive the functionalization.*

positions of the transition energies are established during the fitting process. The shift of the transition energy is -10 meV for the (9,7) nanotube, whereas the transition energy of (8,6) nanotube is almost constant, where 1 meV shift attributed to the measurement inaccuracy. The transition energies are listed in Table 4.6. I attribute the shift of the transition energy to the lattice strain mechanism. The different directions of the E_{22} shifts for (9,7) and (8,7) nanotubes, belonging to the SI and SII types, suggests that this mechanism is dominant. The alternative screening induced mechanism would cause the shift in the same direction, see the discussion in the theoretical Section 4.1.2. A study of the first transition energy displacement in functionalized (9,7) CNT would clearly separate these mechanisms.

The transition energy of the nanotube starts to shift when a high degree of functionalization is achieved. The (8,6) nanotube is functionalized, which is confirmed by the ratio between the D and the G modes in Figure 4.16a. However only a very small shift of the transition energy is observed. Therefore I conclude, that only by I_D/I_G being larger than 0.5, a transition energy shift is expected. The amount of shift is proportional to the DzBr cover density on the nanotube wall. An observation of changes in transition energies is more useful than a D/G ratio, as it can be used to establish the individual functionlization degree for each nanotube chirality.

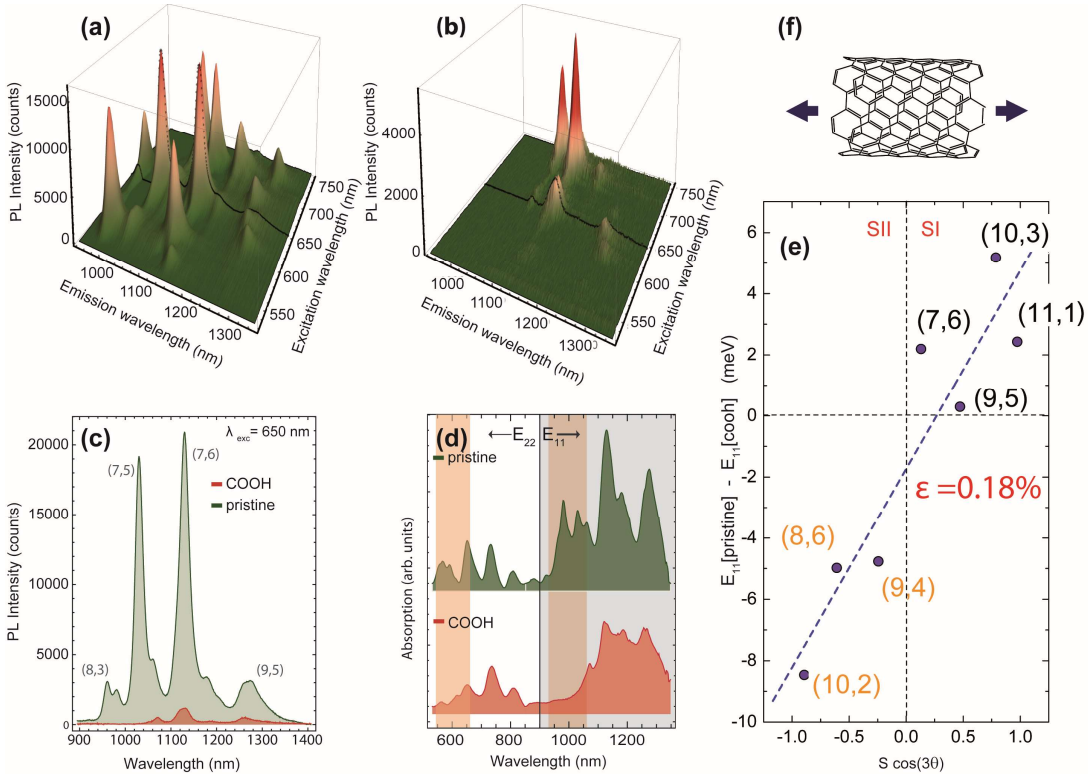

Figure 4.19 *PLE maps of* ***(a)*** *pristine and* ***(b)*** *functionalized sample. The overall emission intensity of the functionalized tubes is quenched.* ***(c)*** *Single excitation line at 1.9 eV, E_{11} transition energies are redshifted by up to 8 meV due to the functionalization. Emission from small diameter tubes is not observed.* ***(d)*** *Absorption peaks from pristine (top panel) and functionalized (bottom panel) nanotubes. The peaks correspond to the E_{11} and E_{22} transition energies from tubes with diameters between 6.0 and 11.5 Å.* ***(d)*** *Shifts in the E_{11} transition energy (pristine minus COOH) plotted against structural parameter S cos(3θ).* ***(f)*** *Direction of the strain induced by the –COOH functional groups.*

4.4. Carboxylation, strain and doping disentanglement [8]

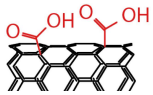

Previously described methods of chemical functionalization cycloaddition and light activated diazonium salt reaction have only recently been developed. Despite many advantages, the effects they provide are relatively weak and make it difficult to distinguish between strain and doping effects. The standard reactions should be able to tune the phonons and excitons. I demonstrate that by treating the nanotubes with the acid. The carboxylation reaction is selected as a well-known procedure of covalent functionalization, providing strong effects [170]. It can provide diameter-dependent selectivity towards the metallic or semiconducting species [171,172]. In this section I show how to estimate the Fermi energy by analysis of Raman spectra.

To investigate the changes in Fermi level, the transport measurements can be performed [173,174] or the optical response such as reflectivity can be analyzed [175]. The transport measurements are precise and reliable, but require a sophisticated system and the instrumental response of many

[8] The contents of this Section are published in "Gordeev, G et. al. *Phys. Status Solidi Basic Res.* **253,** (2016)". The coauthors agree on using the data in this work.

devices. The reflectivity analysis, on the other hand, provides only information about a chirality averaged Fermi energy shift, similar to the XPS analysis presented in Section 4.2.1. As chemical attachment of the functional groups in some cases is diameter selective [176], the investigation of various nanotube species is required.

Optical methods such as photoluminescence excitation (PLE) and Raman spectroscopy provide information about various nanotubes families depending on the excitation wavelength. In our study, we investigate the scattered and reemitted light from the tubes before and after functionalization, obtaining information about the number of defects and shifts of the Fermi energy due to the chemical treatment. Using different laser excitation wavelengths, we access nanotubes of different diameters and separately excite metallic and semiconducting types. The PLE, absorption, and RBM analysis estimate critical diameter of semiconducting nanotubes, surviving the functionalization.

4.5.1 Structural effects in the nanotubes, evaluation of strain

Semiconducting SWNTs have a band-gap between conduction and valence bands and can thus emit light. Usually the nanotubes are excited by the E_{22} and emit by the E_{11} transition energies

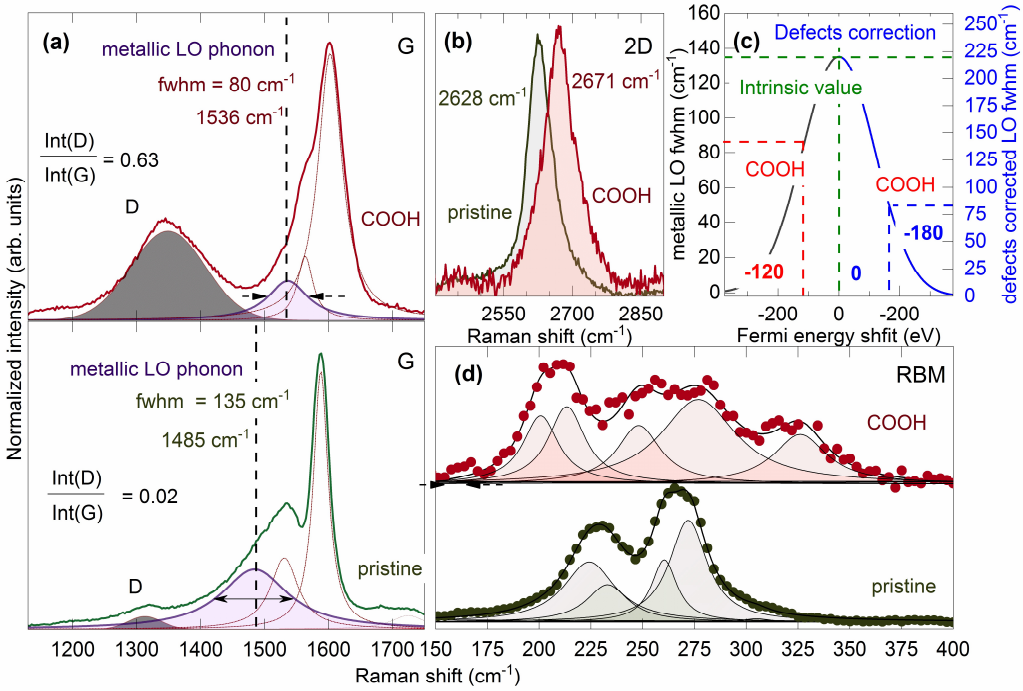

Figure 4.20 *Raman spectra excited at 2.33 eV.* ***(a)*** *G bands of pristine and carboxylated tubes are compared. The metallic LO band narrows after treatment (highlighted in light violet) and the intensity of the D band significantly increases (highlighted in dark grey).* ***(b)*** *The frequency of the 2D mode shifts to higher energies.* ***(c)*** *The dependence of the metallic LO linewidth on the Fermi level* [122]. ***(d)*** *The RBMs change due to the chemical functionalization.*

[177]. As various nanotube species have different transition energies, they can be easily identified on a 2*d* excitation-emission map. Figure 4.19a and b show the 2*d* excitation-emission maps of tubes

Table 4.7 *Fermi energy shifts and fitting parameters for metallic nanotubes at 2.3 eV excitation*

Sample	$\|E_F$ shift$\|$ (eV)	G^- Position (cm^{-1})	G^- FWHM (cm^{-1})	G Area (counts/sec./mW)	D/G	2D Position (cm^{-1})
SWNT	0	1485	135	38300	0.02	2628
SWNT-COOH	-0.65	1536	80	1333	0.63	2671

before and after carboxylation. The emission intensity drops dramatically, the luminescence of some chiralities vanishes. The maps show that nanotubes of larger diameters are more stable towards acid treatment. Figure 4.19c shows a PL excitation line at 1.9 eV (650 nm, line highlighted in black in the excitation-emission maps). The emission bands corresponding to the (7,5) and (8,3) species disappear, whereas the (9,5) and (7,6) bands decrease in intensity and shift by up to 8 meV (10 nm). Shifts of the transition energies of semiconducting nanotubes can result from doping [40] and environmental effects. In case of doping, additional charge carriers can reduce the strength of the Coulomb interactions, leading to a decrease of the quasiparticle band gap.

To investigate whether the lack of signal from some nanotube species indicated the destruction by the functionalization, we performed absorption spectroscopy of the pristine and functionalized samples (Figure 4.19d). Absorption bands from tubes with diameters from 6 to 11.5 Å were observed in our samples [40]. The E_{22} corresponds to the second transition energy and S_{11} to the first transition energy of the semiconducting tubes. In the E_{11} and E_{22} regions we observe that the small diameter bands (short wavelengths) disappear after treatment. This indicates the destruction of the tubes with a diameter below the certain critical transition diameter d_t. To accurately evaluate d_t we analyze the RBMs of nanotubes responsible for 650 nm absorption peak (Figure 4.21c). The peaks at 298 and 284 cm^{-1} originate from species with diameters 7.72 and 8.18 Å and disappear after functionalization. The 262 cm^{-1} peak corresponding to d=8.83 Å remains present, therefore the d_t is estimated as 8.2-8.3 Å [40].

The attachment of a carboxyl group on to the nanotube wall can alter the interatomic distance and thus induce local stress. By the high density of functional groups, the mechanical properties of the nanotube as a whole are considerably changed [178]. The spectral positions of the excitonic peaks are sensitive to the strain in nanotubes. In order to evaluate strain effects due to functionalization we evaluate the amount of the transition energies shifts. The charge carriers of the carboxyl groups attached on the nanotube walls may possibly cause doping related changes in the band structure of CNTs. But even at very high doping levels, achieved by electrolyte gating, no shift of the first excitonic transition was observed [142]. Therefore, we attribute the PLE shifts to the strain effects.

As it was shown in Ref. [179], the uniaxial strain cases inverse shifts in semiconducting nanotubes of different types, depending on the nanotube S mod. By compressing the nanotubes in a polymer matrix in SI nanotubes the E_{11} shift to lower energies and in SII the E_{11} shifts to higher energies [146]. The magnitude of the strain induced transitional energy displacement is proportional to $\cos(3\theta)$, where θ is the chiral angle of the nanotube. Similar results with opposite shifts induced by compressive strain were obtained by a direct stretching of individual suspended nanotubes [180].

Figure 4.19e demonstrates the E_{11} transition energy shift against structural parameter $\cos(3\theta)$ of the remaining species on the PLE map. The opposite displacement of E_{11} for different

Table 4.8 *Fermi energy shifts and fitting parameters for semiconducting nanotubes at 1.94 eV excitation*

Sample	$\|E_F$ shift$\|$ (eV)	G^+ Position (cm^{-1})	G^+ FWHM (cm^{-1})	I_G (counts/sec./mW)	D/G	2D Position (cm^{-1})
SWNT	0	1592.6	16	3400	0.015	2597
SWNT-COOH	-0.5	1600.5	34	1360	0.81	2638

types of nanotubes and chirality dependence indicate, that strain generated by functional groups has a dominating contribution along the nanotube axis. The negative slope of the line points at the negative sign of the strain and corresponds to the compression strain. The scattering of the points can be related to a different coverage density of nanotubes or a chirality dependence of the strain due to the functional groups. These mechanisms were not sufficiently studied. By the line slope the average strain for the present on the Figure 4.19e nanotube species is evaluated as - 0.18 % [146,179,180]. This value is used in the next sections to accurately evaluate the Fermi energy shift.

4.5.2 Electron-phonon coupling in metallic COOH-nanotubes

To calculate the change of the Fermi energy we use the width of the LO peak and compare it with the normalized curve from Ref. [122]. The metallic LO FWHM of the pristine sample was found to be 135 cm^{-1}, in agreement with experiments on isolated metallic nanotubes of similar diameters. This number is close to the theoretical value for nanotubes of similar diameters [102] and indicates that before the functionalization the Fermi energy was close to the charge neutrality point (crossing of valence and conductance bands). The FWHM distribution is shown in Figure 4.20c. A Fermi energy shift of 0.23 eV between functionalized and pristine (FWHM = 80 cm^{-1}) samples was obtained.

The behavior of the 2D mode can be used to distinguish between p- and n-doping. In the electrochemical experiments, the 2D mode shifts to higher frequencies under hole doping. Electron doping, induces a downshift of smaller magnitude [164]. Figure 4.20b shows the 2D mode of our samples. After functionalization, a shift of 43 cm^{-1} to higher frequencies was observed (Table 4.7). The upshift of the 2D indicates hole doping of SWNTs [164], thus a negative sign of the Fermi energy was obtained.

The overall shift of the Raman modes in functionalized nanotubes is related to the local stress and doping. The stress effects result in negative axial strain in nanotubes, evaluated in the previous Subsection. I assume same amount of strain in the metallic species. The (ε =0.18 %) stretching axial strain causes a shift to higher frequencies of the metallic 2D mode by up to 8 cm^{-1} [147]. Extracting this value from the actual 2D displacement we obtain a shift of 51 cm^{-1} only due to the doping.

The magnitude of the 2D mode displacement due to the doping can be also used to evaluate ΔE_F. The 51 cm^{-1} displacement to higher frequencies corresponds to Fermi energy shift of 0.65 eV. The discrepancy between ΔE_F evaluated through the bandwidth and the 2D frequency change is related to defects. The high defect concentration causes additional broadening of the G peak and weakens the line narrowing due to the doping. The different approaches are discussed in the end of next section. The results for the metallic tubes are summarized in Table 4.7.

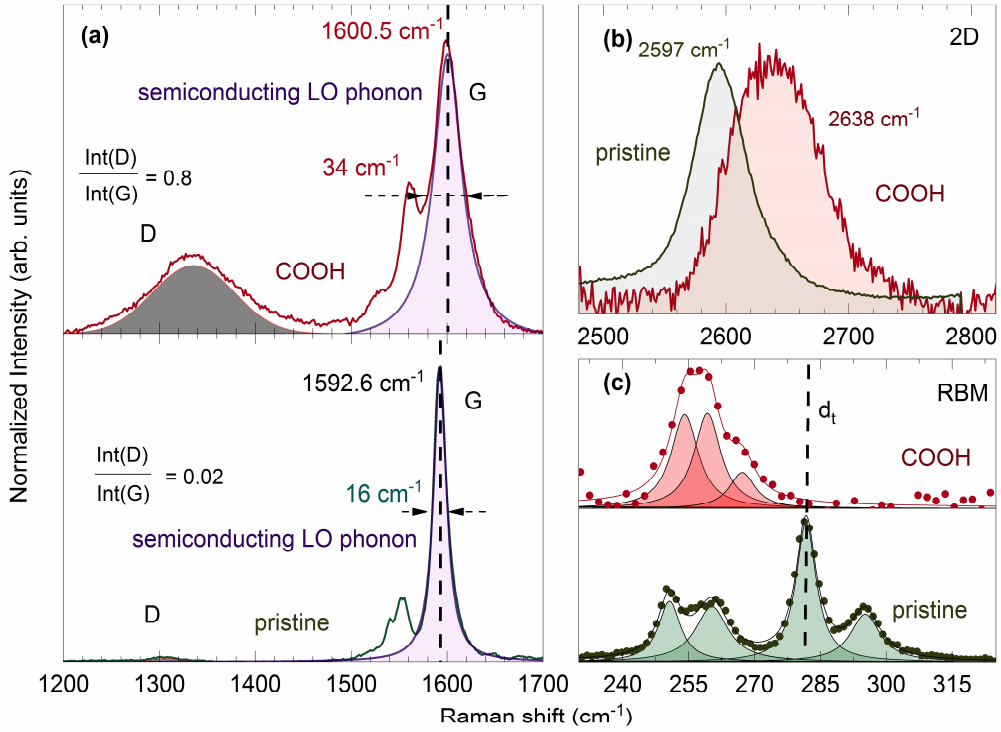

Figure 4.21 *Raman spectra excited at 1.96 eV.* ***(a)*** *G Mode of pristine and functionalized samples, semiconducting LO broadens and shifts after treatment (highlighted in violet) and D Mode intensity highly increases (highlighted dark grey).* ***(b)*** *The frequency of 2D Mode shifts to higher energies* ***(b)*** *and RBMs* ***(c)*** *indicate presence of two nanotubes families of average diameter 8.5 Å and 11 Å.*

4.5.3 Electron-phonon coupling in semiconducting COOH-nanotubes

To investigate the Fermi energy shift in semiconducting nanotubes Raman spectra at E_{las} = 1.94 eV were acquired. Figure 4.21a shows the G and D modes of pristine and acid treated SWNTs. The Raman spectra resemble previously reported ones [181]. At this excitation energy the G mode exhibits a clear semiconducting character with two narrow lines labelled as G^- (TO) and G^+ (LO). We observed an increase of the D/G intensity ratio from 0.018 to 0.81. The fitting parameters for semiconducting tubes are summarized in Table 4.8.

The Raman spectra of semiconducting nanotubes transform differently from metallic upon doping [140]. Noticeable changes appear only by Fermi energy shifts higher than 0.3 eV. The n-doping and p-doping lead to an increase of the G mode frequency and broadening of the line. After functionalization, the G^+ phonon softens and upshifts by 8 cm^{-1}. Assuming that doping and strain have linear contribution in phonon frequencies, we calculate the 3.5 cm^{-1} downshift of the G^+ due to the strain ($\varepsilon = 0.18$ %) [147] and obtain 11.5 cm^{-1} due to doping. Using the shift and considering that our initial sample is undoped we obtain a Fermi energy shift of - 0.4 eV. Similar as for metallic tubes the upshift of the D mode from 1310 to 1336 cm^{-1} indicates a negative sign of the Fermi energy shift.

The FWHM of the G^+ changes from 16 to 34 cm^{-1}. By electrical gate doping FWHM increased from 15 cm^{-1} and reached a maximum of 24 cm^{-1} at -4 eV gate voltage without significant

increase at higher voltages [147]. In our experiment the additional broadening is assigned to defects. At such high defect concentration (D_{area}/G_{area} = 0.8) an additional broadening of the G peak up to a factor of two is expected [182]. The overall linewidth of the G peak can be roughly expressed as

$$G_{FWHM} = \gamma_{int}+\Delta_{doping}+\Delta_{defects}, \quad (4.3)$$

where γ is the internal linewidth (16 cm^{-1}), Δ_{doping} is the broadening due to the doping (+ 8 cm^{-1}) and $\Delta_{defects}$ is the broadening due to the defects. Using values for doped semiconducting nanotubes at -5 eV $\Delta_{defects}$ = 10 cm^{-1} is obtained. In case of semiconducting LO the doping and defects interact positively, overestimating the pure doping effect.

By contributing in the metallic LO linewidth, the defects and doping interact negatively resulting in an underestimation of the doping effect. Assuming similar behavior for metallic tubes due to the defects as for semiconducting tubes, we increased the intrinsic value of the metallic LO FWHM by 160 %. The bandwidth of the functionalized sample then corresponds to -0.35 eV (Figure 4.21c) and is in better agreement with ΔE_F calculated with the 2D shift. Nevertheless, the discrepancy in the results indicates that the interplay of the described broadening mechanisms requires further investigation. The ΔE_F = -0.65 eV and -0.5 eV, as obtained from the phonon frequency change of the 2D and G modes for metallic and semiconducting nanotubes accordingly is in our case more accurate than obtained directly from the phonon linewidth, while neglecting defect consideration. By evaluating the Fermi energy by the low defects concentration it is simpler to obtain values from bandwidth, as the phonon frequencies may be affected by local stress and an investigation of the transition energy shifts is necessary.

4.5.4 Conclusion

After functionalization we observe structural changes in the tubes. Emission and absorption bands as well as RBM peaks for small diameter nanotubes disappear. Nanotubes with diameters less than 8.2 Å get destroyed by the functionalization process. The D_{area}/G_{area} ratio increased up to 45 times. Displacement of the first transition energy indicated extensive uniaxial strain of the semiconducting nanotubes ε = 0.18 %.

We investigated the functionalization effects on electronic properties by Raman spectroscopy. Excitation with different laser wavelengths allowed to access separately metallic and semiconducting tubes. We evaluated the shift of the Fermi energy of functionalized tubes using the FWHM and the positons of the G and 2D peaks, corrected by the strain induced shifts. The ΔE_F was determined as -0.65 eV and -0.5 eV for metallic and semiconducting tubes. The large 2D and D displacement to higher frequency confirmed the p-type doping. The functional groups induce both negative Fermi energy shift (p-doping) and defects of the material due to the covalent functionalization process. At such high density of defects not only doping determines the total linewidth of the G mode but the finite lifetime due to defects as well.

Table 4.9 *Summary over the functionalization methods studied in this work*

Functional. group	Doping type	strain	G metallic	2D metallic	G semiconducting	2D semiconducting
-triazine	n-type	no	yes	yes	no	no
-DzBr	p-type	yes	-	-	yes	yes
-COOH	p-type	yes	yes	yes	yes	yes

4.5. Summary over studied functionalization methods

To introduce the changes in the semiconducting phonons one can apply different functionalization approaches, modifying the nanotube through defect-like covalent bond. In this work the functionalization by diazonium salt and carboxyl group successfully change the frequencies of the G and 2D phonons in semiconducting nanotubes. The maximally achieved shift is 12 and 41 cm^{-1} in the G and 2D phonons, respectively. However, the frequency of the 2D mode can be pushed even stronger; if the strain and doping effects induced by the molecule would shift the phonon is the same direction. In both cases the extensive strain induces a downshift, whereas the doping induces an upshift of the phonon. A molecule inducing an n-type doping is required. The triazine molecules provide a p-type of doping. However, the low magnitude of the doping does not allow the electron-phonon coupling effects to occur in semiconducting phonons, see Table 4.9. The metallic phonons on the other hand are successfully tuned by the cycloaddition reaction. The energy of the metallic G and 2D phonons by 12 cm^{-1}, with LO phonon width change by more than 50 %.

5 | Summary and outlook

The aim of this work was to study the fundamental Raman scattering mechanisms and the low-dimensional coupling between different types of energy quanta in single walled carbon nanotubes. The unique set of interactions is mediated by the exciton, governing the CNT‘s optical properties. In Chapter 2 I explore these effects, related to the strong coupling occurring between the exciton and phonon. This coupling enables phonon mediated higher-order scattering pathways between the bright and dark excitonic states, thus altering resonance Raman profiles of zone center phonons. The structural and transition energy dependence of the exciton-phonon coupling is deduced by analyzing the Stokes and anti-Stokes resonance profiles.

Anti-Stokes Raman scattering. The Stokes profiles reported in the literature do not allow the unambiguous determination of the exciton-phonon matrix elements [23,69]. In order to obtain structural dependence of the exciton-phonon coupling I record the Stokes and anti-Stokes resonance profiles at the second excitonic transition. The resonance Raman profiles of the high-energy LO modes are asymmetric, with incoming resonance dominating in the Stokes and outgoing dominating in the anti-Stokes scattering. I observed this behavior in four different semiconducting nanotube species (8,3), (7,5), (6,4) and (6,5). The resonant factors, including the asymmetry of the resonance Raman profiles, for a future evaluation of Stokes/anti-Stokes ratio are developed and presented in this work. The quantum interference theory including the third- and fifth-order scattering processes fits well with my experimental result. By a simultaneous fitting of the Stokes and anti-Stokes cross sections, I obtained exciton-phonon matrix elements for various carbon nanotubes in agreement with tight binding calculations.

The fifth-order scattering process requires a deeper theoretical investigation in the future. The scattering to the dark excitonic state is simplified to a single point in the current version of the theory. The selection rules allow the bright exciton to scatter into multiple excitonic states with lower energy. Possible interferences may occur between these channels. Additionally the integration over all allowed wave vectors of the CNT is required. The exciton-phonon matrix elements variation over the BZ can be accounted for by following the notes in Section 2.3.6 . Even more scattering pathways can be realized when introducing defects into the material. These defects could alter the coupling between the G phonon and dark excitons. Experimental studies reporting the asymmetry of the resonance Raman profile in the CNTs enriched with defects are lacking because high crystalline quality nanotubes have been used so far.

Apart from fundamental interest, a few applications of LO mode Raman resonances are envisaged. The outgoing resonances of Stokes and anti-Stokes scattering can be exploited for coherent phonon manipulation. The outgoing Stokes resonance (blue detuned from the resonance) can produce coherent phonons. Such phonon emission was reported for atoms trapped in photonic cavities [183]. The idea is supported by the coherent dynamics of the pristine CNT phonons [184]. Another phenomena possibly hosted by carbon nanotubes is phonon cooling. It was reported in the photonic cavities and also in the excitonic crystals [77]. The anti-Stokes should overcome the Stokes process in order for the cooling to occur (red detuned from the resonance). The superior outgoing resonance in the anti-Stokes resonance profile is very important for the sideband cooling. However, a high energy of the G mode is disadvantageous here, as it reduces phonon population.

Resonance G mode profiles at the first excitonic transition. Next, I studied the resonance Raman profiles in several nanotubes when exciting the G mode in resonance with the E_{11} transition.

The resonance profiles of the LO phonon are similar to E_{22}, I reported earlier in Chapter 2. I observe asymmetric profiles of the unequal incoming and outgoing resonances, where the incoming resonance dominated. I found the asymmetry of Raman profile to depend on the nanotubes chirality and transition number. The (6,4) profile is more symmetric and the (8,3) is more asymmetric at the E_{11} transition compared to the E_{22} transition. I attribute the asymmetry to the fifth-order scattering process and find an excellent agreement between the experimental data and a fit of the E_{11} and E_{22} Raman profiles. The change of the asymmetry is due to a competing increase of the bright and dark exciton-phonon coupling elements. Overall, Raman scattering at the E_{11} transition is by a factor of 30 more intense than for the E_{22} transition. This occurs due to the 3-4 times increase in exciton-phonon matrix element M_G^{XP} at the first transition. I observe narrower resonance Raman profiles at the first excitonic transition attributed to the long lifetime of the lowest-energy exciton.

The superior G mode intensity makes the E_{11} excitation region even more attractive for probing CNTs by means of Raman scattering in all kinds of application requiring strong Raman signals. For example in tip enhanced Raman scattering (TERS) the spatial resolution depends among other things on the strength of Raman signal. Previously TERS experiments were performed with laser in resonance with the second and higher transitions [185], whereas in resonance with E_{11} a higher spatial resolution can be expected. Another example, where strong optical signals are required, is the application of nanotubes in biomedicine and in particularly in cell science. Nanotubes easily penetrate cells membranes and may serve as drug delivery capsules. Typically additional functionalization is required to optimize the PL of the drug carriers by attaching dye molecules. No functionalization is required when CNTs are tracked by means of Raman scattering. The G mode of nanotube excited at the first nanotube transition offers even a larger Raman cross section (roughly estimated as 10^{-20} cm^2sr^{-1}) [186] than Raman markers specifically designed for such purposes [187]. The release of the drug can be monitored by the change of RBM frequency, sensitive to its filling. A further advantage of such a use is the energetic position of E_{11} transition of small nanotubes lying inside the transparency region of the tissue (900-1300 nm). The parasitic signals are absent in this region and high laser powers can be applied avoiding the disruption of living cells.

Resonant effects in the 2D mode. Strong light-matter coupling impose a regulation for energy-momentum exchange mechanism between photons and exciton scattered into the dark state, which I reported in Chapter 3. This induces a dispersion of the 2D mode (formed by two K point phonons) with excitation energy mirroring the dispersion of the exciton-polariton. I experimentally established the excitation energy dependence of the position and intensity of the 2D mode in carbon nanotubes. The five chiralities investigated at second excitonic transition demonstrated a uniform behavior with three dispersion regions. The resonant Raman profiles exhibit incoming and outgoing Raman resonances, near E_{22} and $E_{22}+E_{2D}$ respectively. The outgoing resonance is always dominating and provides up to four times stronger intensity. The position of the 2D mode shifts with the excitation energy and its dispersion has three different regions. Below the incoming and above the outgoing resonance, the 2D mode energy increases with excitation energy. Between the resonances, a plateau region is observed. The slope of the plateau varies between chiralities from negative to positive values. The turning points originate from the resonant phonons sliding into the bottleneck of the exciton-polariton dispersion.

The resonant behavior of the 2D mode energy and intensity in (6,5),(8,3), and (6,4) was also measured for the first transition E_{11}. The comparison of the 2D mode dispersion between the transitions allowed me to identify the dark state of E_{11} as the channel contributing most to the second step of the Raman process. The 2D energy of the (6,5) differed by 50 cm^{-1} between the first and

second transitions. The intensity of the 2D mode is up to 50 times higher when excited at the first transition compared to the second transition. The displacement of the 2D mode with excitation energy as well as the resonant Raman profile of the (6,5) nanotube were excellently reproduced by fourth-order perturbation theory when inducting exciton-polariton effects.

The exciton-polariton induced effects are clearly visible in the resonant behavior of the 2D mode energy and intensity. A similar process is expected for the defect induced D mode. Although the defects break the translational symmetry and may scatter to different excitonic states compared to the 2D mode. The comparison between the dispersions of these mode will provide information about a particular defect. The study of quantum defects will be extremely interesting [153]. Further, the exciton-polariton theory may be extended to the D and G phonon modes, where the resonance Raman profiles are determined by the exciton-polariton formation as well.

In Chapter 4, I target the methods to influence the vibrational properties of nanotubes by applying covalent functionalization: [2+1] cycloaddition (Sec. 4.2), light activated diazonium salts functionalization (Sec. 4.3), and carboxylation (Sec. 4.4).

[2+1[Cycloaddition. Photoluminescence-excitation spectroscopy and XPS evidence successful cycloaddition with an open ring triazine configuration in Subchapter c. In this configuration the sp^2 hybridization of carbon atoms are preserved. The XPS shows a different Fermi level between functionalized and pristine CNTs. I studied the vibrational properties of the CNTs by Raman spectroscopy. First, I compare the RBM frequencies of the functionalized metallic and semiconducting nanotubes. The RBMs in metallic nanotubes undergo a shift, up to 3 cm^{-1}, whereas RBMs of semiconducting nanotubes remain constant. The energies and position of the G and 2D phonons of metallic nanotubes are efficiently tuned through electron-phonon interaction. The Fermi level change deduced from Raman scattering correlates with XPS analysis, both showing electron doping. No changes in the phonon energies of semiconducting CNTs were observed.

In regard of the phonon coupling, the cycloaddition can be improved in order to alter the phonons in semiconducting CNTs. An electronegative anchor needs to be attached to the molecule providing stronger doping, moreover the cover density can be amplified by optimizing the synthesis. Many different types of other functional molecules from switches to the dyes can be locked to the nanotube via chlorine atoms at the triazine ring without disturbing the nanotube network. A molecular switch may allow a switchable tuning of the phonon energies and PL [188]. A dye molecule attached to the triazine ring can transfer the energy onto the nanotube, resulting in photoemission in semiconducting and photodoping in metallic nanotubes.

Light activation reaction with diazonium salt. A new in-situ approach to functionalize nanotubes with diazonium salts was developed in Section 4.3. The reaction was triggered by the resonant excitation at 785 nm and the scattered light was analyzed in the Raman setup. The kinetics of the reaction were monitored and tuned by laser power. The Gaussian beam profile induced the same distribution of defects under the laser spot, as verified by lateral Raman mapping. Our method provided a chiral selectivity. I evaluated the shifts of the transition energies by means resonant Raman spectroscopy of the RBMs. The transition energy of (9,7) nanotube, resonant with activation energy ($E_{22} = E_f$), undergoes the largest shift among all nanotube chiralities.

A logical extension of this experiment is the design of CNT photonic devices. Such a device with a semiconducting nanotube light source can be turned into the single photo emitter by our technique, where the emission could be electrically pumped.

Carboxylation. I reported the structural changes in the CNTs induced by the functionalization in Section 4.4. Emission and absorption bands as well as RBM peaks for small diameter nanotubes disappeared. Semiconducting nanotubes with diameters less than 8.2 Å got destroyed by the functionalization process. The D_{area}/G_{area} ratio increased up to 45 times. A characteristic displacement of the first transition energy, downshifting in SI type nanotubes and upshifting in SII type nanotubes was identified as local strain. An expansive uniaxial strain is evaluated $\varepsilon = 0.18$ %.

I further investigated the functionalization effects on electronic properties by Raman spectroscopy. I evaluated the shift of the Fermi energy of functionalized tubes using the FWHM and the positons of the G and 2D peaks, correlated by the strain induced shifts. ΔE_F was determined to be -0.65 eV for metallic and -0.5 eV for semiconducting tubes. The 2D displacement up to 43 cm^{-1} to higher energy confirmed the p-type doping. The functional groups induce both negative Fermi energy shift (p-doping) and defects of the material due to the covalent functionalization process. At such high density of defects not only doping determines the total linewidth of the G mode but the finite lifetime due to defects as well. A metrology for the reliable determination of the physical effects such as strain, doping, and defect influence is developed during this study. Doping and defects induce the changes in phonon lifetimes, whereas doping and strain change the phonon frequencies. Additionally, strain induces an opposite displacement in the transition energies in the SI and SII type CNTs.

Overall, this work provides new insights into the physics of carbon nanotube. The signatures in resonance Raman evidence various peculiar phenomena. The asymmetry in resonance Raman profile of the G mode reflects the strong coupling between the phonon and exciton. The resonant behavior of the 2D mode carries distinct footprints of propagating in the CNT exciton-polariton. The correlative analysis of the exciton and phonon energies provides information on charges and strain redistribution in the nanotube-molecule hybrids. Based on these results the Raman spectroscopy characterization techniques of pristine and functionalized nanotubes need to be revised.

.....

Zusammenfassung

In dieser Arbeit untersuche ich durch Exzitonen entstehenden Streuprozesse in Kohlenstoffnanoröhren, was eine Reihe von faszinierenden Phänomenen hervorruft. Während des Ramanstreuprozesses tritt eine starke Kopplung sowohl zwischen Photon und Exziton, als auch zwischen Exziton und Phonon auf. Zuerst in Kapitel 2 untersuche ich die Exziton-Phonon Kopplung in den Röhren. Nanoröhren existieren in unterschiedlichen Chiralitäten, die ihre optischen und ihre Schwingungseigenschaften bestimmen. Ich zeige, dass die Exziton-Phonon Kopplung enenfalls von der Chiralität abhängt. Um die Kopplung zu evaluieren habe ich die Asymmetrie der G Mode im resonanten Ramanprofilen analysiert. Die Asymmetrie ist eine Folge von Phonon bedingten konkurrierenden Streuprozessen zwischen den dunklen und hellen exzitonischen Zuständen. Ich habe resonante Ramanprofile der Stokes und anti-Stokes Streuung der G Mode aufgenommen und die Daten mit Störungstheorie fünfter Ordnung modeliert. Die korrelierte Analyse der Stokes und anti-Stokes Profile und deren relative Intensität erlaubte mir die Kopplungsfaktoren experimentell zu bestimmen. Diese Faktoren unterscheiden sich sowohl in den Chiralitäten überprüft von der tight-binding Rechnung.

Die Kopplung zwischen Exziton und Phonon kann zusätzlich verstärkt oder geschwächt werden, indem der exzitonische Übergang geändert wird. Mit dem Vergleich des Stokes G Mode Profils des E_{11} Übergangs mit dem E_{22} Übergang habe ich diese Abhängigkeit überprüft. Beim ersten Übergang Die Matrixelemente verdreifachen sich, was eine 30fach höhere Raman Intensität der G Moden induziert verglichen mit dem zweiten Übergang.

In Kapitel 3 untersuche ich die Exziton-Photon Kopplung, die in der Entstehung von einem Exziton-Polariton resultiert. Dieses Quasipartikel bestimmt die Dispersion und Intensität der 2D Mode in der Nanoröhre. Die Dispersion von 2D Mode hat drei deutlich unterschiedliche Winkel wenn angerengt bei E_{22}. Der dunkle Zustand des E_{11} Exzitons beteiligt sich bei der 2D Moden am Streuprozess im zweiten und ersten exzitonischen Übergang. Die abweichende Dispersion und das resonante Raman Profil von der 2D Mode zwischen den ersten und zweiten Übergängen bestätigt diese Hypothese. Störungstheorie vierter Ordnung mit implementierten polaritonischen Effekten hat erfolgreich das experimentelle Verhalten von der 2D Mode der (6,5) Nanoröhren reproduziert.

Im letzten Teil meiner Arbeit (Kapitel 4) nutze ich kovalente Funktionalisierung um die Schwingungseigenschaften von Nanoröhren zu modifizieren. Drei unterschiedlichen Methoden wurden angewendet: [2+1] Cycloaddition, Licht aktivierte Reaktion mit Diazonium Bromidsalz und Carboxylierung. Die dominanten Mechanismen für Phonon Modifikation ist die Dotierung und Verspannung. Die Cycloaddition, beschrieben in Sektion 4.2, verursacht nur in metallischen Röhren Veränderungen der Phononen (RBMs, G und 2D Moden). Resonante Raman Messungen der G Mode zwischen metallischen Röhren von unterschiedlichen Durchmessern zeigten die stärksten Effekte für kleine Röhren. Die Funktionalisierung mit Diazonium Bromidsalz wurde „in situ“ durchgeführt, wo die Schwingungseigenschaften im Verlauf der Reaktion gemessen wurden. Die chirale Selektivität der Reaktion wurde durch die größte Verschiebung von der E_{11} Energie der resonanter Röhre unterstützt. Die Carboxylierung modifiziert die Phononen in metallischen und halbleitenden Nanoröhren. Von den drei untersuchten Methoden sind die Effekte der Carboxylierung am stärksten. Die Energien der 2D und G Moden verschieben um bis zu 50 cm^{-1}. Die COOH- Gruppen verursachen sowohl Dotierung als auch Verspannung. Die Stärke (ε = 0.18 %) und der Typ (einachsig expansiv) der Verspannung folgen aus der Analyse der E_{11} Übergangsenergien.

6 | Additional information

Appendix A:2D mode calculation details

For a defined laser energy, the position and intensity of the 2D mode are deduced from Eq. (3.6). The scattering efficiency is calculated for all pairs of phonons permitted by the phonon dispersion. This efficiency plotted versus the energy sum of phonon pair forms an intensity distribution representing a line shape of the 2D mode at a given energy (see inset in Figure 3.12d). The area of this peak reflects the intensity of the simulated 2D mode and the sum of vector energies forming the maxima correspond to the 2D peak position. The 2D Raman spectra were simulated in reciprocal space for the exciton-polariton formed by the first and second excitonic states. The dark state is provided by the lowest first exciton at the K point of the BZ and is common for the 2D mode excited at both transitions. The integrated intensity of each spectra as a function of excitation energy representing the simulated resonant Raman profile of the 2D mode is shown in Figure 3.12d. The energy of the pair of resonant phonons indicates the displacement with excitation energy of the 2D peak and is shown in Figure 3.12b.

For the dispersion of the uncoupled exciton, we use the parabolic band approximation [51]. The exciton effective mass tunes the exciton dispersion slope in K space. After the photon interaction, the exciton dispersion unfolds in four different branches, described by the Eq. (3.6). For the first approximation, the same value for the effective masses of the first and second excitons is taken. The chiral dependence of the exciton effective mass is considered by Ref. [51]. In (6,5) nanotubes, for a qualitative result, the effective masses were taken to be the same for both transitions M_{11} = M_{22} =0.04 m_0, where m_0 is the free electron mass. The ω_L matches the E_{ii} transition energy of the corresponding bright exciton. For the splitting between transverse and longitudinal EP's (ω_L and ω_T) we use standard values of 0.08 meV for the semiconducting materials [17]. The symmetry of the DRRS process is considered. In chiral tubes, the E_{11} and E_{22} bright exciton in the middle of the BZ has an A_2 symmetry and can be scattered by the phonon to the dark $E_{2\mu}$ symmetry state [26]. The first phonon has a $E_{2\mu}$ and the second phonon scattering back to the bright state has an $E_{-2\mu}$. The angular momentum is conserved when the scattering is mediated by the phonon branch with the rotational quantum number m=2μ.[31]. Additional left-right "selection rule" for phonon linear momenta arises from the nature of EP scattering. The final and initial state have to be located on different sides of the exciton-polariton [110]. A pair of phonons can contribute to the scattering between two particular EP branches only when this selection rule is satisfied for these phonons. Note the selection rule for the exciton like branch is the dominant one. The largest scattering intensity is achieved, when the latter phonons satisfy the conservation of linear pseudo momenta i.e. scattered between real states of excitonic states. In our calculation, we modeled the phonon m=2μ branch dispersion by simple functions. These functions match the ones obtained by zone folding scheme of graphene, the G and D points are fixed at 1595 and 1265 cm^{-1}, respectively. It should be mentioned that a qualitative 2D behavior on the excitation energy is independent within a reasonable parameter variation. For the exciton damping $\Gamma/2$ the value of 0.05 eV extracted from G mode resonance profile of Ref. [24]was used.

Appendix B: Functionalization routines and experimental methods

[2+1] Cycloaddition

Synthesis of the functionalized tubes. HiPCO SWNTs (length: 0.2–1.2 mm, diameter: 0.8–1.2 nm) were supplied by Unidym (batch SP0295). The 2,4,6-trichloro-1,3,5-triazine (cyanuric chloride or triazine), 2,3,3-trimethylindo- lenine and 5-nitrosalicylaldehyde were purchased from Sigma-Aldrich. Sodium acid and N-methyl-2-pyrrolidone were supplied by Merck. A schematic depiction of the reaction steps can be found in Ref. [149].

Conjugating triazine onto the SWNTs: SWNT-low and SWNT-high. Pristine SWNTs (1 g) were added to N-methyl-2-pyrrolidone (150 ml), sonicated for 1 h and then stirred at room temperature for an additional 1 h. The 2,4,6-1,3, 5-trichloro-triazine (10 g, 54 mmol) dissolved in N-methyl-2-pyrrolidone (50 ml) was added to the mixture at 0 °C and stirred for 20 min. Sodium azide (1.76 g, 27 mmol) in solid state was gradually added to the reaction flask at 0 °C; the mixture was stirred at this temperature for 2 h. The temperature was raised to 25 °C and stirred for 1 h. Operating at low temperature ensures the substitution of only one chlorine atom [150] [151]. We thus converted 2,4,6-trichloro-1,3,5-triazine into 2-azido-4,6-dichloro-1,3,5 triazine and prevented the creation of more complicated structures such as di- or tri-azide derivatives, or C3N4 graphitic materials [152]. Details of the characterization of the intermediate product can be found in the Ref. [149]. Thereafter, the suspension was stirred overnight at a temperature of 25 °C (SWNT-low) and at 70 °C (SWNT-high). The mixtures were centrifuged (5,000 r.p.m. for 5min) and the crude products were dispersed in acetone and centrifuged again under the same condition. Dispersion and centrifugation of the product was repeated in water, toluene and chloroform to obtain the purified compounds. The products were lyophilized to obtain 1.08 g black solid compound of SWNT-low and 1.03 g black solid compound of SWNT- high.

XPS measurements were carried out on SWNT, SWNT-low, SWNT-high, and SP-SWNT samples. For this the substances were dispersed in THF and the suspensions carefully dropped onto thin-film gold substrates (300 nm Au(111) on mica, Georg Albert PVD) and left on the bench until the solvent was evaporated. Samples were then brought into ultra-high vacuum (UHV) and measured with a monochromatic high-resolution XPS setup (VG Scienta MX 650 and SES-200) in perpendicular take-off geometry with constant analyzer pass energy of 200 eV. All binding energies (EB) were referenced to the Au substrate 4f7/2 peak at $E_{Binding}$ = 83.96 eV and are correct within 40 meV. The zero of the binding energy scale corresponds to the Fermi level of the Au substrate. Due to the drop-coating preparation the samples did not contain equal absolute amounts of substance and their spectra needed to be normalized. Considering the comparable shape of the C 1s spectra and the fact that the SWNTs were not exposed to any harsh treatments, we assumed that their carbon backbones remained intact and that the established functionalization ratios (FR) did not significantly reduce the amount of sp2 -hybridized carbon atoms. Therefore we chose to normalize all SWNT XP spectra with respect to the carbon backbone, i.e., the intensity of the sp2 -carbon component.

Raman spectra of metallic nanotubes were acquired using an XploRa spectrometer (Horiba), excitation wavelength at 532 nm, equipped with charge-coupled device, 2400 lines/mm gratings and edge filter to block Rayleigh-scattered light. Frequencies were calibrated using a cyclohexane reference sample.

Two-dimensional luminescence was recorded with a Nanolog spectrofluorometer from Horiba, equipped with a Xenon lamp and a liquid-Nitrogen cooled InGaAs detector.

Diazonium salt functionalization

Laser assisted functionalization. The DzBr salt was supplied by Sigma Aldrich. Even though, -5˚C are required, it was stored at -20˚C. Before each functionalization reaction the solution was freshly prepared. On a balance 10 mg of the DzBr was weighed into an UV-protective 10 ml bottle and filled up to 10 g with deionized water. The final solution has a pH-value of 3.6. With a molecular weight of 270.82 g/mol and 96 % purity this leads to a final concentration of 3.85 M/g. For comparison in Ref. [153] 0.7 mg/mL of 3,5-Dichlorophenyldiazonium tetrafluoroborate in nanopure water (resulting in 2.86 M/mL) was used for a low functionalization concentration of the tubes [153]. For the laser assisted functionalization (LAF) the DzBr solution was diluted (1:100) illustrated in Figure 4.11 resulting in a final concentration of 38 nM/g exposed to the nanotube.

Before each LAF a spot with high RBM/G was chosen on the substrate. Once a good spot was found, at least one spectrum was taken covering D- and G-modes. Then, the sample was covered with water and again focused for a second spectrum of the water covered pristine CNTs (Figure 4.11).

A schematic view of the laser assisted kinetic measurements is given in Figure 4.11. The substrate (purple) was placed in a plastic container for the LAF step. The drop casted CNTs (black) were covered with 2 ml of deionized water (blue) and a glass cover swimming on the droplet to overcome the lens effect at the water surface. The measurements were done with excitation powers between 2 and 40 mW with an 5x objective resulting in a power density from 7.9 to 157 W/mm^2 . For higher magnifications like 20x and 50x the incoming laser beam was filtered to keep the power density below 200 W/mm^2. Higher power density can be used for CNTs surrounded by a liquid, since the liquid acts as a heat reservoir [154].

Before adding the diazonium solution several spectra were acquired in water to confirm that no effects occur due to the laser heating. Finally, 20 µL of the reaction solution were added and spectra were acquired each minute for at least 2 hours. Between the measurements the 785 nm laser was kept on to drive the reaction. In the case of static measurement, the grading for the spectral acquisition is fixed and spectra can be quickly recorded in a range of ± 551 cm^{-1} from its central position (e.g. 617 to 1720 cm^{-1}). Using the extended mode longer acquisition times are needed, since the gratings moves to cover a broad spectrum. Therefore, the whole spectrum including RBM, G and D-modes can be recorded. For setup specific reasons the extended mode does not illuminate the sample between multiple acquisitions, in contrast to the static mode which can optionally bleach the sample between the data acquisition.

Raman mapping. After LAF (70 nM/gL; 2mW; 50x objective), a Raman mapping of the irradiated zone and its surroundings was performed with an Xplora Horiba spectrometer. The same excitation energy as for LAF (785 nm) was used, but an objective with higher magnification (x100, N.A. 0.9) was picked to obtain higher lateral resolution. At each x, y position a Raman spectrum, containing the G and D modes was acquired. These modes were fitted with Lorentzian profiles and the intensity (integrated peak area) of the D mode was divided by the intensity of the G$^+$ mode (LO phonon). The ratio between the bands plotted over the lateral position is displayed in Figure 4.15a and b. Individual spectra are shown in Figure 4.15c.

Resonant Raman characterization. the RBMs were recorded before and after LAF (70 nM/gL; 2mW; 50x objective) functionalization. A tunable excitation system was used with a Ti:Sa laser (Coherent MBR 110) providing excitations from 700 to 1000 nm. The backscattered light was collected by a 50x objective before the functionalization and with an 100x objective after the functionalization in order to select nanotubes from the reaction centre. A triple grating system of a T64000 Horiba spectrometer equipped with a 900 line per mm grating and a silicon charge coupled device was used to analyse the backscattered light. Raman shift and intensity were calibrated on the sulphur. Raman spectra in the region of the G and D modes at several excitation energies was recorded in the same set-up before and after the functionalization.

Acid treatment

Sample preparation. The COOH-covalently functionalized tubes were produced using standard acid treatment [155]. We dissolved 1 g of SWNTs (NoPo HiPCO nanotubes) in a mixture of 150 ml of H_2SO_4 and 50 ml of HNO_3. After heating up to 60°C, the blend was stirred for 16 min. To reach pH value of 7, we filtered and washed the blend with water. Finally, the sample was dried overnight at 60°C. We used the dried sample for Raman measurements, whereas for emission and absorption spectroscopy we debundled them according to the previously described routine, see Ref. [156].

Raman measurements. The dried nanotubes samples were excited with a frequency doubled Nd:YAG laser at 2.33 eV (532 nm) and a diode laser at 1.94 eV (638 nm). The signals were recorded with an XploRA (Horiba) spectrometer in the backscattering configuration, acquired with a 10x objective (N.A. = 0.33), 1200 lines/mm gratings and thermoelectrically cooled charge coupled devices (CCD) detector. Benzonitrile and cyclohexane organic molecules were used to calibrate Raman peaks. The laser power was kept under 1 mW and the reduction of laser power up to 10 times had no effect on the G mode FHWM and position in the functionalized and pristine samples. It indicates that additional broadening due to heating can be excluded.

Optical characterization. A Horiba Nanolog system was used for PLE measurements. Single excitation lines from HgXe short arc lamp were selected using a monochromator. A nitrogen-cooled InGaAs detector and a photomultiplier were used to record the spectra. Absorption measurements were carried out at room temperatures with a Perkin Elmer Lambda 950 spectrophotometer.

List of publications

1. Doping in covalently functionalized carbon nanotubes: A Raman scattering study.
   G. Gordeev, A. Setaro, M. Glaeske, S. Jürgensen, and S. Reich
   Phys. Status Solidi Basic Res. **253,** (2016).
2. Resonant anti-Stokes Raman scattering in single-walled carbon nanotubes.
   G. Gordeev, A. Jorio, P. Kusch, B.G.M. Vieira, B. Flavel, R. Krupke, E.B. Barros, and S. Reich
   Phys. Rev. B **96,** 245415 (2017).
3. Inner- and outer-wall sorting of double-walled carbon nanotubes.
   H. Li, G. Gordeev, S. Wasserrot, V.S.K. Chakravadhanula, S.K.C. Neelakandhan, F. Hennrich, A. Jorio, S. Reich, R. Krupke, and B.S. Flavel
   Nat. Nanotechnol. **12,** 1176–1182 (2017).
4. Preserving π-conjugation in covalently functionalized carbon nanotubes for optoelectronic applications.
   A. Setaro, M. Adeli, M. Glaeske, D. Przyrembel, T. Bisswanger, G. Gordeev, F. Maschietto, A. Faghani, B. Paulus, M. Weinelt, R. Arenal, R. Haag, and S. Reich
   Nat. Commun. **8,** 14281 (2017).
5. Fluorescent Polymer—Single-Walled Carbon Nanotube Complexes with Charged and Noncharged Dendronized Perylene Bisimides for Bioimaging Studies.
   K. Huth, M. Glaeske, K. Achazi, G. Gordeev, S. Kumar, R. Arenal, S.K. Sharma, M. Adeli, A. Setaro, S. Reich, and R. Haag
   Small **14,** 1–11 (2018).
6. Asymmetry of resonance Raman profiles in semiconducting single-walled carbon nanotubes at the first excitonic transition.
   G. Gordeev, B. Flavel, R. Krupke, P. Kusch, and S. Reich
   Phys. Rev. B **99,** 45404 (2019).
7. Separation of Small-Diameter Single-Walled Carbon Nanotubes in One to Three Steps with Aqueous Two-Phase Extraction.
   H Li, G. Gordeev, O. Garrity, S. Reich, and B.S. Flavel
   ACS Nano **13,** 2567–2578 (2019).
8. Atomic-Resolution Visualization and Doping Effects of Complex Structures in Intercalated Bilayer Graphene.
   J.P. Bonacum, A. O'Hara, D.-L. Bao, O.S. Ovchinnikov, Y.-F. Zhang, G. Gordeev, S. Arora, S. Reich, J.-C. Idrobo, R.F. Haglund, S.T. Pantelides, and K. Bolotin
   Submitted to *Phys. Rev. X*.
9. Few-Wall Carbon Nanotube Coils.
   D. Nakar, G. Gordeev, L.D. Machado, R. Popovitz-Biro, K. Rechav, E.F. Oliveira, P. Kusch, A. Jorio, D.S. Galvão, S. Reich, and E. Joselevich
   To be submitted

Acknowledgements

I would like to express my gratitude to all the people who supported me during my thesis, and without whom this work would not exist.

First of all, I would like to mention the excellent supervision provided by my Prof. Stephanie Reich. I am thankful to her for leading me through the fascinating one-dimensional world of nanotube physics. Stephanie for carefully evaluating every step of my work and for her great patience and persistence whilst working on my drafts, which improved dramatically under advisement.

I would also like to thank…

…Patryk for letting me feel to be a part of your family, for teaching me how to properly handle and treat the lasers and spectrometers, for being always ready to go have a coffee talk and prepare a new experiment.

…Sören for lending me a hand, whenever I needed help and for being a great office mate.

…Bruno for sharing my interest in matrix elements and fruitful discussions about the Raman scattering theory in carbon nanotubes. The tandem lessons we had were very useful.

…Oisĭn for the enthusiasm in the experiments we performed together and overtaking my lab work through the time of writing my thesis.

…Antonio and Mareen for the inspiring work on the functionalized nanotubes, which has become a significant part of this work. Sabrina for helping with the PLE setup, and setting it up for Raman measurement.

… Sören, Oisĭn, Bruno, Antonio for additional proofreading my manuscripts and this dissertation, I know this work can be quite hard.

…Benjamin Flavel and Ralph Kruke for preparing extremely pure samples, which allowed me to study CNT physics.

…Ado Jorio for introducing the Stokes anti-Stokes photons entanglement and for a great time in the lab in Belo Horizonte. Filomeno and Arthuro for supporting me during my stay in Brazil.

…The entire AG Reich group including Vladka, Svitlana, Kati, Timo, Gudrun, Benjamin, Andre, Jan, and Isabela for the great time here in Berlin.

…My entire family: in particular my father Igor Gordeev for inspiring be to go into the field of natural sciences, my uncle Hans Fink for helping me with my first DAAD proposal, and my grandfather Karl Fink for giving me opportunities in language learning, career advises, and shelter for the first time in Berlin.

…and especially my wife Victoria, who never doubted me, supported, woke me up, and motivated me every day. I appreciate the great patience you showed while I was absent from home working in lab and writing this thesis.

Bibliography

1. Reich, S., Thomsen, C. & Maultzsch, J. *Carbon nanotubes : basic concepts and physical properties*. (WILLEY-VCH, 2004).
2. Jorio, A., Saito, R., Dresselhaus, G. & Dresselhaus, M. S. *Raman Spectroscopy in Graphene Related Systems*. *Raman Spectroscopy in Graphene Related Systems* (WILLEY-VCH, 2011). doi:10.1002/9783527632695
3. Iijima, S. Helical microtubules of graphitic carbon. *Nature* **354,** 56–58 (1991).
4. Bachtold, A., Hadley, P., Nakanishi, T. & Dekker, C. Logic Circuits with Carbon Nanotube Transistors. *Science (80-.).* **294,** 1317 LP-1320 (2001).
5. Baughman, R. H., Zakhidov, A. A. & De Heer, W. A. Carbon nanotubes - The route toward applications. *Science (80-.).* **297,** 787–792 (2002).
6. Snow, E. S., Perkins, F. K., Houser, E. J., Badescu, S. C. & Reinecke, T. L. Chemical detection with a single-walled carbon nanotube capacitor. *Science (80-.).* **307,** 1942–1945 (2005).
7. Eichler, A. *et al.* Nonlinear damping in mechanical resonators made from carbon nanotubes and graphene. *Nat. Nanotechnol.* **6,** 339 (2011).
8. Cohen-Karni, T., Segev, L., Srur-Lavi, O., Cohen, S. R. & Joselevich, E. Torsional electromechanical quantum oscillations in carbon nanotubes. *Nat. Nanotechnol.* **1,** 36 (2006).
9. Baughman, R. H. *et al.* Carbon Nanotube Actuators. *Science (80-.).* **284,** 1340 LP-1344 (1999).
10. He, X. *et al.* Tunable room-Temperature single-photon emission at telecom wavelengths from sp 3 defects in carbon nanotubes. *Nat. Photonics* **11,** 577–582 (2017).
11. Li, H. J., Lu, W. G., Li, J. J., Bai, X. D. & Gu, C. Z. Multichannel ballistic transport in multiwall carbon nanotubes. *Phys. Rev. Lett.* **95,** 1–4 (2005).
12. Yanagi, K. *et al.* Intersubband plasmons in the quantum limit in gated and aligned carbon nanotubes. *Nat. Commun.* **9,** 1–7 (2018).
13. Shi, Z. *et al.* Observation of a Luttinger-liquid plasmon in metallic single-walled carbon nanotubes. *Nat. Photonics* **9,** 515–519 (2015).
14. Wang, F., Dukovic, G., Brus, L. E. & Heinz, T. F. The Optical Resonances in Carbon nanotubes arise from excitons. *Science (80-.).* **308,** 838–841 (2005).
15. Perebeinos, V., Tersoff, J. & Avouris, P. Radiative lifetime of excitons in carbon nanotubes. *Nano Lett.* **5,** 2495–2499 (2005).
16. Avouris, P., Freitag, M. & Perebeinos, V. Carbon-nanotube photonics and optoelectronics. *Nat. Photonics* **2,** 341–350 (2008).
17. Yu, P. Y. & Cardona, M. *Fundamentals of Semiconductors – Physics and Materials Properties*. (Springer, 1995). doi:10.1524/zpch.1997.198.Part_1_2.275
18. Spataru, C. D., Ismail-Beigi, S., Benedict, L. X. & Louie, S. G. Excitonic Effects and Optical Spectra of Single-Walled Carbon Nanotubes. *Phys. Rev. Lett.* **92,** 077402 (2004).
19. Damnjanović, M., Milošević, I., Vuković, T. & Sredanović, R. Full symmetry, optical activity, and potentials of single-wall and multiwall nanotubes. *Phys. Rev. B - Condens. Matter Mater. Phys.* **60,** 2728–2739 (1999).
20. Perebeinos, V., Tersoff, J. & Avouris, P. Effect of exciton-phonon coupling in the calculated optical absorption of carbon nanotubes. *Phys. Rev. Lett.* **94,** 27402 (2005).
21. Torrens, O. N., Zheng, M. & Kikkawa, J. M. Energy of K-momentum dark excitons in carbon nanotubes by optical spectroscopy. *Phys. Rev. Lett.* **101,** 157401 (2008).
22. Qiu, X., Freitag, M., Perebeinos, V. & Avouris, P. Photoconductivity spectra of single-carbon nanotubes: Implications on the nature of their excited states. *Nano Lett.* **5,** 749–752 (2005).
23. Hároz, E. H. *et al.* Asymmetric excitation profiles in the resonance Raman response of armchair carbon nanotubes. *Phys. Rev. B - Condens. Matter Mater. Phys.* **91,** 20544

(2015).
24. Gordeev, G. *et al.* Resonant anti-Stokes Raman scattering in single-walled carbon nanotubes. *Phys. Rev. B* **96,** 245415 (2017).
25. Gordeev, G., Flavel, B. S., Kusch, P., Krupke, R. & Reich, S. Resonant Raman scattering in semiconducting single walled carbon nanotubes at first excitonic transition.
26. Barros, E. B. *et al.* Review on the symmetry-related properties of carbon nanotubes. *Phys. Rep.* **431,** 261–302 (2006).
27. J. Jiang, R. Saito, Ge. G. Samsonidze, S. G. Chou, A. Jorio, G. Dresselhaus, and M. S. D. Electron-phonon matrix elements in single-wall carbon nanotubes. *Phys. Rev. B* **42,** 3169–3176 (2005).
28. Powell, L. R., Kim, M. & Wang, Y. Chirality-Selective Functionalization of Semiconducting Carbon Nanotubes with a Reactivity-Switchable Molecule. *J. Am. Chem. Soc.* **139,** 12533–12540 (2017).
29. Powell, L. R., Piao, Y. & Wang, Y. Optical Excitation of Carbon Nanotubes Drives Localized Diazonium Reactions. *J. Phys. Chem. Lett.* **7,** 3690–3694 (2016).
30. Piao, Y. *et al.* Brightening of carbon nanotube photoluminescence through the incorporation of sp 3 defects. *Nat. Chem.* **5,** 840–845 (2013).
31. Maultzsch, J., Reich, S., Thomsen, C., Milos, I. & Dobardz, E. Phonon dispersion of carbon nanotubes. *Solid State Commun.* **121,** 471–474 (2002).
32. Thomsen, C. & Reich, S. Raman Scattering in Carbon Nanotubes. in *Light Scattering in Solids IX* (eds. Manuel, C. & Merlin, R.) 164–169 (Springer, 2007).
33. Samsonidze, G. G. *et al.* The Concept of Cutting Lines in Carbon Nanotube Science. *J. Nanosci. Nanotechnol.* **3,** 431–458 (2003).
34. Ordejón, P., Artacho, E. & Soler, M. Ab initio structural, elastic, and vibrational properties of carbon nanotubes. *Phys. Rev. B - Condens. Matter Mater. Phys.* **59,** 12678–12688 (1999).
35. R., S., Dresselhaus, G. & Dresselhaus, M. S. *Physical Properties of Carbon Nanotubes*. **39,** (Imperial College Press, 1998).
36. Kasuya, A., Sasaki, Y., Saito, Y., Tohji, K. & Nishina, Y. Evidence for size-dependent discrete dispersions in single-wall nanotubes. *Phys. Rev. Lett.* **78,** 4434–4437 (1997).
37. Dubay, O. & Kresse, G. Accurate density functional calculations for the phonon dispersion relations of graphite layer and carbon nanotubes. *Phys. Rev. B* **67,** 35401 (2003).
38. Maultzsch, J., Reich, S., Thomsen, C., Requardt, H. & Ordejón, P. Phonon Dispersion in Graphite. *Phys. Rev. Lett.* **92,** 075501 (2004).
39. Gunlycke, D., Lawler, H. M. & White, C. T. Lattice vibrations in single-wall carbon nanotubes. *Phys. Rev. B* **77,** 14303 (2008).
40. Maultzsch, J., Telg, H., Reich, S. & Thomsen, C. Radial breathing mode of single-walled carbon nanotubes: Optical transition energies and chiral-index assignment. *Phys. Rev. B - Condens. Matter Mater. Phys.* **72,** 205438 (2005).
41. Araujo, P. T., Jorio, A., Dresselhaus, M. S., Sato, K. & Saito, R. Diameter dependence of the dielectric constant for the excitonic transition energy of single-wall carbon nanotubes. *Phys. Rev. Lett.* **103,** 1–4 (2009).
42. Cambré, S., Schoeters, B., Luyckx, S., Goovaerts, E. & Wenseleers, W. Experimental observation of single-file water filling of thin single-wall carbon nanotubes down to chiral index (5,3). *Phys. Rev. Lett.* **104,** 207401 (2010).
43. Reich, S. & Thomsen, C. Chirality dependence of the density-of-states singularities in carbon nanotubes. *Phys. Rev. B - Condens. Matter Mater. Phys.* **62,** 4273–4276 (2000).
44. Saito, R., Fujita, M., Dresselhaus, G. & Dresselhaus, M. S. Electronic structure of graphene tubules based on C60. *Phys. Rev. B* **46,** 1804–1811 (1992).
45. Reich, S., Maultzsch, J., Thomsen, C. & Ordejón, P. Tight-binding description of graphene. *Phys. Rev. B - Condens. Matter Mater. Phys.* **66,** 354121–354125 (2002).
46. Bluemmel, P. Functionalization of Carbon Nanotubes with Molecular Switches. *Journal of Chemical Physics* **138,** (Freie Universität Berlin, 2013).
47. Zhou, C., Kong, J. & Dai, H. Intrinsic electrical properties of individual single-walled

carbon nanotubes with small band gaps. *Phys. Rev. Lett.* **84,** 5604–5607 (2000).
48. Vuković, T., Milošević, I. & Damnjanović, M. Carbon nanotubes band assignation, topology, Bloch states, and selection rules. *Phys. Rev. B* **65,** 045418 (2002).
49. White, C. T., Robertson, D. H. & Mintmire, J. W. Helical and rotational symmetries of nanoscale graphitic tubules. *Phys. Rev. B* **47,** 5485–5488 (1993).
50. He, X. F. Excitons in anisotropic solids: The model of fractional-dimensional space. *Phys. Rev. B* **43,** 2063–2069 (1991).
51. Pedersen, T. G. Exciton effects in carbon nanotubes. *Carbon N. Y.* **42,** 1007–1010 (2004).
52. Zhao, H. & Mazumdar, S. Electron-electron interaction effects on the optical excitations of semiconducting single-walled carbon nanotubes. *Phys. Rev. Lett.* **93,** 8–11 (2004).
53. Pomraenke, R. *et al.* Two-photon photoluminescence and exciton binding energies in single-walled carbon nanotubes. *Phys. Status Solidi Basic Res.* **243,** 2428–2435 (2006).
54. Flavel, B. S., Moore, K. E., Pfohl, M., Kappes, M. M. & Hennrich, F. Separation of single-walled carbon nanotubes with a gel permeation chromatography system. *ACS Nano* **8,** 1817–1826 (2014).
55. Flavel, B. S., Kappes, M. M., Krupke, R. & Hennrich, F. Separation of single-walled carbon nanotubes by 1-dodecanol-mediated size-exclusion chromatography. *ACS Nano* **7,** 3557–3564 (2013).
56. Li, H., Gordeev, G., Garrity, O., Reich, S. & Flavel, B. S. Separation of Small-Diameter Single-Walled Carbon Nanotubes in One to Three Steps with Aqueous Two-Phase Extraction. *ACS Nano* **13,** 2567–2578 (2019).
57. Vora, P. M., Tu, X., Mele, E. J., Zheng, M. & Kikkawa, J. M. Chirality dependence of the K -momentum dark excitons in carbon nanotubes. *Phys. Rev. B - Condens. Matter Mater. Phys.* **81,** 155123 (2010).
58. Raman, C. V & Krishnan, K. S. A new radiation. *Indian J. Phys* **2,** 387–398 (1928).
59. Kusch, P. Band Gap and Symmetry of Wurtzite GaAs A Resonant Raman Study. (Freie Universität Berlin, 2014).
60. Belitsky, V. I., Cardona, M., Lang, I. G. & Pavlov, S. T. Spatial correlation of electrons and holes in multiphonon resonant Raman scattering in a high magnetic field. *Phys. Rev. B* **46,** 15767–15788 (1992).
61. Dresselhaus, M. S., Dresselhaus, G., Saito, R. & Jorio, A. Raman spectroscopy of carbon nanotubes. *Phys. Rep.* **409,** 47–99 (2005).
62. Thomsen, C. & Reich, S. Double resonant raman scattering in graphite. *Phys. Rev. Lett.* **85,** 5214–5217 (2000).
63. Pesce, P. B. C. *et al.* Calibrating the single-wall carbon nanotube resonance Raman intensity by high resolution transmission electron microscopy for a spectroscopy-based diameter distribution determination. *Appl. Phys. Lett.* **96,** 1–4 (2010).
64. Doorn, S. K., Araujo, P. T., Hata, K. & Jorio, A. Excitons and exciton-phonon coupling in metallic single-walled carbon nanotubes: Resonance Raman spectroscopy. *Phys. Rev. B - Condens. Matter Mater. Phys.* **78,** 1–9 (2008).
65. Telg, H., Maultzsch, J., Reich, S. & Thomsen, C. Resonant-Raman intensities and transition energies of the E11 transition in carbon nanotubes. *Phys. Rev. B - Condens. Matter Mater. Phys.* **74,** 115415 (2006).
66. Jin, B. Y. & Silbey, R. Theory of resonance Raman scattering for finite and infinite polyenes. *J. Chem. Phys.* **102,** 4251–4260 (1995).
67. Kataura, H. *et al.* Optical properties of single-wall carbon nanotubes. *Synth. Met.* **103,** 2555–2558 (1999).
68. Araujo, P. T. *et al.* Third and Fourth Optical Transitions in Semiconducting Carbon Nanotubes. *Phys. Rev. Lett.* **98,** 67401 (2007).
69. Duque, J. G. *et al.* Violation of the condon approximation in semiconducting carbon nanotubes. *ACS Nano* **5,** 5233–5241 (2011).
70. Moura, L. G. *et al.* Raman excitation profile of the G band in single-chirality carbon nanotubes. *Phys. Rev. B - Condens. Matter Mater. Phys.* **89,** 35402 (2014).
71. Kumble, R., Rush, T. S., Blackwood, M. E., Kozlowski, P. M. & Spiro, T. G. Simulation

of Non-Condon Enhancement and Interference Effects in the Resonance Raman Intensities of Metalloporphyrins. *J. Phys. Chem. B* **102,** 7280–7286 (1998).
72. Yang, F. *et al.* Chirality-specific growth of single-walled carbon nanotubes on solid alloy catalysts. *Nature* **510,** 522–524 (2014).
73. Calleja, J. M., Kuhl, J. & Cardona, M. Resonant Raman scatteirng in diamond. *Phys. Rev. B* **17,** 876 (1978).
74. Sowers, B. L., Williams, M. W., Hamm, R. N. & Arakawa, E. T. Optical Properties of Liquid Carbon Tetrachloride, *n* -Hexane, and Cyclohexane in the Vacuum Ultraviolet. *J. Chem. Phys.* **57,** 167–170 (1972).
75. Hirt, R. C. & Howe, J. P. The ultraviolet absorption spectrum of benzonitrile vapor. *J. Chem. Phys.* **16,** 480–485 (1948).
76. Steiner, M., Qian, H., Hartschuh, A. & Meixner, A. J. Controlling nonequilibrium phonon populations in single-walled carbon nanotubes. *Nano Lett.* **7,** 2239–2242 (2007).
77. Zhang, J., Zhang, Q., Wang, X., Kwek, L. C. & Xiong, Q. Resolved-sideband Raman cooling of an optical phonon in semiconductor materials. *Nat. Photonics* **10,** 600–605 (2016).
78. Bahl, G. Laser cooling: Raman cooling in a semiconductor. *Nat. Photonics* **10,** 566–567 (2016).
79. Jorio, A. *et al.* Optical-phonon resonances with saddle-point excitons in twisted-Bilayer graphene. *Nano Lett.* **14,** 5687–5692 (2014).
80. Parra-Murillo, C. A., Santos, M. F., Monken, C. H. & Jorio, A. Stokes-anti-Stokes correlation in the inelastic scattering of light by matter and generalization of the Bose-Einstein population function. *Phys. Rev. B - Condens. Matter Mater. Phys.* **93,** 125141 (2016).
81. Brown, S. *et al.* Anti-Stokes Raman spectra of single-walled carbon nanotubes. *Phys. Rev. B - Condens. Matter Mater. Phys.* **61,** R5137–R5140 (2000).
82. Steiner, M. *et al.* Phonon populations and electrical power dissipation in carbon nanotube transistors. *Nat. Nanotechnol.* **4,** 320–324 (2009).
83. Kneipp, K. *et al.* Surface-enhanced and normal stokes and anti-stokes Raman spectroscopy of single-walled carbon nanotubes. *Phys. Rev. Lett.* **84,** 3470–3 (2000).
84. Fantini, C. *et al.* Optical transition energies for carbon nanotubes from resonant raman spectroscopy: Environment and temperature effects. *Phys. Rev. Lett.* **93,** 147406 (2004).
85. Lieber, C. M. *et al.* Joint density of electronic states for one isolated single-wall carbon nanotube studied by resonant Raman scattering. *Phys. Rev. B - Condens. Matter Mater. Phys.* **63,** 245416 (2001).
86. Wenseleers, W., Cambré, S., Čulin, J., Bouwen, A. & Goovaerts, E. Effect of water filling on the electronic and vibrational resonances of carbon nanotubes: Characterizing tube opening by Raman spectroscopy. *Adv. Mater.* **19,** 2274–2278 (2007).
87. O'Connell, M. J., Sivaram, S. & Doorn, S. K. Near-infrared resonance Raman excitation profile studies of single-walled carbon nanotube intertube interactions: A direct comparison of bundled and individually dispersed HiPco nanotubes. *Phys. Rev. B - Condens. Matter Mater. Phys.* **69,** (2004).
88. Jiang, J. *et al.* Exciton-photon, exciton-phonon matrix elements, and resonant Raman intensity of single-wall carbon nanotubes. *Phys. Rev. B - Condens. Matter Mater. Phys.* **75,** (2007).
89. Jiang, J. *et al.* Chirality dependence of exciton effects in single-wall carbon nanotubes: Tight-binding model. *Phys. Rev. B - Condens. Matter Mater. Phys.* **75,** (2007).
90. Samsonidze, G. G. Photophysics of carbon nanotubes. (Massachusetts Institute of Technology, 2007).
91. Henrik, B. & Karsten, F. *Many-Body Quantum Theory in Condensed Matter Physics: An Introduction*. (Oxford university press, 2004).
92. Porezag, D., Frauenheim, T., Köhler, T., Seifert, G. & Kaschner, R. Construction of tight-binding-like potentials on the basis of density-functional theory: Application to carbon. *Phys. Rev. B* **51,** 12947–12957 (1995).

93. Cantarero, A., Trallero-Giner, C. & Cardona, M. Excitons in one-phonon resonant Raman scattering: Deformation-potential interaction. *Phys. Rev. B* **39,** 8388–8397 (1989).
94. Santos, M. J. M. C., Costa, M. D., Rego, H. M. C., Rubo, J. H. & Santos, G. C. Effect of surface treatments on the bond strength of self-etching adhesive agents to dentin. *Gen. Dent.* **65,** e1–e6 (2017).
95. Tran, H. N. *et al.* Excitonic optical transitions characterized by Raman excitation profiles in single-walled carbon nanotubes. *Phys. Rev. B* **94,** 075430 (2016).
96. Satishkumar, B. C., Goupalov, S. V., Haroz, E. H. & Doorn, S. K. Transition level dependence of Raman intensities in carbon nanotubes: Role of exciton decay. *Phys. Rev. B* **74,** 155409 (2006).
97. Smith, A. M., Mancini, M. C. & Nie, S. Bioimaging: Second window for in vivo imaging. *Nat. Nanotechnol.* **4,** 710–711 (2009).
98. Beg, S. *et al.* Advancement in carbon nanotubes: Basics, biomedical applications and toxicity. *J. Pharm. Pharmacol.* **63,** 141–163 (2011).
99. Heister, E. *et al.* Triple functionalisation of single-walled carbon nanotubes with doxorubicin, a monoclonal antibody, and a fluorescent marker for targeted cancer therapy. *Carbon N. Y.* **47,** 2152–2160 (2009).
100. Bachilo, S. M. *et al.* Structure-assigned optical spectra of single-walled carbon nanotubes. *Science (80-.).* **298,** 2361–2366 (2002).
101. Piao, Y. *et al.* Intensity Ratio of Resonant Raman Modes for (n,m) Enriched Semiconducting Carbon Nanotubes. *ACS Nano* **10,** 5252–5259 (2016).
102. Jorio, A. *et al.* G-band resonant Raman study of 62 isolated single-wall carbon nanotubes. *Phys. Rev. B - Condens. Matter Mater. Phys.* **65,** 1554121–1554129 (2002).
103. Barzykin, A. V. & Tachiya, M. Stochastic models of carrier dynamics in single-walled carbon nanotubes. *Phys. Rev. B* **72,** 075425 (2005).
104. Reich, S. & Thomsen, C. Raman spectroscopy of graphite. *Philos. Trans. R. Soc. A Math. Phys. Eng. Sci.* **362,** 2271–2288 (2004).
105. Ferrari, A. C. & Basko, D. M. Raman spectroscopy as a versatile tool for studying the properties of graphene. *Nat. Nanotechnol.* **8,** 235–246 (2013).
106. Gordeev, G., Flavel, B., Krupke, R., Kusch, P. & Reich, S. Asymmetry of resonance Raman profiles in semiconducting single-walled carbon nanotubes at the first excitonic transition. *Phys. Rev. B* **99,** 45404 (2019).
107. Laudenbach, J., Hennrich, F., Telg, H., Kappes, M. & Maultzsch, J. Resonance behavior of the defect-induced Raman mode of single-chirality enriched carbon nanotubes. *Phys. Rev. B - Condens. Matter Mater. Phys.* **87,** (2013).
108. Moura, L. G. *et al.* The double-resonance Raman spectra in single-chirality (n, m) carbon nanotubes. *Carbon N. Y.* **117,** 41–45 (2017).
109. Maultzsch, J., Reich, S. & Thomsen, C. Chirality-selective Raman scattering of the D mode in carbon nanotubes. *Phys. Rev. B* **64,** 121407 (2001).
110. Brenig, W., Zeyher, R. & Birman, J. L. Spatial dispersion effects in resonant polariton scattering. II. Resonant Brillouin scattering. *Phys. Rev. B* **6,** 4617–4622 (1972).
111. Yu, P. Y. Resonant Brillouin Scattering of Exciton Polaritons. in *Light Scattering in Solids* (eds. Birman, J. L., Cummins, H. Z. & Rebane, K. K.) 143–158 (Springer US, 1979).
112. Hopfield, J. J. Theory of the contribution of excitons to the complex dielectric constant of crystals. *Phys. Rev.* **112,** 1555–1567 (1958).
113. Tait, W. C. Quantum theory of a basic light-matter interaction. *Phys. Rev. B* **5,** 648–661 (1972).
114. Bendow, B. & Birman, J. L. Polariton theory of resonance raman scattering in insulating crystals. *Phys. Rev. B* **1,** 1678–1686 (1970).
115. Ferrari, A. C. Raman spectroscopy of graphene and graphite: Disorder, electron-phonon coupling, doping and nonadiabatic effects. *Solid State Commun.* **143,** 47–57 (2007).
116. Martin, R. M. & Falicov, L. M. Light Scattering in Solids I. in *Topics in Applied Physics Vol. 8* (ed. Cardona, M.) 79 (Springer, 1983).
117. Póscik, I., Hundhausen, M., Koos, M., Berkese, O. & L., L. No Title. in *Proceedings of the*

XVI International Conference on Raman Spectroscopy (ed. Heyns, A. M.) 64 (Wiley-VCH, 1998).
118. Wang, Y., Alsmeyer, D. C. & McCreery, R. L. Raman Spectroscopy of Carbon Materials: Structural Basis of Observed Spectra. *Chem. Mater.* **2,** 557–563 (1990).
119. Endo, M. & Pimenta, M. A. Origin of dispersive effects of the raman d band in carbon materials. *Phys. Rev. B - Condens. Matter Mater. Phys.* **59,** R6585–R6588 (1999).
120. Saito, R., Takeya, T., Kimura, T., Dresselhaus, G. & Dresselhaus, M. S. Raman intensity of single-wall carbon nanotubes. **57,** 4145–4153 (1998).
121. Jorio, A. *et al.* Polarized raman study of single-wall semiconducting carbon nanotubes. *Phys. Rev. Lett.* **85,** 2617–20 (2000).
122. Lazzeri, M., Piscanec, S., Mauri, F., Ferrari, A. C. & Robertson, J. Phonon linewidths and electron-phonon coupling in graphite and nanotubes. *Phys. Rev. B - Condens. Matter Mater. Phys.* **73,** 155426 (2006).
123. MacIel, I. O. *et al.* Electron and phonon renormalization near charged defects in carbon nanotubes. *Nat. Mater.* **7,** 878–883 (2008).
124. Das, A. *et al.* Monitoring dopants by Raman scattering in an electrochemically top-gated graphene transistor. *Nat. Nanotechnol.* **3,** 210–215 (2008).
125. Grimm, S. *et al.* Doping-dependent G-mode shifts of small diameter semiconducting single-walled carbon nanotubes. *Carbon N. Y.* **118,** 261–267 (2017).
126. Caswell, N. & Solin, S. A. Vibrational excitations of pure FeCl3and graphite intercalated with ferric chloride. *Solid State Commun.* **27,** 961–967 (1978).
127. Yang, Z. hong & Wu, H. qing. Electrochemical intercalation of lithium into carbon nanotubes. *Solid State Ionics* **143,** 173–180 (2001).
128. Popeney, C. S. *et al.* Polyglycerol-derived amphiphiles for the solubilization of single-walled carbon nanotubes in water: A structure-property study. *ChemPhysChem* **13,** 203–211 (2012).
129. Wenseleers, W. *et al.* Efficient isolation and solubilization of pristine single-walled nanotubes in bile salt micelles. *Adv. Funct. Mater.* **14,** 1105–1112 (2004).
130. Huth, K. *et al.* Fluorescent Polymer—Single-Walled Carbon Nanotube Complexes with Charged and Noncharged Dendronized Perylene Bisimides for Bioimaging Studies. *Small* **14,** 1–11 (2018).
131. Yanagi, K. *et al.* Tuning of the thermoelectric properties of one-dimensional material networks by electric double layer techniques using ionic liquids. *Nano Lett.* **14,** 6437–6442 (2014).
132. Cottenye, N. *et al.* Raman tags derived from dyes encapsulated inside carbon nanotubes for Raman imaging of biological samples. *Phys. Status Solidi Appl. Mater. Sci.* **211,** 2790–2794 (2014).
133. Ernst, F., Heek, T., Setaro, A., Haag, R. & Reich, S. Energy transfer in nanotube-perylene complexes. *Adv. Funct. Mater.* **22,** 3921–3926 (2012).
134. Glaeske, M. & Setaro, A. Nanoplasmonic colloidal suspensions for the enhancement of the luminescent emission from single-walled carbon nanotubes. *Nano Res.* **6,** 593–601 (2013).
135. Bluemmel, P., Setaro, A., Maity, C., Hecht, S. & Reich, S. Tuning the interaction between carbon nanotubes and dipole switches: The influence of the change of the nanotube-spiropyran distance. *J. Phys. Condens. Matter* **24,** 394005 (2012).
136. Datsyuk, V. *et al.* Thermal transport of oil and polymer composites filled with carbon nanotubes. *Appl. Phys. A Mater. Sci. Process.* **105,** 781–788 (2011).
137. Setaro, A. Advanced carbon nanotubes functionalization. *J. Phys. Condens. Matter* **29,** 423003 (2017).
138. Brown, S. D. M. *et al.* Origin of the Breit-Wigner-Fano lineshape of the tangential G-band feature of metallic carbon nanotubes. *Phys. Rev. B - Condens. Matter Mater. Phys.* **63,** 155414 (2001).
139. Das, A. *et al.* Doping in carbon nanotubes probed by Raman and transport measurements. *Phys. Rev. Lett.* **99,** 136803 (2007).
140. Das, A. & Sood, A. K. Renormalization of the phonon spectrum in semiconducting single-

walled carbon nanotubes studied by Raman spectroscopy. *Phys. Rev. B - Condens. Matter Mater. Phys.* **79,** 235429 (2009).
141. Zaumseil, J., Jakubka, F., Wang, M. & Gannott, F. In situ raman mapping of charge carrier distribution in electrolyte-gated carbon nanotube network field-effect transistors. *J. Phys. Chem. C* **117,** 26361–26370 (2013).
142. Jakubka, F., Grimm, S. B., Zakharko, Y., Gannott, F. & Zaumseil, J. Trion electroluminescence from semiconducting carbon nanotubes. *ACS Nano* **8,** 8477–8486 (2014).
143. Ohno, Y. *et al.* Excitonic transition energies in single-walled carbon nanotubes: Dependence on environmental dielectric constant. *Phys. Status Solidi Basic Res.* **244,** 4002–4005 (2007).
144. Kiowski, O. *et al.* Photoluminescence microscopy of carbon nanotubes grown by chemical vapor deposition: Influence of external dielectric screening on optical transition energies. *Phys. Rev. B - Condens. Matter Mater. Phys.* **75,** 1–7 (2007).
145. Reich, S., Jantoljak, H. & Thomsen, C. Shear strain in carbon nanotubes under hydrostatic pressure. *Phys. Rev. B* **61,** R13389(R) (2000).
146. Leeuw, T. K. *et al.* Strain measurements on individual single-walled carbon nanotubes in a polymer host: Structure-dependent spectral shifts and load transfer. *Nano Lett.* **8,** 826–831 (2008).
147. Cronin, S. B. *et al.* Resonant Raman spectroscopy of individual metallic and semiconducting single-wall carbon nanotubes under uniaxial strain. *Phys. Rev. B - Condens. Matter Mater. Phys.* **72,** 35425 (2005).
148. Streit, J. *et al.* Alkane Encapsulation Induces Strain in Small-Diameter Single-Wall Carbon Nanotubes. *J. Phys. Chem. C* **122,** 11577–11585 (2018).
149. Setaro, A. *et al.* Preserving π-conjugation in covalently functionalized carbon nanotubes for optoelectronic applications. *Nat. Commun.* **8,** 14281 (2017).
150. Lim, J., Mintzer, M. A., Perez, L. M. & Simanek, E. E. Synthesis of odd generation triazine dendrimers using a divergent, macromonomer approach. *Org. Lett.* **12,** 1148–1151 (2010).
151. Whitesides, G. M. *et al.* Noncovalent Synthesis: Using Physical-Organic Chemistry to Make Aggregates. *Acc. Chem. Res.* **28,** 37–44 (1995).
152. Guo, Q. *et al.* Synthesis of carbon nitride nanotubes with the C3N4 stoichiometry via a benzene-thermal process at low temperatures. *Chem. Commun.* 26–27 (2004). doi:10.1039/b311390f
153. He, X. *et al.* Low-Temperature Single Carbon Nanotube Spectroscopy of sp3 Quantum Defects. *ACS Nano* **11,** 10785–10796 (2017).
154. Hooker, S., Migler, K., Migel, K. & Arepalli, S. Measurement Issues in Single Wall Carbon Nanotubes. *Natl. Inst. Stand. Technol. Spec. Publ.* **960–19,** 47 (2008).
155. Yu, R. *et al.* Platinum Deposition on Carbon Nanotubes via Chemical Modification. *Chem. Mater.* **10,** 718–722 (1998).
156. Setaro, A. *et al.* Chiral selectivity of polyglycerol-based amphiphiles incorporating different aromatic cores. *Phys. Status Solidi Basic Res.* **252,** 2536–2540 (2015).
157. Cognet, L. *et al.* Stepwise Quenching of Exciton Fluorescence in Carbon Nanotubes by Single-Molecule Reactions. *Science (80-.).* **316,** 1465 LP-1468 (2007).
158. Gebhardt, B. *et al.* Selective polycarboxylation of semiconducting single-walled carbon nanotubes by reductive sidewall functionalization. *J. Am. Chem. Soc.* **133,** 19459–19473 (2011).
159. Lee, Y. S. & Marzari, N. Cycloaddition functionalizations to preserve or control the conductance of carbon nanotubes. *Phys. Rev. Lett.* **97,** 1–4 (2006).
160. Allouche, J. *et al.* Hybrid spiropyran-silica nanoparticles with a core-shell structure: Sol-gel synthesis and photochromic properties. *J. Mater. Chem.* **20,** 9370–9378 (2010).
161. Farhat, H. *et al.* Softening of the Radial Breathing Mode in Metallic Carbon Nanotubes. *Phys. Rev. Lett.* **102,** 126804 (2009).
162. Dubay, O., Kresse, G. & Kuzmany, H. Phonon Softening in Metallic Nanotubes by a

Peierls-like Mechanism. *Phys. Rev. Lett.* **88,** 235506 (2002).
163. Ouyang, M., Huang, J.-L., Cheung, C. L. & Lieber, C. M. Energy Gaps in 'Metallic' Single-Walled Carbon Nanotubes. *Science (80-.).* **292,** 702–705 (2001).
164. Hatting, B. *et al.* Fermi energy shift in deposited metallic nanotubes: A Raman scattering study. *Phys. Rev. B - Condens. Matter Mater. Phys.* **87,** 165442 (2013).
165. Li, J., Jia, G., Zhang, Y. & Chen, Y. Bond-curvature effect of sidewall [2+1] cycloadditions of single-walled carbon nanotubes: A new criterion to the adduct structures. *Chem. Mater.* **18,** 3579–3584 (2006).
166. Bahr, J. L. & Tour, J. M. Covalent chemistry of single-wall carbon nanotubes. *J. Mater. Chem.* **12,** 1952–1958 (2002).
167. Bahr, J. L. *et al.* Functionalization of carbon nanotubes by electrochemical reduction of aryl diazonium salts: A bucky paper electrode. *J. Am. Chem. Soc.* **123,** 6536–6542 (2001).
168. Bahr, J. L. & Tour, J. M. Highly functionalized carbon nanotubes using in situ generated diazonium compounds. *Chem. Mater.* **13,** 3823–3824 (2001).
169. El-khoury, M., Voisiat, B., Kunze, T. & Lasagni, A. F. Utilizing Fundamental Beam-Mode Shaping Technique for Top-Hat La-ser Intensities in Direct Laser Interference Patterning. *J. Laser Micro/Nanoengineering* **13,** 268–272 (2018).
170. Liu, J. *et al.* Fullerene pipes. *Science (80-.).* **280,** 1253–1256 (1998).
171. Zhang, G. *et al.* Selective etching of metallic carbon nanotubes by gas-phase reaction. *Science (80-.).* **314,** 974–977 (2006).
172. Gebhardt, B. *et al.* Selective polycarboxylation of semiconducting single-walled carbon nanotubes by reductive sidewall functionalization. *J. Am. Chem. Soc.* **133,** 19459–19473 (2011).
173. Ki, K. K. *et al.* Fermi level engineering of single-walled carbon nanotubes by AuCl3doping. *J. Am. Chem. Soc.* **130,** 12757–12761 (2008).
174. López-Bezanilla, A., Triozon, F., Latil, S., Blase, X. & Roche, S. Effect of the chemical functionalization on charge transport in carbon nanotubes at the mesoscopic scale. *Nano Lett.* **9,** 940–944 (2009).
175. Zhou, W. *et al.* Charge transfer and Fermi level shift in p -doped single-walled carbon nanotubes. *Phys. Rev. B - Condens. Matter Mater. Phys.* **71,** 205423 (2005).
176. Setaro, A. *et al.* Polyglycerol-derived amphiphiles for single walled carbon nanotube suspension. *Chem. Phys. Lett.* **493,** 147–150 (2010).
177. Miyauchi, Y. & Maruyama, S. Identification of an excitonic phonon sideband by photoluminescence spectroscopy of single-walled carbon-13 nanotubes. *Phys. Rev. B - Condens. Matter Mater. Phys.* **74,** 35415 (2006).
178. Namilae, S., Chandra, N. & Shet, C. Mechanical behavior of functionalized nanotubes. *Chem. Phys. Lett.* **387,** 247–252 (2004).
179. Berger, S. *et al.* Optical properties of carbon nanotubes in a composite material: The role of dielectric screening and thermal expansion. *J. Appl. Phys.* **105,** 94323 (2009).
180. Huang, M. *et al.* Direct measurement of strain-induced changes in the band structure of carbon nanotubes. *Phys. Rev. Lett.* **100,** 136803 (2008).
181. Haggenmueller, R., Du, F., Fischer, J. E. & Winey, K. I. Interfacial in situ polymerization of single wall carbon nanotube/nylon 6,6 nanocomposites. *Polymer (Guildf).* **47,** 2381–2388 (2006).
182. Abdula, D. *et al.* Influence of defects and doping on optical phonon lifetime and Raman linewidth in carbon nanotubes. *Phys. Rev. B - Condens. Matter Mater. Phys.* **83,** 205419 (2011).
183. Vahala, K. *et al.* A phonon laser. *Nat. Phys.* **5,** 682–686 (2009).
184. Gambetta, A. *et al.* Real-time observation of nonlinear coherent phonon dynamics in single-walled carbon nanotubes. *Nat. Phys.* **2,** 515–520 (2006).
185. Beams, R., Cançado, L. G., Oh, S. H., Jorio, A. & Novotny, L. Spatial coherence in near-field Raman scattering. *Phys. Rev. Lett.* **113,** (2014).
186. Maruyama, S. *et al.* Estimating the Raman Cross Sections of Single Carbon Nanotubes. *ACS Nano* **4,** 3466–3470 (2010).

187. Gaufrès, E. *et al.* Giant Raman scattering from J-aggregated dyes inside carbon nanotubes for multispectral imaging. *Nat. Photonics* **8,** 72–78 (2013).
188. Glaeske, M., Bluemmel, P., Juergensen, S., Setaro, A. & Reich, S. Dipole-switch induced modification of the emissive response of carbon nanotubes. *J. Phys. Condens. Matter* **29,** 454003 (2017).

Selbstständigkeitserklärung

Hiermit versichere ich, dass ich alle verwendeten Hilfsmittel und Hilfen angegeben und die vorliegende Arbeit auf dieser Grundlage selbstständig verfasst habe. Diese Arbeit ist nicht schon einmal in einem früheren Promotionsverfahren eingereicht worden.

Georgy Gordeev